Physik-Department

Chirale Dynamik in Pion-Photon Reaktionen

Chiral Dynamics in Pion-Photon Reactions

Habilitationsschrift
zur Erlangung der venia legendi

eingereicht am Fachbereich Physik
der Technischen Universität München

Jan Michael Friedrich
geboren in Wiesbaden

September 2012

Technische Universität
München

Contents

1 Primakoff Reactions – Overview 15

2 Primakoff Compton Reaction and Pion Polarisability 21
- 2.1 Kinematics . . . 22
  - 2.1.1 The Primakoff Compton Reaction . . . 22
  - 2.1.2 Minimal momentum transfer q_{min} . . . 24
  - 2.1.3 Reconstruction of the momentum transfer . . . 25
  - 2.1.4 Lorentz-invariant variables . . . 26
  - 2.1.5 Back-transformation $p_\gamma(s,t,q^2,\Psi)$ and the range for Ψ . . . 29
  - 2.1.6 Lorentz transformation . . . 30
  - 2.1.7 Real-photon limit $q^2 \to 0$ . . . 33
  - 2.1.8 Constraints on the laboratory angles . . . 35
  - 2.1.9 Cut on the transverse momentum of the scattered pion . . . 36
  - 2.1.10 Relation of Mandelstam and laboratory variables . . . 36
- 2.2 Differential cross section . . . 39
  - 2.2.1 Real Compton scattering . . . 39
  - 2.2.2 Primakoff Compton cross section . . . 39
  - 2.2.3 Pion-nucleus bremsstrahlung . . . 41
  - 2.2.4 Muon Compton scattering . . . 43
- 2.3 Treatment of the q^2 spectrum . . . 43
  - 2.3.1 Weizsäcker-Williams factorization: equivalent-photon method . . . 43
  - 2.3.2 Sampling the equivalent-photon density . . . 44
  - 2.3.3 Atomic scattering factors . . . 44
- 2.4 Influence of pion-nucleus strong interaction . . . 44
  - 2.4.1 Scattering amplitudes from interaction with potentials . . . 44
  - 2.4.2 Eikonal approximation for the pion wave distortion . . . 45
  - 2.4.3 Form factors for the nuclear potentials . . . 47
- 2.5 QED radiative corrections . . . 48

2.5.1 Soft photon emission 48
2.5.2 Virtual photon loops 51
2.5.3 Effect on the polarisability determination 53
2.5.4 Further corrections 54

3 COMPASS Data Analysis for the Pion Polarisability 57
3.1 The COMPASS spectrometer setup 2009 57
3.2 Kinematic distributions 60
3.2.1 Longitudinal and transverse components of $\vec{q}$ 60
3.2.2 Spatial and angular resolution 61
3.2.3 Exclusivity peak and photon energy spectrum 62
3.2.4 Reconstructed momentum transfer distribution 63
3.3 Determination of the pion polarisability 65
3.3.1 Discussion of the polarisability result 65

4 Primakoff Pion Production 67
4.1 Channels accessible at COMPASS 67
4.1.1 Single-π^0 production 67
4.1.2 Two-π^0 production 68
4.2 Primakoff Two-Pion Production 68
4.2.1 Partial-wave analysis 70
4.2.2 Main resonances in the $\pi^-\pi^-\pi^+$ channel 71
4.2.3 Radiative coupling of the $a_2(1320)$ and of the $\pi_2(1670)$ 74
4.2.4 Coulomb-nuclear interference 75
4.2.5 Other radiative couplings 76
4.2.6 Reflectivity doubling 76
4.2.7 Cross-sections for $\pi^-\gamma \to \pi^-\pi^-\pi^+$ 77

5 Silicon Microstrip Detectors for COMPASS 79
5.1 Cooling the COMPASS silicon detectors 79
5.2 Future developments 81

Summary 85

A Formulæ and Algorithms 87
A.1 Series expansions 87
A.2 Integrals and Derivatives 88
A.3 Special functions 92
A.3.1 Gamma function 92

A.3.2 Bessel functions 92
A.4 Coulomb amplitudes in eikonal approximation 94
A.5 Radiative correction – numerical implementation 97

B Further Kinematic Aspects 111
B.1 Higher-order terms in the pion mass 111
B.2 Maximum scattering angles 112
B.3 Range of q^2 114
B.4 The transformation $p_\gamma(s,t,q^2,\Psi)$ 115
B.5 Energy transfer to the nucleus 116
B.6 Solving for $x(s,t,y,\psi)$ 117
B.7 Region of constrained Ψ range 118

C *Reproduction of* COMPASS Publications and Notes 121
C.1 The COMPASS setup for Physics with Hadron Beams, Sec. 5.1 123
C.2 CEDAR performance 2009 129
C.3 Reconstruction of the Pion Beam Energy 149
C.4 COMPASS-II Proposal, Ch. 4 “Experimental studies of ChPT” 153

D Articles on $\pi\gamma$ Reactions (printed version only) 169

Bibliography 171

Introduction

Consider a chair.

[S. Weinberg [67], in Ch. 19
"Spontaneously Broken
Global Symmetries"]

The standard model of elementary particle physics is a caesura of unprecedented depth and success in the human ambition to understand the schemes behind the observations of nature. The developments through the 20th century are, to a good share, based on the sound scientific ground for the natural sciences that quantum physics has created. Its inherent indeterminism may reflect the risks and the chances of further deepening this knowlegde, in terms of technological possibilities, the free will of the humans employing them, but also the openness of future in general.

The present work describes how the frontier of knowledge is pushed in the field of strong interactions. These forces govern the structure of the nuclei, forming the "backbone" of the atoms and molecules usual matter is made of. The knowledge about strong interactions is in an entangled state: While the gross features are understood and used in many earthy applications as well as explaining a vast number of astrophysical observations, both the theoretical and the experimental consolidation of even basic features are still a matter of ongoing research. The standard model is complete in the sense that it provides the basic building blocks for strongly interacting matter - quarks and gluons - and a description of the color force between them in quantum chromodynamics (QCD). It is, however, still a research field given that neither a series expansion in the coupling parameter provides a systematic approach, as it is established and very successful in the case of quantum electrodynamics (QED), nor do brute-force numerical integration methods allow an exact handling of chromodynamics.

A promising approach has been pioneered by S. Weinberg [66] and worked out by J. Gasser and H. Leutwyler [32–34]. The guiding principle is to recognize the symmetries of the QCD Lagrangian, and to exploit the related patterns in a systematic way, including symmetry-breaking. While it is general knowledge how *e.g.* the translational symmetry of space gives rise to momentum conservation, the symmetry of interest here is more complex and even not exact. Its origin is the smallness of the quark masses compared to the mass of the observed particles made up by quarks and gluons. This leads to a decoupling of left- and right-handed quarks inside the bound systems, and their independent transformation properties under flavour-space rotations imposes symmetry constraints on the observed particle spectrum and the corresponding dynamics. This mechanism has been explored by J. Goldstone [35] and worked out by C. G. Callan, S. Coleman et al. [21,23]. Its basic consequence is that spontaneous breaking of the chiral symmetry generates eight massless pseudoscalar meson states, the so-called Goldstone bosons. Explicit breaking of the chiral symmetry by non-zero quark masses - so to speak the back of the chair - leads to small masses of the Goldstone bosons, and consequently the lightest $J^P = 0^-$ meson octet is identified with these Goldstone bosons of spontaneous chiral symmetry breaking. Guided by the idea to describe their interactions from low energies on, the corresponding effective Lagrangian is organized as the derivative (small momenta) expansion in chiral perturbation theory (ChPT). The basic input parameters of ChPT are the masses and the decay constants of the Goldstone bosons. For the description of higher-order corrections, also a finite number of low-energy constants appears, which are *a priori* unknown and have to be adjusted to some experimental information. The theory acquires predictive power on this higher level of precision by linking various physical processes through the constraints of chiral symmetry.

The focus of the present work is on the properties of the lightest strongly-interacting particle, the pion. Its mass and lifetime are accurately known quantities, especially for the charged pion. The most longstanding riddle in establishing ChPT as correct approach for pionic interactions at low energies is posed by the pion polarisabilities. These quantities are determined, within ChPT, by low-energy constants and loop corrections with values that are fixed by other experiments on a high level of precision. The result is a firm prediction, *e.g.* for the electric polarisability $\alpha_\pi^{ChPT} = 2.9 \cdot 10^{-4}\,\mathrm{fm}^3$. Yet, the experiments done so far in the quest for measuring the pion polarisabilities directly[1] have reported a value more than twice as large [4, 11].

The investigation of ultra-peripheral scattering processes, at tiny momentum trans-

---

[1] Experiments on the $\gamma\gamma \to \pi^+\pi^-$ channel are excepted, because they involve a kinematic extrapolation that precludes to speak of a direct measurement [58].

fers where the electromagnetic interaction becomes dominant, *i.e.* the Primakoff effect discussed in detail in the following chapters, is particularily well suited to determine the polarisabilities with high accuracy. However, the pioneering experiment at Serpukhov in the early 1980's [11] could not reach a sufficiently high statistics, especially concerning important studies of systematic effects that can obscure the extraction of the pion polarisability. In 1996, it was proposed by the newly formed COMPASS collaboration (COmmon Muon and Proton Apparatus for Structure and Spectroscopy) to repeat the measurement at higher beam energy and with much higher statistics at the Super Proton Synchrotron (SPS) of the European Organization for Nuclear Research (CERN). This initiative was pushed by the Russian collaborators from Dubna and the German collaborators from Munich. At this higher beam energy, the outgoing particles are strongly boosted in forward direction, and in particular for the Primakoff kinematics their scattering angles are in the range of a few milliradians only, requiring the measurement of the particle trajectories at the limit of the technically and physically achievable resolution in the range of microradians.

In the author's group at the chair of Prof. Stephan Paul (TU München), the measurement was prepared from the year 2001 on by Monte Carlo simulations of the setup [48], and by the development and construction of the required high-precision silicon microstrip tracking detectors [12, 25, 30, 36, 61, 65, 68] for the relevant small angles. The usage of the information of these detectors has been optimized in several steps [49, 72], also extending the concept of detector alignment, which is usually done on a weekly basis, to the level of a few hours [26]. In November 2004, a first pilot run for the Primakoff measurement at COMPASS was done. Extensive analysis efforts were taken [26, 38], but finally it had to be concluded that especially the electromagnetic calorimetry, playing an essential role in determining the reactions of interest, was in a too preliminary state during the 2004 measurement for producing a physics result.

The apparatus was vastly improved in the subsequent time, especially concerning the calorimetry and its stability monitoring. The continuous liquid-nitrogen cooling of the silicon detectors to 200 Kelvin, allowing for a $\sim 20\%$ better spatial resolution, was also achieved [14, 15, 37]. The stable operation was especially challenging due to the specific requirement that the detectors are placed inside the acceptance of the larger-area detectors, and consequently shall not feature a massive cold-head geometry being the usual cryogenic approach. Some experimental artifices are due to the author, including a small phase separator installed in the vincinity of the detectors and ensuring that the thin capillary to the detector module is continuously supplied with purely liquid nitrogen.

In 2009, it was decided to take a two-week Primakoff run with a 190 GeV pion beam. Indeed, the data quality turned out to be much higher, but with the higher precision also a long list of shortcomings became apparent. Those were mostly on the level of an insufficient Monte Carlo description of the apparatus, and they could effectively be handled by refining this description. Examplary, the efficiency of the tracking detectors may be mentioned here. It was previously believed – actually a dangerous word in scientific context – that the redundancy of the more than 200 tracking detector planes is so high, that even larger uncertainties in their description do not affect the overall tracking effiency in a relevant manner. It was realized, however, that this was not the case, as too many detectors were affected. The silicon microstrip detectors were actually found to belong to the few correctly described detector groups. Repairing the insufficiencies settled the previously observed inconsistencies, that had hindered progress in the analysis for several months.

Some of the author's contributions to the data analysis concerning particle identification and beam properties are contained in the COMPASS notes reproduced in App. C.

As a result of all these efforts [53] systematic effects of the experiment are now understood, presumably on the level of the theoretical uncertainty. However, the lengthy procedure of preparing and releasing the result from the 2009 data set is still ongoing, hence an official COMPASS result can not be presented yet here. Especially because the result appears to deviate significantly from the earlier experimental findings and rather confirms the theoretical ChPT expectation, any possible criticism is to be anticipated and has to be seriously considered.

Along with preparing the two-week measurement for November 2009, the plan for a high-statistics Primakoff experiment was worked out by the author of the present work and included in the proposal by the COMPASS collaboration for a second phase COMPASS-II (the relevant chapter 4 is reproduced in the appendix). The program was approved by the SPS Committee in June 2011, and started in 2012 with the currently ongoing Primakoff running. A new development for this beam time, following an idea of the author, is a logics for the digital trigger that allows to select single-cluster events [41], extending the photon energy range in pion bremsstrahlung from previously 60 GeV down to 30 GeV (at a pion beam energy of 190 GeV).

The pion polarisability is determined from the precise measurement of the cross section of pion bremsstrahlung in forward kinematics, *i.e.* $\pi Z \to Z\pi\gamma$. This requires a number of corrections from the theoretical side, such as the QED radiative corrections. Regarding scalar QED as needed for pion interactions, the situation was found in a scientifically unsatisfactory state when this work was started. At the time of the Serpukhov experiment, the corrections had been calculated and published by A. Akhundov et al. only for the specific conditions of that experiment [5–7]. They were thus not available in a general form that would have made them applicable also under the changed conditions of other experiments, as it had been given long before for the electron and spin-

$\frac{1}{2}$-Compton scattering case [18, 51]. Consequently, in collaboration with N. Kaiser (TU München), the radiative corrections were worked out again and published in analytical form [45, 46]. This work confirmed the numercial values employed for the Serpukhov experiment [5]. Along with the implementation of the formulæ [46] for the analysis of the COMPASS data, as explained in detail in chapter 2 and in Sec. A.5, the present author succeeded in further simplifying the involved analytic expressions, also getting rid of the time-consuming numerical integrations given in [45]. This leads to a considerable simplification of the formalism, hence a reduction in computing time up to a factor 100, an aspect which might be of minor importance for the purely theoretical point of view, but which is decisive for the feasibility or at least the accuracy achieved in the required Monte Carlo simulations. In fact, much work has been invested in the present framework to bridge the gap from the basic theoretical understanding and description of the underlying process to the correct application for the actual experimental situation. The present work may partly look theory-overloaded, it nevertheless provides the complete documentation of the formalism as used in the analysis package for the COMPASS Primakoff program.

As a side remark, it is noted that the present author had worked out and implemented earlier, in cooperation with M. Vanderhaeghen and colleagues [29, 63], the QED radiative corrections to virtual Compton scattering off the proton $p\gamma^* \to p\gamma$. Actually this measurement has, complementary to the purely-mesonic case discussed in the present work, confirmed the ChPT prediction for the generalized proton polarisabilities [60]. The respective radiative corrections program code is still in use, *e.g.* for the high-statistics measurement of the proton form factor [13].

Further corrections concern the wave distortion of the scattered charged particle in the Coulomb field of a nucleus – corresponding to multiple photon exchange – and the screening of the nuclear Coulomb field by the atomic electrons. These Coulomb distortions have been treated for the present case of interest by G. Fäldt et al. [27] using the Glauber approach. It is presented with the inclusion of corrections and refinements by the author for a proper application in Sec. 2.4.2 of this work. The screening effect through the electrons can be treated on the same level as a modification of the charge form factor.

Also, for a quantitatively correct determination of the pion polarisabilities from the data, the known contribution to the cross-section from chiral pion loops [20, 31] has to be taken into account. It is implemented in the Monte Carlo generator written by the author for the COMPASS data analysis.

Realizing during the year 2007 that the detection of photons, and consequently of neutral pions $\pi^0 \to \gamma\gamma$, poses severe problems in the COMPASS 2004 data set, triggered the investigation of channels with charged particles in the final state that are related to the same physics of interest. In collaboration with N. Kaiser it was found that the process $\pi^-\gamma \to \pi^-\pi^-\pi^+$ was one of the low-energy $\pi^-\gamma$-induced reactions studied systematically in [44], that is accessible in the 2004 data. Together with D. Ryabchikov (IHEP Protvino) and S. Grabmüller (TU München) the reaction was indeed identified in analyzing a data sample of about 1 million preselected events. The separation from background reactions was only possible by employing a specially adapted partial wave analysis technique, that was published in 2011 in a letter [2] (reproduced in the appendix). The measured cross-section confirmed the tree-level ChPT prediction given in [44], which is not unexpected since ChPT is well established for the $\pi\pi$ scattering amplitude that enters in the considered energy range $< 5m_\pi$. Almost as important as this result can be seen the fact that the analysis employs successfully the Primakoff method as discussed in the following chapters, thus reconfirming its applicability. This is not to be taken as granted, since the formalism has still not often been exploited experimentally for strongly interacting particles. Therefore, establishing the experimental methods is also of high value for other envisaged Primakoff channels such as single π^0 production, governed at low energies by the chiral anomaly $F_{3\pi}$, *i.e.* the coupling of three pions to a photon.

The analysis of the 2004 data still has the potential of being pushed further: In the higher-mass region, the decay width of resonances R^- into the $\pi^-\gamma$ final state can be studied through the time-inverted process $\pi^-\gamma \to R^-$, and promising signals have been observed for the $a_2(1260)$ and $\pi_2(1670)$ resonances. While the radiative coupling of the a_2 has already been measured [52] and can just be checked with the COMPASS data, for the π_2 only now a first value gets in reach. A radiative coupling of the highly debated exotic $\pi_1(1600)$ state has also been searched for, but up to now not found, which is surprising in the light that its coupling to $\pi\rho$ is reported to be observed [8].

In addition, the very precise handling of the described corrections opens new possibilities for investigating the strong interaction. For example, the Coulomb-nuclear interference has been shown in the data analysis of the $\pi\gamma$ coupling to resonances in unprecedented detail: The interference term can be used to extract the relative phase of these two exchange mechanisms. This can be used to get a better understanding of the Pomeron as the effective exchange particle of the strong (absorptive) potential.

So, the investigations initialized within this work were able to broaden the research field, on top of the ambition to solve the riddle around the pion polarisability.

The present text has been started with the goal of being educational and inviting to interested newcomers to the field. However, with the rapid and still ongoing developments – many of the derived formulæ are not or not easily found in the literature, much of the analysis is very fresh – this standard could not be kept all the way through, and leaves it in a somewhat heterogenous state.

Some of the author's work pursued aside the presented topics are neither included in the text nor are the publications reproduced in the appendix. One concerns the non-observation of "pentaquarks" at COMPASS [25], for which the author has worked out the draft and chaired the drafting committee for the publication [3]. Another is the work in collaboration with Suh-Urk Chung (BNL/TU München) on covariant helicity amplitudes published in [22], which is the base for future high-precision partial wave analyses that aim at including relativistic effects in the decay of meson resonances. This omission was done to keep the present document in a reasonable volume.

Chapter 1

Primakoff Reactions – Overview

Quand tu veux construire un bateau, ne commence pas
par rassembler du bois, couper des planches et distribuer du travail,
mais réveille au sein des hommes le désir de la mer grande et large.

[*attributed to* Antoine de Saint-Exupéry]

The treatment of Primakoff reactions, which shall be explained and motivated in the following, is intrinsically a formal and numerical challenge: the relevant kinematic quantities, from the required beam momenta $p \sim 10^2$ GeV/c to the typically appearing momentum transfers to the target nuclei $q \sim 10^{-4}$ GeV/c introduce scales differing by six orders of magnitude, and the path to the desired physics information is prone to oversimplification and inadvertence. Yet, the key of the experimental technique is readily descibed: The high electromagnetic field in the vicinity of nuclei is used as a source of photons γ^*, especially when the collision of *e.g.* unstable particles with photons can not be realized in another more direct way. Such reactions, realizing particle-photon collisions with the photon provided by the Coulomb field of a nucleus, are named Primakoff reactions. This works even for particles that may also interact via the strong interaction with the nucleus, since the momentum transfer introduces an ordering scheme that separates the different interaction mechanisms, as will become clear along Chap. 2.

Primakoff reactions are interpreted with sound theoretical justification as effectively two-body processes in the case when in addition to the scattered incoming particle and the recoiling nucleus only one additional particle is produced (*e.g.* $\pi\gamma^* \to \pi\gamma$). The incoming quasi-real photon is provided by the electromagnetic field of the nucleus, $N \to N'\gamma^*$. It is indispensable for their quantitative understanding to calculate the exact kinematics. The major part of the cross section is focused in a tiny momentum transfer region on the scale $q_{\text{peak}} \sim 10^{-4}$ GeV/c. The cross section features heavy curvature, it vanishes for $q \to 0$, rises rapidly to q_{peak} and then falls off approximately $\propto q^{-2}$, *cf.* Fig. 1.1.

Apart from the experimental challenge to identify such small momentum transfers, the calculations must be carried out with great care, both on the algebraic and on the numerical side. Often the seemingly leading terms vanish or one faces series expansions with very slow convergence, and even when calculating numerically with "double-precision" ($\sim 10^{-15}$), round-off effects become sizeable and at times require specific recasting of the formulae.

Such small momentum transfers appear in ultra-peripheral collisions, when in position space the distance of the projectile and the target is large. For the scattering of a charged particle off a nucleus at a distance a few times larger than the radius of the nucleus, the strong interaction potential has practically vanished, however the electric field is still large. For example, in the vicinity of a lead (Z=82) nucleus at 20 fm distance from its center, the electric field strength is

$$E(r = 20\,\text{fm}) = \frac{1}{4\pi\varepsilon_0}\frac{Ze}{r^2} = 300\,\frac{\text{kV}}{\text{fm}} \tag{1.1}$$

The polarisability of a composed system is the measure for the amount of energy, stored in inner reconfiguration, when the system is exposed to an outer field. In case of an electric field, this response is expressed in terms of the induced electric dipole moment

$$\vec{p} = \alpha_{ch}\,\vec{E} \tag{1.2}$$

where α_{ch} is the electric polarisability. Its index refers to the picture of a pair of *ch*arges torn apart by $\vec{E}$, the SI unit is [C·m^2/V]. With a vacuum permittivity factor $10^6/4\pi\varepsilon_0$ multiplied, the unit becomes [cm^3]. For hadrons with a diameter in the range of a femtometer, the polarisabilities are rather expressed in units of [$10^{-4}\,\text{fm}^3$], *e.g.* for the proton the electric polarisability is precisely measured [55] to be $\alpha_p = 12.0 \cdot 10^{-4}\,\text{fm}^3$. For the pion, the polarisability α_π is expected from ChPT to be around $3.0 \cdot 10^{-4}\,\text{fm}^3$. Under the influence of a field as given in 1.1, this corresponds to a tiny elementary-charge separation of about $0.5 \cdot 10^{-4}$ fm. Assuming fractional charges or more complicated charge distributions, this value certainly varies, but it is obvious that the hadrons appear as extremely rigid objects when exposed to experimentally realizable fields.

Turning to the quantum mechanical description, the electromagnetic interaction of the pion with the Coulomb field of a nucleus is described to first order by the exchange of one virtual photon. In the ultra-peripheral collisions of interest here, the four-momentum of the exchanged photon $q^2 \to 0$ and the photons are quasi-real. Since in this limit the nucleus is elastically recoiling and takes only a vanishing amount of energy $E_r = \frac{q^2}{2M}$, the three-momentum transfer[1] $\vec{q}^2$ is practically the same as q^2. According to QED, the masslessness of the free photon implies a propagator behaviour $\sim 1/q^2$ when the photon appears as exchange particle. The consequence is a strong increase of the cross section for photon-exchange interactions at small momentum transfer.

This was first explored and used in the 1930's to calculate QED processes, specifically bremsstrahlung as discussed in detail in the section 2.2. An important observation, published by *von Weizsäcker* and *Williams* in 1934 [64,69], is that the cross sections for very small momentum transfer decouple into a real-photon cross section on the one hand, and a density of almost real, small-momentum photons on the other hand. Using this approximation for cross sections is called the equivalent photons method. The equivalent photon density increases with the charge number of the scatterer squared Z^2, such that the cross sections become large for heavy nuclei.

It is due to *Henry Primakoff* to propose in the year 1951 [59] the same mechanism for investigating processes of strongly interacting particles with real photons. It was the first method that allowed to measure the lifetime of the neutral pion, by inverting the decay $\pi^0 \to \gamma\gamma$ to induce its production by a real photon beam on a nuclear target

$$\gamma_{[\text{Beam}]} + \gamma_{[\text{Coulomb field of nucleus } Z]} \to \pi^0 \to \gamma + \gamma \tag{1.3}$$

It is noticed here again that seen from the nucleus – internally a complex strongly interacting system – the interaction is purely electromagnetic: The nucleus serves as a high-density source of (quasi-)real photons. The possibility of strong interaction is suppressed at larger impact parameters, where only the long-range Coulomb potential remains. Fig. 1.1 shows the sharply peaked calculated spectrum of q, compared to the measured one (actually measured with a muon beam). It is obvious that the underlying theoretical as well as the resolution-limiting effects of the apparatus must be understood extremely well, when the q-integrated measured cross section shall be interpreted in terms of the theoretical cross section.

The same principle can be applied to investigate the interaction of photons with other strongly interacting particles, as hyperons and the charged pions, worked out 1961 in a paper of *Pomeranchuk* and *Shmuskewich* [57]. Using high-energetic beams allows to observe scattering reactions also with short-lived particles, profiting from the relativistic increase of the decay length. The *Primakoff reactions* are observed with extremely small momentum transfer just above their kinematical threshold, which is described in detail in this work.

---

[1] The nomenclature used in the present work is systematically introduced in Sec. 2.1. In fact, due to the mentioned correspondence, q is (also) used as modulus of the three-momentum transfer

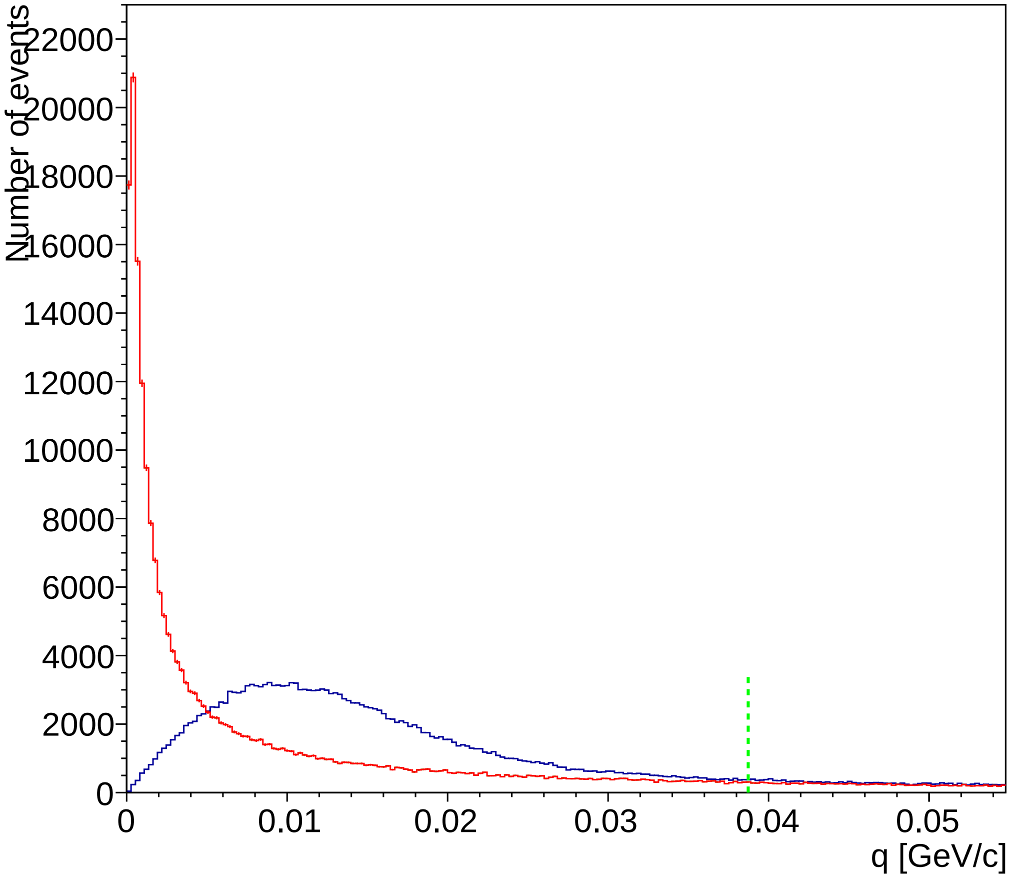

Figure 1.1: Distribution of momentum transfer q in the reaction $\mu\mathrm{Ni} \rightarrow \mathrm{Ni}\mu\gamma$ for the kinematic cuts presented in Ch. 3. The red histogram displays the true cross-section distribution as discussed in Sec. 2.2, the blue histogram is obtained from the analysis of the COMPASS data set taken in the year 2009. The achieved resolution in the range of 10 MeV/c is about a factor of 10 larger than the true peak structure, and allows a kinematic cut in the range 30–40 MeV/c, as indicated by the dashed line. From there on, systematic shifts due to bin migration in q are not relevant anymore. The depicted distribution is from the control measurements taken with a muon beam instead of pions. For the reaction of interest, $\pi\mathrm{Ni} \rightarrow \mathrm{Ni}\pi\gamma$, the q spectrum features additional structure due to the non-electromagnetic contribution from strong interaction, which is discussed along with the data analysis, *cf.* Fig.3.6. Concerning the Primakoff peak width, the pions feature the same values as the muons.

When charged pions scatter off the quasi-real photons surrounding the target nuclei, possible final states to observe are, indicating the addressed physics

$$\pi^\pm + \gamma^{(*)} \to \begin{cases} \pi^\pm + \gamma & \text{Compton reaction, pion polarisabilities} \\ \pi^\pm + \pi^0 & \text{single pion production, chiral anomaly} \\ \pi^\pm + \pi^0 + \pi^0 & \text{double pion production, chiral tree \& loop} \\ \pi^\pm + \pi^+ + \pi^- & \quad \text{contributions, resonances, search for exotics} \end{cases} \tag{1.4}$$

a list which can obviously be continued to more and heavier particles produced, appearing at higher threshold energies.

These interactions are distinguished in the experiment by forward kinematics of the outgoing particles, and the strong correlation of the outgoing particle momenta prescribed by the small momentum transfer to the nucleus.

The first reaction given in 1.4 is treated in great detail in Ch. 2. COMPASS has taken data for this reaction in order to determine the pion polarisability. The analysis of these data is described in Ch. 3. The other reactions are addressed shortly in Ch. 4.

More Primakoff reactions accessible at the COMPASS experiment include channels with one or more η particles in the final state and a similar group of reactions as 1.4 induced by kaons, which make up an $\sim$2.5% fraction of the negative hadron beam at 190 GeV. Their analysis is planned in the future, for which especially the ongoing data taking in 2012 is very promising.

Chapter 2

Pion Polarisability from the Primakoff Compton Reaction

This chapter starts with a complete discussion of the small-momentum transfer kinematics in the Primakoff region, from threshold to the domain where competing processes become important. From this will follow the motivation of the experimental technique to be employed.

Special weight is attributed to the pecularities of Primakoff measurements at the COMPASS experiment using the secondary pion beam of the CERN Super Proton Synchrotron (SPS). The pion beam energy can be chosen around 200 GeV, when the spectrometer covers fully the interesting angular (forward) region for the outgoing particles, and the resolution of the involved detectors is sufficiently high to kinematically identify the Primakoff events. This will be discussed in the coarse of this chapter, as *e.g.* the effect of the minimum transverse momentum of the scattered pion, necessary in order to resolve the interaction point in the target.

Experimentally, the Primakoff Compton events are inevitably admixed with events from the Primakoff process $\pi\gamma \to \pi\pi^0$, which are of physical interest themselves, as will be discussed in Chapter 4. This experimental overlap occurs either when the π^0 decays so asymmetrically, that one photon carries negligible energy and is not detected, or when the π^0 energy is so high that the decay photons "melt" into a single calorimeter cluster. This overlap advises an analysis of the data in terms of the two Primakoff reactions at the same time, featuring the pion polarisability in the former and the chiral anomaly in the latter.

2.1 Kinematics of the Primakoff Compton Reaction

2.1.1 The Primakoff Compton Reaction

The reaction to be identified experimentally is exclusive single photon production in the scattering of a pion off a nucleus with mass number A and charge Z,

$$\pi\ {}^{A}Z \longrightarrow \pi'\ {}^{A}Z'\ \gamma \tag{2.1}$$

Measured (or known) quantities are the energy-momentum vectors of the beam pion $p^{\mu} = (E, \vec{p})$, of the scattered pion $p^{\mu}_{\pi} = (E_{\pi}, \vec{p}_{\pi})$ and of the photon $p^{\mu}_{\gamma} = (E_{\gamma}, \vec{p}_{\gamma})$. The kinematics of the recoiling nucleus is described the momentum transfer vector $q^{\mu} = (-E_r, \vec{q})$, being by definition oriented opposite to the recoil, such that the process 2.1 can be treated effectively as the reaction

$$\begin{array}{cccc c} \pi & \gamma^{*} & \rightarrow & \pi' & \gamma \\ (E, \vec{p}) & (-E_r, \vec{q}) & & (E_{\pi}, \vec{p}_{\pi}) & (E_{\gamma}, \vec{p}_{\gamma}) \end{array} \tag{2.2}$$

with γ^{*} an incoming particle, namely the virtual photon from the Coulomb field of the nucleus. Furthermore, in the following[1] the notation $p = |\vec{p}|$, $p_{\pi} = |\vec{p_{\pi}}|$, $p_{\gamma} = E_{\gamma} = |\vec{p_{\gamma}}|$ is used. The exclusive reaction must be separated from competing (non-exclusive) processes with the same observed particles in the final state, as discussed in detail in Sec. 2.4.

The relative orientation of the particle momenta (*cf.* Fig. 2.1) is described by the scattering angles θ_{π}, θ_{γ}, and the angle between the scattered particles $\theta_{\pi\gamma}$. The kinematics of a specific final state is completely determined by a set of four variables, *e.g.* $(E_{\gamma}, \theta_{\gamma}, \theta_{\pi}, \theta_{\pi\gamma})$. Since the pion has spin zero and only the interaction with the rotationally symmetric Coulomb field of the nucleus is treated, the kinematics is rotationally invariant around the beam axis, and the respective angle ϕ needs not be further considered.

Energy conservation reads

$$E = E_{\pi} + E_{\gamma} + E_r \tag{2.3}$$

E_r is the energy transferred to the nucleus, assumed to be negligibly small, $E_r \rightarrow 0$. In fact, the recoil energy is negligible due to the smallness of the momentum transfer compared to the mass of the nucleus (for the justification of the neglect of nuclear excitations, s. sec. B.5). Hence, the simple relation $E = E_{\pi} + E_{\gamma}$ holds for the energies

---

[1] Units with $\hbar = c = 1$ are used.

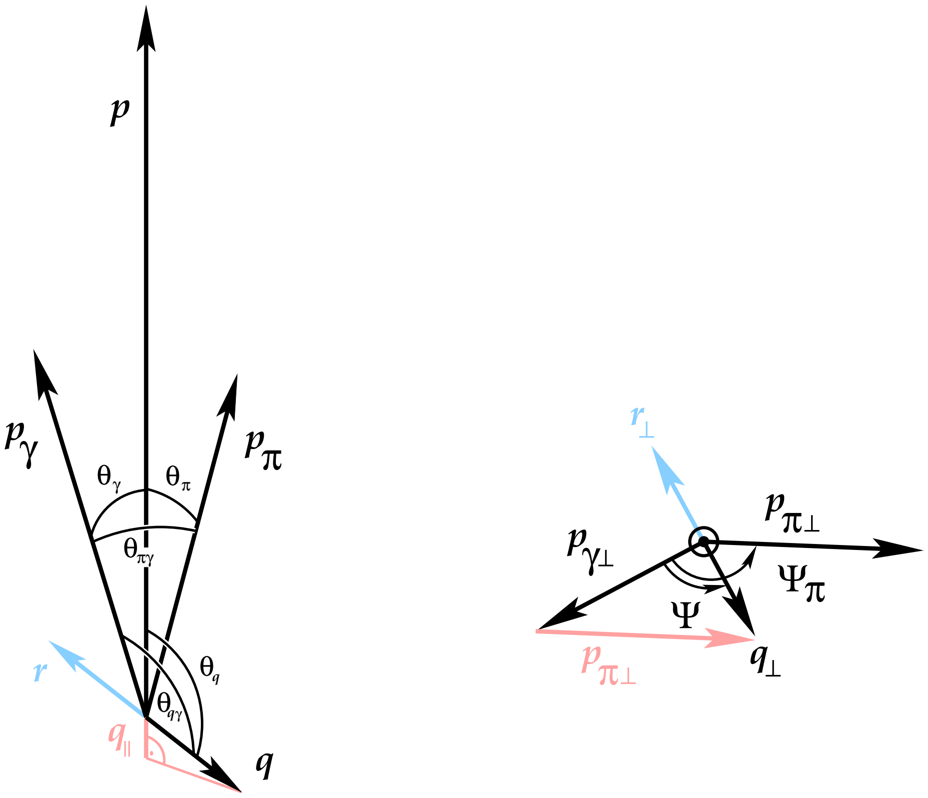

Figure 2.1: Nomenclature for Primakoff Compton kinematics. The incoming beam momentum p is "split" by the interaction with the nucleus into the scattered pion with momentum p_π and the produced photon with momentum p_γ. The momentum transfered to the recoiling nucleus is $\vec{r} = -\vec{q}$. Compared to typical kinematics in the COMPASS experiment, in the figure the angles of the scattered pion and the real photon are enlarged by a factor of about 10 and the length of q by a factor 100. The right graph shows the balance of the momentum components transverse to the incoming beam direction.

of the observed particles. For their momenta, on the other hand, the non-vanishing 3-momentum transfer to the nucleus,

$$\vec{q} = \vec{p}_\pi + \vec{p}_\gamma - \vec{p} \tag{2.4}$$

is of particular importance, since this is the quantity which allows for a separation of the Primakoff reaction *e.g.* from strong-interaction contributions. The sign of $\vec{q}$ is chosen such that $\vec{q}$ is the momentum transfer of the incoming (virtual) photon colliding with the beam pion (cf. Fig. 2.1: The longitudinal component $q_\parallel$ points opposite to the beam momentum), and, formally, $E_q = q^0 < 0$. However, the energy component of the four-vector q^μ is assumed to vanish $E_q = -E_r \to 0$ in the laboratory system (see above), and $q > 0$ can (and will) be used in the following for the modulus of the 4- and 3-momentum equivalently.

2.1.2 Minimal momentum transfer q_{min}

Four-momentum conservation in the process (2.1) implies a lower treshold for q. The minimum momentum transfer q_{min} for a given E_γ is an important kinematical quantity, ruling the q^2 dependence of the differential Primakoff cross section as outlined in Sec. 2.2. This minimum value occurs in exact longitudinal kinematics $\vec{p} \parallel \vec{p}_\pi \parallel \vec{p}_\gamma$ and is given, to leading order in the pion mass (for higher-order terms see Sec. B.1), by

$$q_{\text{min}} = q_{\text{min}}(E_\gamma) \doteq \frac{m_\pi^2 \cdot E_\gamma}{2E(E-E_\gamma)}, \qquad q_{\text{min}}(s) \doteq \frac{s - m_\pi^2}{2p} \tag{2.5}$$

where s is the squared center-of-momentum energy in the pion-photon subsystem.

While the two expressions (necessarily, they are both correct) coincide for any kinematics with $q = q_{\text{min}}$, the right-hand sides differ when evaluated for an arbitrary kinematics where $q > q_{\text{min}}$. The reason is that, when varying $q \to q_{\text{min}}$, two different "paths" through the phase space are to be considered.

The first expression $q_{\text{min}}(E_\gamma)$ refers to the limiting kinematics with the same real photon energy E_γ, and only the laboratory angles are aligned to $\theta_\gamma = \theta_\pi = \theta_{\pi\gamma} = 0$. The exact expression, from which $q_{\text{min}}(E_\gamma)$ is derived for fixed-E_γ kinematics, reads

$$\begin{aligned} q_{\text{min}}(E_\gamma) &= p - p_\pi - p_\gamma \\ &= (E_\pi - p_\pi) - (E - p) \end{aligned} \tag{2.6}$$

and higher terms in m_π^2, beyond the leading term given in Eq. 2.5, are obtained by expanding $(E-p)$ and $(E_\pi - p_\pi)$ according to (A.1). – The use of $q_{\text{min}}(E_\gamma)$ is appropriate *e.g.* in the analysis of experimental data, when the q^2 distribution is examined for a single bin in E_γ. If not otherwise stated, in the following q_{min} refers to this first expression $q_{\text{min}}(E_\gamma)$, as it often occurs in this form also in the formulæ relating kinematical quantities, as e.g. in Eqs. 2.8–2.16.

The second expression $q_{\text{min}}(s)$ in Eq. 2.5 links kinematics with including fixed-s as introduced in Sec. 2.1.4, while varying $q \to q_{\text{min}}(s)$. This may be very different from keeping E_γ constant as can be understood with the relations derived in the following section (see Eq. 2.15): When s is kept constant, the limiting kinematics with $\theta_{\pi\gamma} = 0$ is reached by increasing E_γ to large values, typically close to the beam energy E (unless very small s are considered), and consequently $q_{\text{min}}(s) \gg q_{\text{min}}$. – Further, it is noted that $q_{\text{min}}(s)$ in Eq. 2.5 is the approximation of the exact relation

$$q_{\text{min}}(s) = \frac{s - m_\pi^2}{2p} + \frac{q_{\text{min}}^2(s)}{2p} \tag{2.7}$$

so the exact $q_{\text{min}}(s)$ can be found either by solving this quadratic equation (resulting in the subtraction of two almost equal numbers of the order of p), or by iterating Eq. 2.7, starting with $q_{\text{min}} = 0$. The latter is numerically favorable, since $q_{\text{min}}^2(s)$ is tiny even compared to $s - m_\pi^2$ in all kinematics of interest here, and convergence to double precision is achieved in a single step.

2.1.3 Reconstruction of the momentum transfer

The four-momentum transfer is reconstructed by balancing the observed four-vectors, $q^\mu = p_\pi^\mu + p_\gamma^\mu - p^\mu$. Here, the constraint $q^0 = 0$ helps to partly compensate for the limited precision of the detectors. Since the dominant uncertainty in the direct calculation of q^μ stems from the (calorimetric) photon energy measurement, a full constrained fit of the kinematics can be simplified to an appropriate rescaling of the magnitude of the photon momentum vector. Since the directions of all particles, including the outgoing photon, determine in their sum the transverse momentum balance, and this is the key signature of the Primakoff reaction, they must be measured as precisely as possible.

Since usually there is a strong compensation of the large momenta of the observed particles, yielding the tiny remainder q, it is favorable to use the formal relation ensuring the correct limiting behaviour. For an event with measured quantities $(E_\gamma, \theta_\gamma, \theta_\pi, \theta_{\pi\gamma})$, its modulus is given by

$$q^2 = q_{\text{min}}^2 + 4pp_\gamma \sin^2\frac{\theta_\gamma}{2} + 4pp_\pi \sin^2\frac{\theta_\pi}{2} - 4p_\pi p_\gamma \sin^2\frac{\theta_{\pi\gamma}}{2} \tag{2.8}$$

as it is shown below, *cf.* Eq. 2.17. It is obvious that using this formula for the collinear kinematics $\theta_\gamma = \theta_\pi = 0$, the momentum transfer q takes on the correct value q_{min}. This is numerically problematic if subtracting four-vectors of length ∼100 GeV/c to find q values in the range of 10^{-3} GeV/c. For the considerations in the following sections, the splitting of $\vec{q}$ in components parallel and transverse to the incoming pion direction is needed, given by (defining $q_\parallel$ as a positive quantity; for a visualisation of these quantities cf. Fig. 2.1)

$$\begin{aligned} q_\parallel &= p - p_\gamma \cos\theta_\gamma - p_\pi \cos\theta_\pi \\ &= q_{\text{min}} + 2p_\gamma \sin^2\frac{\theta_\gamma}{2} + 2p_\pi \sin^2\frac{\theta_\pi}{2} \qquad (2.9) \\ q_\perp &= \sqrt{q^2 - q_\parallel^2} \qquad (2.10) \end{aligned}$$

2.1.4 Lorentz-invariant variables

The Mandelstam variables in the pion-photon subprocess are

$$s = (p_\pi^\mu + p_\gamma^\mu)^2 \qquad (2.11)$$

$$t = (p^\mu - p_\pi^\mu)^2 \qquad (2.12)$$

$$u = (p^\mu - p_\gamma^\mu)^2 \qquad (2.13)$$

and fulfill the relationship

$$s + t + u = 2m_\pi^2 - q^2 \qquad (2.14)$$

They are related to the quantities measured in the experiment by

$$s = m_\pi^2 + 2E_\gamma \cdot (E_\pi - p_\pi) + 4p_\pi p_\gamma \sin^2\frac{\theta_{\pi\gamma}}{2} \qquad (2.15)$$

$$t = -q_{\text{min}}^2 - 2\,E_\gamma \cdot q_{\text{min}} - 4p\,p_\pi \sin^2\frac{\theta_\pi}{2} \qquad (2.16)$$

$$u = m_\pi^2 - 2E_\gamma \cdot (E - p) - 4p\,p_\gamma \sin^2\frac{\theta_\gamma}{2} \qquad (2.17)$$

Using Eq. 2.14 one deduces Eq. 2.8. The (rapidly converging) expansion of the terms $(E - p)$ and $(E_\pi - p_\pi)$ in m_π^2 is obtained as given in Appendix A. The range of t is limited for given s and q^2 by

$$t_{\text{min/max}} = -\frac{\bar{s}^2 + q^2(s + m_\pi^2)}{2s} \pm \frac{\bar{s}}{2s}\sqrt{(\bar{s} + q^2)^2 + 4m_\pi^2 q^2} \qquad (2.18)$$

where the short-hand notation

$$\bar{s} = s - m_\pi^2 \tag{2.19}$$

has been introduced. For the cases of interest, $s > m_\pi^2 > q^2$ is usually satisfied, and then from Eq. 2.18 follows $s > -t > 0$. More precisely, the limits of the t range become transparent when the square root term is expanded in orders of $q^2/\left[(\bar{s}+q^2)^2/4m_\pi^2\right]$,

$$t_{\max} = -\frac{q^4}{s}\cdot\frac{m_\pi^2}{(\bar{s}+q^2)}\cdot\left[1+\frac{m_\pi^2\bar{s}}{(\bar{s}+q^2)^2}\right] + \mathcal{O}(q^6) \tag{2.20}$$

$$t_{\min} = -\frac{\bar{s}^2+q^2(s+m_\pi^2)}{s} - t_{\max} \tag{2.21}$$

For later use, especially in section 2.1.5, the positive quantity[2]

$$\tau = t - t_{\min} \tag{2.22}$$

is introduced, in terms of which $t = t_{\min} + \tau$ and

$$u = \frac{m_\pi^4 + q^2 m_\pi^2}{s} + t_{\max} - \tau \tag{2.23}$$

The range of u is

$$u_{\min/\max} = t_{\min/\max} + \frac{m_\pi^4 + q^2 m_\pi^2}{s} \tag{2.24}$$

It shall be emphasized that $u = 0$ lies within the kinematic region of interest, and some care is needed when terms with u in the denominator appear, as *e.g.* in the context of radiative corrections (*cf.* Eq. 2.107 and A.5).

The Mandelstam variables can be interpreted in the center-of-momentum frame (CM) of the pion-photon subsystem, shown in Fig. 2.2. The momenta q_{CM} and p_{CM} of the incoming and outgoing particles, respectively, are determined by s and q^2

$$q_{CM} = \frac{\sqrt{(s-m_\pi^2)^2 + q^2(2s+2m_\pi^2+q^2)}}{2\sqrt{s}} \tag{2.25}$$

$$= \sqrt{q^2 + \frac{(s-m_\pi^2-q^2)^2}{4s}} \tag{2.26}$$

$$p_{CM} = \frac{s-m_\pi^2}{2\sqrt{s}} \tag{2.27}$$

---

[2] this is not to be confused with the (also positive) quantity t' used *e.g.* in diffractive hadron scattering physics, which reads in our notation $t' = -q_\mu q^\mu - q^2_{\min} = q^2 - q^2_{\min}$, keeping in mind that the energy transfer to the nucleus is neglected here.

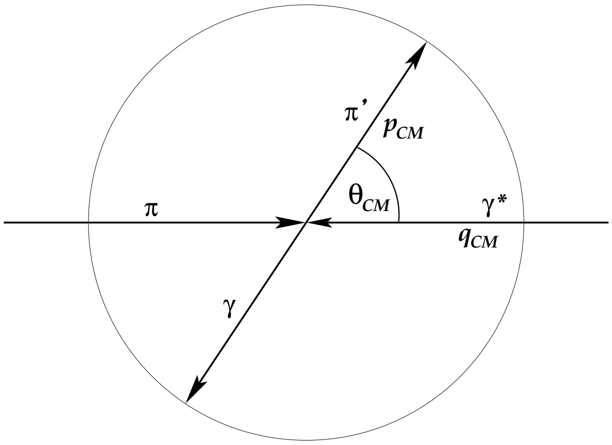

Figure 2.2: Kinematics of the $\pi+\gamma^* \to \pi'+\gamma$ reaction in the center-of-momentum frame. Since the incoming photon has a squared mass $-q^2 < 0$, the momenta of the outgoing particles are smaller than those of the incoming particles (The photon must be "lifted" to its mass shell).

while the *CM* scattering angle is related to the Mandelstam variables by

$$\cos\theta_{CM} = \frac{2t - t_{\max} - t_{\min}}{t_{\max} - t_{\min}} \tag{2.28}$$

where s and q^2 enter indirectly via $t_{\min}$ and $t_{\max}$.

Eq. 2.14 implies that only three of the four variables s, t, u, q^2 are independent, and in the following, the set (s, t, q^2) is taken. In order to complete the set of invariant quantities, the (laboratory frame) angle Ψ between the planes (p, p_γ) and (p, q) is added[3] in the following, leading to a one-to-one relation $(E_\gamma, \theta_\gamma, \theta_\pi, \theta_{\pi\gamma}) \longleftrightarrow (s, t, q^2, \Psi)$. The angle Ψ is obtained from the laboratory quantities by (c.f. Fig. 2.1 regarding the transverse components)

$$\cos\Psi = \frac{q_\perp^2 + p_\gamma^2 \sin^2\theta_\gamma - p_\pi^2 \sin^2\theta_\pi}{2q_\perp p_\gamma \sin\theta_\gamma} \tag{2.29}$$

where $q_\perp$ is given by Eqs. 2.9 and 2.10.

---

[3] Unlike s, t and q^2, the angle Ψ is not an invariant quantity, however it is invariant under a boost along the beam direction $\vec{p}$.

2.1.5 Back-transformation $p_\gamma(s, t, q^2, \Psi)$ and the range for Ψ

Eqs. 2.14–2.17 and 2.29 define completely how to get the set (s, t, q^2, Ψ) when the laboratory quantities $(E_\gamma, \theta_\gamma, \theta_\pi, \theta_{\pi\gamma})$ are known. The respective back-transformation is more involved, however, it is needed in the implementation of the cross-section in the Monte Carlo generator employed for the analysis of the COMPASS data. While the three angles $(\theta_\gamma, \theta_\pi, \theta_{\pi\gamma})$ are easily obtained for given (s, t, q^2) by solving Eqs. 2.15–2.17 once p_γ is known, the way how to find p_γ is tricky.

A key step is to observe that the (laboratory) components of q are given by

$$q_{\|}(s,q^2) \;=\; \frac{s-m_\pi^2+q^2}{2p} \tag{2.30}$$

in consistency with Eq. 2.7 regarding the limit $q \to q_{\min}(s)$, in which $q = q_{\|} = q_{\min}(s)$. Then, one considers

$$\begin{aligned} t &= (p_\gamma^\mu - q^\mu)^2 \\ &= -q^2 - 2p_\gamma(q_{\|}\cos\theta_\gamma + q_\perp \cos\Psi \sin\theta_\gamma) \end{aligned} \tag{2.31}$$

and replacing p_γ as given by Eq. 2.17,

$$p_\gamma \;=\; \frac{m_\pi^2 - u}{2(E - p\cos\theta_\gamma)} \tag{2.32}$$

yields a quadratic equation for $\cos\theta_\gamma$, solved by

$$\cos\theta_\gamma \;=\; \frac{E_\tau p_\tau - q_\tau\sqrt{q_\tau^2 + p_\tau^2 - E_\tau^2}}{p_\tau^2 + q_\tau^2} \tag{2.33}$$

with

$$\begin{aligned} E_\tau &= E\cdot(t+q^2) \\ p_\tau &= p\cdot(t+q^2) \;-\; q_{\|}\cdot(m_\pi^2 - u) \\ q_\tau &= (m_\pi^2 - u)\cdot q_\perp \cos\Psi \end{aligned} \tag{2.34}$$

Putting the solution for $\cos\theta_\gamma$, Eq. 2.33, back into Eq. 2.32 gives an exact formula for $p_\gamma(s, t, q^2, \Psi)$. In order to display the dependence on q and Ψ, the square root term in Eq. 2.33 is written

$$\begin{aligned} q_\tau^2 + p_\tau^2 - E_\tau^2 &= -t(-us + m_\pi^4 + q^2 m_\pi^2) - q^4 m_\pi^2 - q_\perp^2 (m_\pi^2 - u)^2 \sin^2\Psi \\ &= s\,\tau(t_{\max} - t) - q_\perp^2 (m_\pi^2 - u)^2 \sin^2\Psi \end{aligned} \tag{2.35}$$

The region $\tau \approx 0$ ($t \longrightarrow t_{\min}$), featuring a restricted range in Ψ, is discussed in Appendix B.7. It refers to very small pion scattering angles and is not considered in the experiment, since it has to be excluded due to the multiple scattering effect treated in Sec. 2.1.9.

For the region of interest, the second term in Eq. 2.35 is negligible compared to the term proportional to τ, so

$$\cos\theta_\gamma \doteq E_\tau/p_\tau - q_\tau\sqrt{s\,\tau(t_{\max}-t)}\,/\,p_\tau^2 \tag{2.36}$$

and

$$\begin{aligned} p_\gamma &\doteq \frac{p^2}{E}\cdot\frac{-t-q^2-q_\tau\sqrt{s\,\tau(t_{\max}-t)}}{s-m_\pi^2+q^2}+\frac{m_\pi^2-u}{2E} \\ &\approx p\cdot\frac{-t-q^2-q_\tau\sqrt{s\,\tau(t_{\max}-t)}}{s-m_\pi^2+q^2} \end{aligned} \tag{2.37}$$

2.1.6 Parametric description of the Lorentz transformation

Transforming the four-vectors in scattering processes as treated here from *e.g.* the laboratory into the *CM* system is, obviously, a well-established procedure. It is, however, non-trivial to disentangle the involved rotations and boosts and give them in terms of a given set of variables (s, t, q^2, Ψ). Since this is needed in the numerical implementation of the radiative corrections, it is discussed in this section.

The first step is depicted in Fig. 2.3. The boost direction deviates slightly from the beam direction, with an invariant perpendicular component $q_\perp^B$ (the index B used for quantities in the boost frame). For obtaining the quantities in the laboratory frame, with the z axis along the beam direction, the corresponding rotation by the angle θ_p has to be applied as second step. Assuming a given set (p, s, q^2), from the right triangles on both sides of the long dashed line follows

$$(p+q_\parallel)^2+q_\perp^2 = \left(2q_\perp^B\right)^2+\left(\sqrt{p^2-\left(q_\perp^B\right)^2}+q_\parallel^B\right)^2 \tag{2.38}$$

$$\left(q_\perp^B\right)^2 = \frac{p^2(q^2-q_\parallel^2)}{p^2+q^2-2\,q_\parallel\,p} = \frac{p^2}{p^2-\bar{s}}\,q_\perp^2 \tag{2.39}$$

$$= \frac{4p^2q^2-(\bar{s}+q^2)^2}{4(p^2-\bar{s})} \tag{2.40}$$

$$\left(q_\parallel^B\right)^2 = \frac{p^2q_\parallel^2-q^2\bar{s}}{p^2-\bar{s}} = \frac{(\bar{s}-q^2)^2}{4(p^2-\bar{s})} \tag{2.41}$$

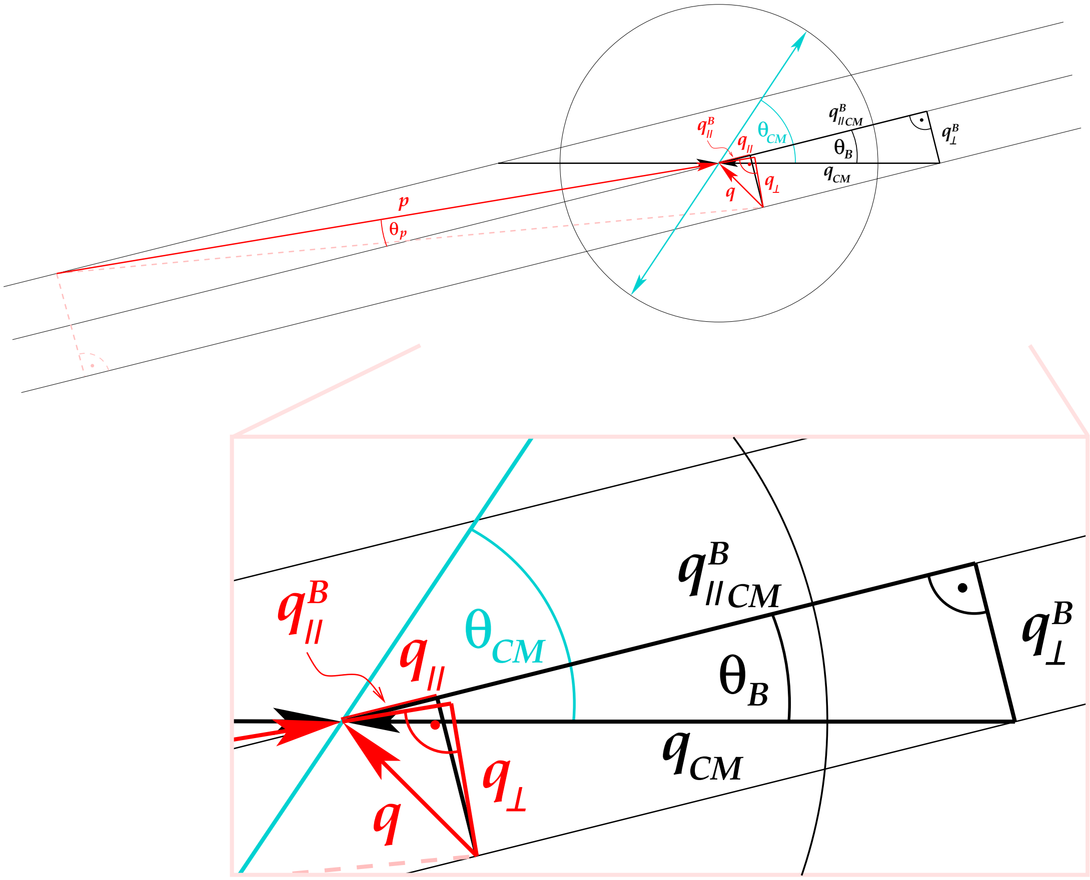

Figure 2.3: Quantities for the incoming particles appearing in the Lorentz transformation from the center-of-momentum frame (black) to the laboratory frame (red). The transformation consists of a boost along the direction of $\vec{q}^{\,B}_{||(CM)}$, and a rotation by θ_p bringing $\vec{p}$ in z direction, with respect to which the decomposition into parallel and perpendicular components is performed. The q components in the laboratory frame are enlarged in the same manner as in Fig. 2.1, and also the boost is shrinked in order to fit the sketch. For better readability, the central geometry is redrawn magnified. The production plane, containing the outgoing particles π' and γ, might be arbitrarily rotated around the incoming particle's axis in the CM, which is to be taken properly into account in the transformation.

where $q_{\|}$ is given by Eq. 2.30 and $\bar{s}$ by Eq. 2.19. The first expression given in Eq. 2.39 follows directly as solution of the quadratic equation 2.38 for $q_{\perp}^{B} = \sqrt{q^2 - (q_{\|}^{B})^2}$, while the second expression displays that $q_{\perp}^{B}$ is almost the same as $q_{\perp}$, except a correction factor approaching unity for large laboratory beam momentum $p \gg \sqrt{s}$. Apart from the additional term in the numerator, Eq. 2.41 shows a similar relation for $q_{\|}^{B}$ and $q_{\|}$. Eq. 2.40 and the second version of Eq. 2.41 present the result in terms of the given quantities (p, s, q^2) and are used in the calculation of Eq. 2.46. As intermediate steps,

$$\begin{aligned} q_{\|_{CM}}^{B} &= \sqrt{q_{CM}^2 - \left(q_{\perp}^{B}\right)^2} = \sqrt{q_{E\,CM}^2 + (q_{\|}^{B})^2} && (2.42) \\ &= \sqrt{q_{CM}^2 - q^2 + (q_{\|}^{B})^2} && (2.43) \\ q_{CM}^2 - q^2 &= \frac{(s - m_{\pi}^2 - q^2)^2}{4s} && (2.44) \end{aligned}$$

are easily calculated, and the Lorentz factor $\gamma = 1/\sqrt{1-\beta^2}$ follows

$$\begin{aligned} q_{\|}^{B} &= -\beta\gamma\, q_{E\,CM} + \gamma\, q_{\|_{CM}}^{B} && (2.45) \\ \gamma &= \frac{q_{\|_{CM}}^{B}}{q_{\|}^{B}} = \frac{E}{\sqrt{s}} && (2.46) \end{aligned}$$

independent of the value of q. The tilt angle θ_B of the boost direction in the *CM* system and the laboratory beam rotation angle θ_p, cf. Fig. 2.3, are obtained via

$$\begin{aligned} \tan\theta_B &= \frac{q_{\perp}^{B}}{q_{\|_{CM}}^{B}} = \frac{p}{E} \cdot \frac{2q_{\perp}\sqrt{s}}{|\bar{s} - q^2|} && (2.47) \\ \tan\theta_p &= \frac{q_{\perp}^{B}}{\sqrt{p^2 - (q_{\perp}^{B})^2}} = \frac{q_{\perp}}{\sqrt{p^2 - \bar{s} - q_{\perp}^2}} && (2.48) \end{aligned}$$

The outgoing momentum vectors in the laboratory frame are then, cf. Fig. 2.4,

$$\begin{aligned} p_{\pi CM} = p_{CM} \begin{pmatrix} x_{CM} \\ y_{CM} \\ z_{CM} \end{pmatrix} &= p_{CM} \begin{pmatrix} -\sin\theta_{CM}\cos\Psi_{CM} \\ -\sin\theta_{CM}\sin\Psi_{CM} \\ \cos\theta_{CM} \end{pmatrix} \\ \longrightarrow \qquad p_{CM} \begin{pmatrix} x_B \\ y_B \\ z_B \end{pmatrix} &= p_{CM} \begin{pmatrix} x_{CM}\cos\theta_B - z_{CM}\sin\theta_B \\ y_{CM} \\ \beta\gamma\epsilon_{CM} + \gamma\,(x_{CM}\sin\theta_B + z_{CM}\cos\theta_B) \end{pmatrix} \\ \longrightarrow \qquad p_{\pi lab} = p_{CM} \begin{pmatrix} x_{lab} \\ y_{lab} \\ z_{lab} \end{pmatrix} &= p_{CM} \begin{pmatrix} x_B\cos\theta_p + z_B\sin\theta_p \\ y_B \\ -x_B\sin\theta_p + z_B\cos\theta_p \end{pmatrix} && (2.49) \end{aligned}$$

where in $\epsilon_{\scriptscriptstyle CM} = \sqrt{1+m^2/p^2_{\scriptscriptstyle CM}}$ the appropriate mass m of the particle to be boosted is to be inserted. For the photon, $p_{\gamma \scriptscriptstyle CM} = -p_{\pi \scriptscriptstyle CM}$ in the first step, then the same two transformations of Eq.2.49 follow. Consequently the angle $\Psi_{\scriptscriptstyle CM}$ is given by

$$\begin{aligned} \sin\theta_{\scriptscriptstyle CM} \sin\Psi_{\scriptscriptstyle CM} &= y_{\scriptscriptstyle lab} = \tan\Psi \cdot x_{\scriptscriptstyle lab} = \tan\Psi \cdot (A + B \cdot \cos\Psi_{\scriptscriptstyle CM}) \qquad (2.50) \\ \text{where} \quad A &= \cos\theta_{\scriptscriptstyle CM} \sin\theta_B \cos\theta_p + \gamma\,(\beta - \cos\theta_{\scriptscriptstyle CM} \cos\theta_B) \sin\theta_p \\ B &= \sin\theta_{\scriptscriptstyle CM} \cos\theta_B \cos\theta_p + \ \gamma\, \sin\theta_{\scriptscriptstyle CM} \sin\theta_B\ \sin\theta_p \\ \cos\Psi_{\scriptscriptstyle CM} &= \frac{-A \cdot B + f\sqrt{f^2+B^2-A^2}}{f^2+B^2} \qquad \text{with} \quad f = \frac{\sin\theta_{\scriptscriptstyle CM}}{\tan\Psi} \qquad (2.51) \end{aligned}$$

This completes the description of how to perform the Lorentz boost from the *CM* into the laboratory reference system for a kinematics given by a set of variables (s, t, q^2, Ψ). In this form, it is used in the implementation of real-photon bremsstrahlung emission as a part of the radiative corrections in the Monte Carlo simulation of the experiment discussed in Sec. 2.5.

2.1.7 Real-photon limit $q^2 \longrightarrow 0$

In the real-photon limit $q^2 = 0$, the compact formulæ

$$\begin{aligned} t_{\max} &= 0 \\ t_{\min} &= -\bar{s}^2/s \qquad (2.52) \\ \cos\theta_{\scriptscriptstyle CM} &= 2\,t\,s/\bar{s}^2 + 1 \approx 1 - 2x_\gamma\, s/\bar{s} \qquad (2.53) \end{aligned}$$

with $x_\gamma = p_\gamma/p$ follow, where $p_\gamma \approx p \cdot (-t/\bar{s})$ from Eq. 2.37 is used. So for small q^2, one realizes that p_γ in the laboratory system plays a role equivalent to $\cos\theta_{\scriptscriptstyle CM}$ in the CM system by its relation to Mandelstam t, c.f. Eq. 2.28.

Lines of constant x_γ in the $(\sqrt{s})$-versus-$(\cos\,\theta_{\scriptscriptstyle CM})$ plane are given by

$$\begin{aligned} 2\,x_\gamma &= (1 - \cos\,\theta_{\scriptscriptstyle CM}) \cdot \left(1 - \frac{m_\pi}{s}\right) \overset{!}{=} \text{const} \\ s &= \frac{m_\pi}{1 - 2x_\gamma/(1-\cos\,\theta_{\scriptscriptstyle CM})} \qquad (2.54) \end{aligned}$$

constraining the physical region to lie within

$$\cos\,\theta_{\scriptscriptstyle CM} < 1 - 2x_\gamma \qquad (2.55)$$

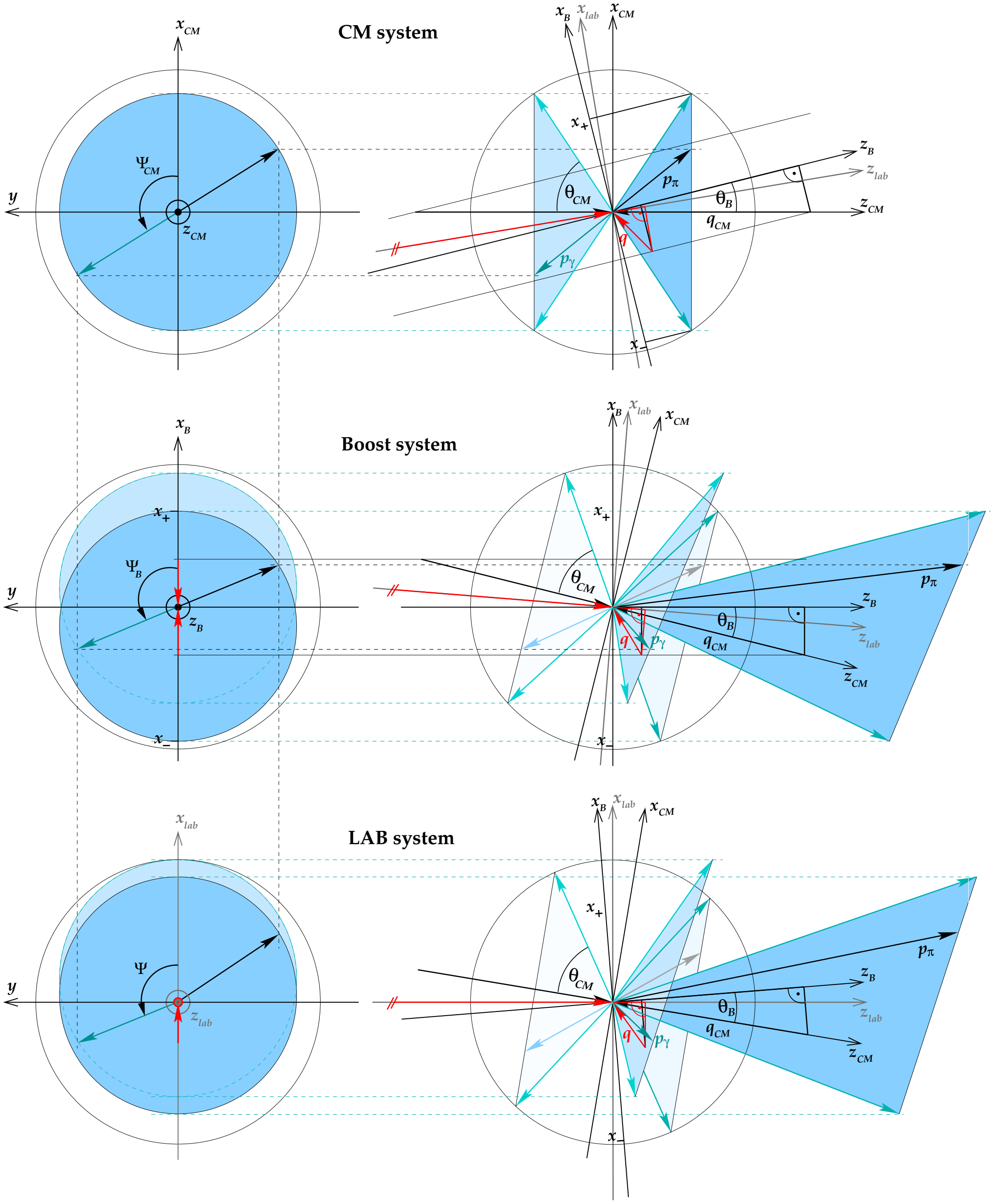

Figure 2.4: Lorentz boost from the *CM* system into the laboratory reference system, according to the steps in Eq. 2.49.

The real-photon limit is best achieved by q^2 taking its minimum value and $q_\perp = 0$, from which $p_{\gamma\perp} = p_{\pi\perp} = p_\perp$ follows. Then, rewriting Eq. 2.11,

$$\begin{aligned} s &= m_\pi^2 + 2(E_\gamma E_\pi + p_{\gamma\perp} p_{\pi\perp} - p_{\gamma\|} p_{\pi\|}) \qquad (2.56) \\ \rightarrow \quad \sqrt{p_\gamma^2 - p_\perp^2}\sqrt{p_\pi^2 - p_\perp^2} &= p_\perp^2 + E_\gamma E_\pi - \bar{s}/2 \\ p_\perp^2 (E^2 - s) &= E E_\gamma \bar{s} - E_\gamma^2 s - \bar{s}^2/4 \\ \rightarrow \quad p_\perp^2 &\approx (1 - \cos^2\theta_{CM})\,\bar{s}^2/4s \end{aligned}$$

solved by

$$s = m_\pi^2 + \frac{2p_\perp^2 + 2p_\perp\sqrt{m_\pi^2(1-\cos^2\theta_{CM}) + p_\perp^2}}{1 - \cos^2\theta_{CM}} \qquad (2.57)$$

where the positive sign of the square root term has been chosen by recasting the solution into Eq. 2.56.

2.1.8 Constraints on the laboratory angles

When considering kinematics with a maximum momentum transfer $q_{\max}$ to the nucleus, the angles of the outgoing particles are restricted. The maximum angles, as treated in detail in sec. B.1, are $\max[\theta_\pi^2] \approx q_{\max} \cdot (2p_\gamma/pp_\pi)$ and $\max[\theta_\gamma^2] \approx q_{\max} \cdot (2p_\pi/pp_\gamma)$. As an example for E=190 GeV and $q_{\max}$=31 MeV, at high photon energy E_γ=160 GeV the angles are restricted to $\theta_\gamma < 7.8$ mrad, $\theta_\pi < 42$ mrad, while for intermediate photon energy E_γ=90 GeV, the ranges are $\theta_\gamma < 19$ mrad, $\theta_\pi < 17$ mrad. Furthermore, $\theta_{\pi\gamma}$ is restricted, apart obviously $|\theta_\pi - \theta_\gamma| < \theta_{\pi\gamma} < \theta_\pi + \theta_\gamma$, by

$$\sin^2\frac{\theta_{\pi\gamma}}{2} = \frac{p}{p_\pi}\sin^2\frac{\theta_\gamma}{2} + \frac{p}{p_\gamma}\sin^2\frac{\theta_\pi}{2} - \frac{q^2 - q_{\min}^2}{4p_\pi p_\gamma} \qquad (2.58)$$

where the full range is obtained by varying q^2 from $q_{\min}^2$ to $q_{\max}^2$. Limits on $s < s_{\max}$ and $q < q_{\max}$ further constrain the angles of the outgoing particles, from Eqs. 2.15 and 2.8,

$$\begin{aligned} 4\,p_\gamma p_\pi \sin^2\frac{\theta_{\pi\gamma}}{2} \quad &< \quad s_{\max} - m_\pi^2 \cdot \frac{E}{E_\pi} \\ \left.\begin{matrix} 4\,pp_\pi \sin^2\dfrac{\theta_\pi}{2} \\ 4\,pp_\gamma \sin^2\dfrac{\theta_\gamma}{2} \end{matrix}\right\} \quad &< \quad s_{\max} - m_\pi^2 \cdot \frac{E}{E_\pi} + q_{\max}^2 - q_{\min}^2 \end{aligned} \qquad (2.59)$$

2.1.9 Cut on the transverse momentum of the scattered pion

Since the interaction point is reconstructed using the change of direction of the scattering pion, the identification of events in the target necessitates a minimum pion scattering angle θ_π. This angle must be significantly larger than the effect of multiple scattering in the target, which is proportional to $p_{\pi\perp}$ (cf. [54] sec. 27.3). Consequently, for a target of 50% radiation length, a cut $p_{\pi\perp} > 45$ MeV/c must be applied to permit a good vertex reconstruction capability. This cut removes at the same time Primakoff events induced by incoming electrons, which radiate with much higher cross section due to their small mass. Since for the 2009 data taking it was decided to reduce the target thickness to 30%, this cut could be reduced to

$$p_{\pi\perp} > 40 \text{ MeV}/c \tag{2.60}$$

This is further treated along the COMPASS data analysis in Ch. 3.

2.1.10 Relation of Mandelstam and laboratory variables

Figs.2.5-2.6 serve for a better understanding of the relation between the quantities measured in the experimental setup and the physically relevant variables. On the x axis, the scattering angle in the *CM* frame of the process $\pi^-\gamma \to \pi^-\gamma$ is drawn, and on the y axis the *CM* energy of the $\pi^-\gamma$ system, $\sqrt{s} = m_{\pi\gamma}$ in units of the pion mass. The plane covers all allowed kinematics for this process. The *CM* angle is taken, rather than Mandelstam-t only because its range $-1, 1$ is independent on $\sqrt{s}$, while the range of t opens with increasing $\sqrt{s}$ according to Eq. 2.21; apart from that, the usage of t and $\cos\theta_{CM}$ is equivalent given Eq. 2.28.

Each point in this $\sqrt{s}$-vs-$\cos\theta_{CM}$ plane has a unique correspondence to the laboratory kinematics of a process $\pi^-\text{Ni} \to \pi^-\text{Ni}\gamma$ when there is no transverse momentum transfer, $q_\perp = 0$. Different lines of constant particle energies and scattering angles are indicated in the plots.

On the lower plot of Fig. 2.5, it is demonstrated how non-zero $q_\perp$ "wash out" this correspondence. The peak contribution of the cross-section, however, lies within the inner band, especially for the low-s region where q_{min} is still very small. The blue lines indicate how a cut on the transverse momentum of the scattered pion, $p_T > 45\,\text{MeV}/c$, affects the quantities of interest: It mainly corresponds to small $\sqrt{s} < 1.5\,m_\pi$, but backward scattering angles are also lost at higher $\sqrt{s}$.

It is also obvious from these figures, that measuring the processes under consideration down to photon energies below 60 GeV is desirable, if the full angular spectrum of the pion Compton scattering process is to be examined, as it will become clear along the next section.

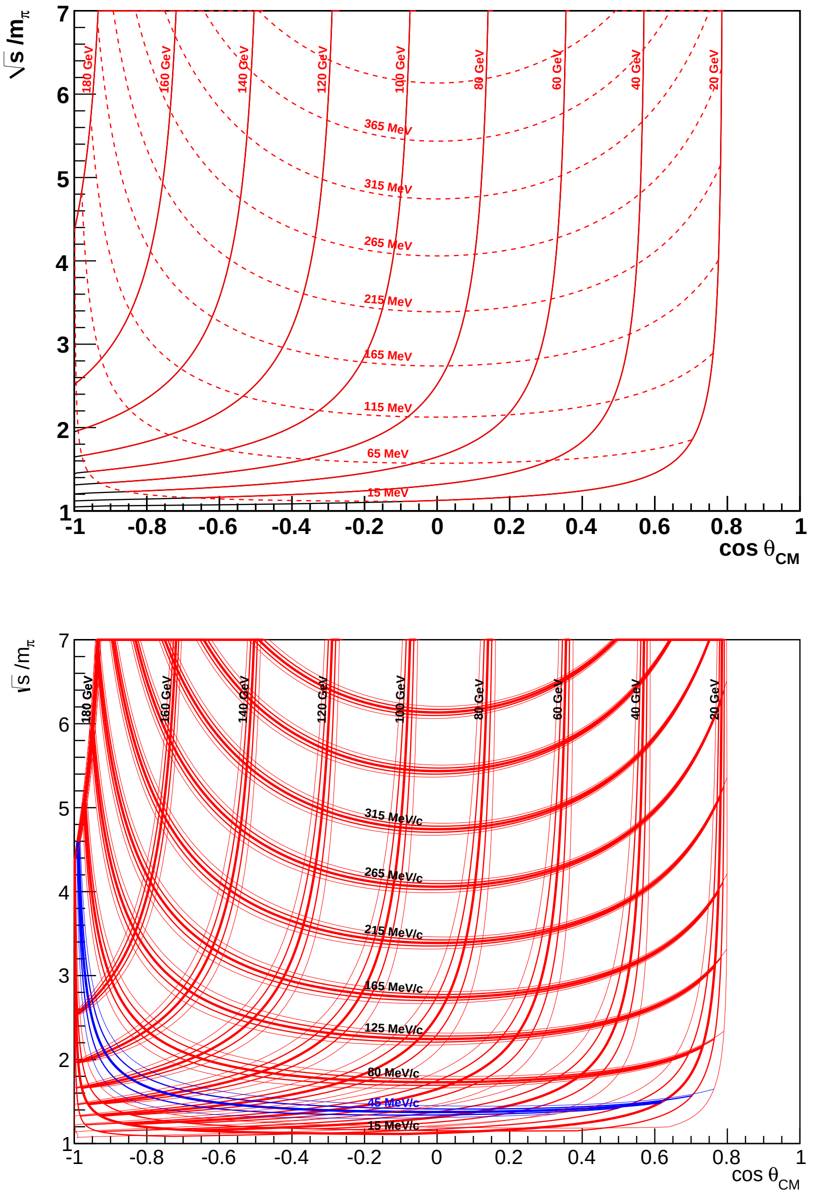

Figure 2.5: Upper figure: Kinematic relation of s and t (t presented through $\cos\theta_{CM}$, cf. Eq. 2.28) with the photon energy E_γ (lines with notation in GeV) and transverse momentum of the outgoing photon and pion (notation in MeV) in case of pure longitudinal momentum transfer, $q_\perp = 0$. Lower figure: For $q_\perp \neq 0$, the described relation washes out. Around the thick central line, representing $q_\perp = 0$, the cases $q_\perp = 0.005\, m_\pi \approx 0.7$ MeV and $q_\perp = 0.01\, m_\pi \approx 1.4$ MeV are shown. The diminishing line widths reflect the lowering cross section with increasing $q_\perp$ in that range.

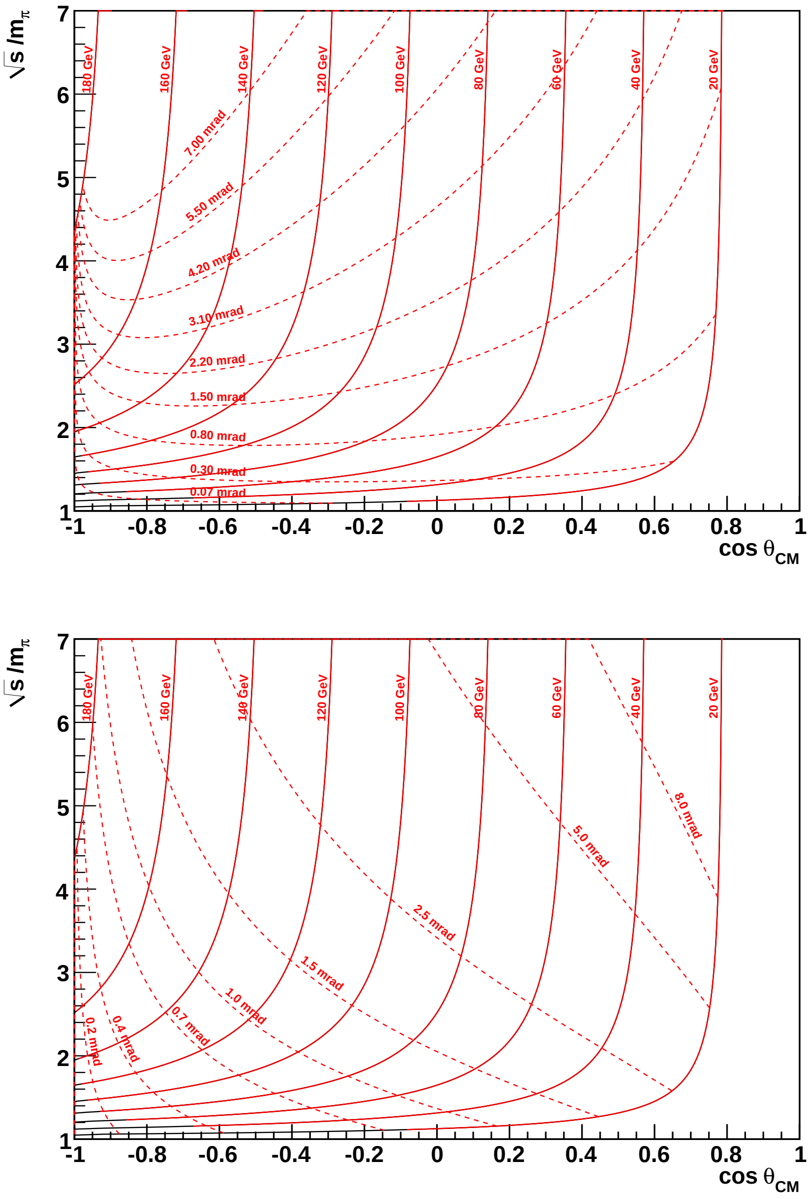

Figure 2.6: Kinematical relation as in Fig. 2.5, here lines with constant pion scattering angle (a) and photon production angle (b) indicated (for the case $q_{\perp} = 0$).

2.2 Differential cross section

2.2.1 Real Compton scattering

The real-photon Compton cross section for a scalar charged particle, *e.g.* $\pi\gamma \to \pi^-\gamma$, reads [44]

$$\frac{d\sigma_{\pi\gamma}}{d\Omega_{CM}} = \frac{\alpha^2(s^2 z_+^2 + m_\pi^4 z_-^2)}{s(sz_+ + m_\pi^2 z_-)^2} - \frac{\alpha\, m_\pi^3 (s-m_\pi^2)^2}{4s^2(sz_+ + m_\pi^2 z_-)} \cdot \mathscr{P} \tag{2.61}$$

where the abbreviation $z_\pm = 1 \pm \cos\theta_{CM}$ is used, and the polarisability contribution is

$$\mathscr{P} = z_-^2(\alpha_\pi - \beta_\pi) + \frac{s^2}{m_\pi^4} z_+^2(\alpha_\pi + \beta_\pi) - \frac{(s-m_\pi^2)^2}{24s} z_-^3(\alpha_2 - \beta_2) \tag{2.62}$$

The polarisabilities have been introduced here according to Gasser *et al.* [31] (there, in the crossed-channel kinematics $\gamma\gamma \to \pi^+\pi^-$), α_π and β_π are the usual electric and magnetic dipole polarisabilities (as discussed in Ch. 1 examplary for α_π), and α_2 and β_2 are the corresponding quadrupole contributions.

Since it is summed over the photon polarisations and consequently, there is no explicit ϕ dependence, in the following the cross section will be used in the form

$$\frac{d\sigma_{\pi\gamma}}{d\cos\theta_{CM}} = 2\pi \frac{d\sigma_{\pi\gamma}}{d\Omega_{CM}} \tag{2.63}$$

2.2.2 Primakoff Compton cross section

When embedding the real Compton process in a Primakoff reaction, *i.e.* $\pi Z \to Z\pi\gamma$, the cross-section reads, employing the equivalent-photon method as described *e.g.* in [44],

$$\frac{d\sigma}{ds\, dq^2\, d\cos\theta_{CM}} = \frac{\alpha}{\pi(s-m_\pi^2)} \cdot F_{\text{eff}}^2(q^2) \cdot \frac{q^2 - q_{\text{min}}^2}{q^4} \cdot \frac{d\sigma_{\pi\gamma}}{d\cos\theta_{CM}} \tag{2.64}$$

where in the effective form factor $F_{\text{eff}}^2(q^2)$ all effects steming from the non-Coulomb structure of the scattering center, as discussed in detail in Secs. 2.3.3 and 2.4.1, are absorbed.

The shape of the cross-section according to 2.64 is shown in Fig. 2.7, together with a simulation representing a statistics that is in reach with the COMPASS experiment. The polarisabilities are assumed in the event generation step to have the values of the ChPT

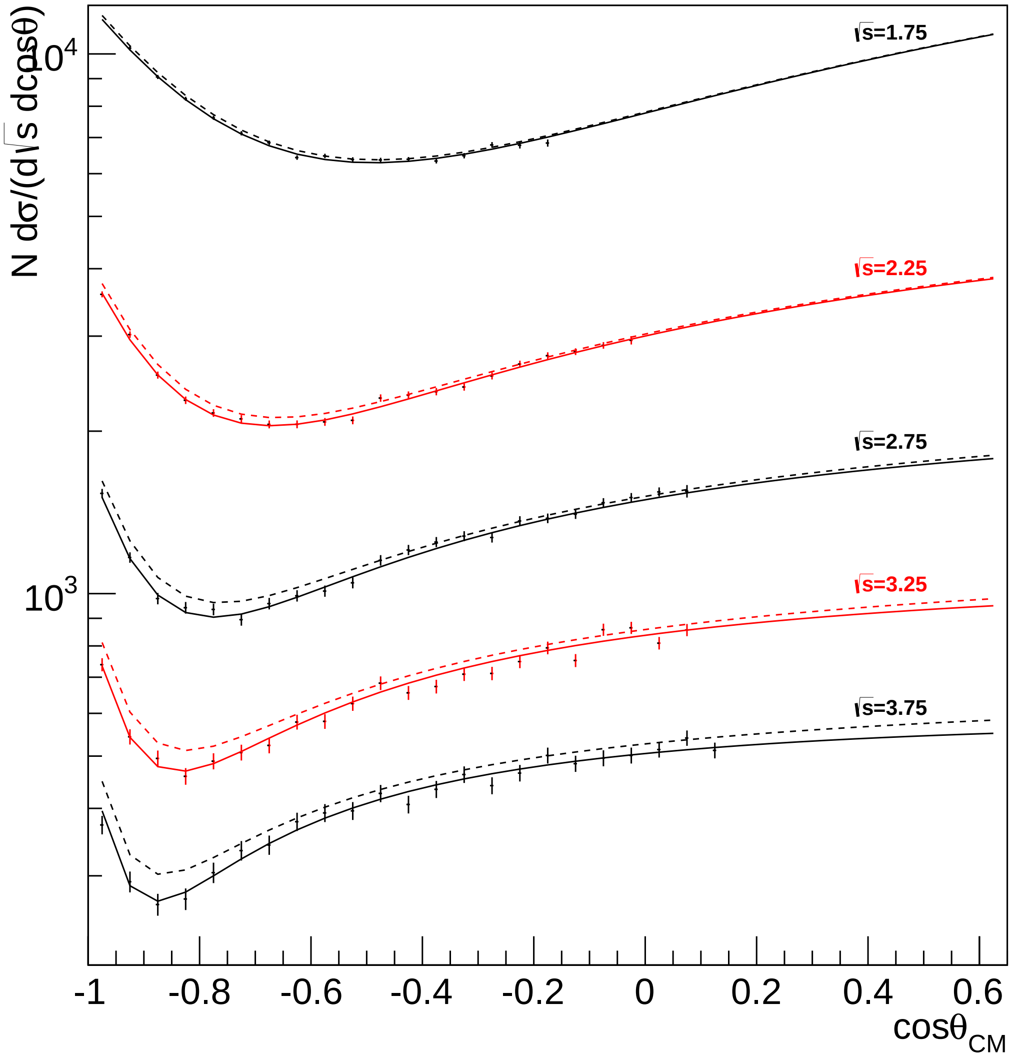

Figure 2.7: Cross-section for the process $\pi^-\mathrm{Ni} \to \mathrm{Ni}\pi^-\gamma$. Dashed lines are based on the Compton cross-section for a structureless boson. The full lines show the fit result on the shown simulated data, leaving the three polarisability contributions $\alpha_\pi - \beta_\pi$, $\alpha_\pi + \beta_\pi$ and $\alpha_2 - \beta_2$, as well as the overall normalization N, as free parameters. All relevant cuts on the kinematic range are applied. The simulated statistics corresponds to that expected for the COMPASS 2012 run (as of 14.8.2012) for the events with $E_\gamma > 76\,\mathrm{GeV}$.

prediction,

$$\begin{aligned} \alpha_\pi - \beta_\pi &= 5.70 \cdot 10^{-4}\,\mathrm{fm}^3 \\ \alpha_\pi + \beta_\pi &= 0.16 \cdot 10^{-4}\,\mathrm{fm}^3 \\ \alpha_2 - \beta_2 &= 4.00 \cdot 10^{-4}\,\mathrm{fm}^5 \end{aligned} \tag{2.65}$$

where the contribution of the quadrupole polarisability has been reduced, as it is supposed to be cancelled by this amount due to the pion loop contributions [31]. Fitting the event distribution, the polarisabilities are retrieved with uncertainties

$$\begin{aligned} \sigma(\alpha_\pi - \beta_\pi) &= 0.97 \cdot 10^{-4}\,\mathrm{fm}^3 \\ \sigma(\alpha_\pi + \beta_\pi) &= 0.04 \cdot 10^{-4}\,\mathrm{fm}^3 \\ \sigma(\alpha_2 - \beta_2) &= 2.50 \cdot 10^{-4}\,\mathrm{fm}^5 \end{aligned} \tag{2.66}$$

The uncertainty on $\alpha_\pi - \beta_\pi$ can be largely reduced by fixing the other two components. This has been done for the analysis of the Serpukhov data [11], and is how the first analysis of the COMPASS 2009 data is on the way, *cf.* Ch. 3.

When $\alpha_\pi + \beta_\pi = 0$ is approximated and also the influence of the quadrupole terms is neglected, only the dependence on a single polarisability parameter α_π remains, and the relative change of the cross-section 2.64 can be expressed by the simple formula

$$r = \left(\frac{d\sigma}{dx_\gamma}\right) \Bigg/ \left(\frac{d\sigma^{\mathscr{P}=0}}{dx_\gamma}\right) = 1 - \frac{3}{2} \cdot \frac{m_\pi^3}{\alpha} \cdot \frac{x_\gamma^2}{1-x_\gamma}\,\alpha_\pi \tag{2.67}$$

which is used in this form in the COMPASS data analysis.

2.2.3 Pion-nucleus bremsstrahlung

It is possible to go beyond the equivalent-photon approximation of Eq. 2.64 by calculating the respective Feynman graphs directly. This has been done by N. Kaiser (TU München), finding

$$\frac{d^3\sigma}{ds\,dt\,dq^2} = \frac{\alpha^3 Z^2}{\pi q^4}\frac{1}{2p^2 q}\int_0^\pi d\Psi\,\frac{1-x^2}{E(xz-y)-p(z-xy)}\,H \tag{2.68}$$

The kinematical factor preceding H involves for photon forward production ($x = 1$) the behaviour $d\sigma \sim \sqrt{1-x}/(E-p) \to \sin\frac{\theta_\gamma}{2}/m_\pi^2$. The squared sum of amplitudes is written

$$H = |\bar{A}|^2 p^2(1-x^2) + |\bar{B}|^2 q^2(1-z^2) + 2\,\mathrm{Re}[\bar{A}\bar{B}^*]\,pq(y-xz) \tag{2.69}$$

with Born-level amplitudes

$$\bar{A}_B = \frac{2E}{s-m_\pi^2} + \frac{2(E-k)}{m_\pi^2 - s - t - q^2}, \qquad \bar{B}_B = \frac{2E}{s-m_\pi^2} \tag{2.70}$$

In this calculation also the $\rho(770)$ resonance contributions have been given as

$$\bar{A}_\rho = \frac{\xi_g\, k\, q(Ez - q - py)}{s - m_\rho^2 + i\sqrt{s}\,\Gamma_\rho(s)}, \qquad \bar{B}_\rho = \frac{\xi_g\, k\, p(p + qy - Ex)}{s - m_\rho^2 + i\sqrt{s}\,\Gamma_\rho(s)} \tag{2.71}$$

where

$$\begin{array}{cc} \xi_g = \dfrac{g_{\rho\pi\gamma}^2}{8\pi\alpha m_\rho^2} & \Gamma_\rho(s) = \dfrac{g_{\rho\pi}^2\left(s - 4m_\pi^2\right)^{\frac{3}{2}}}{48\pi s} \\ g_{\rho\pi\gamma} = 0.17 & g_{\rho\pi} = 6.0 \end{array}$$

The 1-loop ChPT contribution reads, including q-dependence,

$$\begin{aligned} \bar{A}_\chi &= 0 \\ \bar{B}_\chi &= \frac{k\tau^2}{(4\pi f_\pi)^2(\tau^2 - q^2)^2}\Big[\tau^2 - q^2 + 4m_\pi^2\left(\tilde{L}^2(q) - \tilde{L}^2(\tau)\right) \\ &\quad + 2q\sqrt{4m_\pi^2 + q^2}\,\tilde{L}(q) - \frac{2q^2}{\tau}\sqrt{4m_\pi^2 + q^2}\,\tilde{L}(\tau)\Big] \end{aligned} \tag{2.72}$$

using notations $\tilde{L}(q) = \ln\left[\left(\sqrt{4m_\pi^2 + q^2} + q\right)/2m_\pi\right]$ and $\tau = \sqrt{-t}$. Finally, the polarisability contribution is

$$\bar{A}_p = 0 \qquad \bar{B}_p = \frac{\beta_\pi m_\pi k}{\alpha} \tag{2.73}$$

The Ψ spectrum has in fact a particularity, in that not always its full range $[0, 2\pi]$ is kinematically possible, as can also be inferred from Fig. 2.4. The specific shape of the distribution to be integrated is shown for the case $s = 4\ m_\pi^2$ near the backward kinematics $t \approx -2.26\ m_\pi^2$ in Fig. B.4.

The comparison of the more precise description of the cross-section by Eq. 2.68 with the equivalent-photon description by Eq. 2.64 shows that for the small-q range of interest here, they precisely coincide. Differences start to show up at $q^2 \approx 0.5\ \mathrm{GeV}^2/c^2$, where the kinematic limit is reached (depending on s). The equivalent-photon method is "ignorant" of such a limit – it in principle continues up to $q^2 \to \infty$.

For the Monte Carlo simulation of the COMPASS experiment, the form of Eq. 2.68 is implemented on the event generator level.

2.2.4 Muon Compton scattering

The Klein-Nishina formula for Compton scattering of spin-$\frac{1}{2}$ particles can be written

$$\frac{d\sigma}{dt}=\frac{2\pi}{(s-1)^2}\left[\left(\frac{2m_\mu^2}{s-m_\mu^2}+\frac{2m_\mu^2}{u-m_\mu^2}\right)^2+\frac{5m_\mu^2-u}{s-m_\mu^2}+\frac{5m_\mu^2-s}{u-m_\mu^2}\right] \tag{2.74}$$

By inserting this $\mu\gamma$ cross-section in the equivalent-photon formula Eq. 2.64, the Primakoff cross-section for the muon case is found.

2.3 Treatment of the q^2 spectrum

2.3.1 Weizsäcker-Williams factorization: equivalent-photon method

A process dominated by the exchange of a single (virtual) photon factorizes into parts given by the two interaction vertices it connects. If one of the currents undergoes elastic scattering only, its contribution of interaction can be viewed and described as density of virtual (quasi-real) photons. It is derived from the decomposition of the Coulomb field into quasi-real photons and features a q^2 dependence, *cf.* Eq. 2.64,

$$\Phi_{\text{photons}}(q^2)\sim\frac{q^2-q^2_{\text{min}}}{q^4} \tag{2.75}$$

Apart from including higher-order electromagnetic corrections, namely multi-photon exchange, the involved approximation of replacing in a process a virtual photon by a real photon, must be estimated and controlled especially when a high precision is aimed for, as in the polarisability measurement.

The integral over the peak region in q^2 reads

$$\int\limits_{q^2_{\text{min}}(s)}^{q^2_{\text{max}}}\frac{q^2-q^2_{\text{min}}}{q^4}dq^2\;=\;\ln(q^2)-\frac{q^2_{\text{min}}}{q^2}\Bigg|_{q^2_{\text{min}}}^{q^2_{\text{max}}}\;=\;\ln\left(\frac{q^2_{\text{max}}}{q^2_{\text{min}}}\right)-\frac{q^2_{\text{min}}}{q^2_{\text{max}}}+1 \tag{2.76}$$

and so, including the transformation $d\sqrt{s}/ds=1/2\sqrt{s}$,

$$\frac{d\sigma}{d\sqrt{s}\;d\cos\theta_{CM}}\;=\;\frac{Z^2\alpha\cdot2\sqrt{s}}{\pi(s-m_\pi^2)}\cdot\left[\ln\left(\frac{q^2_{\text{max}}}{q^2_{\text{min}}(s)}\right)-\frac{q^2_{\text{min}}(s)}{q^2_{\text{max}}}+1\right]\cdot\frac{d\sigma_{\text{real}}(s)}{d\cos\theta_{CM}} \tag{2.77}$$

where $q^2_{\text{min}}(s)$ takes the value given by Eq. 2.5 (resp. 2.7).

2.3.2 Sampling the equivalent-photon density

The photon density of Eq. 2.75 can be written

$$\frac{d\sigma}{d\ln q^2} = q^2 \frac{d\sigma}{dq^2} \quad \sim \quad 1 - \frac{q^2_{\min}}{q^2} = 1 - e^{\ln q^2_{\min} - \ln q^2} \tag{2.78}$$

which clearly displays the logarithmic divergence of the cross section for large q^2, since $d\sigma / d\ln q^2$ remains constant as $q^2 \to \infty$ in this approximation. In order to keep the integral of the distribution function finite, it must be restricted to some maximum $q_{\max}$. The true reason for the infinite cross section is that the considered approximation ceases to be valid at larger q^2.

For a Monte Carlo simulation, it is of advantage to sample in the distribution of $\ln q^2$, which has not the extreme slopes and curvatures of the q^2 distribution.

2.3.3 Atomic scattering factors

The atomic form factor can be parameterized, following *e.g.* [28],

$$f^0(q) = \sum_{i=1}^{4} a_i \cdot e^{-b_i q^2} + c \tag{2.79}$$

The parameters are given for all relevant elements in [28]. The atomic form factor is combined with the nuclear charge distribution, as handled in the next chapter, in order to completely describe the distortion of the Coulomb field that the incoming particles are exposed to.

2.4 Influence of pion-nucleus strong interaction

2.4.1 Scattering amplitudes from interaction with potentials

This discussion follows that given by Fäldt and Tengblad [27], except where modifications were found to be in place. The authors write the cross-section for $\pi A \longrightarrow A\pi\gamma$ at lowest momentum transfer, where photon exchange dominates and the equivalent-photon method can be employed, in Born approximation for a pointlike nucleus

$$\mathcal{M}_C^{(B)}(\vec{q}) \;=\; \frac{2Z\alpha}{q^2}\,\vec{g}\cdot\vec{q} \;=\; \frac{-1}{2\pi i}\int e^{-i\vec{q}\cdot\vec{r}}\,\vec{g}\cdot\vec{\nabla}V_C(r)\,d^3r \tag{2.80}$$

encoding the reaction dynamics in the vector $\vec{g}$ and making use of the relation

$$\int e^{-i\vec{q}\cdot\vec{r}}\,\vec{\nabla}V_C\;d^3r = i\,\vec{q}\int e^{-i\vec{q}\cdot\vec{r}}\;V_C\;d^3r \tag{2.81}$$

Here, the Coulomb potential of the pointlike charge is $V_C(r) = -Z\alpha/r$; for the uniform charge distribution of the nucleus with radius $r_u = 1.1\,\mathrm{fm}\cdot A^{1/3}$

$$\rho(r) = \begin{cases} Z/\left(\frac{4}{3}\pi r_u^3\right) & \text{for } r < r_u \\ 0 & \text{for } r > r_u \end{cases} \tag{2.82}$$

the Coulomb potential is

$$V_C(r) = \begin{cases} -Z\alpha\cdot(3 - r^2/r_u^2)/2r_u & \text{for } r < r_u \\ -Z\alpha/r & \text{for } r > r_u \end{cases} \tag{2.83}$$

The impact to the matrix element (2.80) by the extended-charge Coulomb potential with $r_u > 0$ as well as the nuclear strong-interaction potential is investigated in the next section.

2.4.2 Eikonal approximation for the pion wave distortion

Soft interaction with the traversed potential may be viewed as a distortion of the one-particle wave function, rather than a full quantum-field-theoretic treatment. In this so-called eikonal approximation (also Glauber or Locher model, for a comprehensive introduction, see *e.g.* the text book of M. Perl [56]), the distortion of the pion wave is taken into account by assuming a straight-line propagation of the particle, and integrating the phase difference along the traversed potential,

$$\mathscr{M}_C(\vec{q}) \;=\; \frac{-1}{2\pi i}\int e^{-i\vec{q}\cdot\vec{r}}\,\vec{g}\cdot\vec{\nabla}V_C(r)\,e^{i\chi_C(\vec{b})}\,d^3r \tag{2.84}$$

with $\vec{b}$ the impact parameter coordinates perpendicular to the incoming beam direction, which defines the z coordinate. For a rotationally invariant potential, the Coulomb phase function $\chi_C(b)$ depends only on the modulus $b = |\vec{b}\,|$,

$$\chi_C(b) \;=\; -\frac{1}{v}\int\limits_{-\infty}^{\infty} V_C(b,z)\,dz = \lim_{a\to\infty} -\frac{1}{v}\int\limits_{-a}^{a} V_C(b,z)\,dz \tag{2.85}$$

and is evaluated to[4]

$$\chi_C(b) = \begin{cases} \eta\left[\ln\left(a/b+\sqrt{1+a^2/b^2}\right)-\ln\left(r_u/b+\sqrt{r_u^2/b^2-1}\right)\right] \\ \qquad +\frac{\eta}{2}\left(\frac{8}{3}-\frac{2}{3}\frac{b^2}{r_u^2}\right)\sqrt{1-b^2/r_u^2} \\ \xrightarrow{a\gg b}\eta\left[\ln(2a/r_u)-\ln\left(1+\sqrt{1-b^2/r_u^2}\right)\right. \\ \qquad \left.+\left(\frac{4}{3}-\frac{1}{3}\frac{b^2}{r_u^2}\right)\sqrt{1-b^2/r_u^2}\,\right] & \text{for } b<r_u \\ \\ \eta\ln\left(a/b+\sqrt{1+a^2/b^2}\right)\xrightarrow{a\gg b}\eta\ln(2a/b) & \text{for } b>r_u \end{cases} \tag{2.86}$$

using the abbreviation $\eta = 2Z\alpha/v$.

If the interaction can be described with the vector $\vec{g}$ in the impact parameter plane, $\vec{g}=\vec{g}_\perp$, then in evaluating $\vec{g}\cdot\vec{\nabla}$ the z component can be neglected. With the operator $\vec{\nabla}_b=(\partial/\partial x,\partial/\partial y,0)^T$,

$$\vec{g}\cdot\vec{b}\;\partial_b\,\chi_C(b) = b\;\vec{g}\cdot\vec{\nabla}_b\,\chi_C(b) = \int\limits_{-\infty}^{\infty} dz\;\vec{g}\cdot\vec{\nabla}V_C(\vec{b},z) \tag{2.87}$$

The derivatives are in the limit $a \gg b$,

$$b\,\partial_b\,\chi_C(b) = \begin{cases} -\eta+\eta\cdot\left(1-b^2/r_u^2\right)^{3/2} & \text{for } b<r_u \\ -\eta & \text{for } b>r_u \end{cases} \tag{2.88}$$

and for arbitrary a, the term $\eta\,b^2/(a^2+b^2+\sqrt{a^2+b^2})$ is to be added to both expressions. For evaluating the influence of the finite nuclear size, the expression

$$\begin{aligned} b\,\partial_b\left[e^{i\chi_C(b)}-e^{i\eta\ln(2a/b)}\right] &= i\,b\left[e^{i\chi_C(b)}\partial_b\,\chi_C(b)+\eta\cdot e^{i\eta\ln(2a/b)}\right] \\ &= i\,\eta\,c\left[e^{i\eta\left[-\ln\left(1+\bar{\beta}\right)+\bar{\beta}+\bar{\beta}^3/3\right]}\left(\bar{\beta}^3-1\right)+e^{-i\eta\ln\beta}\right] \end{aligned} \tag{2.89}$$

is entering, with the b-independent factor $c=e^{i\eta\ln(2a/r_u)}$ and using the abbreviations $\beta=b/r_u$ and $\bar{\beta}=\sqrt{1-\beta^2}$.

---

[4] In [27], the term $\left(\frac{4}{3}-\frac{1}{3}\frac{b^2}{r_u^2}\right)$ is wrongly given as $\left(\frac{1}{3}+\frac{2}{3}\frac{b^2}{r_u^2}\right)$. As a consequence, in Eq. 2.89 the term $\left(\bar{\beta}^3-1\right)$ would read, with Fäldt's assumptions, $\left(3\bar{\beta}-2\bar{\beta}^3-1\right)$.

2.4.3 Form factors for the nuclear potentials

The form factor contribution due to the finite extension of the nucleus reads, in the notation of Fäldt,

$$\delta F_C^u(q_\perp, q_\parallel) = i \int_0^{r_u} db\, b^2 \frac{J_1(bq_\perp)}{bq_\perp} \partial_b \left[e^{i\chi_C(b)} - e^{i\eta \ln(2a/b)} \right] \tag{2.90}$$

$$= -\eta\, c \frac{r_u^2}{\gamma} \int_0^1 d\beta\, J_1(\beta\gamma) \left[e^{i\eta\left[-\ln\left(1+\bar\beta\right)+\bar\beta+\bar\beta^3/3\right]} \left(\bar\beta^3 - 1\right) + e^{-i\eta\ln\beta} \right] \tag{2.91}$$

with $\gamma = r_u q_\perp$. The Bessel function is effectively evaluated for small arguments $x < 50$ with the expansion [17]

$$J_n(x) = \frac{x^n}{2^n \Gamma(n+1)} \left(1 - \frac{x^2}{2\cdot(2n+2)} + \frac{x^4}{2\cdot 4\cdot(2n+2)\cdot(2n+4)} - \dots \right) \tag{2.92}$$

Fäldt derives the contribution due to the strong interaction of the pion with the nucleus by the replacement

$$\vec\nabla V_C(r) \quad\to\quad \vec\nabla(V_C(r) + V_N(r)) \tag{2.93}$$

with the strong-interaction potential approximated by

$$V_N(r) = \begin{cases} -\frac{\sigma}{2}(i+\alpha)\cdot\rho_N & \text{for } r < r_u \qquad (i.e.\ |z| < \sqrt{r_u^2 - b^2}) \\ 0 & \text{for } r > r_u \end{cases} \tag{2.94}$$

taking $\rho_N = A/\left(\frac{4}{3}\pi r_u^3\right) \approx 0.179/\,\mathrm{fm}^3$ constant inside the nucleus. While the derivative contribution $\vec\nabla V_N$ in fact vanishes (apart from an ill-defined contribution on the nuclei rim), the strong-interaction potential gives rise to the additional phase shift analogous to Eq. 2.85, approximating the particle velocity $v = c = 1$,

$$\chi_N(b) = -\frac{1}{v} \int_{-\infty}^{\infty} V_N(b,z)\, dz = \frac{\sigma}{2}(i+\alpha)\cdot T_A(b) \tag{2.95}$$

with the nuclear thickness function

$$T_A(b) = \rho_N \cdot 2\sqrt{r_u^2 - b^2} \tag{2.96}$$

2.5 QED radiative corrections

Reactions involving charged particles that change their momentum, may it be in direction or in modulus or in both, are affected by virtual photon loop and real photon emission processes. Those can not be isolated experimentally from the leading-order processes under study. However, with QED as well-established and calculable theory, the effects can be taken into account in terms of a radiative correction, based on the perturbative expansion of QED. At first order, they appear as a factor with respect to the leading-order process,

$$\sigma_{\text{corrected}} = (1+\delta)\cdot\sigma_{\text{non-radiative}} \tag{2.97}$$

where δ is usually in the order of a few percent, depending on the kinematics. It is composed of a part steming from the virtual-photon loop contributions, δ_v, and a part from the emission of real photons, $\delta_r(\lambda)$, that depends on the upper limit λ of their energy.

2.5.1 Soft photon emission

The emission of real soft photons along with a hard reaction $p_1+k_1 \to p_2+k_2$ (involving charged particles p_1, p_2 of mass m and neutral particles k_1, k_2) appears with a relative weight

$$\begin{aligned}
\delta_r(\lambda_1 < |\vec{l}| < \lambda_2) &= \frac{\alpha}{\pi} \int\limits_{\lambda_1<|\vec{l}|<\lambda_2} \frac{d^3 l}{4\pi l_0} \left(\frac{2p_1\cdot p_2}{p_1\cdot l \; p_2\cdot l} - \frac{m^2}{(p_1\cdot l)^2} - \frac{m^2}{(p_2\cdot l)^2} \right) \qquad (2.98) \\
&= \frac{\alpha}{\pi} \int\limits_{\lambda_1}^{\lambda_2} \frac{dl}{l} \int\limits_{-1}^{1} \frac{dx_l}{2} \int\limits_{0}^{2\pi} \frac{d\phi}{2\pi} \left(\frac{2p_1\cdot p_2}{p_1\cdot \hat{l} \; p_2\cdot \hat{l}} - \frac{m^2}{(p_1\cdot \hat{l}\,)^2} - \frac{m^2}{(p_2\cdot \hat{l}\,)^2} \right)
\end{aligned}$$

where the spherical coordinates $x_l = \cos\theta$ and ϕ of the soft photon momentum direction $\hat{l} = \vec{l}/|\vec{l}|$ will be further used, with respect to the axis $z = \hat{p}_1$ and $\vec{p}_2$ in the $xz-$plane. This integral exhibits the famous infrared divergence $\lambda_1 \to 0$, which must be properly regularized, taking into account corresponding divergences on the side of virtual photon loop corrections, as extensively discussed in the literature, *e.g.* [43] and Refs. therein.

While the removal of the divergent contribution leads to a (typically small) finite correction factor to the original non-radiative process, the real-photon emission correction (2.98) involves also the production of additional photons with a specific energy and angular dependence. Those lead to a distortion of the original kinematics, and become visible experimentally in terms of the radiation tail towards lower energies of the outgoing observed particles.

The way pursued here to account for these effects is to subdivide the radiative tail into a lower- and a higher-energetic part. The lower-energetic part involves only the emission of real photons that do not play a role experimentally, but are to be accounted for the in the radiative correction factor. The higher-energetic part is still to be considered soft, such that the emitted photons follow the distribution 2.98, but may lead to a distortion of the kinematics that is to be taken into account in the analysis.

This is achieved on the level of the Monte Carlo simulation. For the implementation, the indefinite integrals of 2.98 are of use and discussed in the following, extending the expressions given in [43] for the full-range integral. The quantity $x_2 = \cos(\angle(\vec{p}_1, \vec{p}_2))$ is introduced, such that the structures in (2.98) can be written in terms of

$$\begin{aligned}
p_1 \cdot \hat{l} &= E - p\,x_l && (2.99)\\
p_2 \cdot \hat{l} &= E - p\,x_2\,x_l - p\sqrt{1-x_2^2}\sqrt{1-x_l^2}\,\sin\phi &&\\
&= E_x - p_x \sin\phi && (2.100)\\
E^2 - p^2 &= m^2 &&\\
E_x^2 - p_x^2 &= m^2 + p^2\,x_2^2 - 2Ep\,x_2\,x_l + p^2\,x_l^2 && (2.101)\\
&= m^2(1-x_l^2) + (E\,x_l - p\,x_2)^2 &&\\
\kappa &= p^{-1}\sqrt{(E^2-p^2x_2)^2 - m^4} &&
\end{aligned}$$

The ϕ integration can be performed analytically for a fixed x_l [(A.10),(A.11)],

$$\begin{aligned}
&\int d\phi\,\frac{2(E^2-p^2x_2)}{(E-p\,x_l)\,(E_x-p_x\sin\phi)} - \frac{m^2}{(E-p\,x_l)^2} - \frac{m^2}{(E_x-p_x\sin\phi)^2} \;=\\
=\;& \frac{-m^2\phi}{(E-p\,x_l)^2} + \frac{m^2\,p_x\cos\phi}{(E_x^2-p_x^2)(E_x-p_x\sin\phi)} \qquad (2.102)\\
&+\left(\frac{-m^2\,E_x}{E_x^2-p_x^2} + \frac{2(E^2-p^2x_2)}{E-p\,x_l}\right)\frac{2}{\sqrt{E_x^2-p_x^2}}\arctan\frac{E_x\tan(\phi-\pi)/2+p_x}{\sqrt{E_x^2-p_x^2}}
\end{aligned}$$

which is useful in this indefinite form for the Monte Carlo simulation of the radiative tail. Carried out over the full range,

$$
\begin{aligned}
&\int_0^{2\pi} d\phi\ \frac{2(E^2-p^2x_2)}{(E-p\,x_l)\,(E_x-p_x\sin\phi)}-\frac{m^2}{(E-p\,x_l)^2}-\frac{m^2}{(E_x-p_x\sin\phi)^2}\\
&= 2\pi\left(\frac{-m^2}{(E-p\,x_l)^2}+\left(\frac{-m^2\,E_x}{E_x^2-p_x^2}+\frac{2(E^2-p^2x_2)}{E-p\,x_l}\right)\frac{1}{\sqrt{E_x^2-p_x^2}}\right) \qquad (2.103)
\end{aligned}
$$

is obtained, for which now in the same manner the indefinite integral over x_l is considered,

$$
\begin{aligned}
&\int dx_l\ \frac{-m^2}{(E-p\,x_l)^2}+\left(\frac{-m^2\,E_x}{E_x^2-p_x^2}+\frac{2(E^2-p^2x_2)}{E-p\,x_l}\right)\frac{1}{\sqrt{E_x^2-p_x^2}}\\
= \quad & -\frac{m^2}{p(E-p\,x_l)}-\frac{E\,x_l-p\,x_2}{\sqrt{E_x^2-p_x^2}}+\\
& +\frac{2(E^2-p^2x_2)}{p\kappa}\ln\frac{\kappa\sqrt{E_x^2-p_x^2}+(1-x_2)(m^2-x_2p^2+Ep\,x_l)}{d-x_l} \qquad (2.104)
\end{aligned}
$$

with full-range integration yielding

$$
\begin{aligned}
&\int_{-1}^{1} dx_l\ \frac{-m^2}{(E-p\,x_l)^2}+\left(\frac{-m^2\,E_x}{E_x^2-p_x^2}+\frac{2(E^2-p^2x_2)}{E-p\,x_l}\right)\frac{1}{\sqrt{E_x^2-p_x^2}} =\\
= \quad & -4+\frac{2(E^2-p^2x_2)}{p\kappa}\ln\frac{(E+p)[\kappa(E-px_2)+(1-x_2)(m^2-x_2p^2+Ep)]}{(E-p)[\kappa(E+px_2)+(1-x_2)(m^2-x_2p^2-Ep)]} \qquad (2.105)
\end{aligned}
$$

in agreement with the first term of Eq. (20) in [43].

When a real soft photon is emitted, the kinematics is, at least somewhat, distorted with respect to the non-radiative process used in the ansatz 2.97, *e.g.* as starting point in the Monte Carlo simulation. At least, energy-momentum conservation should be accounted for, such that only kinematically allowed processes are simulated. Since for a given s and emitted soft photon vector $\vec{p}_s$ the distorted kinematics is not unique, as approximation the kinematics is chosen where the outgoing pion does not change its direction[5], that is $\vec{p}_\pi \to \eta\vec{p}_\pi$ with a number η close to one when the momentum of the

---

[5] this kinematics is "most nearby" in the way that the angular correlation of the emitted soft photon and the charged particle is kept.

soft photon p_s is small. A straight-forward calculation shows

$$\eta = \frac{p_c s_p + \sqrt{p_c^2 s_p^2 - (4m_\pi^2 e_p^2 - s_p^2)(e_p^2 - p_c^2)}}{2p_{\scriptscriptstyle CM}(e_p^2 - p_c^2)} \tag{2.106}$$

$$\begin{aligned} p_c &= p_s \cos\theta_{\gamma\gamma} \\ s_p &= s + m_\pi^2 - 2\sqrt{s}\,p_s \\ e_p &= \sqrt{s} - p_s \end{aligned}$$

and $p_{\scriptscriptstyle CM}$ is given by Eq. 2.27.

In general, it is favorable to "hand over" the description of the bremsstrahlung kinematics from the soft-photon limit given here, starting from some intermediate photon energy to the exact spectrum as given in [44]. This has not been integrated in the COMPASS analysis software yet, but should be envisaged for the future analysis especially of the high-statistics 2012 data set.

2.5.2 Virtual photon loops

The virtual-photon loop corrections for pion Compton scattering are published in [45]. In the present work, these investigations have been extended for a more suitable implementation on the level of the analysis computer program. This is, on the one hand, the collection of repeatedly appearing terms. Cancellation brings their number down from originally 100 to 10, with the merit of a faster computing time and better numerical precision. On the other hand, the highest-order loop integrals had not been solved analytically in [45], but it was proposed to handle them by numerical integration. This poses problems, due to the infinite range of the integrals $\{1,\infty\}$, and because they partly feature a pole that is integrable, but its principal value needs to be extracted. Computer algebra packages as Mathematica can certainly handle the involved problems, but with unaffordably high computing time for the intended purpose of implementing the corrections on event-by-event basis. On the way of implementation, it was found out by the author that the integrals can all be solved analytically, which reduces the required computing time by about a factor of 100, and makes the handling of numerical round-off effects much easier.

The contributions of the Feynman graphs at one-photon loop order, separated in the classes presented in Fig. 2.8, are sorted in amplitudes A and B according to the decomposition of the T-Matrix as given by Eq. (1) of [45]. Summing all contributions, and

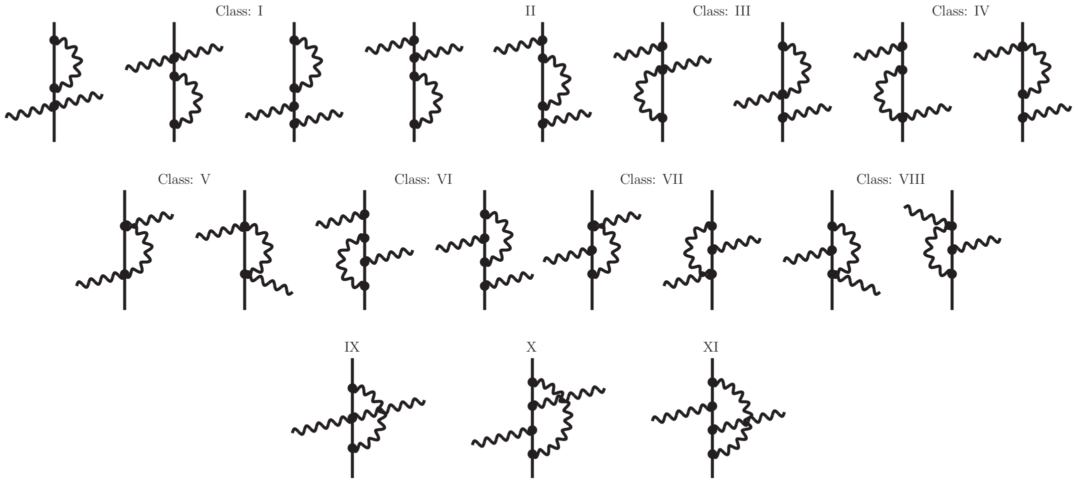

Figure 2.8: Classification of the Feynman graphs for pion Compton scattering at one-photon loop order, as treated in [45].

solving the parameter integrals as described in the Appendix A.5, one arrives at

$$\begin{aligned}\mathrm{Re}\left[A_{(1\text{-loop})}\right] &= \frac{\alpha}{2\pi}\left[-\frac{3}{2}+\frac{\hat{u}-1}{\hat{u}}\ln(1-\hat{u})+\frac{\hat{s}-1}{\hat{s}}\ln(1-\hat{s})\right.\\ &\qquad\left.+\,\mathrm{Li}_{2t}(\hat{t})-2L^2(\hat{t})+A_I(\hat{s},\hat{t})+A_I(\hat{u},\hat{t})\right]\end{aligned} \tag{2.107}$$

and

$$\begin{aligned}\mathrm{Re}\left[B_{(1\text{-loop})}\right] &= \frac{\alpha}{2\pi}\left[\frac{\hat{s}-1}{\hat{u}-1}\left(\mathrm{Li}_{2t}(\hat{t})-2\right)-\frac{\hat{u}-1}{\hat{u}}\ln(1-\hat{u})-\frac{\hat{s}-1}{\hat{s}}\ln(1-\hat{s})\right.\\ &\qquad\left.-\,\frac{\hat{t}}{\hat{u}-1}\Big(\left[2+L_t(\hat{t})\right]\ln(1-\hat{u})+\mathrm{Li}_{2h}(\hat{t})\Big)+B_I^s(\hat{s},\hat{t})+B_I^u(\hat{u},\hat{t})\right]\end{aligned} \tag{2.108}$$

The functions $A_I(m,\hat{t})$ and $B_I^m(m,\hat{t})$, which are given in integral form in [45], are evaluated using formulæ A.95, A.101 and A.107, respectively.

For the case of $A_I(m,\hat{t})$, it was examined examplarily that using the analytic form delivers the 10-digit precise result more than 5000 times faster than solving the integral numerically to 3-digit precision, when a standard Newton-Cotes (equal step width) procedure is employed. Certainly with more elaborate methods (variable transformation to a finite integration interval, adaptive step widths etc.) a significant speed-up of

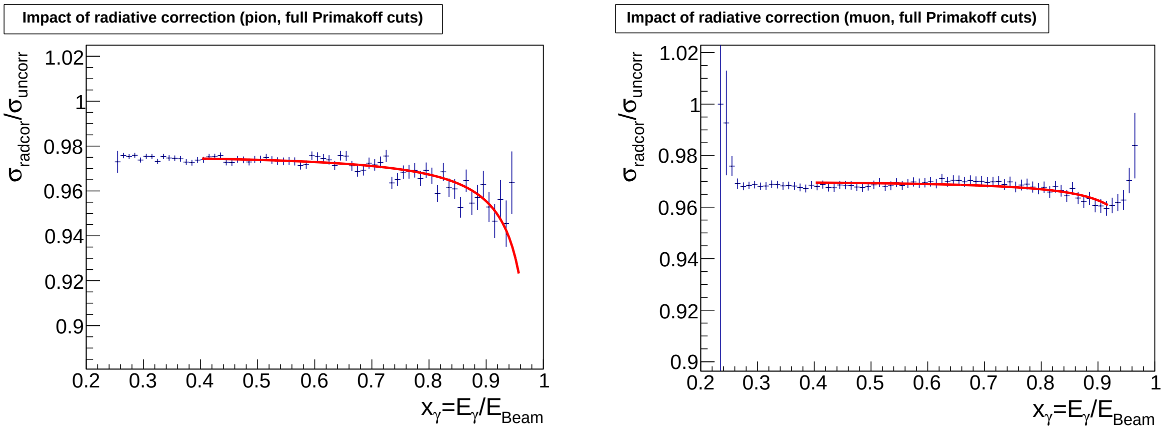

Figure 2.9: Effect of the QED radiative corrections on the photon energy spectrum, examined by a high-statistics simulation of the experimental conditions during the 2009 measurement [53]. For pions (left plot), the dependence of the radiative correction on x_γ matches accidentically quite well with a "polarisability" contribution and can be fitted, using Eq. 2.67, with $\alpha_\pi \approx 0.3 - 0.4 \cdot 10^{-4}\,\text{fm}^3$ (depending on the fit range). For muons (right plot), the trend is a little different, with a smaller dependence on x_γ. It is fitted with the same curve as the pion data, despite there is obviously no "muon polarisability" expected here.

the numerical procedure can be expected, however the care that is to be taken for the contained singularities remains, and just emphasizes again the special value of having the analytic solution at hand.

The respective radiative corrections for muon bremsstrahlung, used as systematic control measurements at COMPASS, are published in [43] in a handy form already, and thus are not reproduced here. They have been implemented in the COMPASS analysis software analogously to the pion case.

2.5.3 Effect on the polarisability determination

Summing real and virtual photon contributions, the total effect on the cross section is evaluated for each simulated event. The average value does not have an impact on the polarisability determination, since only the ratio, Eq. 2.67, is considered with leaving the normaization as a free parameter. However, a relative change of the radiative correction with x_γ is potentially misinterpreted as polarisability contribution. This effect is presented in Fig. 2.9. It is realized that the QED radiative corrections have an effect that for pions is accidentially very similar to that of the polarisability combination $\alpha_\pi - \beta_\pi$, just its size is about a factor of 10 suppressed with respect to the ChPT prediction for the polarisability signal, *cf.* Eq. 2.65. This observation is in agreement with the earlier findings of Akhundov *et al.* [6].

For muons, a similar trend is also seen, however, the radiative corrections do show a slightly different behaviour at the edges of the x_γ spectrum. Their application is indispensable for a precise interpretation of the data taken with muon beam in terms of controlling the apparatus description on the precent level.

2.5.4 Further corrections

Apart from the QED radiative corrections discussed so far, further effects are to be taken into account:

- The QED radiative corrections depend themselves slightly on the polarisabilities. The effect is less than 5% of the structure-independent radiative corrections [45], so the polarisabilities can be accurately determined from the data by neglecting this dependence in a first step, and taking the result into account in a second iteration of the analysis procedure.

- The QED radiative corrections depend on the virtuality q^2 of the exchanged photon, changing their magnitude [46] by some 20% when going from the kinematic threshold $q^2 = q^2_{\text{min}}$ to $q^2 = m^2_\pi \approx 0.02\,\text{GeV}^2/c^2$. It is a tiny effect when the peak structure is taken into account, concentrating the main part of the cross-section in the region well below 0.001 GeV^2/c^2. However, if the region at higher q^2 is under consideration, this effect is not negligible.

- The corrections presented so far assume the soft-photon limit, *i.e.* the distortion of the kinematics by the additional photon is not taken into account. The presciption how this should be done accurately (in next-to-leading order in QED) is given in [45], but this is not yet implemented on the Monte Carlo generator level in the COMPASS analysis framework.

- Multiple soft-photon emission is not yet taken into account. An exponentiation procedure, analogous to that applied in electron scattering [29, 70], may be envisaged, but since the leading-order correction still lies in the range of 1–3% the effect is not expected to be large (in electron scattering, the corrections are typically above 20%). In addition it is conceptually not really consistent to treat multiple emission of real soft photons on the quantum mechanical level, while multiple virtual photon exchange is treated as continous wave distortion of the scattered pion, *cf.* Sec. 2.4.2.

- Higher-order terms from the ChPT chiral-loop expansion [19, 20, 31, 45] do influence the pion Compton cross-section also in the region from which the polarisability is extracted. These chiral-loop effects are to be clearly distinguished from the pure polarisability effect. The calculation of the chiral loops in ChPT shows that they have in general the opposite trend than the polarisability effects, *i.e.* they enlarge the cross-section, while the polarisabilities are expected to lower the cross-section. The two structure effects can be separated if the statistics is sufficient to distinguish their different dependence on the kinematic variables. For the COMPASS 2009 data, the chiral loop contribution is assumed to be present as predicted by ChPT in the Monte Carlo simulation, and only the polarisability contribution is left as a free parameter. With the new high-statistics data, the separation can possibly be made without that assumption.

Chapter 3

COMPASS Data Analysis for the Pion Polarisability

3.1 The COMPASS spectrometer setup 2009

The principle of the measurement is depicted in Fig. 3.1, and the full apparatus is presented in Fig. 3.2. The incoming 190 GeV hadron beam traverses two CEDAR (ChErenkov Differential counter with Achromatic Ring focus) detectors that identify kaons employing the method developed by the author and explained in the COMPASS note reproduced in C.2.

Before the beam particles hit a solid-state target, their trajectories are accurately measured by the silicon beam telescope, consisting of three stations as described in Chap. 5. The targets are mounted inside the recoil proton detector (RPD), which was used for the prior measurements of diffractive reactions, mainly with the liquid hydrogen target, *cf.* Fig. 5.1. The RPD has been kept in place mainly for the practical reason

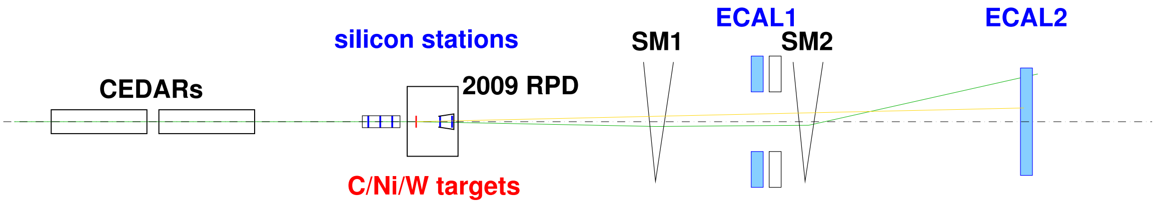

Figure 3.1: Principle of the measurement of the reaction $\pi^- Z \rightarrow Z \pi^- \gamma$ with COMPASS. The hadron beam enters from the left.

of providing the holding structure for the required equipment in the target region, however, it was also read out during the Primakoff data taking and it was shown in the analysis that a small part of the Primakoff events also feature signals, mainly from δ electrons.

Immediately downstream of the target, two silicon stations are placed in the conical cryostat, which is adapted to the confined space between the opening acceptance of the spectrometer and the photomultipliers of the RPD. In this configuration, the outgoing particle trajectories are measured with a precision in the range of 30 μrad, and accordingly the scattering angles measured with a precision that is limited by the multiple scattering in the target and, much thinner but also unavoidable, the detector material.

For the scattered pion, the high-resolution tracking capacity of the spectrometer is employed, determining the charged-particle momenta with a relative precision of about 10^{-4} over a wide range 1-180 GeV. This is achieved with about 200 tracking planes through the two stages of the magnetic spectrometer, the first magnet, SM1, featuring a bending power of about 1 Tm, and the second, SM2, about 4 Tm.

The produced real photon is detected in the electromagnetic calorimeter ECAL2, situated about 32 meters downstream of the target. For the Primakoff reactions of interest here, the angles of all photons are so small that they are detected only in this second stage. For the competing channels involving neutral pions, however, it is important to have also the imformation of the first stage, ECAL1, 18 m downstream of the target, in order to cover the largest part of the π^0 decay kinematics.

The signals of ECAL2 are the core input of the employed digital trigger system, constructed by the Munich COMPASS group under the supervision of I. Konorov [41, 47]. Since 2009, the energy sum in the relevant central region of the calorimeter can be determined; when they exceed the programmable threshold, a trigger is formed. This causes a kinematic cut at about 60 GeV, present in all analysis plots in this chapter.

The granularity of ECAL2, consisting of cells with an edge size of about $4 \times 4\,\mathrm{cm}^2$ perpendicular to the incoming beam direction, matches the size of the electromagnetic showers such that always several cells are hit (for energies above 10 GeV). By amplitude weighting, spatial resolutions in the range of 1 mm are achievable. This required an enormous effort taken by the Munich group, starting from the original finding and description of the problem during the years 2006-2009 [26], and continued with a task force of four people working intensively to solve the issue during 2010-2011 [47, 53, 62]. The achieved resolution leads to angular uncertainties for the photon in the same range as that for the charged pion, such that from combining the two informations the momentum balance can be calculated, as explained further in Sec. 3.2.1.

The signals from the RICH1 detector, allowing for particle identification $\pi/K/p$ in the momentum range below 50 GeV/c, have not yet been employed in the present analysis.

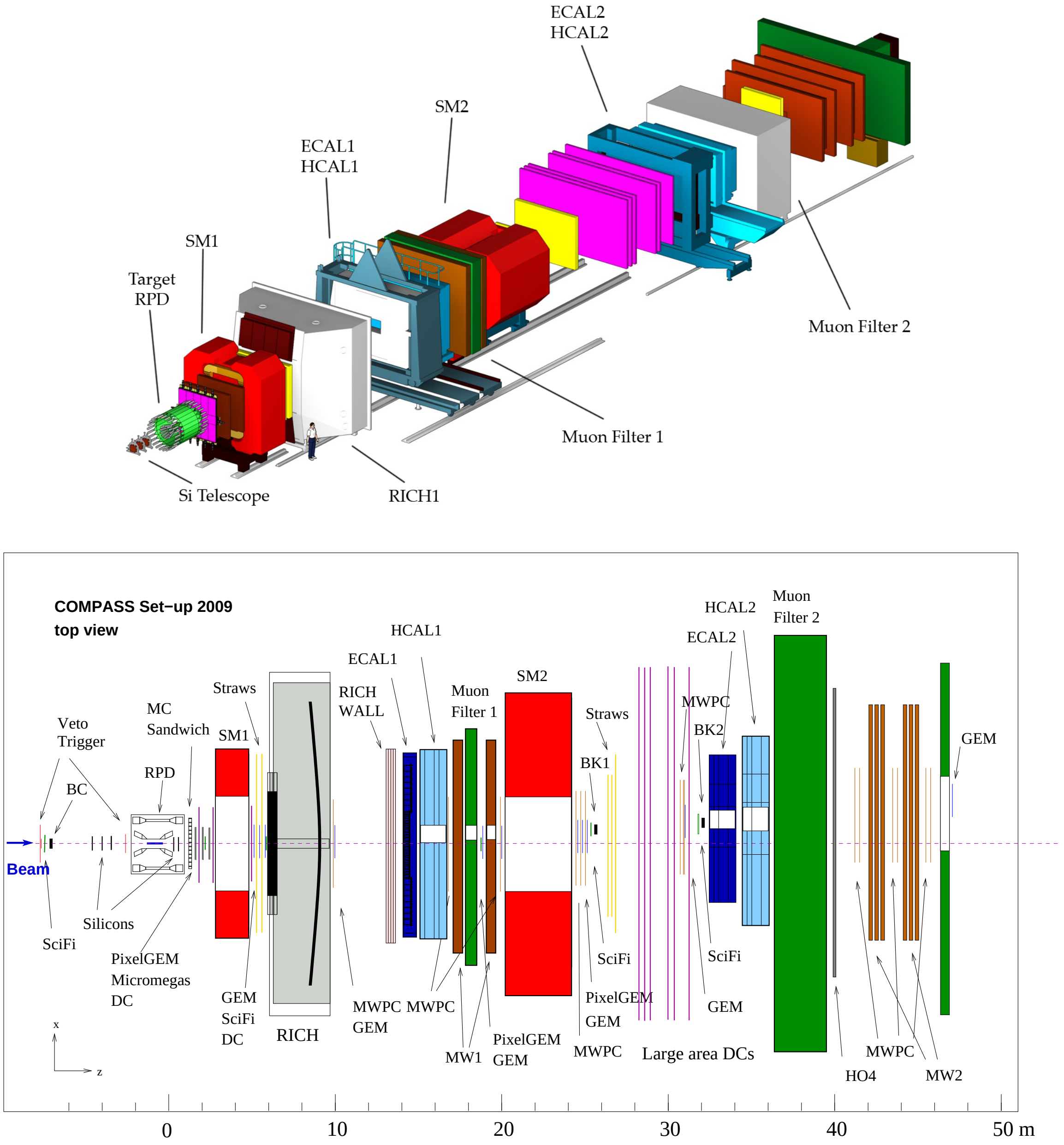

Figure 3.2: The COMPASS setup of 2009. The CEDAR detectors, placed about 20 m upstream of the target region, are not within the selected region. Figures from [24].

A peculiarity of the COMPASS setup is the possibility to change over in a short time, within an hour, from pion to muon beam. This is exhaustively used in this measurement, since practically the same measurement as the one of interest, $\pi^- \mathrm{Ni} \to \mathrm{Ni}\,\pi^-\gamma$, can be done with muons, $\mu^- \mathrm{Ni} \to \mathrm{Ni}\,\mu^-\gamma$. The advantage of the muon process is that it is completely descibed by QED and no structure effects are expected, so all deviations from the theoretical expectation appearing in the analysis of the experimental data are, at least with very high probability, due to apparative effects or missing corrections.

All apparative effects concerning resolution, acceptance and efficiency are taken into account in a dedicated Monte Carlo simulation on the base of the CERN GEANT program package, described in detail in [53]. Adapting this description of the apparatus was in fact the main challenge of the analysis, aiming at an unprecedented precision for a COMPASS measurement.

3.2 Kinematic distributions

3.2.1 Longitudinal and transverse components of $\vec{q}$

The resolution of the transverse component of the momentum transfer $\sigma(q_\perp) \approx 10\,\mathrm{MeV}/c$, as already presented in Fig. 1.1, is a remarkable value given that the outgoing particles have momenta of typically $100\,\mathrm{GeV}/c$.

It is achieved from balancing the momentum vectors of the two outgoing particles and the incoming beam particle. Since the energy balance is limited to a level of about 1.5 % given by the shower fluctuations in the calorimetric measurement of the photon, an experimental artifice is employed, decoupling transverse and longitudinal components in the momentum balance which are differently affected by the energetic uncertainty. First, energetically exclusive events are selected within the achievable resolution. Their exclusivity is studied by the shape of the exclusivity peak (see Sec. 3.2.3 below) and by investigating the contribution of background events, which stems mainly from reactions in which at least one π^0 is produced. Then, for the selected events, exclusivity is assumed, and the momenta are varied within the uncertainty of the measurement such that the reaction is energetically exclusive. Since the direction of the particles is known to much better precision than their modulus, this effectively amounts to a rescaling of the length of the momentum vectors. After this procedure, it is mainly the transverse component of q which remains and gives rise to the experimental distribution as depicted in Figs. 1.1 and 3.6.

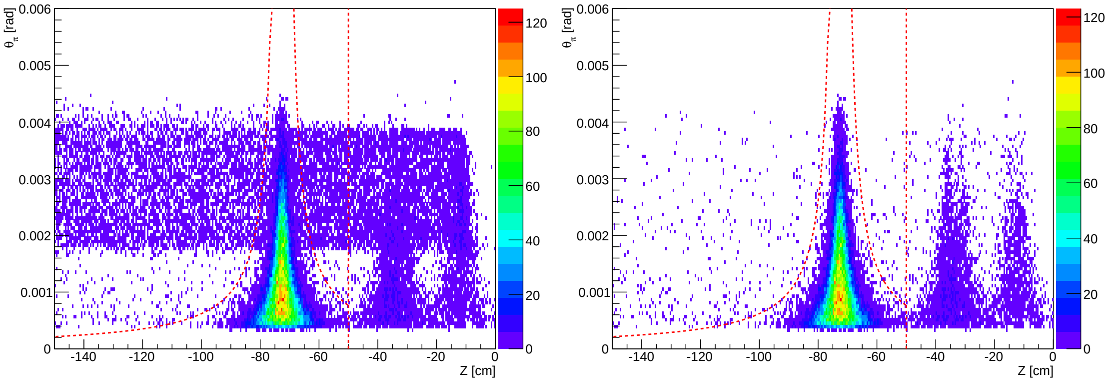

Figure 3.3: Distribution of the pion scattering angle versus the position of the interaction vertex, both determined from the trajectories of the incoming and the scattered charged track. Left: Primakoff events after kinematic cuts. Right: The signals due to incoming kaons are efficiently suppressed using the CEDAR information. In both plots, the cut on the events from the target is indicated.

3.2.2 Spatial and angular resolution

The reconstruction of the interaction point is presented in Fig. 3.3. The coordinate z along the incoming beam direction is the most difficult one to determine, as the two tracks, the vertex is reconstructed from, are collinear within a few mrad, and the resolution depends strongly on the scattering angle, as can be inferred from the figure. Due to the angular uncertainty caused by multiple scattering, a cut on the transverse momentum $p_T > 40\,\mathrm{MeV}/c$ is applied, leading to a lower limit of the scattering angles of 0.3 mrad for the highest-energetic pions with $130\,\mathrm{GeV}/c$.

On the left plot in Fig. 3.3, the influence of the kaon component in the beam is apparent. Their free decay $K^- \to \pi^-\pi^0$ appears all along the beam line, also in the target region and independent of traversed material. The kaons enter the selection of the $\pi Z \to Z\pi\gamma$ reaction, if one of the decay photons is lost, too low-energetic or merged in one cluster with the other photon. Due to the decay kinematics and the minimal energy of the photon due to the trigger selection, the respective pion decay angles lie in a band between 2 and 4 mrad. They inevitably overlap with the reactions of interest when accidentially decaying near the target, since their decay is free of recoil, and accordingly features a spike near zero in momentum transfer, just as the Primakoff events. This emphasizes the importance to identify their contribution. This is realized with high efficiency and high purity, *i.e.* at very little loss of true pion-induced signals, employing

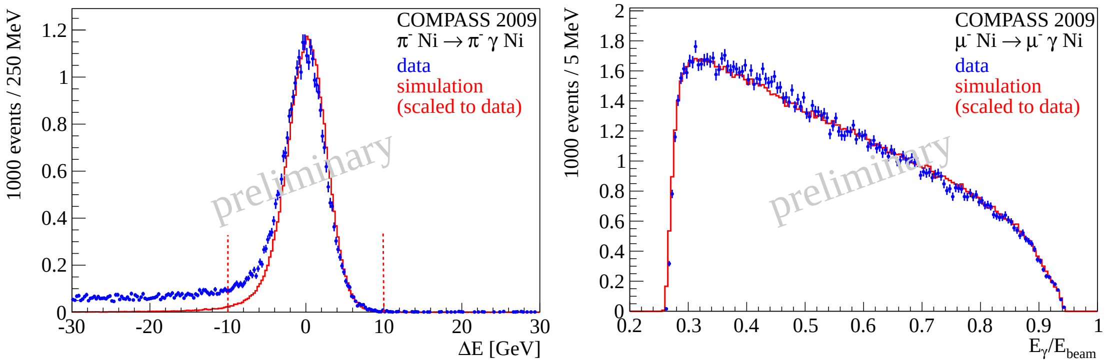

Figure 3.4: Left plot: Primakoff exclusivity signal for pions. The height of the simulated spectrum is scaled to the real data statistics, visualizing the good agreement of the peak width. The applied exclusivity cut is indicated. The right plot compares the photon energy spectrum of the muon control measurement with its simulation.

the CEDAR signals as presented in C.2. The effect of this suppression is shown in the right plot of Fig. 3.3. The inefficiency of this procedure, *i.e.* the fraction of pions lost due to the CEDAR cut , is less than 2%, and the impurity, *i.e.* the fraction of kaons remaining in the sample, is less than 4%. The latter number is to be multiplied with the fraction of kaons in the beam of 2.5%, such that the remainder of kaons is completely negligible.

3.2.3 Exclusivity peak and photon energy spectrum

The vertices formed by an incoming pion and a scattered charged particle track and found within the cuts displayed in Fig. 3.3, are combined with the highest-energetic cluster in ECAL2 that appeared coincidently with the two charged-particle tracks. The distributio of their energy balance $\Delta E = E_{\text{beam}} - E_\pi - E_\gamma$ is displayed in Fig. 3.4. The height of the simulated spectrum is scaled to the real data statistics in order to visualize the good agreement of the peak width for both distributions. A significant background contribution is visible as a tail towards lower energies, steming mainly from the K^- decay contribution, which is not subtracted in this distribution. Fig. 3.5 clarifies the effect. Since only one photon is considered in the energy balance, the kinematics for kaon decay $K^- \to \pi^-\pi^0 \to \pi^-\gamma\gamma$ is not complete and features a tail towards lower energy. This is correlated with a shift in the invariant mass of the outgoing pion-photon system $m_{\pi\gamma}$ with respect to the kaon mass $m_{K^-} \approx 0.493\,\text{GeV}/c^2$.

The same effect appears for the contribution from the $\rho(770)$ resonance, produced

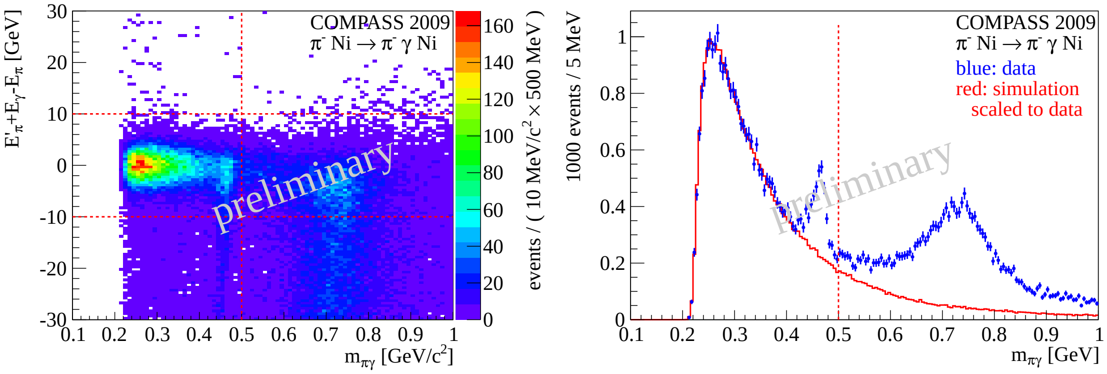

Figure 3.5: Exclusivity versus $\sqrt{s} = m_{\pi\gamma}$. The background contributions due to the $\rho(770)$ resonance, as well as from the free decay of beam kaons, is visible, as discussed in the text.

in reactions $\pi^-\mathrm{Ni} \longrightarrow \mathrm{Ni}\pi^-\pi^0$, eventually featuring another, low-energetic π^0 such that strong-interaction production is not suppressed by G-parity, *cf.* Ch. 4. While the dominant part of the background is removed by constraining the analysis on $m_{\pi\gamma} < 0.5\,\mathrm{GeV}/c^2$, a tail into this region of interest can not be suppressed by cuts on the vertex position or the CEDAR signal. In order to account for this background, an elaborate description of it has been developed following an idea by the author, making use of the events where the two photons are observed and the neutral pion(s) reconstructed. For those events, the π^0 decay kinematics is randomized according to its expected theoretical angular distribution and used in this modified form on the Monte Carlo input level. By this method, the background contribution to regions, where the background process overlaps with the pocess under investigation and cannot be distinguished from it in this experiment, is determined. The respective spectra have not yet been available at the time of writing up this document.

3.2.4 Reconstructed momentum transfer distribution

The distribution of the momentum transfer q for the previously discussed event selection is shown in Fig. 3.6, comparing pion and muon data. The shape of the Primakoff peak at low q is the same in both cases. For the muon data, the simulation reproduces exactly the shape of the spectrum [53], prodived the Ni form factor is taken into account (not shown here).

The correct way to handle the diffractive contribution, *i.e.* the contribution via the

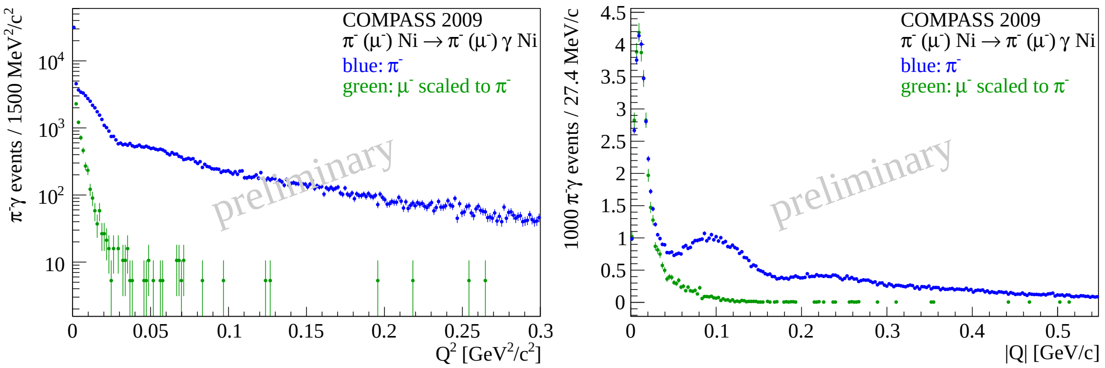

Figure 3.6: Primakoff peak in q^2 and q (named with capital letters in the plots, *cf.* the discussion in Ch. 2), for the reactions $\pi^-\mathrm{Ni} \to \mathrm{Ni}\pi^-\gamma$ and $\mu^-\mathrm{Ni} \to \mathrm{Ni}\mu^-\gamma$. The distribution of q^2 (left plot, observe the logarithmic scale) amplifies the strong peaking as $q^2 \to 0$. The q distribution (right plot) displays the details of the Primakoff peak at $q < 0.03\,\mathrm{GeV}/c$, which matches precisely for pions and muons. In case of the pions, at higher q the additional strong-interaction contribution becomes dominant, showing the typical diffractive pattern.

strong interaction which is seen clearly in the q-distribution, is to include its full description as given in Sec. 2.4 in the reference cross-section of the simulation.. This takes the overlap of the electromagnetic and the strong-interaction part correctly into account, also concerning interference effects. While this is prepared in terms of the calculus, the implementation in the Monte Carlo simulation is still on the way.

Momentarily, the diffractive contribution is treated by extrapolating its shape (by a model *e.g.* linear in q^2 or quadratic in q) from the region where it dominates (*e.g.* 0.003-0.007 GeV^2/c^2) under the Primakoff peak. The estimated contribution is then subtracted separately in each x_γ bin.

So for the following step, the q interval is chosen such that, on the one side, resolution effects are not dominant and their handling by the simulation can be fully trusted, and on the other side the strong-interaction contribution is not too large to introduce a significant uncertainty. This has been shown to be the case [53] for cut-off values $q_{\max} = 0.0008\text{–}0.002\,\mathrm{GeV}^2/c^2$.

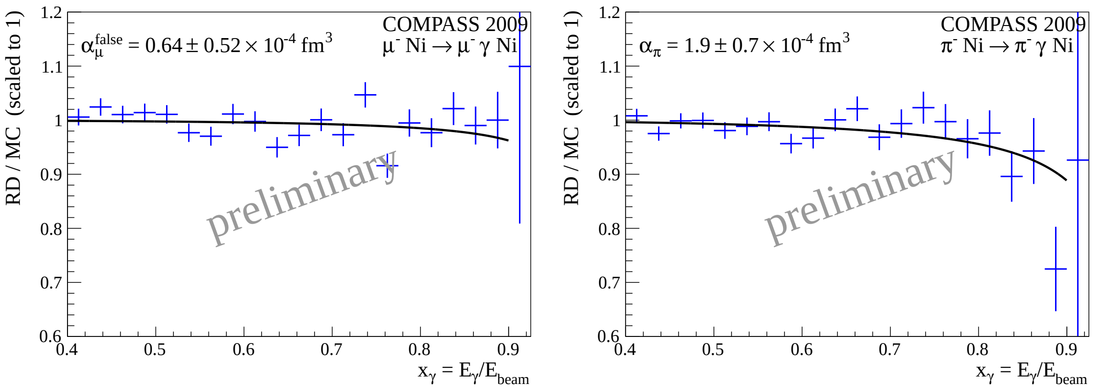

Figure 3.7: Polarisability signal for the muon control sample (left plot) and for the pion sample (right plot) taken with COMPASS in 2009. "RD/MC" refers to the ratio of the real-data event number to the Monte Carlo event number, with normalizing the simulated statistics such that the shown fit approaches 1 for $x_\gamma \rightarrow 0$. In the simulation, the QED radiative corrections as described in section 2.5 have been taken into account.

3.3 Determination of the pion polarisability

With the data selected as described in the previous section, the x_γ distribution is compared to the shape expected for a structureless spin-0 particle in case of the pion data, and for a structureless spin-$\frac{1}{2}$ particle in case of the muon control data.

For the muons, fitting a hypothetical "muon polarisability" to the observed spectrum, results in $\alpha_\mu^{\text{false}} = 0.64 \pm 0.52$ as given in Fig. 3.7. This is the correct value for the muon, almost within the 1-σ uncertainty of 0.52, and is taken as uncertainty estimate for sources common to pions and muons, *e.g.* tracking and the photon's calorimetry.

For the pion, the polarisability determined from the COMPASS 2009 data is, *cf.* Fig. 3.7,

$$\alpha_\pi \;=\; 1.9 \,\pm\, 0.7_{\text{stat}} \,\pm\, 0.8_{\text{syst}} \;\times 10^{-4}\,\text{fm}^3 \qquad (3.1)$$

in the approximation $\alpha_\pi + \beta_\pi = 0$ described along with Eq. 2.67, and with a systematic error estimate that is summarized in Tab. 3.1 and described in detail in reference [53].

3.3.1 Discussion of the polarisability result

While the COMPASS result (3.1) is still preliminary, its major impact on the scientific view on the pion polarisability includes the following points.

uncertainty source	estimated magnitude CL = 68 % $[10^{-4}\,\mathrm{fm}^3]$
tracking	0.6
radiative corrections	0.3
background subtraction in Q	0.4
pion-electron scattering	0.2
quadratic sum	0.8

Table 3.1: Systematic uncertainties estimated on 68 % confidence level

- The COMPASS result is in major tension with the other experimental findings, especially with the dedicated determinations [4, 11] as depicted in Fig. 3.8. About the reasons for this deviation can only be speculated at this point.

- The COMPASS result decreases the tension with respect to the theoretical expectation from ChPT dramatically, to the point that agreement within the uncertainties of both theory and experiment is achieved.

- Given this long-lasting riddle on the pion polarisability appears to be solved, it is desirable to further push the limit of experimental knowledge on this observable to the level where is can help to refine the theoretical approach within ChPT, or even beyond.

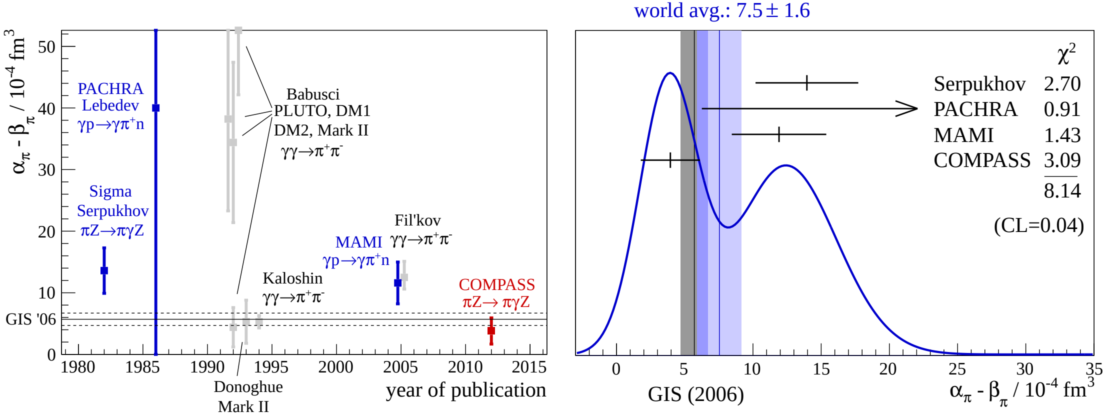

Figure 3.8: Placement of the COMPASS result for the pion polarisability in the world data. Dedicated experimental determinations in blue, re-analyses in grey (from [53]).

Chapter 4

Primakoff Pion Production

4.1 Channels accessible at COMPASS

The data presented in the previous chapter were recorded in 2009 predominantly for the pion polarisability measurement, but they contain also a major contribution from reactions with neutral pions in the final state, since the calorimetric signals of their decay photons are also accepted by the digital trigger described in 3.1. They partly stem from Primakoff reactions, identified with a similar signature in the momentum transfer spectrum as it appears for the bremsstrahlung process treated in the previous chapters. A preliminary analysis of those channels, done by the author in March 2011, had indicated that both channels involving neutral pions listed in 1.4 are indeed present in the data and worth to be analysed, *cf.* Fig. 4.1.

4.1.1 Single-π^0 production

The single-π^0 production $\pi^-\gamma \to \pi^-\pi^0$ shows a strong contribution of the $\rho(770)$ resonance in the invariant mass $m_{\pi^-\pi^0}$ spectrum (*cf.* Fig. 4.1, left plot), which is actually also visible in the single-photon spectra, *cf.* Fig. 3.5, when one of the decay photons is lost.

On the low-mass side of the $\rho(770)$ contribution, a tail is present in the spectrum that extends down to the kinematic threshold which is not driven by a resonant behaviour but by the chiral anomaly. This effect allows the three pions a point-coupling to the photon via the relativistic Levi-Civita-Tensor $\epsilon_{\mu\nu\alpha\beta}$ and it defines the respective coupling constant $F_{3\pi}$. It has been measured in the same Serpukhov experiment [10] that has measured the pion polarisability via the Primakoff effect [11], resulting in a value for $F_{3\pi}$ with a relative error of about 10%. With the COMPASS data, the results of this

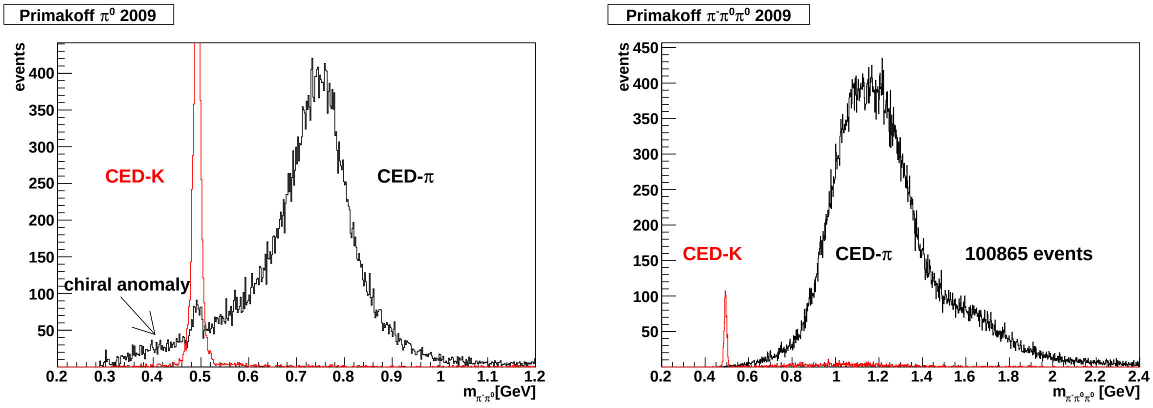

Figure 4.1: The single (left plot) and double (right plot) π^0 Primakoff production channels observed in a preliminary analysis of 2009 COMPASS data. Since *e.g.* calibrations were not final, only a fraction of the actually obtainable statistics is shown here. Also, the method to identify the beam kaons was not yet finalized, therefore a fraction of free kaon decays $K^- \to \pi^-\pi^0$ is left in the sample dubbed "CED-π". The red "CED-K" curves show the kaon events identified with CEDAR analysis software in a preliminary state.

measurement can be checked, along with a list of further work, also in the framework of ChPT, for this quantity [9, 39, 50].

4.1.2 Two-π^0 production

Furthermore, the data contain a large number of events from the exclusive reaction $\pi^-\text{Ni} \to \text{Ni}\,\pi^-\pi^0\pi^0$, also depicted in Fig. 4.1. While the transition of the incoming π^- into a pair $\pi^-\pi^0$ can not be mediated by Pomeron exchange, leading to a comparatively clean Primakoff event sample in that case, the transition into $\pi^-\pi^0\pi^0$ is perfectly allowed by G-parity conservation and is thus mediated also by Pomeron exchange. Its treatment is analogous to the case of three charged pions in the final state as presented in the next section.

4.2 Primakoff Two-Pion Production

In the year 2004, the first attempt was taken to measure Primakoff reactions at COMPASS. As it was found out afterwards, the electromagnetic calorimetry was not yet in a

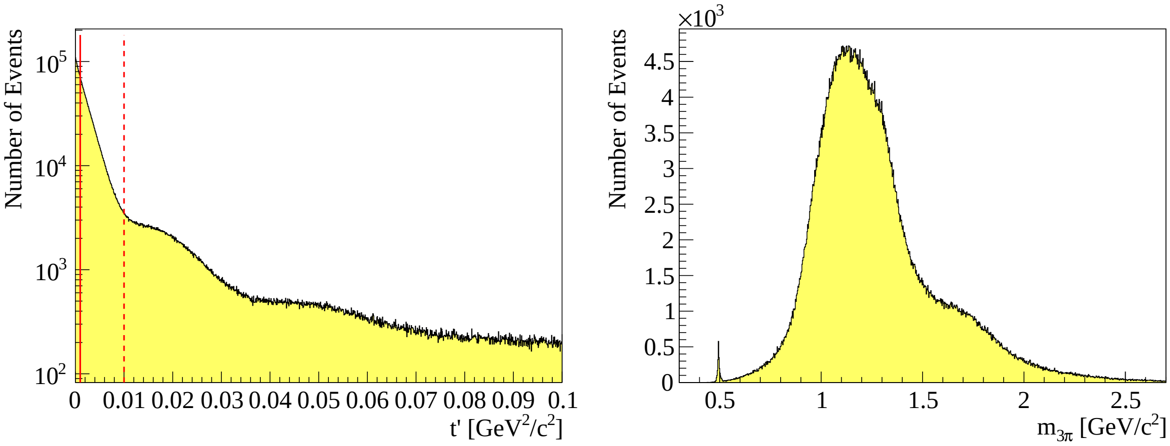

Figure 4.2: Kinematic distributions for the $\pi^-\,\mathrm{Pb} \rightarrow \mathrm{Pb}\pi^-\pi^-\pi^+$ reaction from the 2004 run. In the momentum transfer distribution (left plot, observe the logarithmic y-scale), the regions below 0.001 GeV$^2/c^2$, where the Primakoff effect contributes, and the region up to 0.01 GeV$^2/c^2$, dominated by Pomeron exchange, are indicated by the red lines. In the mass spectrum (right plot), the peak due to the free kaon decay is visible.

status to deliver reliable physics data, in contrast to the 2009 measurement for which it has been proven now to be the case on a unprecedented level of precision, and presented in the previous chapter.

However, in 2004, in parallel to the calorimetric trigger, data were taken with an additional trigger, consisting of a scintillator disk installed immediately downstream of the 3 mm thick lead target. The threshold on the amplitude of the scintillating light was adjusted such that a trigger was delivered if two or more charged tracks cross the disk, in coincidence with the signals of the incoming beam particle that are taken with a beam counter, which was installed upstream of the target. This so-called multiplicity counter turned out to work as foreseen, and it delivered data that lead already to some publications [2, 8], and still shows the potential for more physics output, as shall be discussed in the following.

In the analysis for the reaction to be discussed in the following, $\pi^-\,\mathrm{Pb} \rightarrow \mathrm{Pb}\,\pi^-\pi^-\pi^+$, events are selected where two negatively and one positively charged track form, within the uncertainty of their spatial resolution, an interaction point with the incoming beam trajectory in the target volume. Energetic exclusivity was ensured with a cut similar to what has been presented for the Primakoff Compton reaction in Sec. 3.4. Since no particle identification was available for these data, it is assumed in the following that all particles are pions.

In Fig. 4.2, kinematic distributions for these events are presented. The momentum transfer, reconstructed from the incoming and the three outgoing pions, shows the clear exponential drop-off in the range below 0.01 GeV^2/c^2, which is associated with Pomeron exchange. In the adjacent spectrum, also inelastic processes on the lead nucleus play a role and make the interpretation of the spectrum more difficult.

Here and in the following, the momentum transfer to the nucleus is named t, and its modulus, reduced by its minimum value, is abbreviated $t' = |t| - |t|_{\mathrm{min}}$. This quantity has been denoted q^2 ($= t$ of now) in the previous chapters, as it is done in the literature on structure physics more generally. The usage of t' is common practice in the field of diffractive reactions, and for this reason adopted in the present context. It is somewhat in tension with the usage of t as Mandelstam variable in the $\pi\gamma$ subsystem, as it has been done in the previous chapters in tune with the notation in the literature relevant there.

4.2.1 Partial-wave analysis

The understanding of the mass spectrum depicted in Fig. 4.2 requires the framework of partial wave analysis (PWA), which has been employed and shall be quoted in the following, but is too complex to be introduced in a satisfactory manner here. The reader is referred to the carefully written text book of M. Perl [56] for general aspects, and to the publications by the author [2, 8] for the concrete realization in the present work.

The guiding principle is that the intermediate states, into which the pion is excited through the interaction, are mesonic resonances with well-defined quantum numbers, determined by spin J, parity P and charge-conjugation parity C (for the latter in case of charged resonances, the C-parity of the neutral partner in their constituent-quark multiplett). In addition to those, two more quantum numbers are specified for some considered transition: First, the projection M of the resonance spin J onto the incoming-particle axis (in the *CM* of the resonance). Secondly, the reflectivity ϵ of the transition is determined. It expresses, using the parity of the incoming and outgoing system and the involved orbital angular momentum, whether the exchange particle has natural ($J^P = 0^+, 1^-, 2^+, \ldots$) or unnatural ($0^-, 1^+, 2^-, \ldots$) quantum numbers.

Next, it is assumed that the decay of the resonance R into the observed three pions goes through some "isobar" configuration, meaning that the decay proceeds in fact in two steps of two-body decays. In the first step, the resonance decays into a bachelor pion and a two-pion isobar resonance r, *i.e.* $R \to \pi r$, where r, for the mass range of interest here, is typically a $\rho(770)$ or an $f_2(1270)$. In the second step, the isobar decays into two pions, $r \to \pi\pi$, and the final state is reached. A specific spin configuration in such a resonance decay is thus given by $J^{PC} M^{\epsilon} r \pi L$, where L determines the orbital angular momentum between r and the bachelor π in the first decay step.

All such excitations to existing resonances that decay into three pions, give rise to an amplitude that contributes to the total transition probability. This probability is obtained by squaring the total amplitude, to which the single amplitudes have been summed up.

The key feature of PWA is that due to their quantum numbers, the contributing resonance decays have different angular patterns in the 5-dimensional decay volume. The correlations between the variables is sufficiently high, such that even with only a limited knowledge of the three-pion distribution, the contributing amplitudes can be concluded without ambiguity. Additionally, due to the squaring of the amplitude sum, the respective interference terms must be present in the three-pion distribution.

The interference terms are useful in a two-fold way: First, they can serve to identify small-resonance contributions. If an amplitude is small with respect to another, overlapping contribution, then the interference term is possibly much larger and can be identified already at lower statistics. Secondly, at this point it becomes relevant that a resonance is described on the quantum-mechanical level by a complex phase, running from 0 (on the low-energetic side of the resonance) through π (on top of the resonance) and approaching 2π when the exciting energy is much higher than the resonance energy. This phase determines the size and the sign of the interference term, or in turn, from knowing the interference term, the phase motion can be concluded.

4.2.2 Main resonances in the $\pi^-\pi^-\pi^+$ channel

The PWA of the three-pion spectrum of Fig. 4.2 is presented along with Figs. 4.3 and 4.4. The dominant contributions can be recognized already by eye in the mass spectrum of Fig. 4.2, once one is pointed to their position and strength. Firstly, they are the $a_1(1260)$ and the $a_2(1320)$, and their decay amplitudes in $1^{++}0^{+}\rho\pi S$ and $2^{++}1^{+}\rho\pi D$, respectively, are presented in Fig. 4.3 (upper-left and middle-left plot). The side bump at higher energy of the three-pion mass spectrum is due to the $\pi_2(1670)$ resonance. Its main decay amplitude $2^{-+}(0/1)^{+} f_2 \pi S$ is shown in Fig. 4.4 (upper and middle left plot). The two plots for the $\pi_2(1670)$ represent the two spin orientations $M = 0$ and $M = 1$ of the resonance.

In all cases, the contribution to the mass spectrum is shown for two ranges of momentum transfer: In red the contribution for extremely low values $t' < 0.0005$, which is even only half of what is usually considered the Primakoff range, but anyway referred to in the following as the Primakoff region. And in black the contribution for the disjunct window determined by $0.0015 < t' < 0.01$, called in the following the diffractive region.

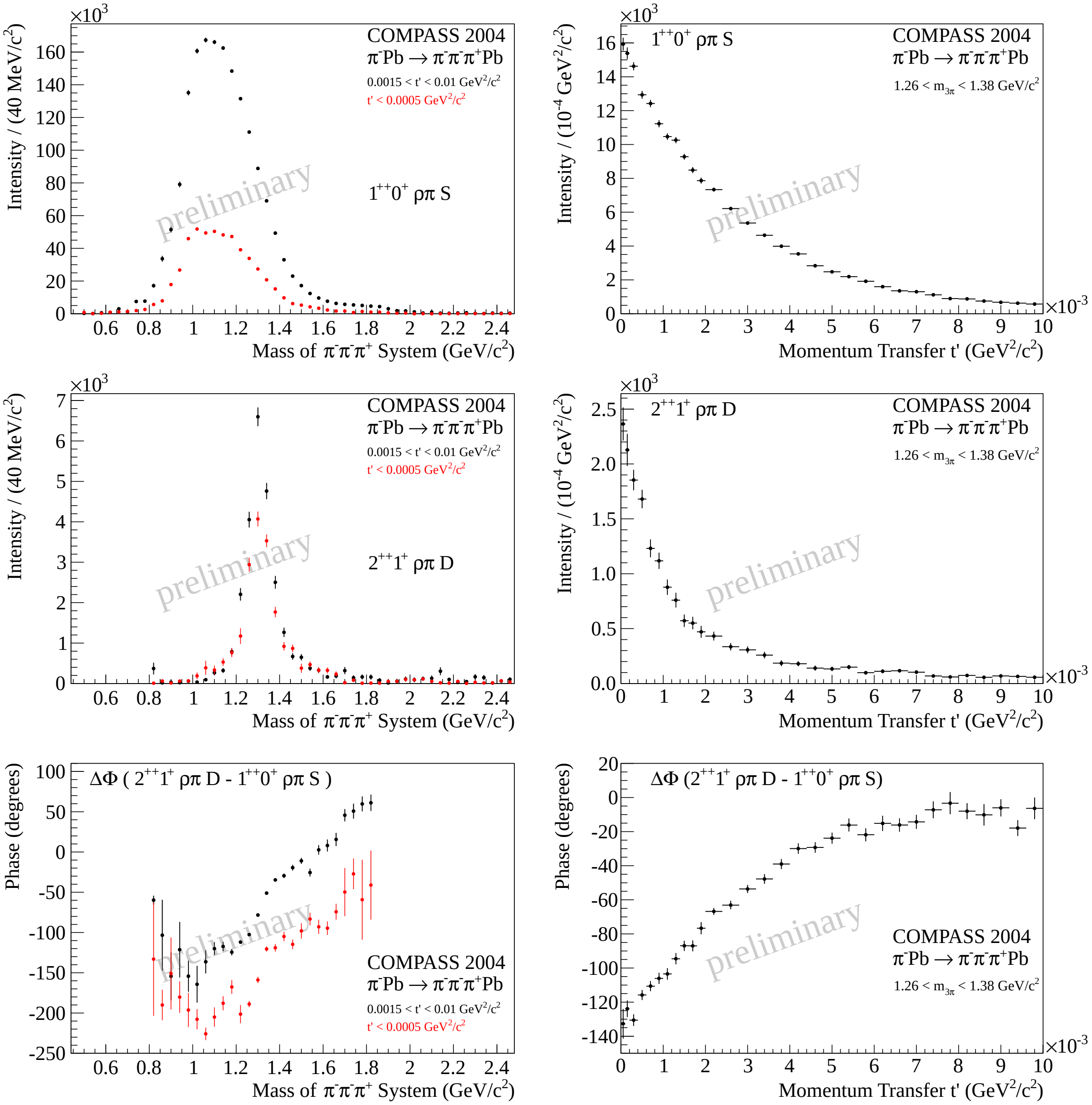

Figure 4.3: Interference between the a_1 and a_2 resonances for different ranges of momentum transfer.

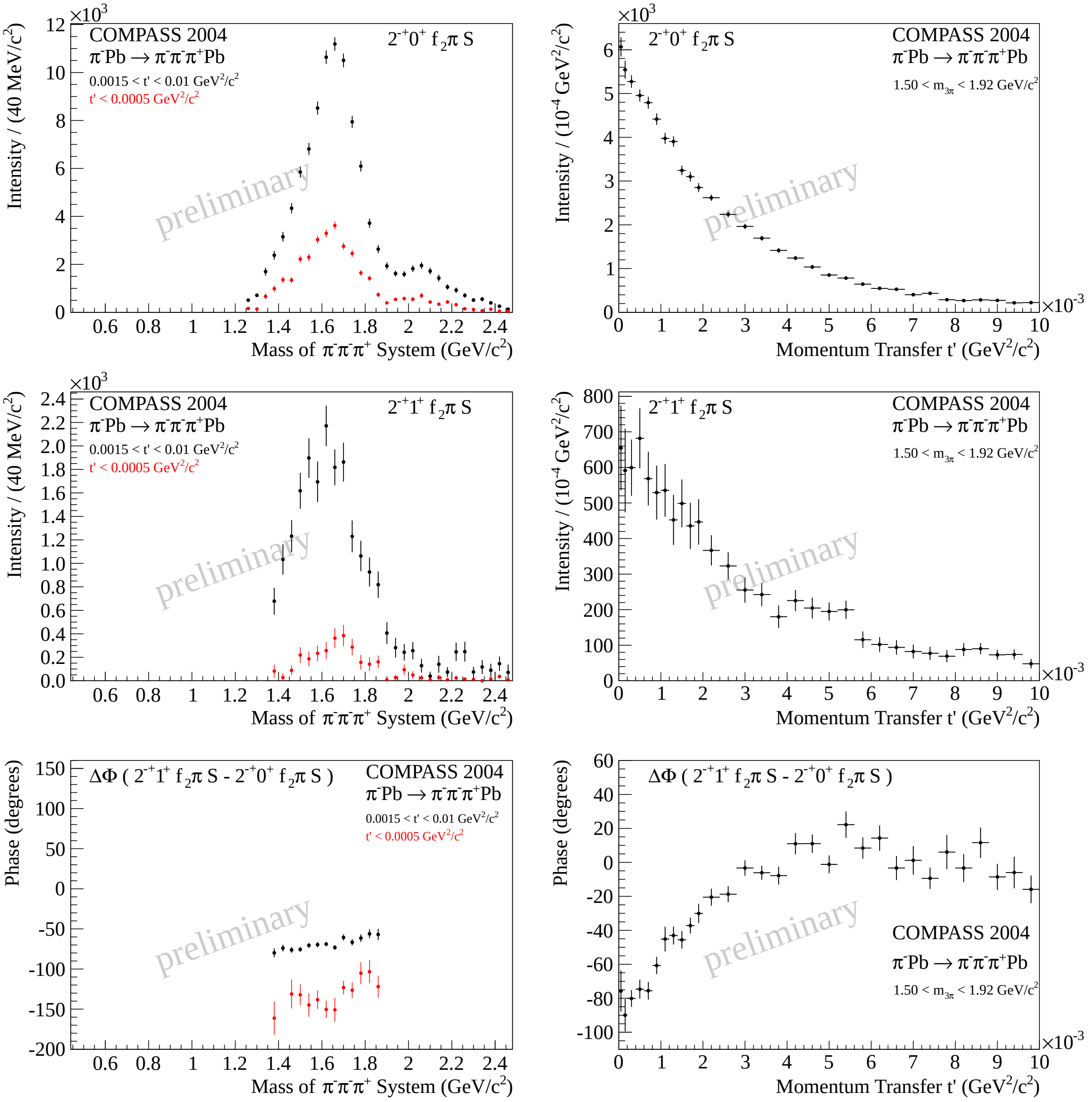

Figure 4.4: Interference between the two spin components $M = 0$ and $M = 1$ of the π_2 resonance for different ranges of momentum transfer.

In the lower-left plot of the two figures, the phase motion extracted from the interference term between the two resonances is shown. In the case of the a_1 and the a_2 resonances, the full resonance behaviour of the a_2 can be recognized on the high-energetic shoulder of the a_1, where the a_1 exhibits only little phase motion. Looking at the relative phase motion between the two spin projections of the π_2, it is demonstrated that, indeed, the same resonance decays in two ways: the phase motion between the two contributions does not change at all with mass.

Comparing the relative strengths present for the two t' ranges in the various resonances, indicates already that they must be of quite different origin: While the a_2 strength in the Primakoff region is at the 70% level of the diffractive region, for the a_1 it amounts to only 40%. The reason for this behaviour is discussed in the next section.

4.2.3 Radiative coupling of the $a_2(1320)$ and of the $\pi_2(1670)$

For understanding better the different strengths observed in the two t' windows, the PWA is repeated in thin t' slices, which is presented in Figs. 4.3 and 4.4 on their right-hand columns. Doing so, it is recognized that the increased strength of the a_2 decay amplitude $2^{++}1^{+}\rho\pi D$ at smallest t' belongs to a sharp rise at the smallest measured t' values.

This is at first sight surprising. For Pomeron exchange, one expects on theoretical grounds (see *e.g.* [56]) that the amplitude exhibits a t'-dependence $\propto t'^{(M/2)}\exp(-bt')$ with the slope parameter $b \approx 400(\mathrm{GeV}/c)^{-2}$ being determined by the diffractive radius of the target Pb nucleus. This value of b describes indeed very well the slope for the $1^{++}0^{+}\rho\pi S$ and $2^{-+}0^{+}f_2\pi S$ partial waves (displayed in the upper right plots in the figures). Following this prescription, one would expect for the $M = 1$ cases (middle rows of in figures) a $\propto t'\exp(-bt')$ behaviour, implying that it vanishes at smallest momentum transfer $t' \rightarrow 0$, rises smoothly to a maximum at $t'_{\mathrm{max}} = b^{-1} \approx 0.0025$ and then also falls off exponentially.

However, the peaking happens on a completely different scale, in case of the a_2 $M = 1$ component more than a factor 10 narrower. What is observed here is the Primakoff effect, being responsible for the narrow peaking near $t' = 0$. The fact that the exchange particle is an almost real photon necessitates that it shows up with $M = 1$, since the photon, with helicity $+1$ oder -1, collides with a (spin-0) pion to form the resonance.

For the a_2, the coupling $a_2 \leftarrow \pi\gamma$ has in fact already been observed in a similar measurement via the Primakoff effect by the SELEX collaboration [52].

For the π_2, the observation of its radiative coupling is a new observation by the COMPASS collaboration, and the publication, along with the figures presented here, is envisaged. For extracting the actual value of the radiative width, the obtained strength must

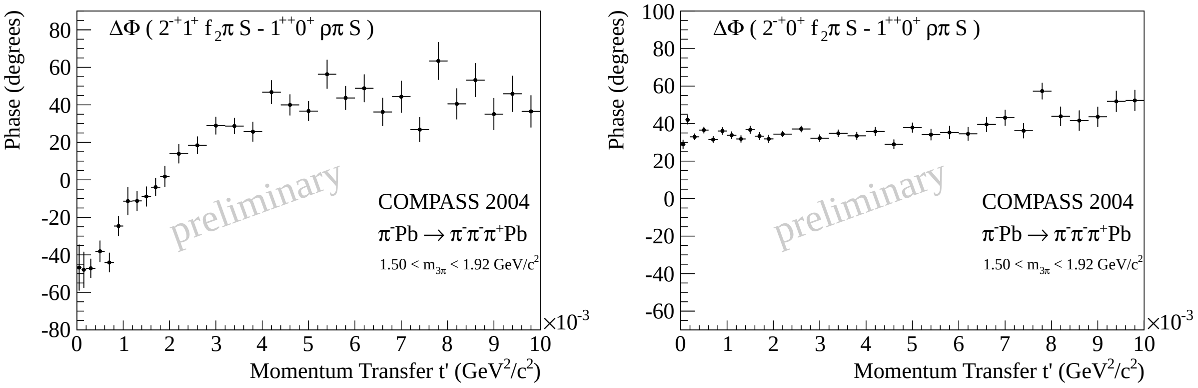

Figure 4.5: Interference between the π_2 components and the a_1: The $M = 1$ component (left plot) features a phase motion due to photon exchange, which is absent in the $M = 0$ case (right plot).

still be normalized, which is planned to be done in a same way as the absolute normalization has been obtained in [2], using beam kaon decays $K^- \to \pi^-\pi^-\pi^+$, appearing as small spike in Fig. 4.2. The fact that the π_2 features a radiative width does not only show up when it is interfering with its own $M = 0$ strong-interaction component, but also in interference with the a_1 resonance, *cf.* Fig. 4.5.

4.2.4 Coulomb-nuclear interference

A novel aspect in the observations discussed so far is the exact study of the phase motions.

On the one hand, there is an overall shift observed when comparing the phase motion in the two t' regions, as it is done in the lower-left plots in Figs. 4.3 and 4.4: The (red) Primakoff-region data show exactly the same resonance behaviour as the (black) diffractive-region data (that is, one looks at the same object), they are just shifted by about 90 degrees. This is exactly what should be observed, given that the electromagnetic interaction is a real-amplitude scattering process, while the strong interaction stems from an imaginary-amplitude absorptive process, *cf.* Eq. 2.94.

This analysis can be done, with the COMPASS data for the first time, in much greater detail using thin t' slices, *cf.* the lower-right plots in Figs. 4.3 and 4.4. The phase shift starts at angles bigger than 90 degrees, in case of the a_2 rather 120 degrees, at $t' = 0$, and then falls off to 0 with larger t'. It is anticipated that this interference behaviour

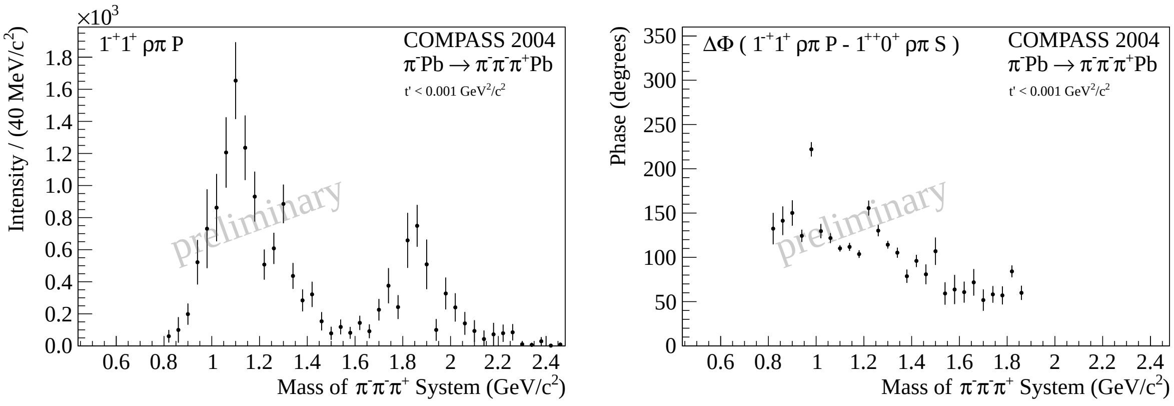

Figure 4.6: No evidence for a Primakoff 1^{-+} signal.

can be modeled by the methods presented in Sec. 2.4. On the one hand, the Coulomb phase steming from multiple-photon exchange is relevant here, but on the other hand, those data can be used to study the details of the formation of the strong-interaction potential seen by the pion excitation process, *i.e.* getting a more detailed understanding of the Pomeron.

4.2.5 Other radiative couplings

Along the same line, the COMPASS data were searched for more indications for light-meson radiative couplings. There is no Primakoff behaviour visible anywhere for the a_1 signal, so it is inferred that there is no significant radiative coupling of the a_1, which is at variance with the findings in [71].

Another study has been done for the spin-exotic $1^{-+}1^{+}\rho\pi P$ wave, presented in Fig. 4.6. It shows no evidence for a radiative coupling of a $\pi_1(1600)$, which comes a little as surprise, given that such a state was reported to couple to $\rho\pi$ in [8].

4.2.6 Reflectivity doubling

An important effect, when using PWA in the extreme forward kinematics of the Primakoff processes, is caused by the limited resolution on the particle's angles. At some point, the direction of the momentum transfer can not be safely reconstructed anymore, and it may take on some arbitrary direction, in case the multiple scattering effect is larger than the transverse momentum transfer.

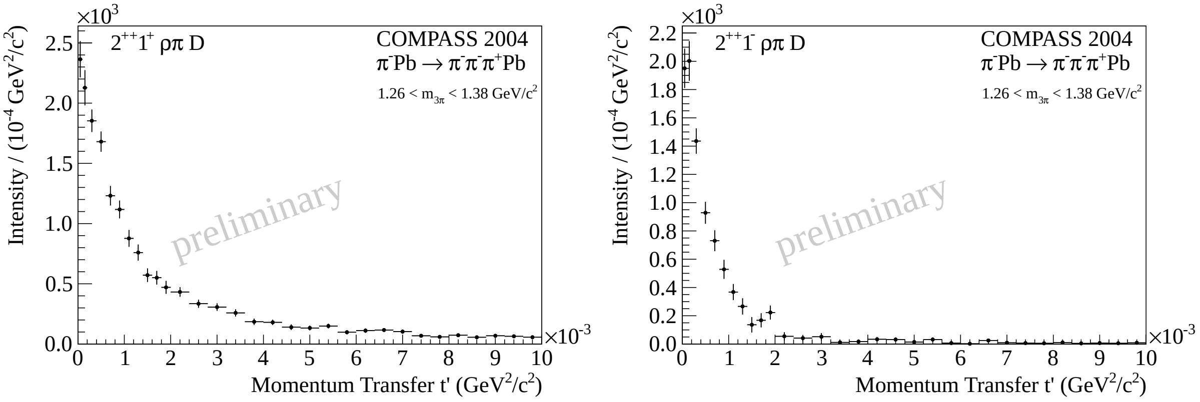

Figure 4.7: Appearence of negative reflectivity at very low momentum transfers.

For M=0-components, this poses not a problem, since they have no ϕ dependence, however for $M = 1$ the PWA algorithm relies on a correct determination of the recoil direction. It was shown in a specific Monte Carlo simulation by Dima Ryabchikov (Protvino / TU München), that this effect leads to a wrong determination of the reflectivity. This means, that even if in the experiment only positive-reflectivity components appeared, they give rise to intensities in both reflectivities in the PWA. This is demonstrated in Fig. 4.7 for the case of the a_2 Primakoff signal. It is clearly displayed that the effect appears only at very small t', above 0.002 there is no negative-reflectivity intensity visible at all.

It is of great importance to take this effect into account when the radiative widths are determined. The mentioned Monte Carlo study has shown that this is correctly done by summing up the contributions found in the two reflectivities.

4.2.7 Cross-sections for $\pi^-\gamma \to \pi^-\pi^-\pi^+$

The Primakoff reaction $\pi^-\gamma \to \pi^-\pi^-\pi^+$, that has been examined in the previous chapters in terms of resonance couplings, is also of interest from the ChPT point of view, since for this process, at its kinematic threshold a firm prediction is possible at tree level, and was given in [44]. N. Kaiser has also given the 1-loop corrections for this process in [42].

The region to be examined is displayed in Fig. 4.2, visible in the three-pion mass distribution as the lower-energetic foot around the kaon peak. Technically, the determination of this chiral contribution was done be implementing the fully-differential form of the cross-section,

$$\begin{aligned}
d\sigma_r(s) \;=\;& \frac{\alpha\cdot s}{(s-m_\pi^2)^3 f_\pi^4}\cdot 8\pi\,\cdot\, d\Phi_3(p+k,q_1,q_2,q_3)\,\cdot \\
& \Bigg[\frac{\vec{q}_1\times\hat{k}}{\omega_1-\vec{q}_1\cdot\hat{k}}\left(p_0(r-\omega_2)-r\omega_1-\vec{k}\cdot\vec{q}_2\right)+ \\
& \frac{\vec{q}_2\times\hat{k}}{\omega_2-\vec{q}_2\cdot\hat{k}}\left(p_0(r-\omega_1)-r\omega_2-\vec{k}\cdot\vec{q}_1\right)+ \\
& \frac{\vec{q}_3\times\hat{k}}{\omega_3-\vec{q}_3\cdot\hat{k}}\left(rk_0-p_0\omega_3-\vec{k}\cdot\vec{q}_3\right)\Bigg]^2
\end{aligned} \tag{4.1}$$

as an own partial wave in the framework of the PWA software, as described in [2].

Integrating the 4-momentum conserving δ function in the phase space element, using rotational symmetry around the z axis, and carrying out the square, the form published in [44] is obtained,

$$\begin{aligned}
d\sigma_r(s) \;=\;& \frac{\alpha\cdot s}{(s-m_\pi^2)^3 f_\pi^4}\cdot\frac{1}{8\pi^3}\cdot d\omega_1\, d\omega_2\, dx\, d\phi\,\cdot \\
& \Bigg[\frac{q_1^2(1-x^2)}{(\omega_1-q_1x)^2}\cdot\Big(2\left[p_0(r-\omega_2)-r\omega_1-k_0q_2y\right]^2+\left[k_0r-p_0\omega_1-k_0q_1x\right]^2\Big) \\
& +\frac{2q_1q_2(z-xy)}{(\omega_1-q_1x)(\omega_2-q_2y)}\cdot \\
& \Big(\left[p_0(r-\omega_2)-r\omega_1-k_0q_2y\right]\cdot\left[p_0(r-\omega_1)-r\omega_2-k_0q_1x\right]+ \\
& 2\left[k_0r-p_0\omega_2-k_0q_2y\right]\cdot\left[p_0(\omega_1+\omega_2)-r\omega_1+k_0(q_1x+q_2y)\right]\Big)\Bigg]
\end{aligned} \tag{4.2}$$

The procedure has been extended by including the chiral loops [42] as well as a preliminary version of non-resonant $\pi\rho(770)$ coupling and other interesting extensions. This work is still to be finalized, but indications have already be seen that a much bigger fraction of the spectrum can be understood following this approach, than has been explored by now [2].

With this, I close the journey through the field of Primakoff reactions. It has been started on the will to solve the riddle around the pion polarisability. On the way, it was found the the experimental technique is much richer, and lends itself for the study of strong interaction in much more and exciting aspects.

Chapter 5

Silicon Microstrip Detectors for COMPASS

The silicon microstrip detectors for the COMPASS experiment have been developed in a group at the chair of Prof. Stephan Paul (TU München), whose coordination the author of the present work has taken over in 2001. The development profited from that for another experiment (HERA-B), especially in terms of taking over the silicon sensors when they were not needed for the original purpose anymore, and also from the large experience that members of the team, first to mention I. Konorov, have brought with them from employing silicon detectors in the WA89 experiment at CERN.

A complete characterization of these detectors is not given here, but is found *e.g.* in the respective section of publication [1] (and upcoming [24]) which is also reproduced in the Appendix of the present work, and in all detail in various works of the involved students [12,14,25,26,30,36,37,40,49,61,65,68,72]. It shall only be emphasized that the employed detectors feature a double-sided readout, which minimizes the material that the particles have to cross, and also allows the usage of amplitude correlations between the signals of the two sides in the analysis [49].

5.1 Cooling the COMPASS silicon detectors

The original proposal of the COMPASS experiment foresaw that the employed silicon microstrip detectors are cooled to 130 Kelvin and make use of the "Lazarus effect", referring to a "revival" of heavily irradiated silicon detectors at cryogenic temperatures [16], in order to cope with the expected fluences and the related radiation damage. It was found out much later, that the radiation impact especially of high-energetic pions is

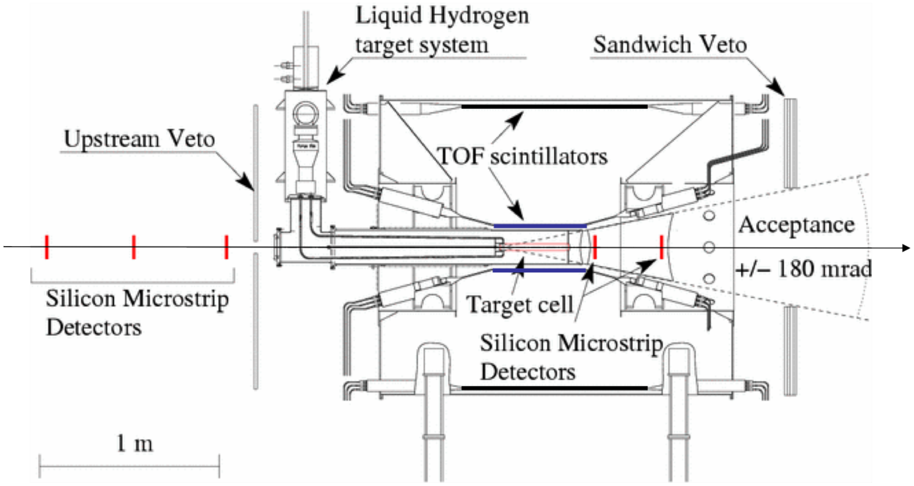

Figure 5.1: Target region in 2009. The silicon detectors are all operated in cryogenic mode, requiring cryostats that provide an insulation vacuum on the level of 10^{-5} mbar. This is specifically difficult to achieve in the confined space directly downstream of the target, where the cryostat has precisely the conical opening of the apparatus acceptance and the available space in the recoil proton detector.

not as high as it was previously assumed [37, 68], and also that it is of advantage for the whole experiment to employ a different beam optics than originally foreseen. The hadron beam is now not focused in the target region, but rather at the position of ECAL2 (*cf.* Fig. 3.2), where the required beam hole is reduced to a minimal size in order to cover as much of the phase space for high-energetic photons as possible. This is, obviously, a reasoning unrelated to the silicon detectors, but has the effect of a widened beam profile in the target region, reducing the local radiation damage by about one order of magnitude.

Thus, the original reasons for cooling were weakened with time. However, its envisaged and finally successful realisation and installation in the setup, as sketched in Fig. 5.1, turned out to be of great use in other ways.

Firstly, the temperature stabilization made the silicon detectors robust against the annual temperature variations present in the experimental area, which is situated above ground and follows the meteorological conditions. One of the influences of temperature variations is the moving of detectors due to thermal expansion of their support structures. This has been found to concern, for the 2004 data, also the silicon detectors with daily variations on the level up to 50 μm, about an order of magnitude larger than their

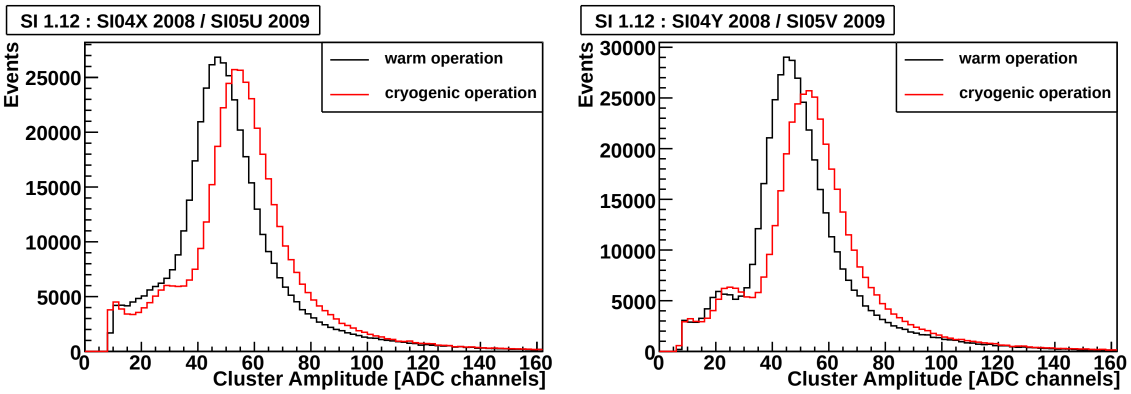

Figure 5.2: Signal amplitudes for warm (black histograms) and cold (red histograms) detectors, from [37]. Signals from the same silicon sensor, named "SI1.12", are shown in all histograms. The detector was employed in the position called SI04XY during the year 2008 in warm operation, and in the position SI05UV during 2009 in cold operation.

spatial resolution. Following ideas by the author, a first version of a "run-by-run" alignment (*i.e.* position correction for the detectors on the time scale of a few hours) was implemented [26], which is by now integrated in the alignment package of COMPASS as established procedure for the data taking with a hadron beam.

Secondly, the cooling has a benficial effect on the signal-to-noise ratio, as depicted in Fig. 5.2, which increases by about 20%, as discussed in [37]. Part of this increase is due to a different behavior of the employed APV readout ASIC. Its operation was found to be most stable when the detector is cooled to 200 Kelvin, and since no radiation damage is observed for the cold detectors yet, there is no need to reach the originally planned 130 Kelvin, where is was observed that the APV chips tend to become unstable [12] .

The increase in amplitude translates to an enhancement of the spatial and time resolution on the same relative level, and typical values of 7μm spatial and 1.5 ns time resolutions are achieved.

5.2 Future developments

As an example for possible further developments, a promising analysis of the silicon detector signals is shown in Fig. 5.3. The signal amplitudes in the silicon detectors are read out with a high precision, as can be inferred from Fig. 5.2, mainly for the purpose of enhancing the spatial resolution by charge weighting, using the relative height of neigh-

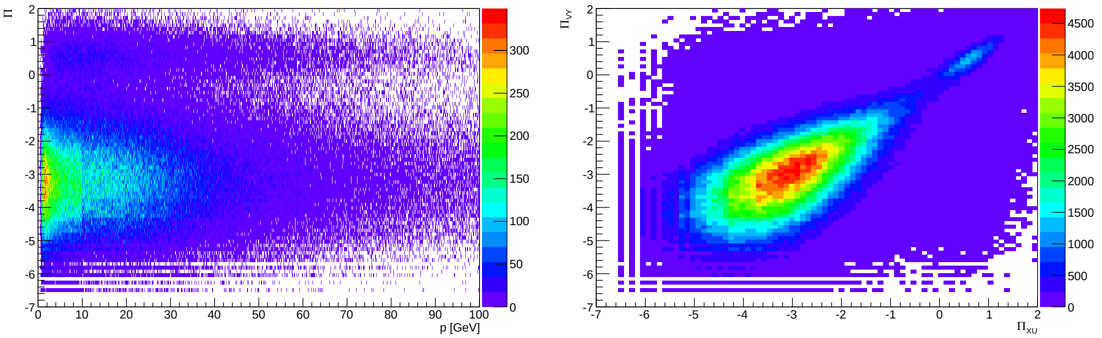

Figure 5.3: Left plot: The quantity Π, defined in Eq. 5.1, for the four signals of the detector planes in the conical cryostat measuring the horizontal coordinate (named "XU") is shown versus the momentum of the respective trajectory. The band above zero is associated with double-tracks, as explained in the text. The right plot shows the strong correlation observed between the signals from the "XU" detectors and those from the vertical "YV" projections.

boring strips. The amplitudes belonging to a particle trajectory combined, are a measure of the energy loss, which is approximately Landau-distributed.

The amplitude informations a_i for a particle trajectory of the four silicon detectors in the concial cryostat (see Fig. 5.1) can be combined using a specially adapted transformation, where only events are selected where all amplitudes are bigger than the most probable amplitude, $a_i > \hat{a}_i$,

$$\Pi = \sum_i \log\left(\frac{a_i - \hat{a}_i}{\hat{a}_i}\right) \qquad \text{requiring all } a_i > \hat{a}_i \tag{5.1}$$

in order to make visible when all amplitudes are commonly above a certain threshold. Formula 5.1 is constructed such that if all amplitudes are more than twice the most probable value $a_i > 2\hat{a}_i$, its value is above zero.

This offers a novel way to recognize so-called double-tracks, where two particles are so close to each other in space, that they can not be separated by the silicon detectors. This happens especially for the electron-positron pairs emerging from the conversion of a high-energetic photon, $\gamma Z \rightarrow Z e^+ e^-$, since the opening angle between the e^+ and the e^- is extremely small. The quantity Π allows for a clean separation of such double-tracks, requiring $\Pi > 0$.

Especially channels with several photons in the final state suffer from loss of some of the photons due to conversion. The approach presented here has the potential to recover a part of them.

Summary

As the lightest particle of the strong force, the pion plays a central role in the field of strong interactions, and understanding its properties is of prime relevance for understanding the strong interaction in general.

The low-energy behaviour of pions is of particular interest. Although the quark-gluon substructure and their quantum chromodynamics is not apparent then, this specific inner structure causes the presence of approximate symmetries in pion-pion interactions and in pion decays, which gives rise to the systematic description of processes involving pions in terms of few low-energy constants. Specifically, the chiral symmetry and its spontaneous and explicit breaking, treated in chiral perturbation theory (ChPT), leads to firm predictions for low-energy properties of the pion. To those belong the electromagnetic polarisabilities of the pion, describing the leading-order structure effect in pion Compton scattering.

The research presented in this work is concerned with the interaction of pions and photons, including pion Compton scattering, and also the production of neutral and charged pions in pion-photon collisions. Common to all investigated processes is, that the collision energy is in the range below a few pion masses. This region is reigned by the chiral dynamics as said before. For all processes, predictions have been available, or were obtained along this work.

From the year 2000 on, the COMPASS experiment at CERN has been prepared in several steps for precision measurements of such processes. The pion-photon interaction is studied through the Primakoff effect by scattering high-energetic pions off the quasi-real photons of a nuclear Coulomb field. The principal characteristic of Primakoff events is extremely small momentum transfer to the target nucleus, below 10^{-3} GeV$^2/c^2$. Their reconstruction requires detectors for the charged and neutral particles at the limit of the physical feasibility. For high-precision charged-particle tracking, silicon microstrip detectors were built, and their operation continuously enhanced. Furthermore, a thorough understanding of QED effects is mandatory in order to really get a handle on the strong-interaction aspect. A good part of the present work was dedicated to solve the open QED issues for the measurements.

From data taken with COMPASS in the year 2004, the Primakoff reaction of the process $\pi^-\gamma \to \pi^-\pi^-\pi^+$ could be isolated and analyzed in terms of the absolute cross-section. The published result confirms the leading-order ChPT prediction. More results could be obtained from the same data concerning the radiative widths of meson resonances, where that of the $\pi_2(1670)$ is a novel observation. The interplay of electromagnetic and strong effects could be observed with unprecedented detail and is subject to further investigations.

In the year 2009 data have been taken that were shown in the present work to be of sufficiently high quality, along with a very detailed unterstanding of the apparative effects, such that the aimed-at determination of the pion polarisability is now in reach.

Some of these results are expected to be completed and published within the next 3-6 months.

Appendix A

Formulæ and Algorithms

A.1 Series expansions

High-relativistic form of $E-p$. Noting that

$$\sqrt{1\pm x} \;=\; 1 \pm \frac{x}{2} - \frac{x^2}{8} \pm \frac{x^3}{16} - \frac{5x^4}{64} \pm \ldots$$

one expands the difference $(E-p)$ of a high-relativistic particle with mass m, energy $E \gg m$ and momentum $p \approx E$

$$\begin{aligned} E-p &= \sqrt{p^2+m^2}-p \\ &= \frac{m^2}{2p} - \frac{m^4}{8p^3} + \frac{m^6}{16p^5} - \ldots \end{aligned} \tag{A.1}$$

used on p.24

Logarithmic series in radiative corrections. Especially when the Mandelstam variable u is near 0, for the evaluation of the virtual photon loops series expansions are needed, and some short-hand notations are introduced:

$$\mathrm{Lf}_0(x) \;=\; \ln(1-x) \;=\; -x-\frac{x^2}{2}-\frac{x^3}{3}-\frac{x^4}{4}-\ldots \tag{A.2}$$

$$\mathrm{Lf}_1(x) \;=\; \frac{\ln(1-x)}{x} \;=\; -1-\frac{x}{2}-\frac{x^2}{3}-\frac{x^3}{4}-\frac{x^4}{5}-\ldots \tag{A.3}$$

$$\mathrm{Lf}_2(x) \;=\; \frac{\ln(1-x)+x}{x^2} \;=\; -\frac{1}{2}-\frac{x}{3}-\frac{x^2}{4}-\frac{x^3}{5}-\ldots \tag{A.4}$$

and

$$\mathrm{Lf}_0(x) - \mathrm{Lf}_1(x) \quad = \quad (1 - x^{-1})\ln(1-x) \quad = \quad 1 - \frac{x}{2} - \frac{x^2}{6} - \frac{x^3}{12} - \dots \tag{A.5}$$

A.2 Integrals and Derivatives

Most of the following integrals and derivatives are contained in collections of mathematical formulæ(*e.g.* [17]) or can be obtained using computer algebra programs (*e.g.* Mathematica®), and are given here for convenience in the specific form as used in the main text. The relation $E^2 = p^2 + m^2$ is sometimes employed in an obvious way.

$$\int \left(3 - \frac{x^2+b^2}{r_u^2}\right) dx \quad = \quad \left(3 - \frac{b^2}{r_u^2}\right) x - \frac{1}{3r_u^2} x^3 \tag{A.6}$$

$$\begin{aligned}
\int\limits_{-\sqrt{r_u^2-b^2}}^{\sqrt{r_u^2-b^2}} \left(3 - \frac{x^2+b^2}{r_u^2}\right) dx \quad &= \quad 2r_u \left(3 - \frac{b^2}{r_u^2} - \frac{r_u^2-b^2}{3r_u^2}\right) \sqrt{1 - b^2/r_u^2} \\
&= \quad 2r_u \left(\frac{8}{3} - \frac{2}{3}\frac{b^2}{r_u^2}\right) \sqrt{1 - b^2/r_u^2}
\end{aligned} \tag{A.7}$$

$$\int \frac{c}{\sqrt{x^2+b^2}}\, dx \quad = \quad c \ln\left(\sqrt{x^2+b^2} + x\right) \tag{A.8}$$

$$\int\limits_0^{\sqrt{r_u^2-b^2}} \frac{b^2}{(x^2+b^2)^{3/2}}\, dx \quad = \quad \left.\frac{x}{\sqrt{x^2+b^2}}\right|_0^{\sqrt{r_u^2-b^2}} \quad = \quad \sqrt{1 - b^2/r_u^2} \tag{A.9}$$

$$\begin{aligned}
\int \frac{d\phi}{E - p\sin\phi} \quad &= \quad \frac{2}{\sqrt{E^2-p^2}} \arctan \frac{E\tan\phi/2 - p}{\sqrt{E^2-p^2}} \\
&\qquad \text{(monotonically increasing in } -\pi < \phi < \pi) \\
&= \quad \frac{2}{\sqrt{E^2-p^2}} \arctan \frac{E\tan(\phi-\pi)/2 + p}{\sqrt{E^2-p^2}} + c \\
&\qquad \text{(monotonically increasing in } 0 < \phi < 2\pi)
\end{aligned} \tag{A.10}$$

$$\int \frac{d\phi}{(E - p\sin\phi)^2} \quad = \quad \frac{-p\cos\phi}{(E^2-p^2)(E - p\sin\phi)} + \frac{E}{E^2-p^2} \int \frac{d\phi}{E - p\sin\phi} \tag{A.11}$$

used on p.49

$$\int \frac{x\,dx}{(a-2b\,x+c\,x^2)^{3/2}} = \frac{a-b\,x}{(b^2-a\,c)\sqrt{a-2b\,x+c\,x^2}} \tag{A.12}$$

$$\int \frac{dx}{(a-2b\,x+c\,x^2)^{3/2}} = \frac{b-c\,x}{(b^2-a\,c)\sqrt{a-2b\,x+c\,x^2}} \tag{A.13}$$

$$\int \frac{dx}{(d-x)\sqrt{a-2b\,x+c\,x^2}} = \frac{1}{\kappa}\ln\frac{\kappa\sqrt{a-2b\,x+c\,x^2}+a-bd+(cd-b)x}{d-x}$$

$$\text{with } \kappa=\sqrt{a-2b\,d+c\,d^2} \tag{A.14}$$

With the identifications

$$a=m^2+p^2x_2^2 \qquad b=Epx_2 \qquad c=p^2 \qquad d=E/p \tag{A.15}$$

$$\begin{aligned}
b^2-a\,c &= -p^2m^2(1-x_2^2)\\
a-b\,d &= m^2-x_2(E^2-p^2x_2)\\
c\,d-b &= Ep(1-x_2)\\
E_x &= E-p\,x_2\,x_l\\
E_x^2-p_x^2 &= a-2b\,x_l+c\,x_l^2\\
&= (E\,x_l-p\,x_2)^2+m^2(1-x_l^2)\\
\kappa &= \sqrt{a-2b\,d+c\,d^2}\\
&= p^{-1}\sqrt{(E^2-p^2x_2)^2-m^4}
\end{aligned}$$

the integrals (A.12), (A.13), (A.14) are used in finding

$$\int \frac{m^2\,dx_l}{(E-p\,x_l)^2} = \frac{m^2}{p(E-p\,x_l)} \tag{A.16}$$

$$\int_{-1}^{1} \frac{m^2\,dx_l}{(E-p\,x_l)^2} = 2 \tag{A.17}$$

$$\begin{aligned}
\int \frac{m^2\,E_x\,dx_l}{(E_x^2-p_x^2)^{3/2}} &= \frac{E(Epx_2-p^2x_l)-px_2(m^2+p^2x_2^2-Epx_2x_l)}{-p^2(1-x_2^2)\sqrt{E_x^2-p_x^2}} \\
&= \frac{p^3x_2(1-x_2^2)-Ep^2x_l(1-x_2^2)}{-p^2(1-x_2^2)\sqrt{E_x^2-p_x^2}} \\
&= \frac{E\,x_l-p\,x_2}{\sqrt{E_x^2-p_x^2}} \qquad \text{(A.18)}
\end{aligned}$$

$$\int_{-1}^{1} \frac{m^2\,E_x\,dx_l}{(E_x^2-p_x^2)^{3/2}} = 2 \qquad \text{(A.19)}$$

$$\int \frac{p\kappa\,dx_l}{(E-p\,x_l)\sqrt{E_x^2-p_x^2}} = \ln\frac{\kappa\sqrt{E_x^2-p_x^2}+(1-x_2)(m^2-x_2p^2+Ep\,x_l)}{d-x_l} \qquad \text{(A.20)}$$

$$\int_{-1}^{1} \frac{p\kappa\,dx_l}{(E-p\,x_l)\sqrt{E_x^2-p_x^2}} = \ln\frac{(E+p)[\kappa(E-px_2)+(1-x_2)(m^2-x_2p^2+Ep)]}{(E-p)[\kappa(E+px_2)+(1-x_2)(m^2-x_2p^2-Ep)]} \qquad \text{(A.21)}$$

and finally

$$\begin{aligned}
&\int dx_l\;\frac{-m^2}{(E-p\,x_l)^2}+\left(\frac{-m^2\,E_x}{E_x^2-p_x^2}+\frac{2(E^2-p^2x_2)}{E-p\,x_l}\right)\frac{1}{\sqrt{E_x^2-p_x^2}} = \\
&= -\frac{m^2}{p(E-p\,x_l)}-\frac{E\,x_l-p\,x_2}{\sqrt{E_x^2-p_x^2}}+ \\
&\quad+\frac{2(E^2-p^2x_2)}{p\kappa}\ln\frac{\kappa\sqrt{E_x^2-p_x^2}+(1-x_2)(m^2-x_2p^2+Ep\,x_l)}{d-x_l} \qquad \text{(A.22)}
\end{aligned}$$

$$\begin{aligned}
&\int_{-1}^{1} dx_l\;\frac{-m^2}{(E-p\,x_l)^2}+\left(\frac{-m^2\,E_x}{E_x^2-p_x^2}+\frac{2(E^2-p^2x_2)}{E-p\,x_l}\right)\frac{1}{\sqrt{E_x^2-p_x^2}} = \\
&= -4+\frac{2(E^2-p^2x_2)}{p\kappa}\ln\frac{(E+p)[\kappa(E-px_2)+(1-x_2)(m^2-x_2p^2+Ep)]}{(E-p)[\kappa(E+px_2)+(1-x_2)(m^2-x_2p^2-Ep)]} \qquad \text{(A.23)}
\end{aligned}$$

used on p.50

Derivatives appearing in the eikonal approximation. In the context of Eq. 2.88 and the footnote on *p.* 46, the following derivatives are used:

$$\frac{\partial}{\partial x}L_a=\frac{\partial}{\partial x}\left(\ln\left(1+\sqrt{1+x^2}\right)\right) \quad = \quad \frac{x}{x^2+1+\sqrt{1+x^2}} \tag{A.24}$$

$$\frac{\partial}{\partial x}L=\frac{\partial}{\partial x}\left(\ln\left(1+\sqrt{1-x^2}\right)\right) \quad = \quad \frac{x}{x^2-\left(1+\sqrt{1-x^2}\right)} \tag{A.25}$$

$$= \quad \frac{1}{x}+\frac{\sqrt{1-x^2}}{x(x^2-1)} \tag{A.26}$$

$$\frac{\partial}{\partial x}S_1=\frac{\partial}{\partial x}\left(\left(\frac{1}{3}+\frac{2}{3}x^2\right)\sqrt{1-x^2}\right) \quad = \quad \frac{x\,(1-2x^2)}{\sqrt{1-x^2}} \tag{A.27}$$

$$\frac{\partial}{\partial x}S_2=\frac{\partial}{\partial x}\left(\left(\frac{4}{3}-\frac{1}{3}x^2\right)\sqrt{1-x^2}\right) \quad = \quad \frac{x\,(x^2-2)}{\sqrt{1-x^2}} \tag{A.28}$$

$$\begin{aligned}
\frac{\partial}{\partial x}(S_1-L) &= 2x\sqrt{1-x^2}+\frac{\sqrt{1-x^2}-1}{x} \\
&= x\left[2\sqrt{1-x^2}-\frac{1}{\sqrt{1-x^2}+1}\right] \\
&= \frac{(1+2x^2)\sqrt{1-x^2}-1}{x} \qquad \text{(A.29)} \\
&= \frac{3\sqrt{1-x^2}-2\,(1-x^2)^{3/2}-1}{x} \qquad \text{(A.30)}
\end{aligned}$$

$$\frac{\partial}{\partial x}(S_2-L) \quad = \quad \frac{(1-x^2)^{3/2}-1}{x} \tag{A.31}$$

A.3 Special functions

A.3.1 Gamma function

The Gamma function is defined [17]

$$\Gamma(x) = \int_0^\infty e^{-t}\, t^{x-1}\, dt \tag{A.32}$$

and can be evaluated, for complex argument $z = a + ib$ when $a > 0.75$, using

$$\begin{aligned}
\Gamma(z) &= \int_0^\infty e^{-t+(z-1)\cdot\ln t}\, dt && \text{(A.33)}\\
&= \int_0^{\pi/2} e^{-\tan\xi+(z-1)\cdot\ln\tan\xi}\,(\tan^2\xi+1)\, d\xi && \text{(A.34)}\\
&= \int_0^{\pi/2} [\cos(b\cdot\ln\tan\xi) + i\sin(b\cdot\ln\tan\xi)]\cdot\\
&\qquad \cdot e^{-\tan\xi+(a-1)\cdot\ln\tan\xi}\,(\tan^2\xi+1)\, d\xi && \text{(A.35)}
\end{aligned}$$

A.3.2 Bessel functions

The Bessel function $J_n(z)$, solution of the differential equation

$$z^2\frac{d^2w}{dz^2} + z\frac{dw}{dz} + (z^2 - n^2)w = 0 \tag{A.36}$$

is

$$J_n(z) = \frac{i^{-n}}{\pi}\int_0^\pi e^{iz\cos\phi}\cos(n\phi)\, d\phi = \left(\frac{z}{2}\right)^2 \sum_{k=0}^\infty \frac{(-z^2/4)^k}{k!\,\Gamma(n+k+1)} \tag{A.37}$$

The modified Bessel function K_n can be evaluated

$$\begin{aligned}
K_n(z) &= \int_0^\infty e^{-z\cosh(t)}\cosh(n\cdot t)\,dt && \text{(A.38)}\\
&= \frac{1}{2}\int_0^\infty e^{-z\cosh(t)+n\cdot t}+e^{-z\cosh(t)-n\cdot t}\,dt && \text{(A.39)}\\
&= \frac{1}{2}\int_0^{\pi/2}\left[e^{-z\cdot ct(\xi)+n\cdot\tan\xi}+e^{-z\cdot ct(\xi)-n\cdot\tan\xi}\right]\left(\tan^2\xi+1\right)\,d\xi && \text{(A.40)}
\end{aligned}$$

using the variable $\tan\xi = t$ and the abbreviation $ct(\xi) = \cosh(\tan\xi)$, or, taking $\tan^2\xi = t$ and $ct^2(\xi) = \cosh(\tan^2\xi)$,

$$K_n(z) = \int_0^{\pi/2}\left[e^{-z\cdot ct^2(\xi)+n\cdot\tan^2\xi}+e^{-z\cdot ct^2(\xi)-n\cdot\tan^2\xi}\right]2\tan\xi(\tan^2\xi+1)\,d\xi \qquad \text{(A.41)}$$

For small z, $K_1(z)$ can be expanded into (valid to better than 10^{-8} for $z < 0.1$)

$$zK_1(z) = 1+\frac{2\ln z-\kappa}{4}\cdot z^2+\frac{4\ln z-2\kappa-3}{64}\cdot z^4+\dots \qquad \text{(A.42)}$$

with $\kappa = 1+2\ln 2-2\gamma \approx 1.231863$, which is much faster to evaluate than Eq. A.41.

A.4 Coulomb amplitudes in eikonal approximation

The Coulomb form factor for a pointlike charge is

$$\begin{aligned}
\mathscr{M}_C &= \frac{-Z\alpha}{2\pi i}\int e^{-i\vec{q}\cdot\vec{r}}\,\vec{g}\cdot\vec{\nabla}\,V_C(r)\,f(b)\,d^3r \qquad &(A.43)\\
&= \frac{-Z\alpha}{2\pi i}\int e^{-i\vec{q}\cdot\vec{r}}\,\frac{\vec{g}\cdot\vec{r}}{r^3}\,f(b)\,d^3r &(A.44)\\
&= \frac{-Z\alpha}{2\pi i}\int_{-\infty}^{\infty} dz\int_{0}^{2\pi} d\phi\int_{0}^{\infty} b\,db\;e^{-i(\vec{q}_\perp\cdot\vec{b}+q_\parallel z)}\,\frac{\vec{g}\cdot\vec{b}}{(z^2+b^2)^{3/2}}\,f(b) &(A.45)\\
&= \vec{q}_\perp\cdot\vec{g}\,\frac{2Z\alpha}{q_\perp}\int_{0}^{\infty} q_\parallel b\;K_1(q_\parallel b)\,J_1(q_\perp b)\,f(b)\,db &(A.46)
\end{aligned}$$

using the integrals

$$\begin{aligned}
\int_{-\infty}^{\infty} dz\,\frac{\cos(q_\parallel z)}{(z^2+b^2)^{3/2}} &= \int_{-\infty}^{\infty}\frac{dz'}{q_\parallel}\,\frac{\cos(z')}{((z'/q_\parallel)^2+b^2)^{3/2}} \qquad &(A.47)\\
&= q_\parallel^2\int_{-\infty}^{\infty} dz'\,\frac{\cos(z')}{(z'^2+(q_\parallel b)^2)^{3/2}} &(A.48)\\
&= q_\parallel^2\,\frac{2}{q_\parallel b}\,K_1(q_\parallel b) &(A.49)
\end{aligned}$$

and, introducing the angle $\alpha = \angle(q_\perp, g)$,

$$\begin{aligned}
\int_{0}^{2\pi} d\phi\;e^{-i\vec{q}_\perp\cdot\vec{b}}\;\vec{g}\cdot\vec{b} &= \int_{0}^{2\pi} d\phi\;e^{-iq_\perp b\cos\phi}\;g\,b\cos(\phi-\alpha) \qquad &(A.50)\\
&= 2\int_{0}^{\pi} d\phi\;e^{-iq_\perp b\cos\phi}\;g\,b\cos(\phi)\cos(\alpha) &(A.51)\\
&= -2\pi i\;J_1(q_\perp b)\,b\,\frac{\vec{q}_\perp\cdot\vec{g}}{q_\perp} &(A.52)
\end{aligned}$$

Along the same reasoning, the Coulomb form factor for a uniform charge distribution is

$$
\begin{aligned}
\mathscr{M}_C^u \;=\;& \frac{-Z\alpha}{2\pi i}\int\limits_{-\infty}^{\infty} dz \int\limits_{0}^{2\pi} d\phi \,\cdot \\
& \cdot \left[\int\limits_{0}^{b_u(z)} b\,db\;\vec{g}\cdot\vec{\nabla}\left(\frac{3}{2r_u}-\frac{r^2}{2r_u^3}\right)+\int\limits_{b_u(z)}^{\infty} b\,db\;\vec{g}\cdot\vec{\nabla}\left(-\frac{1}{r}\right)\right] e^{-i\vec{q}\cdot\vec{r}}\,f^u(b)
\end{aligned}
$$

$$
\begin{aligned}
=\;& \frac{-Z\alpha}{2\pi i}\int\limits_{-\infty}^{\infty} dz \int\limits_{0}^{2\pi} d\phi \,\cdot \\
& \cdot \left[\int\limits_{0}^{b_u(z)} b\,db\;\frac{\vec{g}\cdot\vec{b}}{r_u^3}+\int\limits_{b_u(z)}^{\infty} b\,db\;\frac{\vec{g}\cdot\vec{b}}{(z^2+b^2)^{3/2}}\right] e^{-i(\vec{q}_\perp\cdot\vec{b}+q_\parallel z)}\,f^u(b) \qquad \text{(A.53)}
\end{aligned}
$$

$$
\begin{aligned}
=\;& \vec{q}_\perp\cdot\vec{g}\;\frac{2Z\alpha}{q_\perp}\int\limits_{r_u}^{\infty} q_\parallel b\;K_1(q_\parallel b)\,J_1(q_\perp b)\,f^u(b)\,db \;-\; \frac{Z\alpha}{2\pi i}\int\limits_{0}^{r_u} b\,db\int\limits_{0}^{2\pi} d\phi\,\cdot \\
& \cdot 2\cdot\left[\int\limits_{0}^{z_u(b)} dz\;\frac{\vec{g}\cdot\vec{b}}{r_u^3}+\int\limits_{z_u(b)}^{\infty} dz\;\frac{\vec{g}\cdot\vec{b}}{(z^2+b^2)^{3/2}}\right]\cos(q_\parallel z)\,e^{-i\vec{q}_\perp\cdot\vec{b}}\,f^u(b) \qquad \text{(A.54)}
\end{aligned}
$$

$$
\begin{aligned}
=\;& \vec{q}_\perp\cdot\vec{g}\;\frac{2Z\alpha}{q_\perp}\left\{\int\limits_{r_u}^{\infty} q_\parallel b\;K_1(q_\parallel b)\,J_1(q_\perp b)\,f^u(b)\,db \;+\;\int\limits_{0}^{r_u} b^2\,db\;\cdot\right. \\
& \left.\cdot\left[\int\limits_{0}^{z_u(b)} dz\;\frac{\cos(q_\parallel z)}{r_u^3}+\int\limits_{z_u(b)}^{\infty} dz\;\frac{\cos(q_\parallel z)}{(z^2+b^2)^{3/2}}\right] J_1(q_\perp b)\,f^u(b)\right\} \qquad \text{(A.55)}
\end{aligned}
$$

$$= \vec{q}_\perp \cdot \vec{g}\, \frac{2Z\alpha}{q_\perp} \left\{ \int_0^\infty q_\| b\ K_1(q_\| b)\, J_1(q_\perp b)\, f^u(b)\, db \right.$$

$$\left. + \int_0^{r_u} b^2\, db \int_0^{z_u(b)} dz \left[\frac{\cos(q_\| z)}{r_u^3} - \frac{\cos(q_\| z)}{(z^2+b^2)^{3/2}} \right] J_1(q_\perp b)\, f^u(b) \right\} \tag{A.56}$$

where

$$b_u(z) = \begin{cases} \sqrt{r_u^2 - z^2} & \text{for } z < r_u \\ 0 & \text{for } z > r_u \end{cases}, \qquad z_u(b) = \begin{cases} \sqrt{r_u^2 - b^2} & \text{for } b < r_u \\ 0 & \text{for } b > r_u \end{cases}$$

The difference to the pointlike case emerges as the expression

$$\mathscr{M}_C^u - \mathscr{M}_C = \vec{q}_\perp \cdot \vec{g}\, \frac{2Z\alpha}{q_\perp} \int_0^{r_u} db\ J_1(q_\perp b) \left[q_\| b\ K_1(q_\| b)\ [f^u(b) - f(b)] \right.$$

$$\left. + \int_0^{z_u(b)} dz \left(\frac{b^2 \cdot \cos(q_\| z)}{r_u^3} - \frac{b^2 \cdot \cos(q_\| z)}{(z^2+b^2)^{3/2}} \right) f^u(b) \right] \tag{A.57}$$

where the limit of integration of the first term has been constrained to the region where is integrand is different from zero.

In the limiting case $q_\| \to 0$, the term $q_\| b\ K_1(q_\| b) \to 1$, the z integral can be carried out analytically using the formula A.9,

$$\begin{aligned} \int_0^{\sqrt{r_u^2 - b^2}} dz \left(\frac{b^2}{r_u^3} - \frac{b^2}{(z^2+b^2)^{3/2}} \right) &= \left(\frac{b^2}{r_u^2} - 1 \right) \sqrt{1 - b^2/r_u^2} \\ &= -(1 - b^2/r_u^2)^{3/2} \\ &= -\left[1 + b\, \partial_b\, \chi_C(b)/(2Z\alpha) \right] \end{aligned} \tag{A.58}$$

where the replacement in the last line has been made according to Eq. 2.88. Then expression A.57 simplifies, with inserting $f(b) = e^{i\eta \ln(2a/b)}$ and $f^u(b) = e^{i\chi_C(b)}$,

$$\begin{aligned} \mathcal{M}_C^u - \mathcal{M}_C &= \vec{q}_\perp \cdot \vec{g} \int_0^{r_u} db\, \frac{J_1(q_\perp b)}{q_\perp} \left(-2Z\alpha\, f(b) - \left[b\, \partial_b\, \chi_C(b)\right] f^u(b)\right) \\ &= \vec{q}_\perp \cdot \vec{g}\; i \int_0^{r_u} db\, \frac{J_1(q_\perp b)}{q_\perp}\, b\, \partial_b \left[f^u(b) - f(b)\right] \end{aligned} \tag{A.59}$$

in agreement with the findings in [27], there Eq. (31).

A.5 Numerical implementation of the radiative correction for pion Compton scattering

Nur noch kurz die Welt retten.

[Tim Bendzko, 2011]

This treatment extends the calculations in [45]. The nomenclature is kept, and further abbreviations are introduced,

$$\mathrm{Li}_{2m}(x) = \frac{1}{x-1}\left[\frac{\pi^2}{6} - \mathrm{Li}_2(x)\right] \tag{A.60}$$

$$\mathrm{Li}_{2t}(t) = \frac{t-2}{\sqrt{t^2-4t}}\left[\mathrm{Li}_2(w) - \mathrm{Li}_2(1-w) + \frac{1}{2}\ln^2 w - \frac{1}{2}\ln^2(1-w)\right] \tag{A.61}$$

$$\text{where} \qquad w = \frac{1}{2} - \frac{1}{2}\sqrt{\frac{-t}{4-t}} \qquad \text{with} \quad t < 0$$

$$\mathrm{Li}_{2h}(t) \;=\; \frac{t-2}{\sqrt{t^2-4t}}\,[\,\mathrm{Li}_2(h_-)-\mathrm{Li}_2(h_+)\,] \tag{A.62}$$

$$\text{where} \qquad h_\pm = \frac{t\pm\sqrt{t^2-4t}}{2}$$

$$L(t) \;=\; \frac{1}{\sqrt{-t}}\ln\frac{\sqrt{4-t}+\sqrt{-t}}{2} \tag{A.63}$$

$$L_4(t) \;=\; \sqrt{4-t}\;L(t) \tag{A.64}$$

$$L_t(t) \;=\; \frac{t-2}{\sqrt{t^2-4t}}\cdot 4\sqrt{-t}\;L(t) \tag{A.65}$$

The dilogarithmic function $\mathrm{Li}_2(x)$ is, along with two relations used in the following (reproduced from [29], App. B.1)

$$\mathrm{Li}_2(x) \;=\; -\int_0^x \frac{\ln|1-\xi|}{\xi}d\xi \tag{A.66}$$

$$\mathrm{Li}_2(x) \;=\; -\mathrm{Li}_2(1-x)-\ln|x|\ln|1-x|+\frac{\pi^2}{6} \tag{A.67}$$

$$\mathrm{Li}_2(x) \;=\; -\mathrm{Li}_2\left(\frac{1}{x}\right)-\frac{1}{2}\ln^2\left(-\frac{1}{x}\right)-\frac{\pi^2}{6} \tag{A.68}$$

Special care has to be taken when the argument of $\ln^2(\cdot)$ is negative,

$$\mathrm{Re}\,[\ln^2(-a)] = \ln^2(a)-\pi^2 \tag{A.69}$$

Also, for $\mathrm{Li}_2(x)$ in its general (analytic) definition, the logarithm in the integrand is entering without taking the modulus of its argument, and accordingly an imaginary part appears for $x > 1$. However in the present circumstances, only the real part of this function enters, and thus taking the definition as A.66 is sufficient.

When calculating the virtual-photon loops for scalar Compton scattering, the following integrals appear.

First, integrals with polynomials of order 3 or 4 in the denominator are discussed. The indices j and k are meant to complete, together with i, the set $\{0,1,2\}$. Due to the symmetry of the expressions under $j \longleftrightarrow k$ the ordering choice for j and k is arbitrary.

$$\int\frac{(a_{-1}x^{-1}+a_0+a_1x)\,dx}{(x-r_0)(x-r_1)(x-r_2)} \;=\; -\frac{a_{-1}\ln x}{r_0r_1r_2}+\sum_{i=0}^{2}\frac{(a_{-1}{r_i}^{-1}+a_0+a_1r_i)\ln(x-r_i)}{(r_i-r_j)(r_i-r_k)} \tag{A.70}$$

$$\int \frac{(c_0+c_1x)\ln(x)\,dx}{(x-r_0)(x-r_1)(x-r_2)} = \sum_{i=0}^{2}\frac{(c_0+c_1r_i)\,[\mathrm{Li}_2(x/r_i)+\ln(x)\ln(1-x/r_i)]}{(r_i-r_j)(r_i-r_k)} \tag{A.71}$$

For the required definite integrals $\int_1^\infty \cdots$ the relations

$$\sum_{i=0}^{2}\frac{1}{(r_i-r_j)(r_i-r_k)} = \sum_{i=0}^{2}\frac{r_i}{(r_i-r_j)(r_i-r_k)} = 0 \tag{A.72}$$

$$\sum_{i=0}^{2}\frac{1}{r_i(r_i-r_j)(r_i-r_k)} = \frac{1}{r_0r_1r_2} \tag{A.73}$$

$$\lim_{x\to\infty}[\mathrm{Li}_2(x/r_i)+\ln x\ln(1-x/r_i)] = \frac{1}{2}\ln^2\left(\frac{1}{x}\right)-\frac{1}{2}\ln^2\left(-\frac{1}{r_i}\right)-\frac{\pi^2}{6} \tag{A.74}$$

are used to obtain

$$\begin{aligned} I_{A1}(a_{-1},a_0,a_1,r_0,r_1,r_2) &= \int_1^\infty \frac{(a_{-1}x^{-1}+a_0+a_1x)dx}{(x-r_0)(x-r_1)(x-r_2)} \\ &= -\sum_{i=0}^{2}\frac{a_{-1}r_i{}^{-1}+a_0+a_1r_i}{(r_i-r_j)(r_i-r_k)}\ln(1-r_i) \end{aligned} \tag{A.75}$$

used on pp.104 and 108

$$\begin{aligned} I_{A2}(c_0,c_1,r_0,r_1,r_2) &= \int_1^\infty \frac{(c_0+c_1x)\ln(x)dx}{(x-r_0)(x-r_1)(x-r_2)} \\ &= -\sum_{i=0}^{2}\frac{(c_0+c_1r_i)}{(r_i-r_j)(r_i-r_k)}\left[\mathrm{Li}_2\left(\frac{1}{r_i}\right)+\frac{1}{2}\ln^2\left(-\frac{1}{r_i}\right)\right] \\ &= \sum_{i=0}^{2}\frac{(c_0+c_1r_i)}{(r_i-r_j)(r_i-r_k)}\,\mathrm{Li}_2(r_i) \end{aligned} \tag{A.76}$$

used on p.104

Later, the special case of Eqs. A.75 and A.76 with $r_2 = {r_1}^{-1}$ is needed, and for this, the handy notation with skipping the last argument is introduced

$$\begin{aligned} I_{A1}(a_{-1}, a_0, a_1, r_0, r_1) &= I_{A1}(a_{-1}, a_0, a_1, r_0, r_1, {r_1}^{-1}) \\ I_{A2}(c_0, c_1, r_0, r_1) &= I_{A2}(c_0, c_1, r_0, r_1, {r_1}^{-1}) \end{aligned} \tag{A.77}$$

Next, integrals with polynomials of order five in the denominator are given. For $n = 0, 1, 2, 3$

$$\begin{aligned} \int \frac{x^n\,dx}{(x-r)(x-r_1)^2(x-r_2)^2} &= \frac{r^n \ln(x-r)}{(r-r_1)^2(r-r_2)^2} + \sum_{j=1}^{2} \left(\frac{r_j^n}{(r_j-r)(r_j-r_k)^2(r_j-x)} \right. \\ &\qquad \left. + \frac{P_{njk} \cdot \ln(x-r_j)}{(r-r_j)^2(r_j-r_k)^3} \right) \end{aligned} \tag{A.78}$$

and

$$\begin{aligned} \int \frac{x^n \ln(x)\,dx}{(x-r)(x-r_1)^2(x-r_2)^2} &= \frac{r^n\,[\mathrm{Li}_2(x/r) + \ln(x)\ln(1-x/r)]}{(r-r_1)^2(r-r_2)^2} \\ &\quad + \sum_{j=1}^{2} \left(\frac{r_j^{n-1}((r_j-x)\ln(x-r_j) + x\ln(x))}{(r_j-r)(r_j-r_k)^2(r_j-x)} \right. \\ &\qquad \left. + \frac{P_{njk} \cdot \left[\mathrm{Li}_2(x/r_j) + \ln(x)\ln(1-x/r_j)\right]}{(r-r_j)^2(r_j-r_k)^3} \right) \end{aligned} \tag{A.79}$$

where j and k now form the set $\{1, 2\}$ (their order does matter here), and the polynomials P_{njk} are defined as

$$\begin{aligned} P_{0jk} &= 2r - 3r_j + r_k \\ P_{1jk} &= r(r_j + r_k) - 2r_j^2 \\ P_{2jk} &= r_j(2rr_k - r_j^2 - r_jr_k) \\ P_{3jk} &= r_j^2(3rr_k - rr_j - 2r_jr_k) \end{aligned}$$

The respective definite integrals are

$$\begin{aligned}
I_{B1}(b_0,b_1,b_2,r,r_1,r_2) &= \int\limits_1^\infty \frac{(b_0+b_1x+b_2x^2)\,dx}{(x-r)(x-r_1)^2(x-r_2)^2} \\
&= -\frac{(b_0+b_1r+b_2r^2)}{(r-r_1)^2(r-r_2)^2}\ln(1-r) - \sum_{j=1}^{2}\left(\frac{b_0+b_1r_j+b_2r_j^2}{(r_j-r)(r_j-r_k)^2(r_j-1)}\right. \\
&\qquad \left. - \frac{(b_0P_{0jk}+b_1P_{1jk}+b_2P_{2jk})}{(r-r_j)^2(r_j-r_k)^3}\ln(1-r_j)\right) \qquad \text{(A.80)}
\end{aligned}$$

$$\begin{aligned}
I_{B2}(d_0,d_1,d_2,r,r_1,r_2) &= \int\limits_1^\infty \frac{(d_0+d_1x+d_2x^2)\ln(x)\,dx}{(x-r)(x-r_1)^2(x-r_2)^2} \\
&= \frac{(d_0+d_1r+d_2r^2)}{(r-r_1)^2(r-r_2)^2}\mathrm{Li}_2(r) \\
&\quad + \sum_{j=1}^{2}\left(\frac{(d_0r_j{}^{-1}+d_1+d_2r_j)(1-r_j)\ln(1-r_j)}{(r_j-r)(r_j-r_k)^2(r_j-1)}\right. \\
&\qquad \left. + \frac{(d_0P_{0jk}+d_1P_{1jk}+d_2P_{2jk})}{(r-r_j)^2(r_j-r_k)^3}\mathrm{Li}_2(r_j)\right) \qquad \text{(A.81)}
\end{aligned}$$

Analogously to A.77 short-hand notations are introduced,

$$\begin{aligned}
I_{B1}(b_0,b_1,b_2,r,r_1) &= I_{B1}(b_0,b_1,b_2,r,r_1,r_1{}^{-1}) \qquad \text{(A.82)} \\
I_{B2}(d_0,d_1,d_2,r,r_1) &= I_{B2}(d_0,d_1,d_2,r,r_1,r_1{}^{-1})
\end{aligned}$$

In [45], the Feynman graphs are grouped in 11 classes I–XI, and the calculation is presented separately for these classes. The terms proportional to $\mathrm{Lf}_i(s,u)$ are added up and give

$$\begin{aligned}
A_{\mathrm{Lf}} &= \frac{\alpha}{2\pi}\cdot\left(-\mathrm{Lf}_1(\hat{u})-\mathrm{Lf}_1(\hat{s})+\mathrm{Lf}_0(\hat{u})+\mathrm{Lf}_0(\hat{s})-\frac{3}{2}\right) \qquad \text{(A.83)} \\
B_{\mathrm{Lf}} &= \frac{\alpha}{2\pi}\cdot\left(\mathrm{Lf}_1(\hat{u})+\mathrm{Lf}_1(\hat{s})-\mathrm{Lf}_0(\hat{u})-\mathrm{Lf}_0(\hat{s})+2+\frac{\hat{t}}{\hat{u}-1}\left(-2\mathrm{Lf}_0(\hat{u})+2\right)\right)
\end{aligned}$$

The dilogarithmic and logarithmic loop contributions are combined, and read

$$\begin{aligned}
A_L &= \frac{\alpha}{2\pi}\Bigg[\underbrace{\mathrm{Li}_{2m}(\hat{s})}_{\mathrm{VII}}\underbrace{+\mathrm{Li}_{2m}(\hat{u})}_{\mathrm{VIII}}\underbrace{+L_4(\hat{t})+\mathrm{Li}_{2t}(\hat{t})}_{\mathrm{IX}} \\
&\qquad \underbrace{-\tfrac{1}{2}L_4(\hat{t})-L^2(\hat{t})-\mathrm{Li}_{2m}(\hat{s})}_{\mathrm{X}}\underbrace{-\tfrac{1}{2}L_4(\hat{t})-L^2(\hat{t})-\mathrm{Li}_{2m}(\hat{u})}_{\mathrm{XI}}\Bigg] \\
&= \frac{\alpha}{2\pi}\left[\mathrm{Li}_{2t}(\hat{t})-2L^2(\hat{t})\right] \qquad \text{(A.84)}
\end{aligned}$$

$$\begin{aligned}
B_L &= -A_L+\frac{\alpha}{2\pi}\Bigg[\underbrace{-L^2(\hat{t})}_{\mathrm{X}}\underbrace{-L^2(\hat{t})}_{\mathrm{XI}}\Bigg] \\
&\quad +\frac{\alpha}{2\pi}\frac{\hat{t}}{\hat{u}-1}\Bigg[\underbrace{-\mathrm{Li}_{2m}(\hat{u})}_{\mathrm{VIII}}\underbrace{+\mathrm{Li}_{2m}(\hat{u})}_{\mathrm{XI}}\underbrace{-\mathrm{Li}_{2t}(\hat{t})-L_t(\hat{t})\ln(1-\hat{u})-\mathrm{Li}_{2h}(\hat{t})}_{\mathrm{XI}}\Bigg] \\
&= \frac{\alpha}{2\pi}\left[\frac{\hat{s}-1}{\hat{u}-1}\mathrm{Li}_{2t}(\hat{t}) - \frac{\hat{t}}{\hat{u}-1}\big(L_t(\hat{t})\ln(1-\hat{u}) + \mathrm{Li}_{2h}(\hat{t})\big)\right] \qquad \text{(A.85)}
\end{aligned}$$

Collecting the terms up to here, one finds the expressions

$$A_{nI}(\hat{s},\hat{u}) = \frac{\alpha}{2\pi}\left[-\frac{3}{2} + \frac{\hat{u}-1}{\hat{u}}\ln(1-\hat{u}) + \frac{\hat{s}-1}{\hat{s}}\ln(1-\hat{s}) + \mathrm{Li}_{2t}(\hat{t})-2L^2(\hat{t})\right] \qquad \text{(A.86)}$$

and

$$\begin{aligned}
B_{nI}(\hat{s},\hat{u}) &= \frac{\alpha}{2\pi}\Bigg[2 - \frac{\hat{u}-1}{\hat{u}}\ln(1-\hat{u}) - \frac{\hat{s}-1}{\hat{s}}\ln(1-\hat{s}) + \frac{\hat{s}-1}{\hat{u}-1}\mathrm{Li}_{2t}(\hat{t}) \\
&\qquad + \frac{\hat{t}}{\hat{u}-1}\big(2 - 2\ln(1-\hat{u}) - L_t(\hat{t})\ln(1-\hat{u}) - \mathrm{Li}_{2h}(\hat{t})\big)\Bigg] \qquad \text{(A.87)} \\
&= \frac{\alpha}{2\pi}\Bigg[\frac{\hat{s}-1}{\hat{u}-1}\big(\mathrm{Li}_{2t}(\hat{t})-2\big) - \frac{\hat{u}-1}{\hat{u}}\ln(1-\hat{u}) - \frac{\hat{s}-1}{\hat{s}}\ln(1-\hat{s}) \\
&\qquad - \frac{\hat{t}}{\hat{u}-1}\big(\left[2+L_t(\hat{t})\right]\ln(1-\hat{u}) + \mathrm{Li}_{2h}(\hat{t})\big)\Bigg] \qquad \text{(A.88)}
\end{aligned}$$

There remain four integral expressions in class X and XI as given in [45], for which it was proposed to solve them numerically. A new analytic treatment has been developed along the present work. First, the integral

$$A_I(m,\hat{t}) \;=\; \int\limits_1^\infty \frac{dx}{(x-m)}\frac{2-\hat{t}}{((x-1)^2+\hat{t}x)}\left[(x+1)\ln x \;+\; 2(1-x)\sqrt{4-\hat{t}}\,L(t)\right] \qquad \text{(A.89)}$$

is considered, rewriting it with the replacement $\hat{t} \rightarrow \xi$

$$\begin{aligned} -\hat{t} \;&=\; \frac{(\xi-1)^2}{\xi}, \qquad \xi \;=\; 1+\frac{-\hat{t}+\sqrt{-\hat{t}}\sqrt{4-\hat{t}}}{2} \\ &\qquad\qquad\qquad\;\;\; =\; 1-h_- \;=\; \frac{1}{1+h_+} \\ &\qquad\qquad\qquad\;\;\; >\; 1 \end{aligned} \qquad \text{(A.90)}$$

for which the relations

$$\begin{aligned} 2\sqrt{\xi} \;&=\; \sqrt{4-\hat{t}}+\sqrt{-\hat{t}} \\ (\xi+1)/\sqrt{\xi} \;&=\; \sqrt{4-\hat{t}} \\ (\xi^2+1)/\xi \;&=\; 2-\hat{t} \\ \frac{\sqrt{\xi}}{2(\xi-1)}\ln\xi \;&=\; L(\hat{t}) \\ h_\pm \;&=\; \pm(\xi^{\mp 1}-1) \end{aligned}$$

hold. This turns A.89 into

$$A_I(m,\xi) \;=\; -\frac{\xi^2+1}{\xi(\xi-1)}\int\limits_1^\infty \frac{dx}{x-m}\cdot\frac{(x-1)(\xi+1)\ln\xi \;-\; (\xi-1)(x+1)\ln x}{(x-\xi)(x-\xi^{-1})} \qquad \text{(A.91)}$$

This shows explicitely that at $x=\xi$ the numerator and the denominator of the integrand vanish at the same time, and only at $x=m$ occurs a pole that necessitates the determination of the principal value when integrating numerically. It is, however, preferable to solve the integral analytically, by using Eqs. A.75 and A.76 with

$$\begin{aligned} r_0 \;&=\; m \\ r_1 \;&=\; \xi \\ r_2 \;&=\; \xi^{-1} \end{aligned} \qquad \text{(A.92)}$$

The common factor

$$f_A = -\frac{\xi^2+1}{\xi(\xi-1)} \tag{A.93}$$

is used in specifying

$$a_0^A = -a_1^A = -f_A\,(\xi+1)\ln\xi \qquad c_0^A = c_1^A = -f_A\,(\xi-1) \tag{A.94}$$

in terms of which the solution of integral A.91 is written, employing A.77,

$$\begin{aligned} A_I(m,\xi) &= I_{A1}(0,\, a_0,\, a_1,\, m,\xi) + I_{A2}(c_0,\, ,c_1,\, m,\xi) \\ &= f_A \cdot \sum_{i=0}^{2} \frac{[(\xi+1)\ln\xi]\,(1-r_i)\ln(1-r_i) - (\xi-1)(1+r_i)\mathrm{Li}_2(r_i)}{(r_i-r_j)(r_i-r_k)} \end{aligned} \tag{A.95}$$

used on p.52

Next, the integral

$$\begin{aligned} B_I(m,\hat{t}) &= \int_1^\infty \frac{dx}{(x-m)} \frac{2-\hat{t}}{((x-1)^2+\hat{t}x)^2} \Bigg[\hat{t}x(x+1)\ln x \,+\, ((x-1)^2+\hat{t}x)(x-1) \\ &\qquad + \frac{2(x-1)}{\sqrt{4-\hat{t}}} \left[\hat{t}^2 x - 6\hat{t}x - 2(x-1)^2\right] L(t) \Bigg] \end{aligned} \tag{A.96}$$

is considered, starting with the rearrangement

$$\begin{aligned} B_I(m,\hat{t}) &= \int_1^\infty \frac{dx}{(x-m)} \frac{(2-\hat{t})(x-1)}{((x-1)^2+\hat{t}x)} \left[1 - \frac{4}{\sqrt{4-\hat{t}}} L(t) \right] \\ &\quad + \int_1^\infty \frac{dx}{(x-m)} \frac{(2-\hat{t})\,\hat{t}x}{((x-1)^2+\hat{t}x)^2} \left[(x+1)\ln x \,-\, 2(x-1)\sqrt{4-\hat{t}}\, L(t) \right] \end{aligned} \tag{A.97}$$

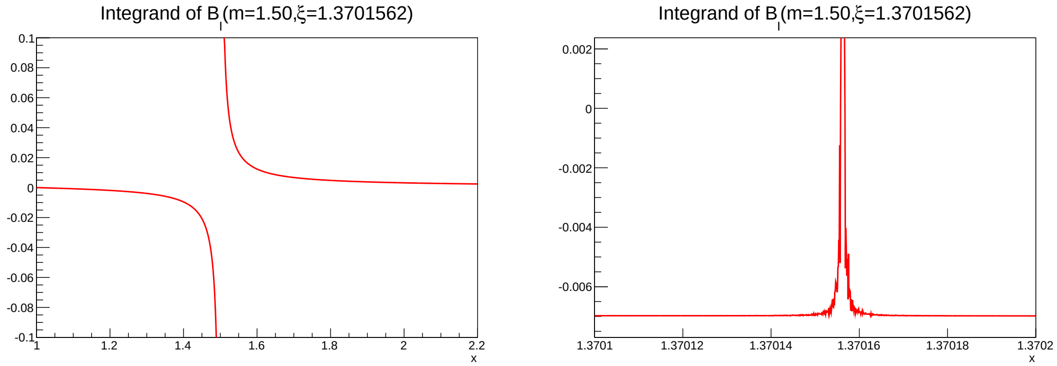

Figure A.1: The integrand of B_I as given in Eq. A.96 for the case $m = 1.5$, $t = -0.1$. The integrand exhibits a pole at $x = m$, whose contribution is finite when the principal value is considered. While the region around $x = \xi \approx 1.37016$ is a smooth function of x (left plot), numercial imprecision leads to unpredictable results near this point, where numerator and denominator vanish commonly (right plot).

for which the substitution A.90 turns it into

$$
\begin{aligned}
B_I(m,\xi) \quad = \quad & -\frac{\xi^2+1}{\xi(\xi^2-1)}\int_1^\infty \frac{dx}{(x-m)}\cdot\frac{(1-x)\,(\xi^2-1-2\xi\ln\xi)}{(x-\xi)(x-\xi^{-1})} \\
& -\frac{(\xi^2+1)(\xi-1)}{\xi^2}\int_1^\infty \frac{dx}{(x-m)}\cdot\frac{x\,((\xi-1)(x+1)\ln x-(x-1)(\xi+1)\ln\xi)}{(x-\xi)^2\,(x-\xi^{-1})^2}
\end{aligned}
\tag{A.98}
$$

The finiteness of the integrand at $x = \xi$ is now less transparent then in the case of Eq. A.91, and requires the recombination of the two contributions. Possible ways to treat this region of integration are:

- Define a region around $x = \xi$ in which the limiting behavior of the integrand is worked out analytically, and use the respective series expansion instead of the original expression A.96.
- Replace in a region around $x = \xi$ the integrand by its value in the vincinity, where the numerical unstability is still small. This is a practical method for finding the value in a specific case, when the introduced error can be estimated by eye, but

for the general case the systematics of the involved approximation has to be determined.

- Solve the integral analytically. This avoids the mentioned numerical problems and is much faster in computation, and thus the way pursued here.

Isolating a common factor

$$f_B = -\frac{\xi^2+1}{\xi^2} = f_A \cdot \frac{\xi-1}{\xi} \tag{A.99}$$

the ξ-dependent parameters in A.98 are written

$$\begin{aligned} a_0 &= -a_1 = f_B\,\xi\,(1-2\xi\,(\xi^2-1)^{-1}\ln\xi) \\ b_1 &= -b_2 = f_B\,(\xi^2-1)\ln\xi \\ d_1 &= d_2 = f_B(\xi-1)^2 \end{aligned} \tag{A.100}$$

and the integral A.98 is solved, using the notation of Eqs. A.77 and A.82, by

$$\begin{aligned} B_I(m,\,\xi) = {} & I_{A1}(0,\,a_0,\,a_1,\,m,\,\xi) \\ & + I_{B1}(0,\,b_1,\,b_2,\,m,\,\xi) + I_{B2}(0,\,d_1,\,d_2,\,m,\,\xi) \end{aligned} \tag{A.101}$$

The last integral appears in B_{XI} and is rearranged in the following way

$$\begin{aligned} B_{I'}(m,\hat{t}) = {} & \int\limits_1^\infty \frac{dx}{(x-m)}\frac{2-\hat{t}}{((x-1)^2+\hat{t}x)^2}\Bigg[\hat{t}(x+1)(2-\hat{t}-x)\ln x \\ & \qquad + ((x-1)^2+\hat{t}x)\left(x-1+\hat{t}+\frac{\hat{t}}{x}\right) \\ & + \frac{2L(t)}{\sqrt{4-\hat{t}}}\left[\hat{t}^3(x+1)+\hat{t}^2(3x^2-3x-4)+2\hat{t}(x^3-4x^2+2x+1)-2(x-1)^3\right]\Bigg] \\ = {} & B_I(m,\hat{t}) + \int\limits_1^\infty \frac{dx}{(x-m)}\frac{2-\hat{t}}{((x-1)^2+\hat{t}x)^2}\Bigg[\hat{t}(x+1)(2-\hat{t}-2x)\ln x \\ & \qquad + ((x-1)^2+\hat{t}x)\left(\hat{t}+\frac{\hat{t}}{x}\right) \\ & + \frac{2L(t)}{\sqrt{4-\hat{t}}}\left[\hat{t}^3(x+1)+\hat{t}^2(2x^2-2x-4)+2\hat{t}(x^3-x^2-x+1)\right]\Bigg] \end{aligned} \tag{A.102}$$

$$\begin{aligned} B_{I'}(m,\hat{t}) &= B_I(m,\hat{t}) + \int_1^\infty \frac{dx}{(x-m)} \frac{(2-\hat{t})\hat{t}}{((x-1)^2+\hat{t}x)} \left[\frac{1}{x} + 1 + \frac{4L(t)}{\sqrt{4-\hat{t}}} + x\frac{4L(t)}{\sqrt{4-\hat{t}}}\right] \\ &\quad + \int_1^\infty \frac{dx}{(x-m)} \frac{(2-\hat{t})\hat{t}(x+1)}{((x-1)^2+\hat{t}x)^2} \left[(2-\hat{t}-2x)\ln x \; - \; 2\hat{t}\sqrt{4-\hat{t}}\,L(t)\right] \end{aligned} \tag{A.103}$$

and after the replacement $\hat{t} \to \xi$ according to A.90

$$\begin{aligned} B_{I'}(m,\xi) &= B_I(m,\xi) \\ &\quad - \frac{(\xi^2+1)}{\xi^2}\frac{(\xi-1)}{(\xi+1)} \int_1^\infty \frac{x^{-1}(\xi^2-1) + (\xi^2-1+2\xi\ln\xi) + x(2\xi\ln\xi)}{(x-m)(x-\xi)(x-\xi^{-1})}\,dx \\ &\quad - \frac{(\xi^2+1)(\xi-1)^2}{\xi^3} \int_1^\infty \frac{((\xi^2+1) + x(\xi-1)^2 - x^2\,2\xi)\ln x + (x+1)(\xi^2-1)\ln\xi}{(x-m)(x-\xi)^2(x-\xi^{-1})^2}\,dx \end{aligned} \tag{A.104}$$

The common factor is abbreviated

$$f'_B = -\frac{(\xi^2+1)(\xi-1)}{\xi^3(\xi+1)} = f_B\,\frac{\xi-1}{\xi(\xi+1)} \tag{A.105}$$

in the ξ-dependent parameters

$$\begin{aligned} a'_{-1} &= f'_B\,\xi\,(\xi^2-1) \\ a'_0 &= f'_B\,\xi\,(\xi^2-1+2\xi\ln\xi) \\ a'_1 &= f'_B\,\xi\,2\xi\ln\xi \\ b'_0 = b'_1 &= f'_B\,(\xi^2-1)(\xi^2-1)\ln\xi \\ d'_0 &= f'_B\,(\xi^2-1)(\xi^2+1) \\ d'_1 &= f'_B\,(\xi^2-1)(\xi-1)^2 \\ d'_2 &= f'_B\,(\xi^2-1)(-2\xi) \end{aligned}$$

and the integral $B_{I'}$ is found to be, in terms of I_{A1} (A.77), I_{B1} and I_{B1} (A.82),

$$\begin{aligned} B_{I'}(m,\,\xi) &= B_I(m,\,\xi) + I_{A1}(a'_{-1},\,a'_0,\,a'_1,\,m,\,\xi) \\ &\quad + I_{B1}(b'_0,\,b'_1,\,b'_2,\,m,\,\xi) + I_{B2}(d'_0,\,d'_1,\,d'_2,\,m,\,\xi) \end{aligned} \tag{A.106}$$

or, combining with the expression A.101 for B_I,

$$\begin{aligned} B_{I'}(m,\xi) &= I_{A1}(a'_{-1},\, a'_0+a_0,\, a'_1+a_1,\, m,\, \xi) \\ &\quad + I_{B1}(b'_0,\, b'_1+b_1,\, b'_2+b_2,\, m,\, \xi) \\ &\quad + I_{B2}(d'_0,\, d'_1+d_1,\, d'_2+d_2,\, m,\, \xi) \end{aligned} \tag{A.107}$$

Finally, the integrals are combined in the way they appear in the radiative correction expression,

$$\begin{aligned} B_I^s(m,\xi) &= B_I(m,\xi)-A_I(m,\xi) \\ &= \quad I_{A1}(a^s_{-1},\, a^s_0,\, a^s_1,\, m,\, \xi) \\ &\quad + I_{A2}(c^s_0,\, c^s_1,\, m,\, \xi) \\ &\quad + I_{B1}(b^s_0,\, b^s_1,\, b^s_2,\, m,\, \xi) \\ &\quad + I_{B2}(d^s_0,\, d^s_1,\, d^s_2,\, m,\, \xi) \end{aligned} \tag{A.108}$$

$$\begin{aligned} B_I^u(m,\xi) &= B_{I'}(m,\xi)-A_I(m,\xi) \\ &= \quad I_{A1}(a^u_{-1},\, a^u_0,\, a^u_1,\, m,\, \xi) \\ &\quad + I_{A2}(c^u_0,\, c^u_1,\, m,\, \xi) \\ &\quad + I_{B1}(b^u_0,\, b^u_1,\, b^u_2,\, m,\, \xi) \\ &\quad + I_{B2}(d^u_0,\, d^u_1,\, d^u_2,\, m,\, \xi) \end{aligned} \tag{A.109}$$

with 22 ξ-dependent parameters

	$m=\hat{s}$	$m=\hat{u}$
a^m_{-1}	0	a'_{-1}
a^m_0	$a_0 - a_0^A = \quad a_0^B$	$a'_0 + a_0 - a_0^A = a'_{-1} + a'_1 + a_0^B$
a^m_1	$a_1 - a_1^A = -a_0^B$	$a'_1 + a_1 - a_1^A = \quad a'_1 - a_0^B$
b^m_0	0	b'_0
b^m_1	b_1	$b'_1 + b_1 = b'_0 + b_1$
b^m_2	$b_2 = -b_1$	$b_2 = -b_1$
c^m_0	$-c_0^A$	$-c_0^A$
c^m_1	$-c_1^A = -c_0^A$	$-c_1^A = -c_0^A$
d^m_0	0	d'_0
d^m_1	d_1	$d'_1 + d_1 = d'_0 + d'_2 + d_1$
d^m_2	$d_2 = d_1$	$d'_2 + d_2 = \quad d'_2 + d_1$

(A.110)

They feature 9 different terms, which are all needed for the case $m = \hat{u}$, and a subset of 4 appears for $m = \hat{s}$. The newly introduced combination a_0^B is, making use of A.99,

$$\begin{aligned} a_0^B &= f_B\,\xi\left(1-\frac{2\xi}{\xi^2-1}\ln\xi\right) - f_B\,\frac{\xi}{\xi-1}(\xi+1)\ln\xi \\ &= f_B\,\xi\left(1-\frac{2\xi+(\xi+1)^2}{\xi^2-1}\ln\xi\right) \end{aligned} \tag{A.111}$$

and the others

$$b_1 = f_B(\xi^2-1)\ln\xi \tag{A.112}$$

$$c_0^A = f_A(\xi-1) = f_B\,\xi \tag{A.113}$$

$$d_1 = f_B(\xi-1)^2 \tag{A.114}$$

This is the form how the radiative corrections are implemented at the time of writing up this document. A promising further step for simplification is clearly, to group the contribtions according to

$$\begin{aligned} B_I^m(m,\xi) &= \beta_0\,\ln(1-m) + \beta_{L0}\,\mathrm{Li}_2(m) \\ &\quad + \beta_1\,\ln(1-\xi) + \beta_{L1}\,\mathrm{Li}_2(\xi) \\ &\quad + \beta_2\,\ln(1-\xi^{-1}) + \beta_{L2}\,\mathrm{Li}_2(\xi^{-1}) \end{aligned}$$

and make use of the relations between logarithmics and dilogarithmic functions. Indicating the terms appearing only for $m = \hat{u}$ in square backets $[+\cdots]_{m=\hat{u}}$,

$$\begin{aligned} \beta_0 &= \underbrace{\frac{-a_0^B(1-m)}{(m-\xi)(m-\xi^{-1})}}_{I_{A1}} + \underbrace{\frac{b_1\,m(1-m)}{(m-\xi)^2(m-\xi^{-1})^2}}_{I_{B1}} \\ &\quad \left[+\underbrace{\frac{(-a'_{-1}\,m^{-1}-a'_1)(1+m)}{(m-\xi)(m-\xi^{-1})}}_{I_{A1}} + \underbrace{\frac{-b'_0(1+m)}{(m-\xi)^2(m-\xi^{-1})^2}}_{I_{B1}}\right]_{m=\hat{u}} \\ &= \frac{(1-m)\,(-a_0^B\kappa+b_1 m)\,\left[+(1+m)\left((-a'_{-1}\,m^{-1}-a'_1)\kappa-b'_0\right)\right]_{m=\hat{u}}}{(m-\xi)^2(m-\xi^{-1})^2} \end{aligned} \tag{A.115}$$

$$\beta_{L0} = \underbrace{\frac{-c_0^A(1+m)}{(m-\xi)(m-\xi^{-1})}}_{I_{A2}} + \underbrace{\frac{d_1\, m(1+m)}{(m-\xi)^2(m-\xi^{-1})^2}}_{I_{B2}} \left[+\underbrace{\frac{(d'_0+d'_2\, m)(1+m)}{(m-\xi)^2(m-\xi^{-1})^2}}_{I_{B2}}\right]_{m=\hat{u}}$$

$$= (1+m)\frac{-c_0^A\kappa + d_1 m\ \left[+d'_0+d'_2\, m\right]_{m=\hat{u}}}{(m-\xi)^2(m-\xi^{-1})^2} \tag{A.116}$$

$$\beta_1 = \underbrace{\frac{-a_0^B(1-\xi)}{(\xi-m)(\xi-\xi^{-1})}}_{I_{A1}} + \underbrace{\frac{b_1\, m(1-m)}{(m-\xi)^2(m-\xi^{-1})^2}}_{I_{B1}} \tag{A.117}$$

$$\left[+\underbrace{\frac{(-a'_{-1}\, m^{-1}-a'_1)(1+m)}{(m-\xi)(m-\xi^{-1})}}_{I_{A1}} + \underbrace{\frac{-b'_0(1+m)}{(m-\xi)^2(m-\xi^{-1})^2}}_{I_{B1}}\right]_{m=\hat{u}}$$

$$= \kappa^{-2}\left((1-m)\,(-a_0^B\kappa+b_1 m)\ \left[+(1+m)\left(\frac{-a'_{-1}-a'_1\, m}{m}\kappa-b'_0\right)\right]_{m=\hat{u}}\right)$$

with $\kappa=(m-\xi)(m-\xi^{-1})$ and $F_B=f_b/\kappa^2$

$$B_I^m(m,\xi) = \ln(1-m)\left[\underbrace{\frac{-a_0^B(1-m)}{(m-\xi)(m-\xi^{-1})}}_{I_{A1}} + \underbrace{\frac{b_1\, m(1-m)}{(m-\xi)^2(m-\xi^{-1})^2}}_{I_{B1}}\right. \tag{A.118}$$

$$\left.\overset{m=\hat{u}}{+}\left(\underbrace{\frac{(-a'_{-1}\, m^{-1}-a'_1)(1+m)}{(m-\xi)(m-\xi^{-1})}}_{I_{A1}} + \underbrace{\frac{-b'_0(1+m)}{(m-\xi)^2(m-\xi^{-1})^2}}_{I_{B1}}\right)\right]$$

$$+\operatorname{Li}_2(m)\left[\underbrace{\frac{-c_0^A(1+m)}{(m-\xi)(m-\xi^{-1})}}_{I_{A2}} + \underbrace{\frac{d_1\, m(1+m)}{(m-\xi)^2(m-\xi^{-1})^2}}_{I_{B2}}\right]$$

$$+\ldots \tag{A.119}$$

Appendix B

Further Kinematic Aspects

B.1 Higher-order terms in the pion mass

The minimum momentum transfer $q_{\min}$ for constant E_γ (appearing in longitudinal kinematics $\vec{p} \parallel \vec{p}_\pi \parallel \vec{p}_\gamma$) is given by

$$q_{\min} = \frac{m_\pi^2}{2E} \cdot \frac{E_\gamma}{E_\pi} \left(1 + \frac{m_\pi^2 (E^2 + E E_\pi + E_\pi^2)}{4 E^2 E_\pi^2} + \mathcal{O}\left(\mu_\pi^4\right) \right) \tag{B.1}$$

$$= \frac{m_\pi^2}{2p} \cdot \frac{p - p_\pi}{p_\pi} \left(1 - \frac{m_\pi^2 (p^2 + p p_\pi + p_\pi^2)}{4 p^2 p_\pi^2} + \mathcal{O}\left(\mu_\pi^4\right) \right) \tag{B.2}$$

Higher-order terms are classified in powers of

$$\begin{aligned} \mu &= m_\pi/E, \quad m_\pi/p \\ \mu_\pi &= m_\pi/E_\pi, \quad m_\pi/p_\pi \\ \mu_\gamma &= m_\pi/E_\gamma \end{aligned} \tag{B.3}$$

where the high-relativistic case $\mu_{\pi,\gamma} \approx 0$ is assumed for all particles, and the same symbol μ is used, independent whether E or p in the denominator applies.

The Mandelstam variables in the pion-photon subprocess are related to the quantities measured in the laboratory system by

$$s = m_\pi^2 + \frac{p_\gamma}{p_\pi} m_\pi^2 + 4 E_\gamma p_\pi \sin^2 \frac{\theta_{\pi\gamma}}{2} \tag{B.4}$$

$$t = -q_{\min}^2 - 2 E_\gamma \cdot q_{\min} - 4 p p_\pi \sin^2 \frac{\theta_\pi}{2} \tag{B.5}$$

$$u = m_\pi^2 - \frac{p_\gamma}{p} m_\pi^2 - 4 p p_\gamma \sin^2 \frac{\theta_\gamma}{2} \tag{B.6}$$

$$\begin{aligned} s &= m_\pi^2 + 2E_\gamma \left(E_\pi - p_\pi + 2p_\pi \sin^2 \frac{\theta_{\pi\gamma}}{2} \right) && \text{(B.7)} \\ &= m_\pi^2 + E_\gamma p_\pi \left(\frac{m_\pi^2}{p_\pi^2} + 4 \sin^2 \frac{\theta_{\pi\gamma}}{2} \right) + \mathcal{O}\left(\mu_\pi^4\right) && \text{(B.8)} \end{aligned}$$

$$t = -m_\pi^2 \frac{E_\gamma^2}{E E_\pi} - 4 E E_\pi \sin^2 \frac{\theta_\pi}{2} \left(1 - \frac{m_\pi^2}{E_\pi^2} - \frac{m_\pi^2}{E^2} + \mathcal{O}\left(\mu_\pi^4\right) \right) \tag{B.9}$$

$$q^2 = q_{\min}^2 + 4p \left(p_\gamma \sin^2 \frac{\theta_\gamma}{2} + p_\pi \sin^2 \frac{\theta_\pi}{2} \right) - 4 p_\pi p_\gamma \sin^2 \frac{\theta_{\pi\gamma}}{2} \tag{B.10}$$

B.2 Maximum scattering angles

A first idea on the range of the scattering angles is obtained by the following kinematic consideration: For a maximum momentum transfer $q_{\max}$ to the nucleus, the angles of the outgoing particles are restricted. The relation derived from the geometrical construction of Fig. B.1 reads

$$\begin{aligned} 1 + \cos(\pi - [\theta_{\pi\gamma}]_{\max}) &= 1 + \frac{q_\gamma^2 + q_\pi^2 - q_{\max}^2}{2 q_\gamma q_\pi} && \text{(B.11)} \\ &= \frac{q_{\max}(2p - q_{\max}) - q_{\min}(2p - q_{\min})}{2 p_\pi p_\gamma} && \text{(B.12)} \end{aligned}$$

The quantities q_π and q_γ can be understood from Fig. B.1. From Eq. B.12 the handy expression $\max[\theta_{\pi\gamma}^2] \approx (2p/p_\pi p_\gamma) q_{\max}$ follows. The angles of the scattered particles with respect to the incoming pion beam directions are restricted by

$$\begin{aligned} \sin^2 \frac{[\theta_\pi]_{\max}}{2} &= \frac{q_{\max}(2p_\gamma + q_{\max}) - q_{\min}(2p_\gamma + q_{\min})}{4 p p_\pi} && \text{(B.13)} \\ \sin^2 \frac{[\theta_\gamma]_{\max}}{2} &= \frac{q_{\max}(2p_\pi + q_{\max}) - q_{\min}(2p_\pi + q_{\min})}{4 p p_\gamma} && \text{(B.14)} \end{aligned}$$

with approximations $\max[\theta_\pi^2] \approx (2p_\gamma/p p_\pi) q_{\max}$ and $\max[\theta_\gamma^2] \approx (2p_\pi/p p_\gamma) q_{\max}$ such that $\max[\theta_{\pi\gamma}] \approx \max[\theta_\pi] + \max[\theta_\gamma]$.

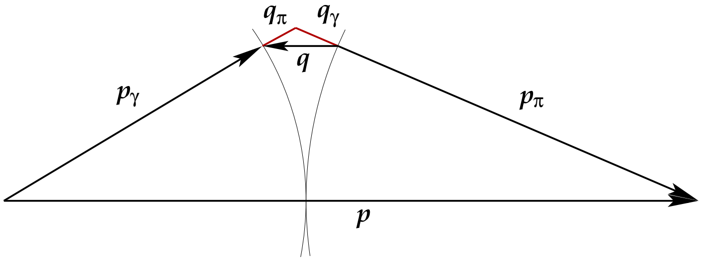

Figure B.1: Kinematics in the case of maximum angle $\theta_{\pi\gamma}$. q_π and q_γ extend the vectors of the scattered particle's momenta to the intercepting point. As throughout this work, the energy transfer to the nucleus is neglected, and consequently, for fixed modulus p and p_γ, the modulus of p_π is also fixed, from $E_\pi = E - E_\gamma$. Allowed kinematics for fixed p_γ and p_π are constructed with the vectors $\vec{p}_\gamma$ and $\vec{p}_\pi$ on spheres with respective radii. The spheres do not touch, but have the tiny minimal distance $q_{\min}(E_\gamma)$, cf. Eq. 2.5.

p_γ [GeV]	$\theta_{\gamma,\max}$ [mrad]		p_π [GeV]	$\theta_{\pi,\max}$ [mrad]	
		$q_\perp < 0.1$			$q_\perp < 0.1$
20	16.7	14.3	170	5.7	2.3
30	13.7	11.8	160	5.9	2.8
70	8.9	7.2	120	6.8	4.5
80	8.4	6.5	110	7.2	4.9
170	5.7	2.3	20	16.7	14.3

Table B.1: Constraints on the laboratory angles for different kinematics with fixed p_π and p_γ, valid for $s + q^2 < 55\, m_\pi^2$.

Along the same line, the consideration is refined by taking into account the constraint on the component $q_{||}$ of the momentum transfer given by the range in s via Eq. 2.30. Namely, for the investigations in the present work, $s < 49\, m_\pi^2$ is relevant, and so $q_{||} < q_{||}(s_{\max}) \approx 2.8\,\mathrm{MeV}$ (valid for the region $q^2 < 0.1\,\mathrm{GeV}^2/c^2$).

This leads to constraints on the scattering angles of the particles

$$\cos\theta_{\pi[\gamma],\max} > 1 - \frac{q_{||}(s_{\max})}{p_{\pi[\gamma]}} \qquad \text{or} \qquad \theta_{\pi[\gamma],\max} < \sqrt{\frac{2\, q_{||}(s_{\max})}{p_{\pi[\gamma]}}} \tag{B.15}$$

leading to maximum angles $\theta_{\gamma,\max}$ and $\theta_{\pi,\max}$ as given in Tab. B.2 When the range of q^2 is restricted, the allowed scattering angles are further reduced. This follows from consid-

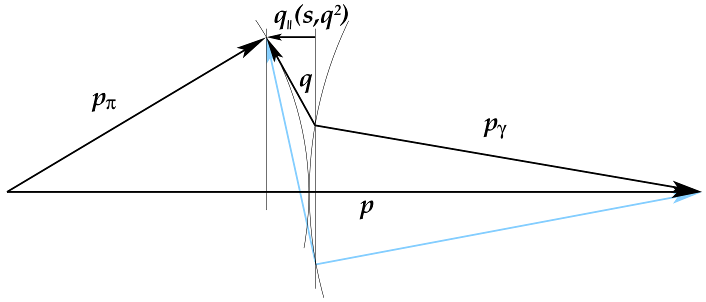

Figure B.2: Kinematics for constrained $q_{\|}(s,q^2)$.

ering the component

$$\begin{aligned} q_\perp &= p_{\pi\perp} - p_{\gamma\perp} \qquad \text{(B.16)} \\ &= \sqrt{p_\pi^2 - (p_\pi - q_{\|\pi})^2} - \sqrt{p_\gamma^2 - (p_\gamma - q_{\|\gamma})^2} \\ &\doteq \sqrt{2p_\pi q_{\|\pi}} - \sqrt{2p_\gamma(q'_{\|} - q_{\|\pi})} \qquad \text{(B.17)} \end{aligned}$$

with $q'_{\|} = q_{\|} - q_{\min}$. In turn, the parallel component is obtained from $q_\perp$ by

$$q_{\|\pi} = \frac{q'_{\|} \cdot p_\gamma p' - q_\perp^2 \cdot (p_\gamma - p_\pi)/2 + q_\perp \cdot \sqrt{p_\pi p_\gamma (2p' q'_{\|} - q_\perp^2)}}{p'^2} \qquad \text{(B.18)}$$

using the notation $p' = p_\pi + p_\gamma$.

B.3 Range of q^2

$s_{\min}(E_\gamma) =$ The kinematic limit for q^2 for constrained $s < s_{\max}$ at fixed E_γ is obtained by maximizing, analogously to (B.17),

$$\begin{aligned} \frac{\partial}{\partial q_{\|\pi}} q_\perp &\doteq \frac{\partial}{\partial q_{\|\pi}} \left[\sqrt{2p_\pi q_{\|\pi}} + \sqrt{2p_\gamma(q'_{\|} - q_{\|\pi})} \right] \overset{!}{\doteq} 0 \qquad \text{(B.19)} \\ q_{\|\pi}(q_{\perp\max}) &= \frac{p_\pi}{p_\pi + p_\gamma} q'_{\|} \qquad \text{(B.20)} \\ \longrightarrow \qquad q_{\perp\max} &= \sqrt{2p\, q'_{\|}} = \sqrt{s - m_\pi^2 + q^2 - 2p\, q_{\min}} \qquad \text{(B.21)} \end{aligned}$$

B.4 The transformation $p_\gamma(s, t, q^2, \Psi)$

Some intermediate steps in the derivation of Eq. 2.37 are displayed starting from

$$p_\gamma^2(q_\parallel'^2 + 2\epsilon' q_c^2) \;+\; p_\gamma(q_\parallel' t' - 2\mu' q_c^2) \;+\; (t'/2)^2 + \mu^2 q_c^2 \;=\; 0 \tag{B.22}$$

where

$$\begin{array}{rcl}
q_c &=& q_\perp \cos\Psi \qquad\qquad\qquad q_\parallel' \;=\; q_\parallel(1+\epsilon) - q_{\min} - \epsilon\, p \\
t' &=& t + q^2 + q_{\min}(2p - q_{\min}) - 2\mu\, q_\parallel \\
\epsilon &=& (E-p)/p \qquad\qquad\qquad\; \epsilon' \;=\; \epsilon(1+\epsilon/2) \\
\mu &=& (m_\pi^2 - u)/2p \qquad\qquad\quad \mu' \;=\; \mu(1+\epsilon)
\end{array} \tag{B.23}$$

This equation does not render p_γ directly (as solution of a quadratic equation), since the expressions $q_\parallel'$ and t' contain an implicit (non-linear) p_γ dependence through $q_{\min}$, c.f. Eq. 2.5. However, $q_{\min}$ is small compared to the other terms, and for a first approximation can be neglected, $q_{\min} = 0$. Using the result, Eq. B.22 is iterated to the desired precision.

The solution of Eq. B.22 (as quadratic equation), with the terms worked out such that the dependence on q_c is displayed, reads

$$p_\gamma \;=\; \frac{\frac{1}{2} q_\parallel' t' - \mu' q_c^2 + q_c \sqrt{q_c^2 \mu^2 - \left(t' + \frac{1}{2}\epsilon t' + q_\parallel' \mu\right)\left(\frac{1}{2}\epsilon t' + q_\parallel' \mu\right)}}{q_\parallel'^2 + 2\epsilon' q_c^2} \tag{B.24}$$

where only the positive sign of the square root term solves the problem.

Some intermediate steps in the derivation of the back-transformation $p_\gamma(s, t, q^2, \Psi)$ are given here:

$$\begin{array}{rcll}
2 q_\perp p_{\gamma\perp} \cos\Psi &=& q^2 - q_\parallel^2 + p_\gamma^2 - p_{\gamma\parallel}^2 - p_\pi^2 + p_{\pi\parallel}^2 & \\
&=& q^2 - q_{\min}^2 + 2(p - q_\parallel)(p_\gamma - p_{\gamma\parallel}) - 2(p - p_\gamma)(q_\parallel - q_{\min}) & \text{(B.25)} \\
&=& -q_{\min}^2 + 2(p - q_\parallel)(\mu - \epsilon p_\gamma) - 2\delta_{\min} p + 2 p_\gamma (q_\parallel - q_{\min}) & \text{(B.26)} \\
&=& 2 p_\gamma (q_\parallel - q_{\min} - \epsilon(p - q_\parallel)) + 2\mu(p - q_\parallel) - 2\delta_{\min} p - q_{\min}^2 & \text{(B.27)} \\
&=& 2 p_\gamma\, q_\parallel' + t' & \text{(B.28)}
\end{array}$$

where

$$
\begin{aligned}
q_{\parallel} &= \frac{s-m_\pi^2+q^2}{2p} && \text{(B.29)}\\
\delta_{\min} &= \frac{s-m_\pi^2}{2p} - q_{\min} && \text{(B.30)}\\
p_\gamma - p_{\gamma\parallel} &= \frac{m_\pi^2-u}{2p} - \frac{E-p}{p}\, p_\gamma \;=\; \mu - \epsilon\, p_\gamma && \text{(B.31)}\\
p_{\gamma\parallel} &= \frac{u-m_\pi^2}{2p} + \frac{E}{p} p_\gamma \;=\; -\mu + (1+\epsilon)\, p_\gamma && \text{(B.32)}\\
t' &= 2\mu(p-q_{\parallel}) - 2\delta_{\min} p - q_{\min}^2 && \text{(B.33)}\\
&= t + q^2 + q_{\min}(2p-q_{\min}) - 2\mu\, q_{\parallel} && \text{(B.34)}\\
p_{\gamma\perp}^2 &= (\mu-\epsilon\, p_\gamma)((2+\epsilon)p_\gamma - \mu) && \text{(B.35)}\\
&= -\epsilon(2+\epsilon)\, p_\gamma^2 + (2+2\epsilon)\mu\, p_\gamma - \mu^2 && \text{(B.36)}\\
&= -2\epsilon'\, p_\gamma^2 + 2\mu'\, p_\gamma - \mu^2 && \text{(B.37)}
\end{aligned}
$$

So with $q_c = q_\perp \cos\Psi$ follows $(p_\gamma q_{\parallel}' + u')^2 = p_{\gamma\perp}^2 q_c^2$ and

$$
p_\gamma^2(q_{\parallel}'^2 + 2\epsilon' q_c^2) + p_\gamma(2q_{\parallel}' u' - 2\mu' q_c^2) + u'^2 + \mu^2 q_c^2 \;=\; 0 \qquad \text{(B.38)}
$$

B.5 Energy transfer to the nucleus

splitting up $E_r = E_q + E_{excit}$ into the kinetic and nuclear excitation energy. where for small momentum transfer $\vec{q} = \vec{p}_\pi + \vec{p}_\gamma - \vec{p}$

$$
E_q = \frac{q^2}{2M_Z} \approx 0 \qquad \text{(B.39)}
$$

is assumed (meaning that also no excitation of the nucleus occurs), such that q can be used in the following for the modulus of the 4- and 3-momentum equivalently.

B.6 Solving for $x(s,t,y,\psi)$

Short-hand notations are introduced,

$$
\begin{array}{rcl}
\left.\begin{array}{rcl} x & = & \cos\theta_\gamma \\ x_\pi & = & \cos\theta_\pi \end{array}\right\} & > 0 \text{ and } \lesssim 1 & \text{(forward kinematics)} \\
y & = & \cos\theta_q \; < \; 0 \\
z & = & \cos\theta_{\gamma q} \; = \; xy + \sqrt{(1-x^2)(1-y^2)}\cos\Psi \\
z_\pi & = & \cos\theta_{\pi\gamma} \; = \; x x_\pi + \sqrt{(1-x^2)(1-x_\pi^2)}\cos\Psi_\pi
\end{array}
\tag{B.40}
$$

Measured angular quantities are x, x_π and z_π. The expression for z_π determines $\Psi_\pi \in [0,\pi]$. Examining the longitudinal and transverse components of the momenta (s. Fig. 2.1)

$$
\begin{array}{rcl}
q_\parallel & = & -qy \; = \; p - x_\pi p_\pi - x p_\gamma \\
q_\perp & = & \sqrt{q^2 - q_\parallel^2} \\
p_{\pi\perp} & = & p_\pi \sqrt{1-x_\pi^2} \\
p_{\gamma\perp} & = & p_\gamma \sqrt{1-x^2} \\
p_{\pi\perp}^2 & = & p_{\gamma\perp}^2 + q_\perp^2 - 2 p_{\gamma\perp} q_\perp \cos\Psi
\end{array}
\tag{B.41}
$$

allows to solve for y, $q_\perp$ and Ψ, such that the last variable z can be calculated using Eq. B.40.

The Mandelstam variables in terms of the kinematical variables Eq. B.40 read

$$
s \;=\; m_\pi^2 - 2pqy - q^2 \tag{B.42}
$$

Find $x(s,t,y,\psi)$ given that

$$
t = -q^2 \frac{E - px + 2pyz}{E - px - qz} = -q^2 \left[1 + \frac{(q+2py)z}{E - px - qz} \right] \tag{B.43}
$$

$$
E - px - qz = -q^2 \frac{(q+2py)z}{t+q^2} \tag{B.44}
$$

$$
px - E = \left[q^2 \frac{(q+2py)}{t+q^2} - q \right] z \tag{B.45}
$$

where $z(x,y,\Psi)$ is defined in Eq. B.40. Introducing

$$a = \frac{q^2(q+2py)}{t+q^2} - q, \qquad c = a\cos\Psi\sqrt{1-y^2}$$

$$b = p - ay$$

from eq. (B.45) follows

$$xb - E = c\sqrt{1-x^2}$$

or, for $\xi = \sqrt{1-x^2}$,

$$b\sqrt{1-\xi^2} - E = c\xi$$

$$(c^2+b^2)\xi^2 + 2cE\xi + E^2 - b^2 = 0$$

$$\xi_\pm = \frac{-cE \pm b\sqrt{b^2+c^2-E^2}}{b^2+c^2}$$

where only ξ_+ solves eq. (B.43).

B.7 Region of constrained Ψ range

The angle Ψ has a limited range for extreme values of t near $t_{\min}$, formally connected to the square root term in Eq. 2.33, from which $q_\tau^2 > E_\tau^2 - p_\tau^2$ or

$$q_\tau^2 \;>\; (t+q^2)\left[m_\pi^2(q^2+m_\pi^2)+(s+t+q^2-2m_\pi^2)(s+q^2)\right] - q_\parallel^2(m_\pi^2-u)^2 \tag{B.46}$$

follows, meaning a constraint on the Ψ range if $q_\perp \neq 0$ and if t is below t_Ψ given by, neglecting the tiny term proportional to $q_\parallel^2$,

$$\begin{aligned} t \;<\; t_\Psi &= -s + 2m_\pi^2 - q^2 - \frac{m_\pi^2(q^2+m_\pi^2)}{s+q^2} \qquad \text{(B.47)} \\ &< -\frac{(s-m_\pi^2)^2}{s} \end{aligned}$$

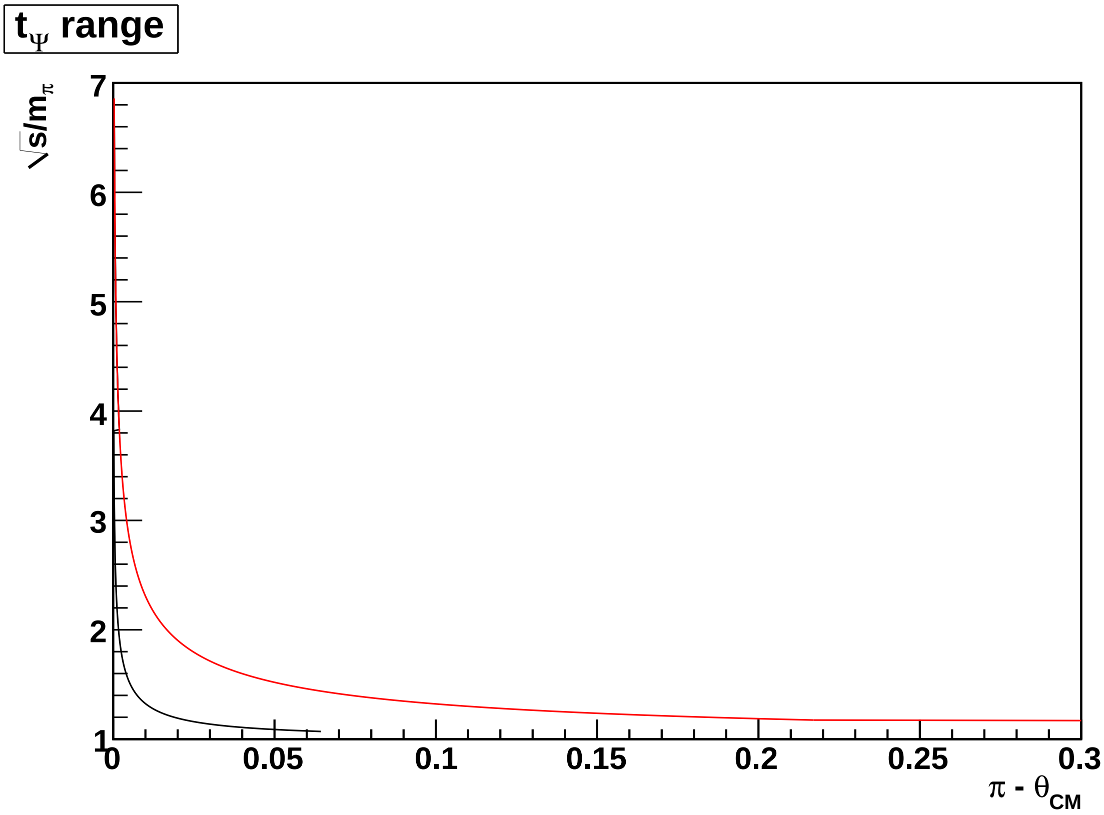

Figure B.3: Limit given by t_Ψ for $q = 0.005\ m_\pi$ (black line) and $q = 0.05\ m_\pi$ (red line), in the extreme backward scattering regime.

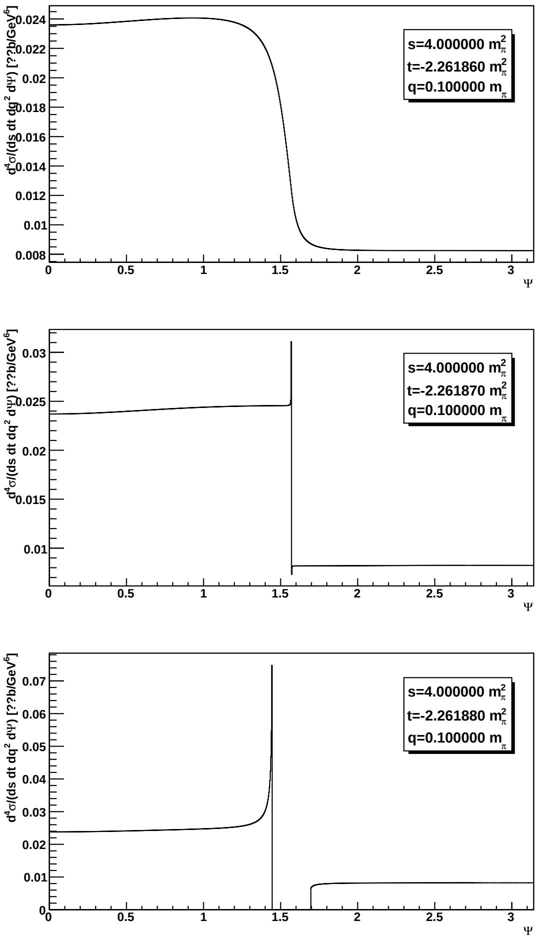

Figure B.4: Differential cross section

Appendix C

Reproduction of COMPASS Publications and Notes

Not reproduced in this edition: The COMPASS experiment at CERN
P. Abbon et al. [The COMPASS Collaboration] [1]
Sec. 5.1.2 “Silicon microstrip detectors”, resp. references
edited and drafted by J. M. Friedrich

p. 123*ff* The COMPASS setup for Physics with Hadron Beams
[The COMPASS Collaboration], *draft version as of 14. August 2012*
reproduced are: title pages, Sec. 5.1 “Silicon microstrip detectors”
edited and drafted by J. M. Friedrich

p. 129*ff* COMPASS note 2010-15,
J. M. Friedrich: CEDAR performanace 2009

p. 149*ff* COMPASS note 2012-2
J. M. Friedrich, M. Krämer: Reconstruction of the Pion Beam Energy from Beam Optics

p. 153*ff* COMPASS-II Proposal
COMPASS-II Proposal
F. Gautheron et al. [The COMPASS Collaboration]
Chap. 4 “Experimental studies of chiral perturbation theory”
edited and drafted by J. M. Friedrich

DRAFT version

The COMPASS Setup for Physics with Hadron Beams

Preprint submitted to Elsevier *August 21, 2012*

5 Tracking Detectors

The tracking system of COMPASS is composed of several tracking stations, each consisting of a set of planar tracking detectors of different sizes, granularities and resolutions. On the one hand, large areas of several square meters have to be covered in order to detect slow particles scattered at large angles and deflected by the magnets, while, on the other hand, the particle rates quickly increases with decreasing distance to the undeflected beam, requiring fast detectors with good resolution. The large-area tracking is provided by several variants of wire-based gas detectors such as Multiwire Proportional Chambers (MWPC), Drift Chambers, and Straw Tube Chambers. The region close to the beam, where the particle rates are too high for wire-based detectors, is covered by two types of Micropattern Gaseous Detectors (MPGD) with strip readout, the Micromegas and the GEM detectors. The beam region itself, where rates above $1 \cdot 10^5\,\mathrm{mm}^{-2}\mathrm{s}^{-1}$ are observed, is equipped with Scintillating Fibre Detectors and novel GEM detectors with pixel readout, the PixelGEMs. Tracking immediately upstream and downstream of the target is performed by Silicon Microstrip detectors. This section focuses on the upgrades of the tracking system for the hadron program with respect to the setup used for muon beams, detailed in [1]. The wire and strip detectors measure different projections of a particle penetration point, which are called X (horizontal) Y (vertical), and U and V for orthogonal projections rotated by a given angle with respect to X and Y.

5.1 Silicon Microstrip Detectors

For the hadron program, the COMPASS silicon microstrip tracking system consists of three stations upstream of the target which are used as a beam telescope, as well as a double station downstream of the target, used for vertex reconstruction. As these detectors are traversed by the beam and practically all the forward-boosted reaction products, they are prone to radiation damage. In order to minimise the various effects of this damage, like an increase of the depletion voltage or the increase of the leakage current, they are cooled with a liquid nitrogen cooling system. Since the leakage current decreases with temperature, noise caused by radiation damage is suppressed. In addition to reducing the effects of radiation damage, the cooling leads to a significant improvement of the spatial and time resolution compared to room-temperature operation, as discussed below.

One station consists of two silicon detectors with a stereo angle of 5° between their strip orientations in order to enhance the multi-track ambiguity resolution. The detectors consist of a 300 µm thick silicon sensor with an active area

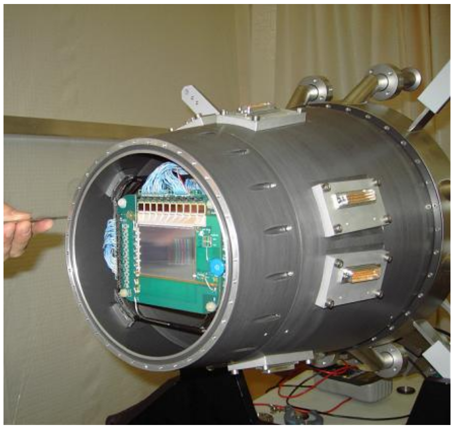

Figure 17. The conical cryostat with the upstream beam window dismounted.

of $5 \times 7\,\mathrm{cm}^2$. The readout is designed double-sided with 1280 readout strips on the n-side and 1024 strips on the p-side, perpendicular to the n-side strips. The sensors are glued onto two L-shaped FR4 printed circuit boards which hold the APV25-S1 [9] based readout electronics. There are three upstream cryostats for the beam stations and one special cryostat, shown in Fig. 17, matching the very constrained space downstream of the target (cf. Fig. 3), housing together the last two stations, *i.e.* four detectors.

A specific challenge in cooling the COMPASS silicon detectors with the attached front-end chips is that no massive parts are to be brought nearby, as the detectors are necessarily mounted in the acceptance of the spectrometer. This forbids traditional ways of connecting the detectors, e.g. to a massive coldhead to dissipate the heat created by the electronics. The technology developed for the COMPASS silicon detectors consists of evaporation of liquid nitrogen in thin capillaries on the PCBs. For allowing a heat removal of about 8 W at each detector in this light-weighted way, the nitrogen must be provided in pure liquid phase to the capillary. For this purpose, a dedicated phase separator is incorporated in each cryostat. The whole cooling infrastructure increases the effective radiation length of the PCB part by less than 10%.

The nitrogen arrives from the central COMPASS Dewar and is led by a 100 m long vacuum isolated flexible transfer line to a valve box nearby the stations. The valve box acts primarily as a buffer for the liquid nitrogen which is kept at 1.8 bar. By opening cryogenic valves the liquid nitrogen in is allowed to flow through 2–3 m long transfer lines to each station. Within the shielding vacuum, the nitrogen reaches the phase separator, on top of which gas evaporated in the transfer line is allowed to escape. At the bottom two capillaries are connected, one for each detector. The capillaries are connected by soldering dots to the L-boards. The temperature of the detector is regulated through the gaseous exhaust flow with a rapid feedback time in the order of one second.

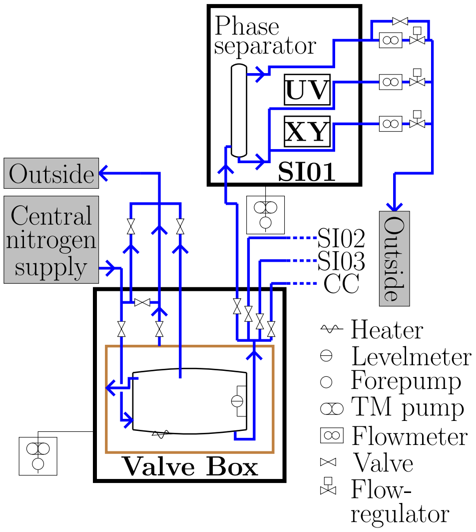

Figure 18. Functional schematics of the valve box.

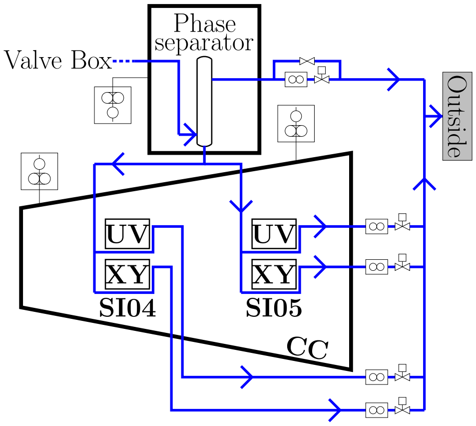

Figure 19. Functional schematics of the conical cryostat. Symbols as in Fig. 18.

All involved components are operated by a Programmable Logic Controller (PLC, SIMATIC S7 300), utilising a Proportional Integral Derivative (PID) algorithm for the temperature regulation. The programming is realised as Java$^{\text{TM}}$ based application developed at CEA-Saclay called Anibus$^{\text{TM}}$, featuring real-time monitoring, remote control, data storage and an alarm system.

For the first time in 2009, all silicon stations were cooled to 200 K. The stability of the system is shown in table 4. These values were obtained from all temperature data collected in 2009. The data were then filtered to include only time intervals where the corresponding station was in cold operation and no other anomalies were present. The second column shows the ratio between data used for the analysis and the complete data set where the station concerned was connected. The cooling system proved very stable cooling on the level of ± 1 K.

Table 4
Operation characteristics of the silicon detectors during the 2009 run

Station	Gaussian σ (K)	RMS$_X$(µm)	RMS$_Y$ (µm)	σ_t (ns)	HV (V)
SI01 A	0.60	9.4	7.2	0.97	75
SI01 B	0.18	8.1	7.4	1.02	95
SI02 A	0.57	—	6.8	[1.84]	130
SI02 B	0.51	7.4	6.8	1.26	135
SI03 A	0.30	8.4	7.1	1.15	60
SI03 B	0.13	7.7	6.9	1.03	85
SI04 A	1.66	6.7	7.8	1.18	110
SI04 B	1.81	6.8	7.3	1.25	115
SI05 A	> 2	5.8	6.6	1.32	120
SI05 B	> 2	5.0	6.7	1.30	105

To calculate the spatial residuals, data taken in standard muon run conditions was used, only using the silicon detectors. With these settings, the track error typically is less than 3 µm and can be easily deconvoluted to obtain the intrinsic detector resolution. The spatial resolution strongly depends on the cluster size, i. e. the number of adjacent strips which are combined to one cluster. One strip clusters offer only limited spatial information, because the cluster position is assigned to the strip centre, whereas for two strip clusters the cluster position can be refined using the strip amplitudes as weighting factor. In addition an empirical correction, compensating for nonlinear charge sharing effects, is applied for two strip clusters. The ratio of size two clusters mainly depends on the wafer design were for the p-side (i.e. Y-, V-planes) and on some detectors also for the n-side (i.e. X-,U-planes) intermediate strips improve the charge sharing. The average fraction of two strip clusters is 0.55 for the X-like detectors and 0.57 for the Y-like detectors. Therefore, the Y-like detectors show a better spatial resolution compared to the X-like detectors. The average intrinsic spatial resolution of the COMPASS silicon detectors is 5.3 µm (see Fig. 22) for the p-side and 6.9 µm for the n-side. The best observed spatial resolution is 3.7 µm. This is a significant improvement compared to the resolution observed in room-temperature operation (8 µm and 11 µm for p- and n-side, respectively). While the specific causes for this enhancement have not yet been fully disentangled, an important aspect is the associated cooling of the front-end chips.

The average efficiency for standard muon run conditions, where hits within a spatial window of $\pm 3\sigma$ around the extrapolated track position are accepted, is above 99%. Fig. 21 shows a typical two dimensional efficiency plot for one COMPASS silicon detector.

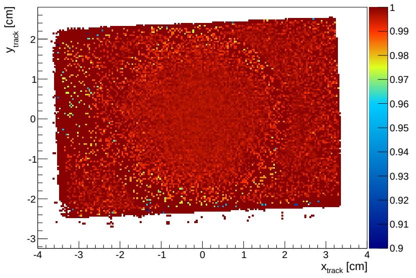

Figure 20. Two dimensional efficiency plot for a plane from the beam telescope.

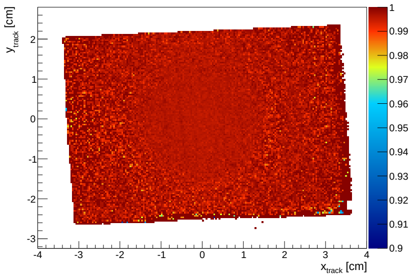

Figure 21. Two dimensional efficiency plot for a plane downstream of the target.

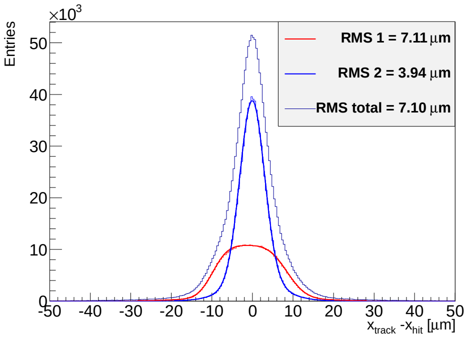

Figure 22. Residual distribution for one Silicon Y-plane. The blue and red histogram show the distribution for one and two strip clusters, respectively.

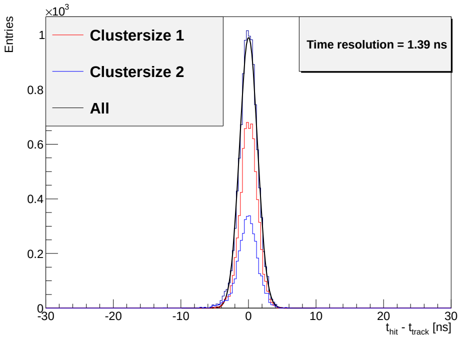

Figure 23. Temporal residuum of a single projection of a silicon detector.

The time resolution was shown to be better than 2.5 ns for each single plane with an average resolution of $\langle \sigma_t \rangle = 2.1$ ns. A typical signal time distribution for a single silicon plane is shown in Fig. 23.

CEDAR performance 2009

Jan Friedrich

Physik-Department, TU München

December 2010

Abstract

The performance of beam particle identification by the two CEDAR detectors in the COMPASS beam line during the 2009 Primakoff data taking is investigated. The work was started with the urge to conclude on the CEDAR performance for the envisaged future measurements, in view of state-of-the-art usage of the detector information, the multiplicity cut (identifying kaons when at least 6 photomultipliers of one CEDAR have a signal). This is known to have a bad overall efficiency of about 40%, bringing up the challenge which enhancements are in place for a high-statistics Primakoff data taking, which aims also at the first determination of the kaon polarisability.

The presented log-likelihood evaluation of the CEDAR information increases the efficiency to about 80%. The investigation also reveals the good hardware performance of the CEDARs, leaving potential for additional improvement only in a slight change of the beam aligment with respect to the CEDAR setup, apart from the obvious gain of information, that the installation of a third CEDAR could bring.

The presented log-likelihood method can be also used in order to filter pion samples. The kaon content can be reduced by more than a factor 20, at a pion efficiency larger than 90%.

1 Data set and definitions

The fraction of kaons in the COMPASS 190 GeV/c hadron beam is around 3.5% at the production target, and 2.5% at the target. By restricting the recorded events to a subsample by kinematic cuts on the spectrometer information, kaons may be enriched or sparsified. The sample used in the following contains events from the two reactions

$$\begin{aligned} K^- &\longrightarrow \pi^-\pi^0 && \text{free kaon decay} && (1)\\ \pi^-\ N &\longrightarrow N\ \pi^-\pi^0 && \text{diffractive / Primakoff } \pi^0 \text{ production} && (2)\end{aligned}$$

The produced $\pi^0 \to \gamma\gamma$ triggers the readout of such events, and a high statistics could be collected in the few days of data taking in November 2009. About 47% of the first test production with LED corrections for ECAL2 was used (T38). The reactions were selected by requiring

- the reconstructed π^0 mass and the energy sum of the outgoing particles in the ranges as shown on Fig. 1 and 2.
- the momentum transfer $q = p_\pi - p_{\pi'} - p_{\pi^0}$ to be restricted $0 > q^2 > -0.01$, cf. Fig. 1. The nucleus in reaction (2) is assumed to recoil elastically, carrying away only a negligible amount of energy.

Since the π^0 calibration for the ECAL2 cells was missing at the time of this analysis, the reconstructed π^0 mass is off the PDG value and broader than finally achieved. The obtained distribution

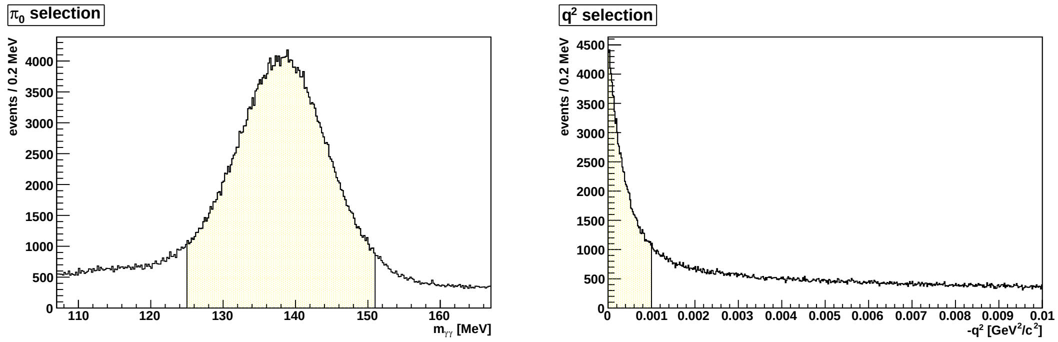

Figure 1: Left: The reconstructed π^0 mass and the selected region for the further analysis. Right: Q^2 distribution, indicating the Primakoff region < 0.001 GeV$^2/c^2$. The peak corresponds to the cross section dominance of photon exchange in pion-nucleus scattering at small momentum transfer, and being exactly zero in case of the free kaon decay. It is broadened in a very similar manner for both cases by the experimental resolution.

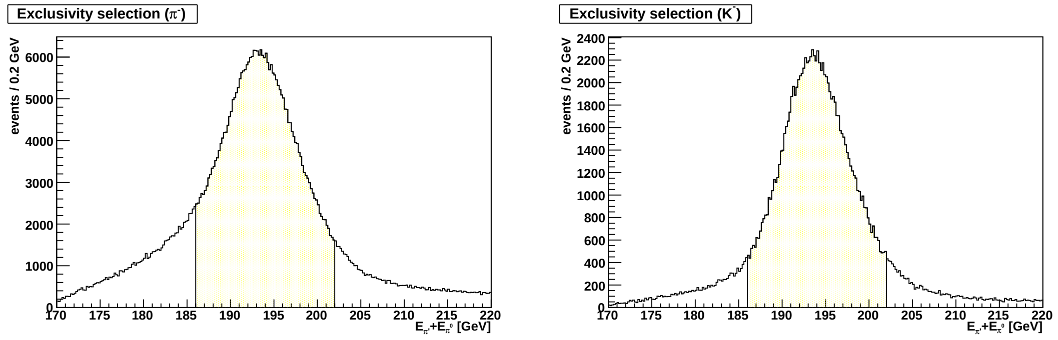

Figure 2: Total energy of the final state particles for the selected sample (left), and for the Primakoff region, where the exclusivity condition is more strictly realized (right). The distribution is broadened mainly due to the energy resolution of the calorimeter, and peaks at a higher value than expected (beam energy 190 GeV) due to the missing calibration in this preproduction of the data.

of the final-state mass $m_{\pi\pi^0}$ is repesented in Fig. 3. It features clear signatures for the two contributing processes: The free kaon decay leads to the peak at $m_K \approx 0.5$ GeV/c^2 and a tail towards lower masses from (semi-)leptonic decays. The Primakoff and diffractive scattering of pions is seen by the predominant contribution of the $\rho(770)$ resonance. The samle contains about 765 000 events, enriched by the chosen cuts to a content of about 14.5% kaons.

It turns out that the CEDAR response strongly depends on the angle under which the beam particle traverse it. The beam divergence, propagated from the measured information of the COMPASS beam telescope to the CEDAR position, is presented in Fig. 5. It lies in a narrow cone of about 200 μrad in both spatial directions. The symmetry axes of the CEDARs are positioned close to the peak intensity of the beam, with some tilt angle between the two, which actually increases the overall efficiency. For both CEDARs, the incoming particle direction is converted to a radial offset r_1 and r_2 with respect to these symmetry centers, and azimuthal position ϕ_1 and ϕ_2.

2 CEDAR information

Both CEDARs are equipped with 8 photomultipliers, circularly positioned near the focus of the Cherenkov rings produced by the traversing particles. The principle and design is exhaustively discussed in [1].

The response of the PMs is processed by collecting the in-time signals in subgroups G0$\cdots$G8, which are determined by the beam tilt direction with respect to the symmetry axis of the CEDAR detectors as shown in Fig. 6. From the data, the number of PM signals in each group is determined for pion and kaon samples obtained by the appropriate kinematical cuts. The radial dependence of this expectation is parameterized as shown in Figs. 7–10. The function by which the data are fitted is

$$\mathrm{prob}_g^{nK,\pi}(j,r) = p_{g0}^{nK,\pi} + \sum_{i=1}^{\text{up to 4}} p_{g3i}^{nK,\pi} \arctan((r - p_{g1i}^{nK,\pi})/p_{g2i}^{nK,\pi}) \tag{3}$$

where $n = 1, 2$ is the number of the CEDAR, $j = 0, 1, 2$ is the number of signals in the respective group $g = 0, ..., 8$. It is seen that within a single group, the expectation for a pion may change from no signal at small r to 2 signals at larger r, and vice versa. The overall response of one CEDAR detector is then judged by multiplying the probabilities for each group response (or rather adding the respective logarithms),

$$\begin{aligned}
\mathrm{C}n\mathrm{G0KLOG} &= \sum \log \mathrm{prob}_{0,2,4,6,8}^{nK}(j,r) && (4)\\
\mathrm{C}n\mathrm{G1KLOG} &= \sum \log \mathrm{prob}_{1,3,5,7}^{nK}(j,r) && (5)\\
\mathrm{C}n\mathrm{G0PLOG} &= \sum \log \mathrm{prob}_{0,2,4,6,8}^{n\pi}(j,r) && (6)\\
\mathrm{C}n\mathrm{G1PLOG} &= \sum \log \mathrm{prob}_{1,3,5,7}^{n\pi}(j,r) && (7)
\end{aligned}$$

where either G0 or G1 is chosen, depending on the particle direction.

Those probabilities are further investigated in their r dependence, shown in Figs. 11–14 examplary for CEDAR1. r-dependent cuts are chosen such that the kaon-like region does certainly not contain pions, and vice versa. The cut functions are parameterized similar to the probability curves above, e.g.

$$\begin{aligned}
\mathrm{C1G0KKLIM} &= -3.5 + 1.8 * \arctan(CED1r/7e-5-1) && (8)\\
\mathrm{C1G0KPLIM} &= -10.4 + 5.0 * \arctan((CED1r+5e-5)/8e-5) && (9)
\end{aligned}$$

Events in the remaining “common” region (between the black lines) are left untagged by the respective CEDAR.

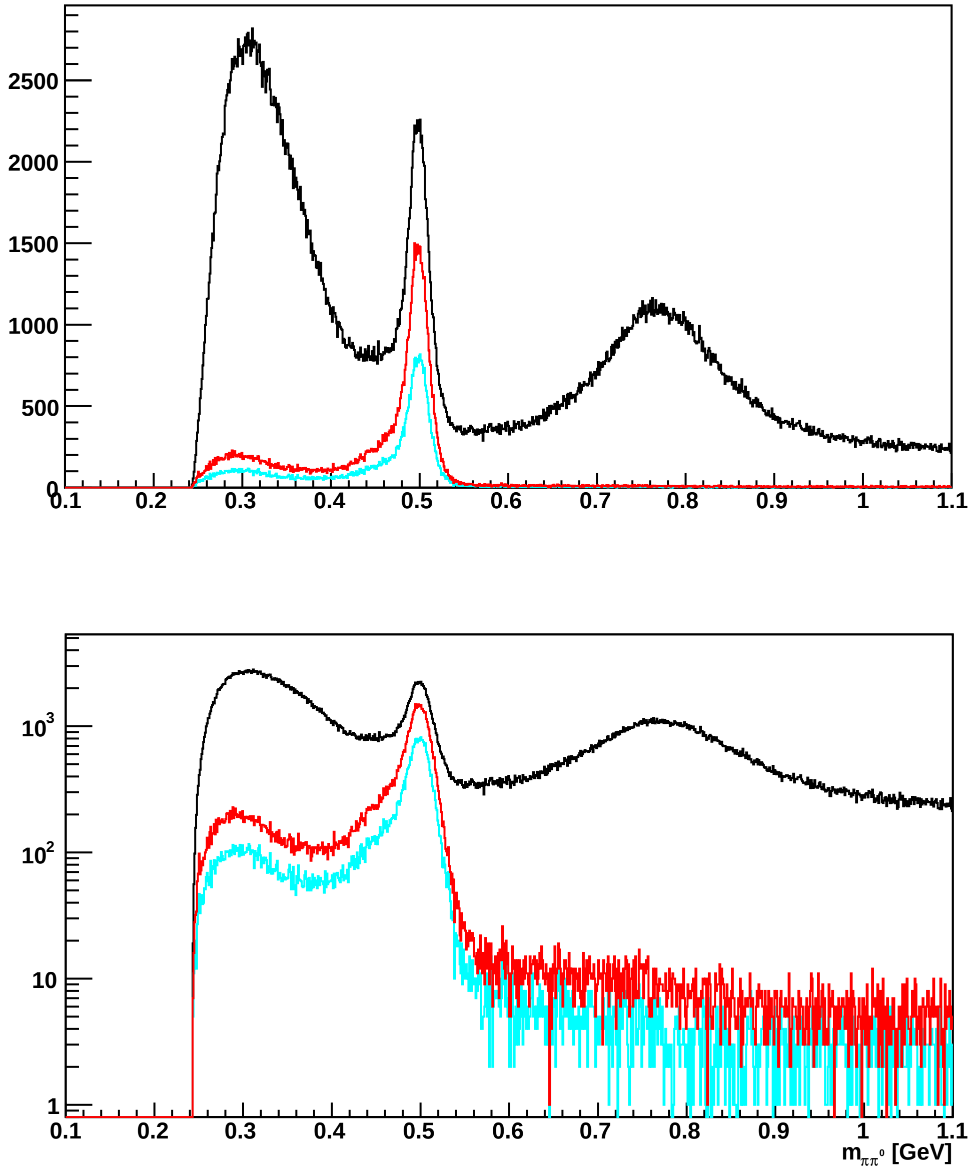

Figure 3: Efficiency of CEDAR cuts on kaon identification. The black curve is the raw $m_{\pi\pi^0}$ distribution without cuts on CEDAR or beam characteristics. The multiplicity cut leads to the light-blue curve with about 43% of the kaon signal, the log-likelihood cut results in the red distribution containing 80% of the original kaon signal. The values have been determined as explained in Fig. 4.

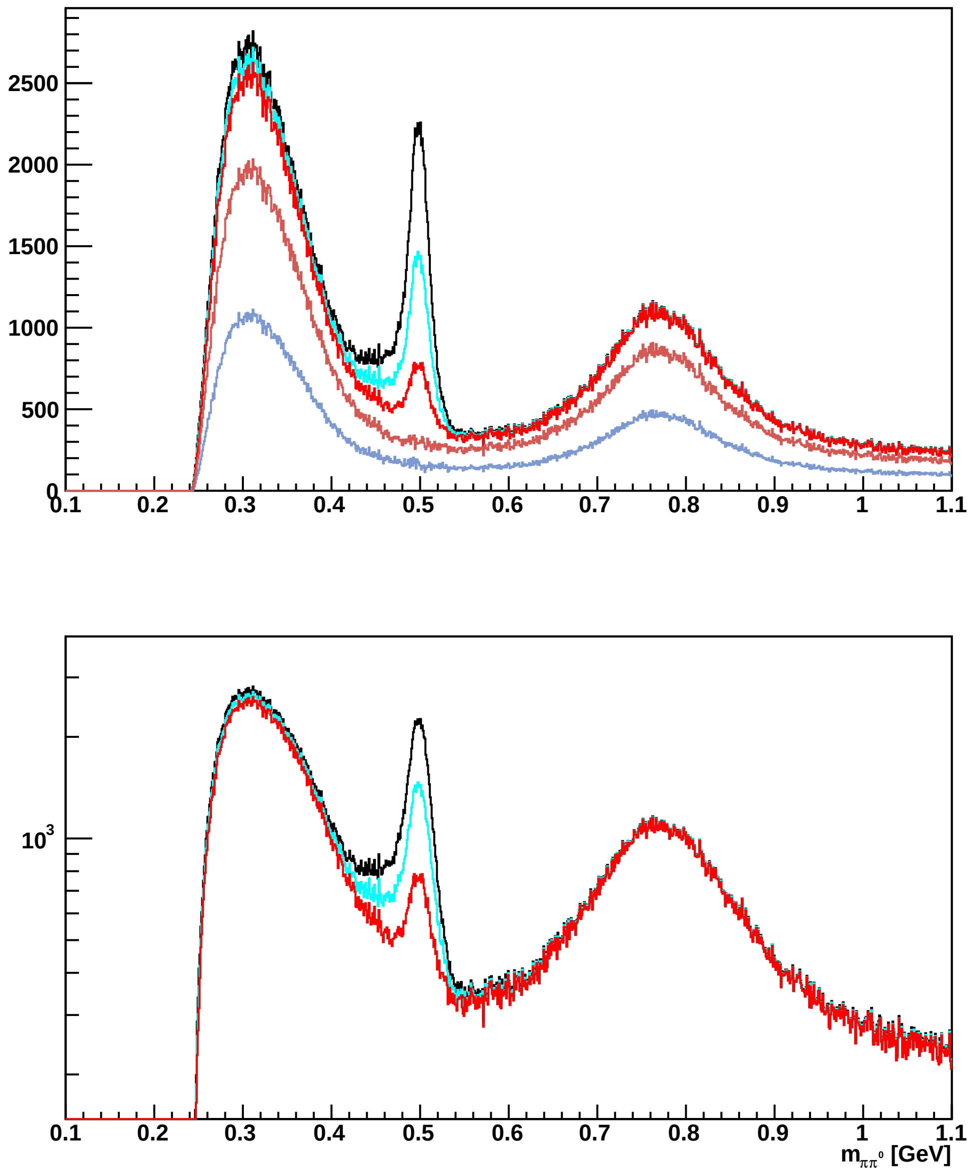

Figure 4: Inefficiency of the kaon identification cuts. The strengths of the remaining kaon peaks are determined to be 21% in case of the log-likelihood cut, and 57% in case of the multiplicity cut. Those numbers have been obtained by subtracting from the inefficiency histograms the original histogram scaled by the factors 0.21 and 0.57, respectively, chosen such that the remaining histogram (the two lower curves) turn out smooth in the region of the kaon peak.

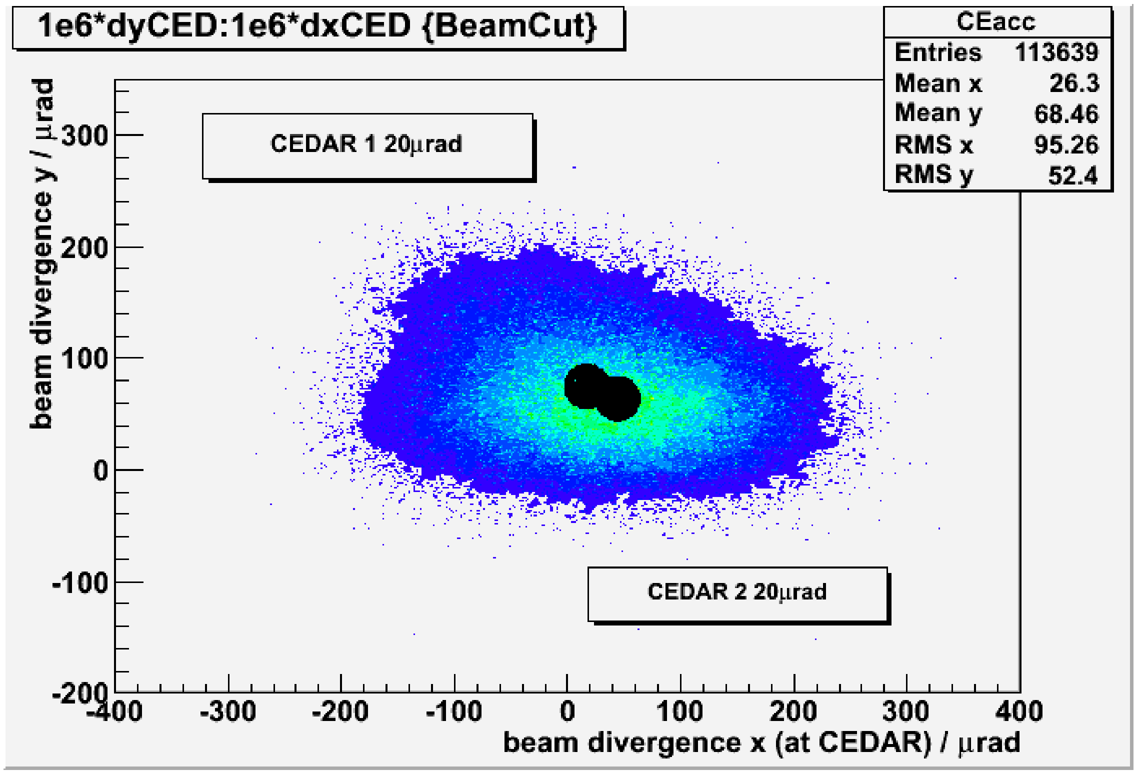

Figure 5: Angular distribution of the beam at the CEDAR position. The symmetry centers of the two CEDARs are indicated by the black plobs, determined from the position of multiplicity-8 kaons.

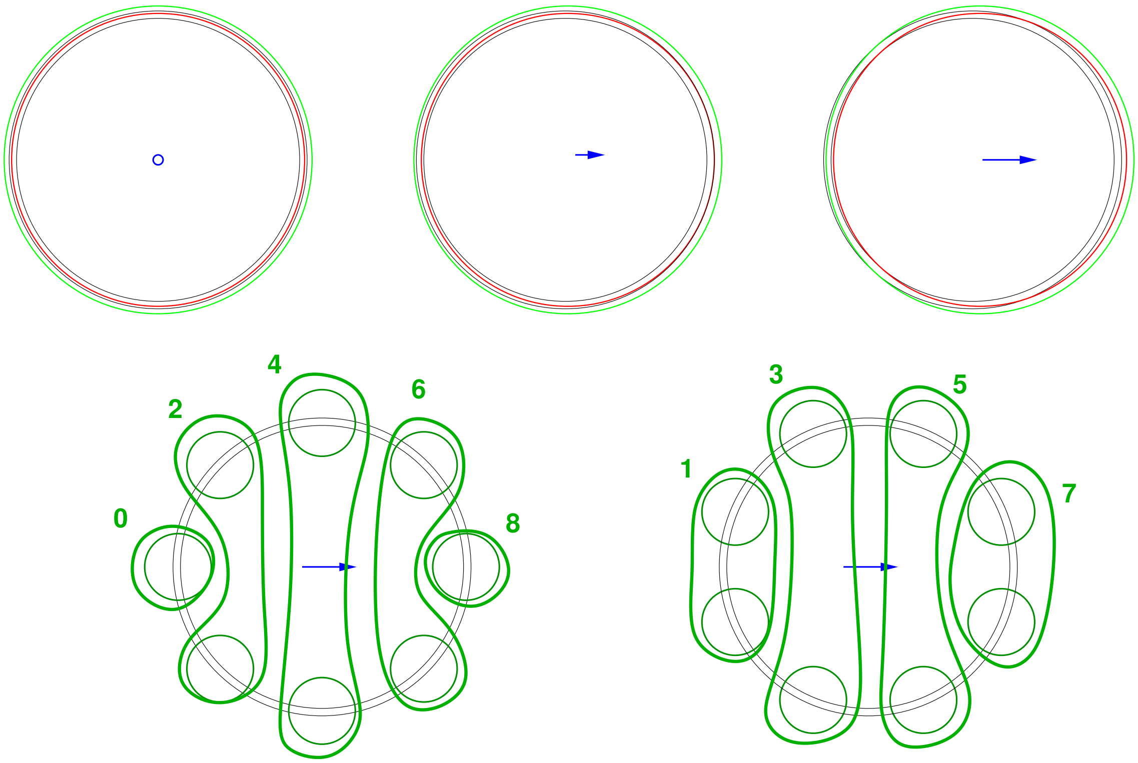

Figure 6: Geometry of the Cherenkov rings with respect to the diaphragm, showing the dependence of expected signals on the direction under which the particle crosses the detector (upper row). The left graph shows the case when the particle trajectory coincidences with the symmetry axis of the CEDAR optics, and only the kaon ring is detectable. On the other two graphs, there is an increasing tilt angle, when first the kaon ring leaves the acceptance of the diaphragm, and then the pion ring enters it on the opposite side. The lower plots introduce the grouping convention of the photomultipliers with respect to the tilt direction of the beam particle. In case the tilt plane lies close to the center of a photomultiplier, the grouping in 0,2,4,6,8 shown in the left figure is made, if the lies between two neighboring PMs, the grouping 1,3,5,7 shown in the right figure applies.

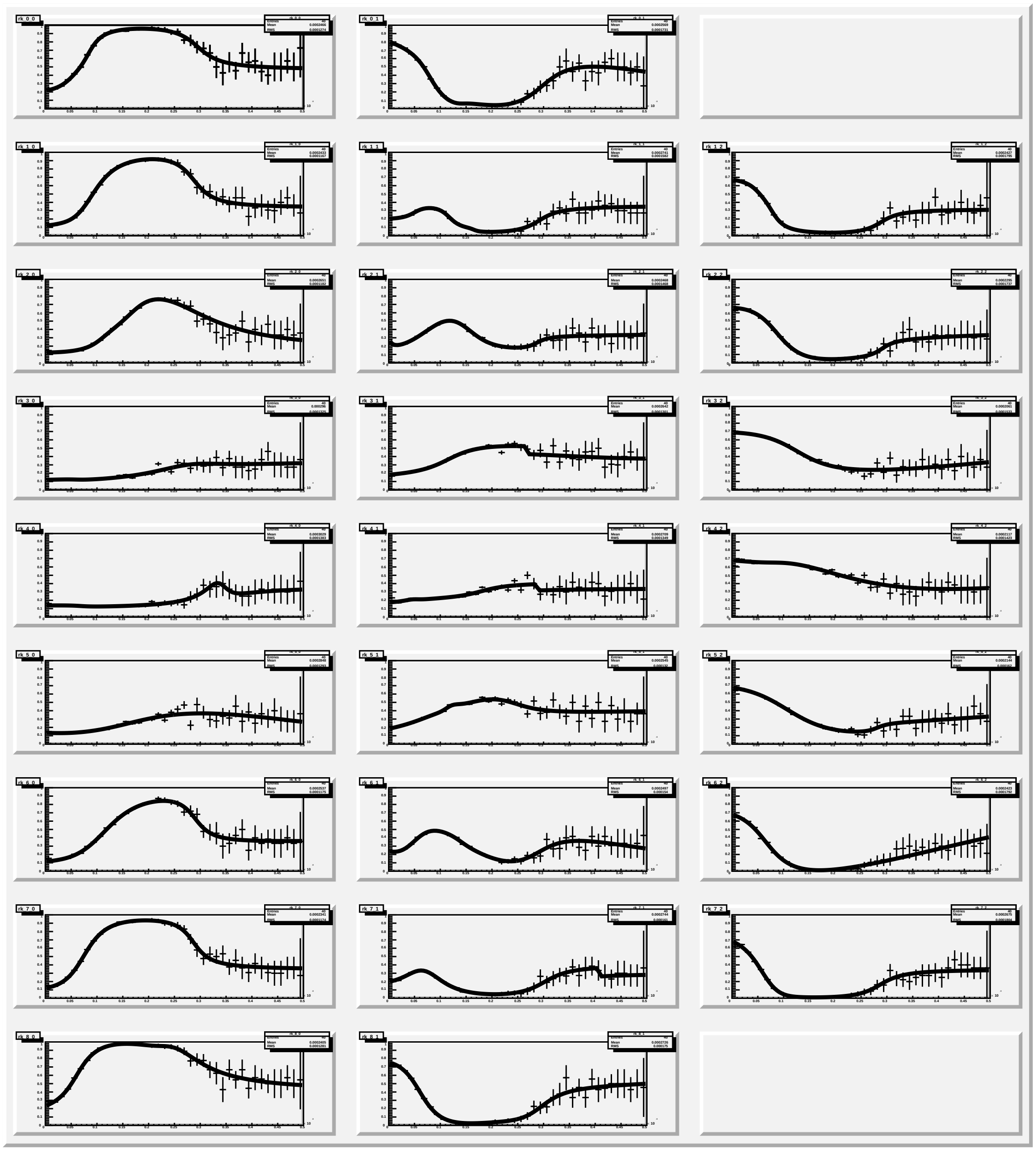

Figure 7: Probabilities for the possible responses for *kaons* in CEDAR1. From top to bottom, the groups G0...G8 are shown. The leftmost histogram shows the probability curve for zero signals, the next histogram for one signal, and the rightmost for 2 photomultiplier signals.

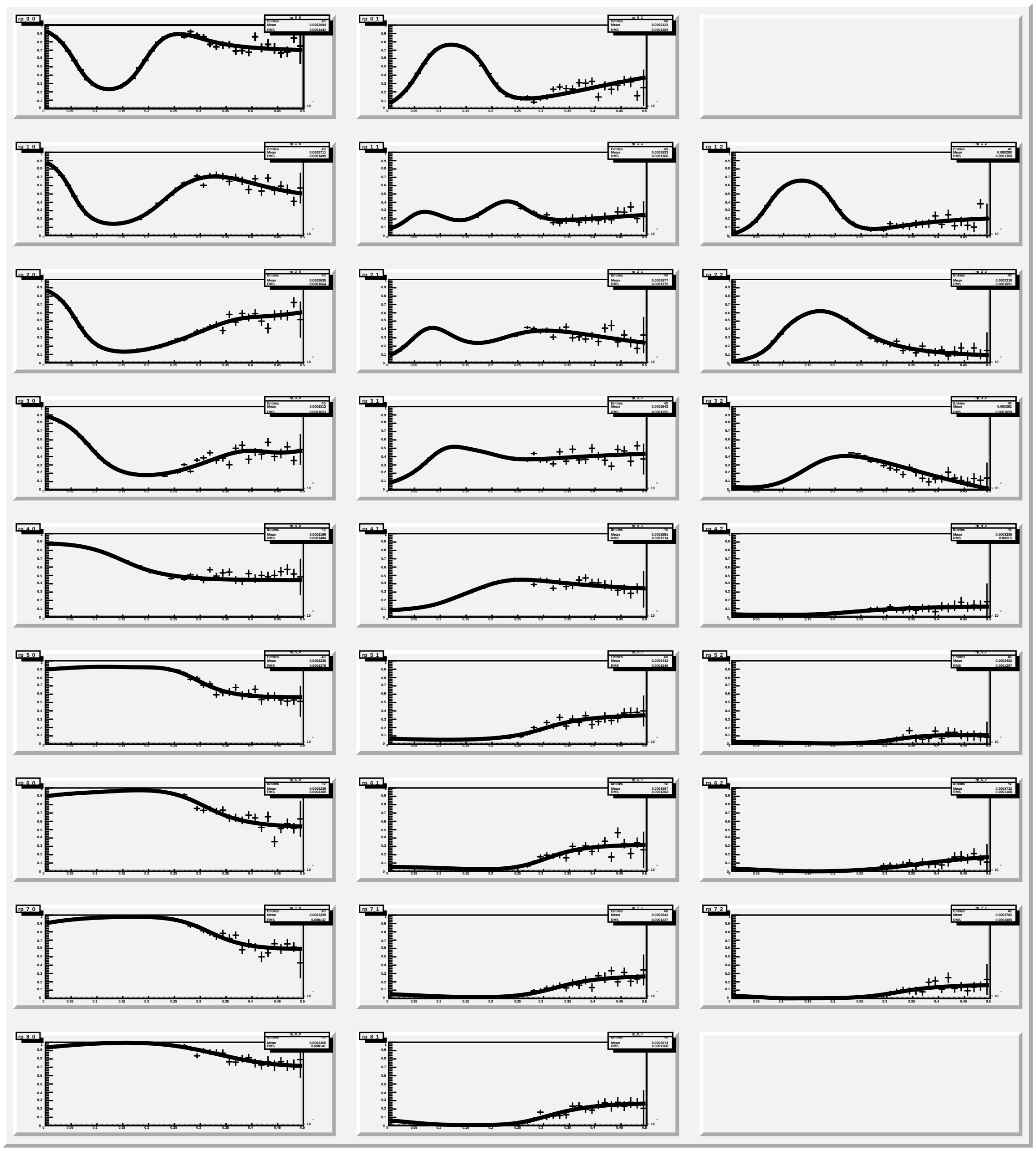

Figure 8: Probabilities for the possible responses for *pions* in CEDAR1. Same meaning of the histograms as in Fig. 7.

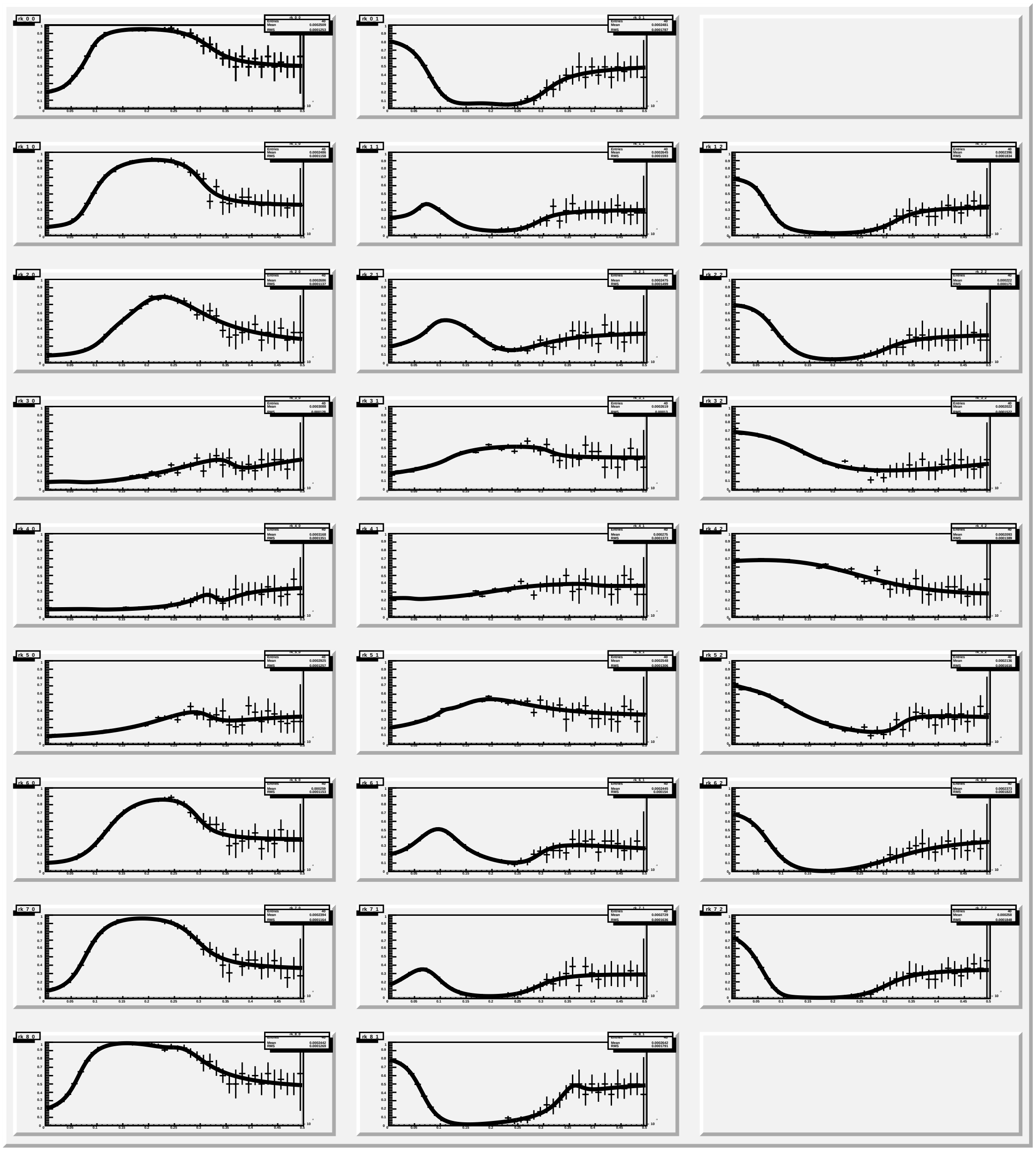

Figure 9: Probabilities for the possible responses for *kaons* in CEDAR2. Same meaning of the histograms as in Fig. 7.

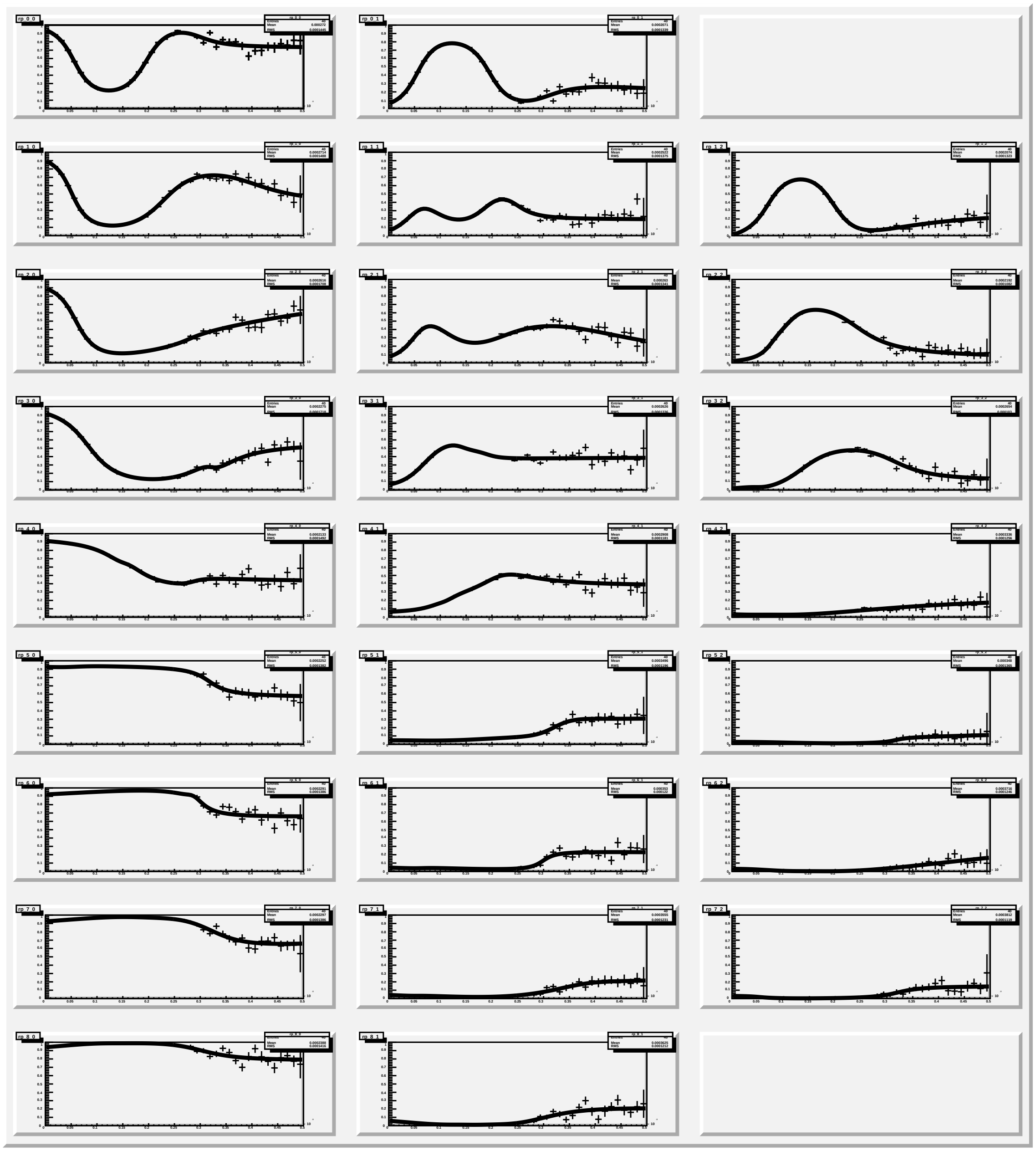

Figure 10: Probabilities for the possible responses for *pions* in CEDAR2. Same meaning of the histograms as in Fig. 7.

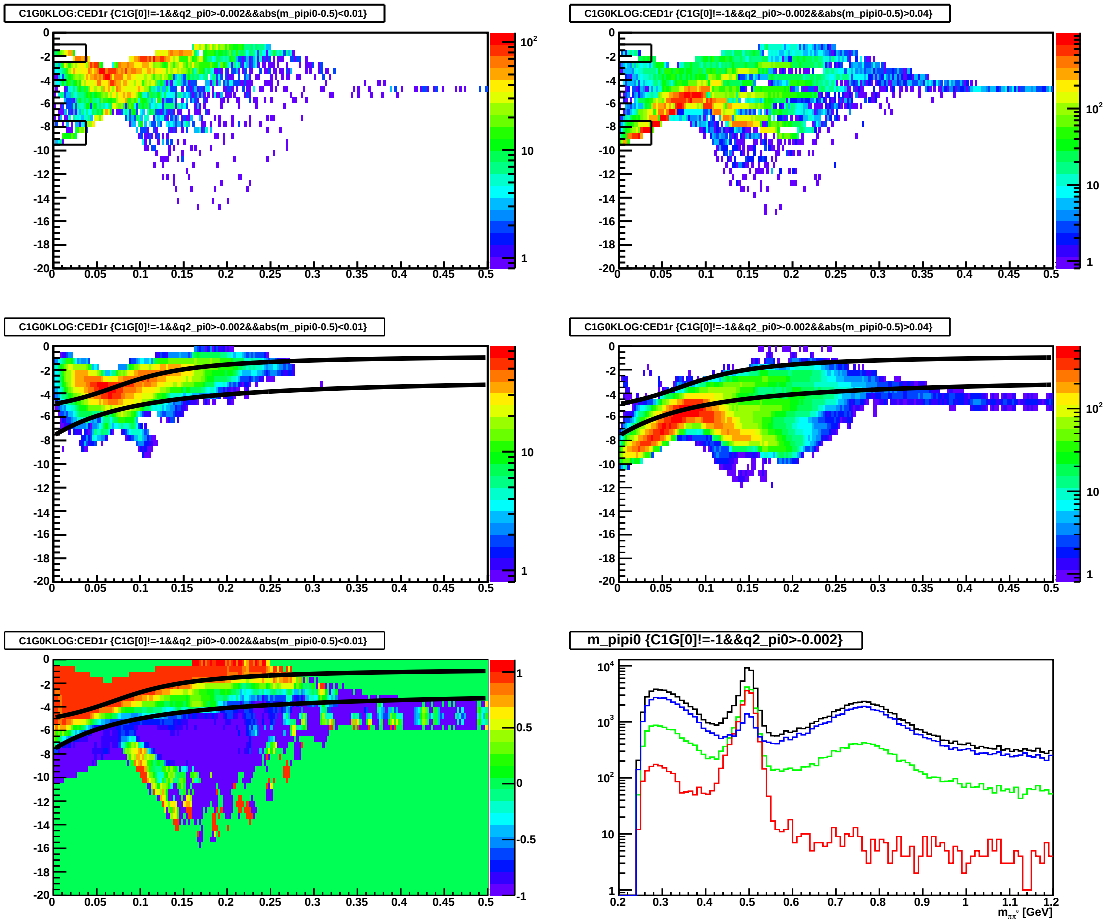

Figure 11: Log-likelihood for kaons in CEDAR1 in G0, dependent on r.

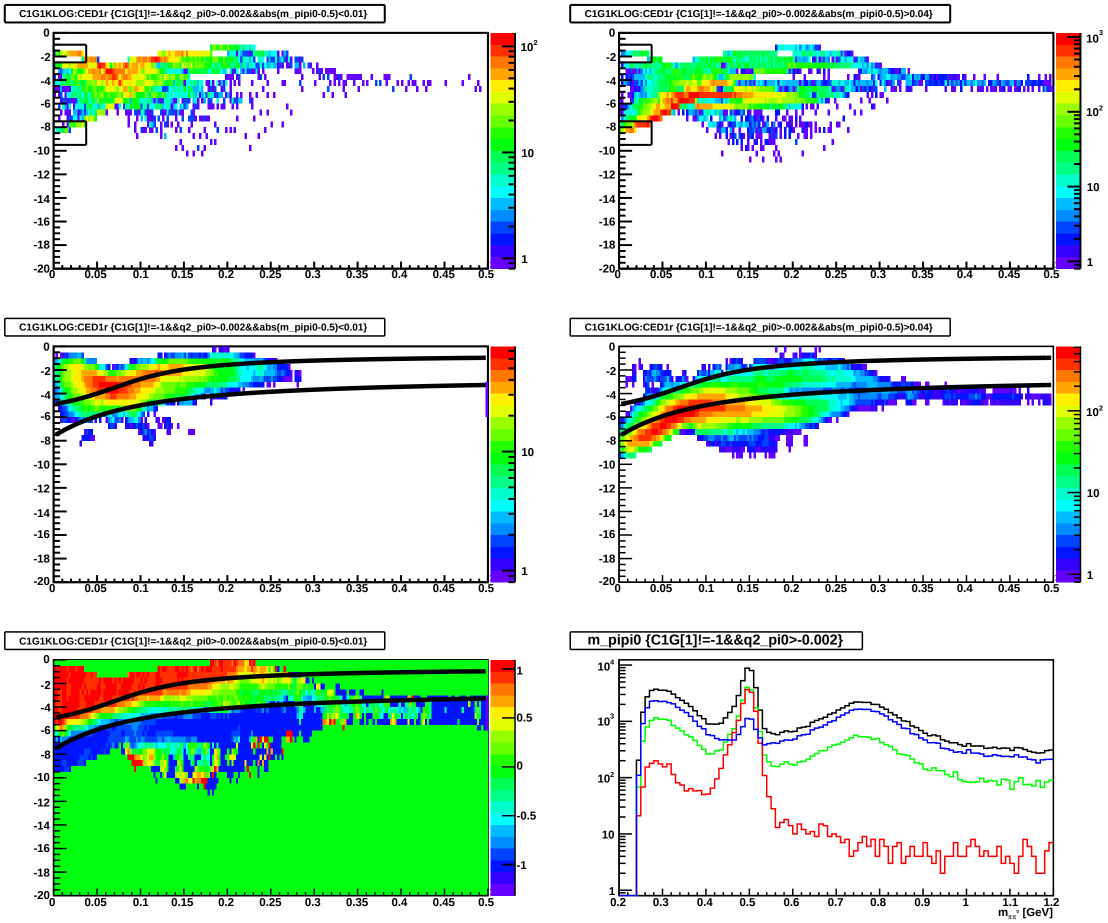

Figure 12: Log-likelihood for kaons in CEDAR1 in G1, dependent on r.

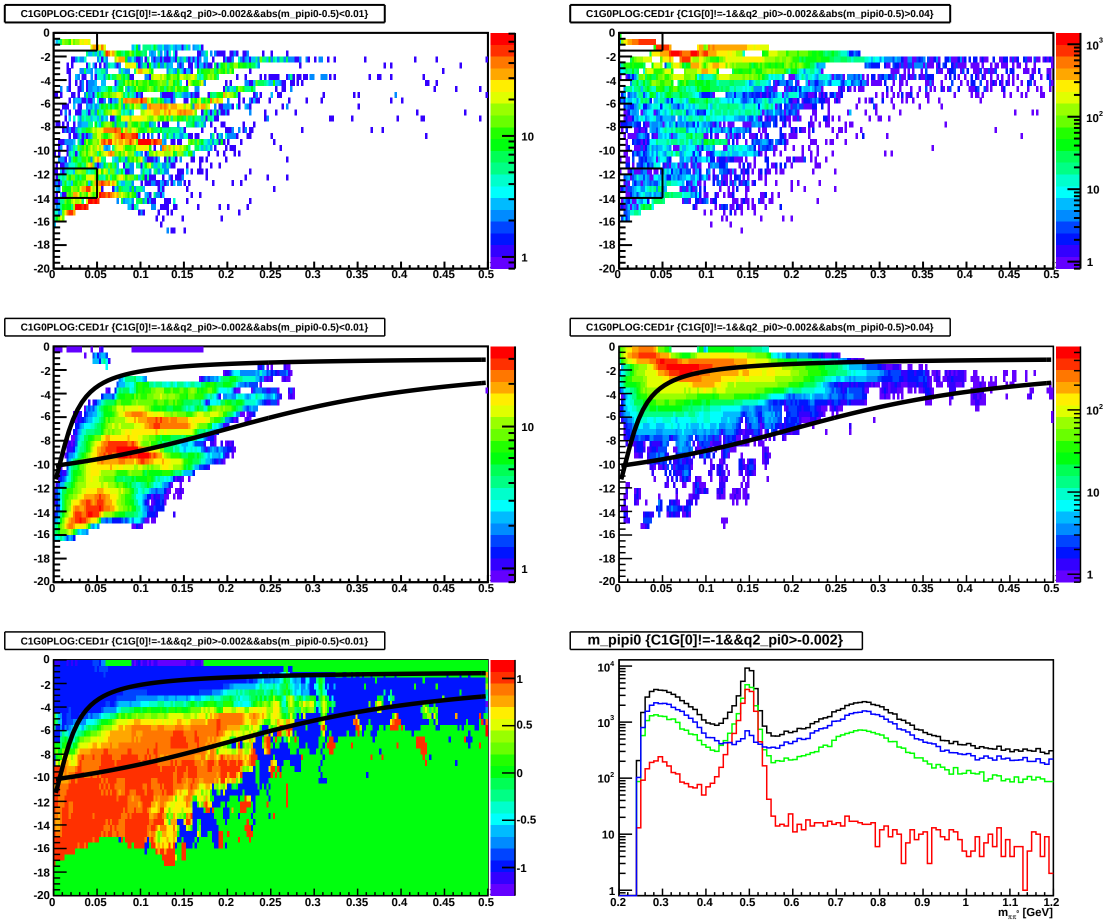

Figure 13: Log-likelihood for pions in CEDAR1 in G0, dependent on r.

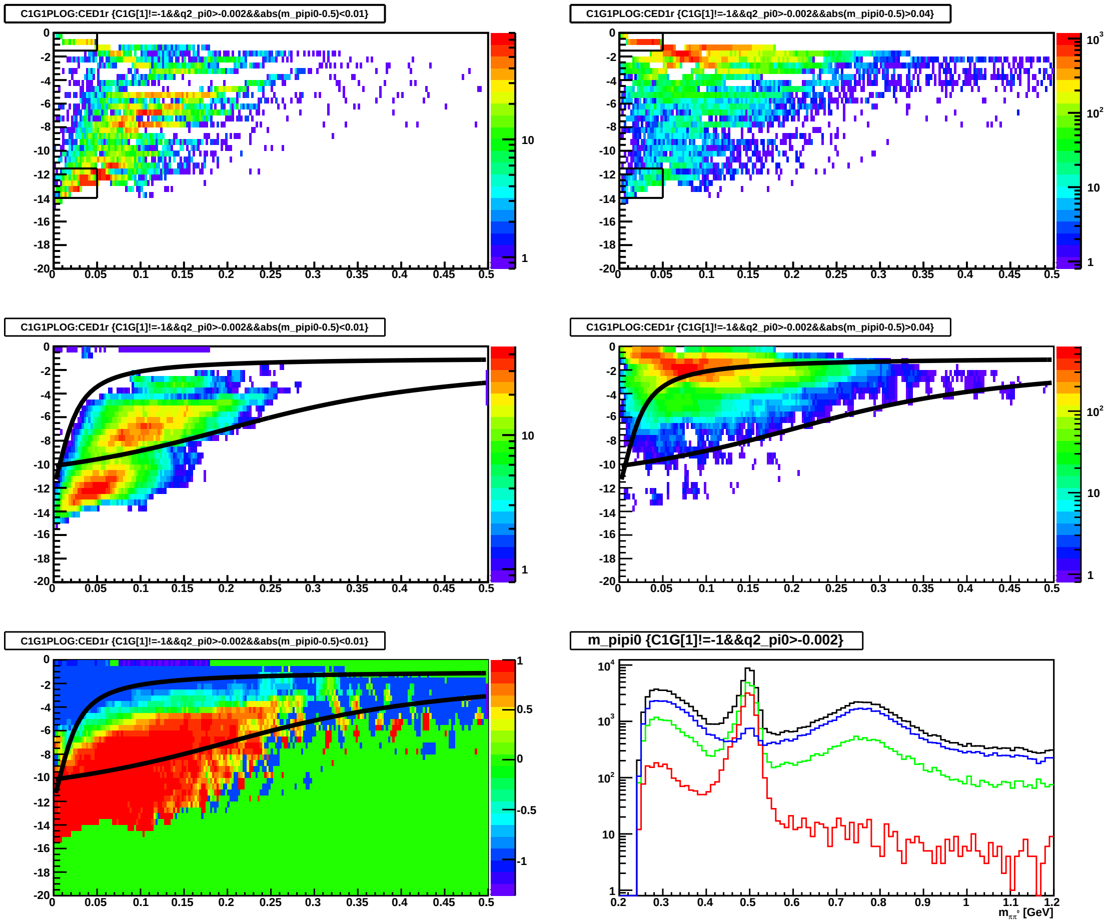

Figure 14: Log-likelihood for pions in CEDAR1 in G1, dependent on r.

3 PID by the likelihoods

The following explains a sample usage of the log-likelihoods in order to obtain the beam particle identification. Logical expressions ($A > B$) are to be read as 1 if fulfilled and 0 if not, according to the C++/root standard. The PID proposals of each CEDAR are given by

$$\begin{aligned}
\mathrm{C}n\mathrm{KLOGID} &= \sum_{g=0,1} (\mathrm{C}n\mathrm{G}g\mathrm{KLOG} > \mathrm{C}n\mathrm{G}g\mathrm{KKLIM}) - (\mathrm{C}n\mathrm{G}g\mathrm{KLOG} < \mathrm{C}n\mathrm{G}g\mathrm{KPLIM}) \\
\mathrm{C}n\mathrm{PLOGID} &= \sum_{g=0,1} (\mathrm{C}n\mathrm{G}g\mathrm{PLOG} < \mathrm{C}n\mathrm{G}g\mathrm{PKLIM}) - (\mathrm{C}n\mathrm{G}g\mathrm{PLOG} > \mathrm{C}n\mathrm{G}g\mathrm{PPLIM}) \qquad (10)
\end{aligned}$$

which assume the value +1 for a kaon, −1 for a pion, and 0 for "no decision". Further, the information of the two CEDARs is combined using

$$\begin{aligned}
\mathrm{C1PID} &= (\mathrm{C1KLOGID} + \mathrm{C1PLOGID} > 0) - (\mathrm{C1KLOGID} + \mathrm{C1PLOGID} < 0) \\
\mathrm{C2PID} &= (\mathrm{C2KLOGID} + \mathrm{C2PLOGID} > 0) - (\mathrm{C2KLOGID} + \mathrm{C2PLOGID} < 0) \qquad (11)
\end{aligned}$$

and finally

$$\mathrm{CPID} = (\mathrm{C1PID} + \mathrm{C2PID} > 0) - (\mathrm{C1PID} + \mathrm{C2PID} < 0) \qquad (12)$$

For the investigated data sample containing 764 292 events, 613 305 (80.2%) incoming particles are identified as pions, 84 203 (11.0%) as kaons and the remaining 66 784 (8.7%) events belong to the unattributed "flat wave". From the kinematic signature of the resulting spectra, the efficiencies and impurities of these identifications are derived as summarized in Tab. 3. The histograms are shown in Fig. 16.

By applying more strict cuts on the Primakoff signature, a subsample with a further enriched kaon component is obtained, the mass distributions are given in Fig. 17. The efficiencies and impurities for pion and kaon identification are consistent in both cases on the sub-percent level. Assuming them also for the unbiased beam and taking the known fractions of pions, kaons and anti-protons into account, the values given in the last line of Tab. 3 is found.

The presented method allows for an identification of kaons with 82% efficiency. The misidentification probability of a pion as a kaon (η_π) is below $5 \cdot 10^{-4}$, consequently an unbiased sample of beam particles with CEDAR identification as kaons will at most contain a 2.2% admixture of pions.

Selecting pions by the respective CEDAR condition has an efficiency of 94%. Misidentifying kaons as pions has a probability of 6%, leading to an admixture of about 0.1% kaons in an unbiased sample. This is a suppression of the original content of kaons by a factor 20, such that for most analyses a very good estimate of the desired pure pion spectra should be feasible.

References

[1] C. Bovet *et al.*, The CEDAR counters for particle identification in the SPS secondary beams: a description and an operation manual, CERN**82-13**, Geneva.

Table 1: CEDAR particle identification. For each investigated sample, the relative strength of finding CPID$= 1, 0, -1$ is given. By statistical subtraction of the obtained $m_{\pi\pi^0}$ distributions from eachother, determining the weight factor that makes the wrong signature disappear, the relative true particle contributions are found. Since the flat and the K distributions are found very similar in shape, their relative admixture in the 1% contamination of the pion sample cannot be distinguished on the present statistical precision.

	π			K			flat / $\bar{p}$			
		CPID$= -1$			CPID$= 1$			CPID$= 0$		
	kin.	π	K/flat	kin.	π	K	kin.	π	K	flat/$\bar{p}$
Full sample 764 000 events	85%	80.2%		13.3%	11.0%		$\approx 1.7\%$	8.7%		
		0.990	0.010		< 0.004	≈ 1		0.55	0.27	0.18
		$\varepsilon_\pi = 0.943$			$\varepsilon_K = 0.824$					
		$\eta_K = 0.06$			$\eta_\pi < 0.0005$					
Primakoff 121 000 events	63.5%	59.3%		35.6%	29.4%		$\approx 0.9\%$	11.3%		
		0.963	0.037		< 0.001	≈ 1		0.37	0.55	0.09
		$\varepsilon_\pi = 0.934$			$\varepsilon_K = 0.825$					
		$\eta_K = 0.06$			$\eta_\pi < 0.0005$					
Beam at target	96.8%	91.0%		2.4%	2.0%		0.8%	7.0%		
		0.999	0.001		< 0.022	> 0.978		0.83	0.06	0.11

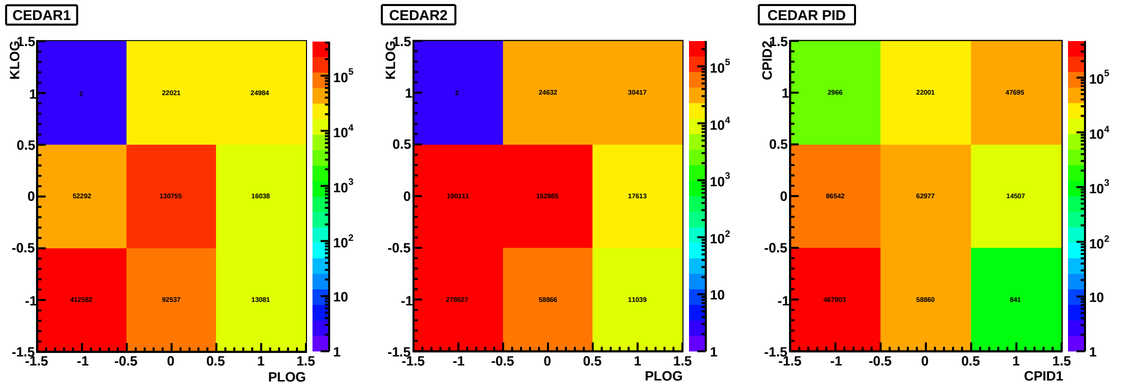

Figure 15: Left: Statistics in the log-likelihood regions as defined in Figs. 11–14 for kaon and pion identification with CEDAR1, as expected strongly anti-correlated. Middle: same picture for CEDAR2. Right: Combining the information of the CEDARs according to Eqs. 11.

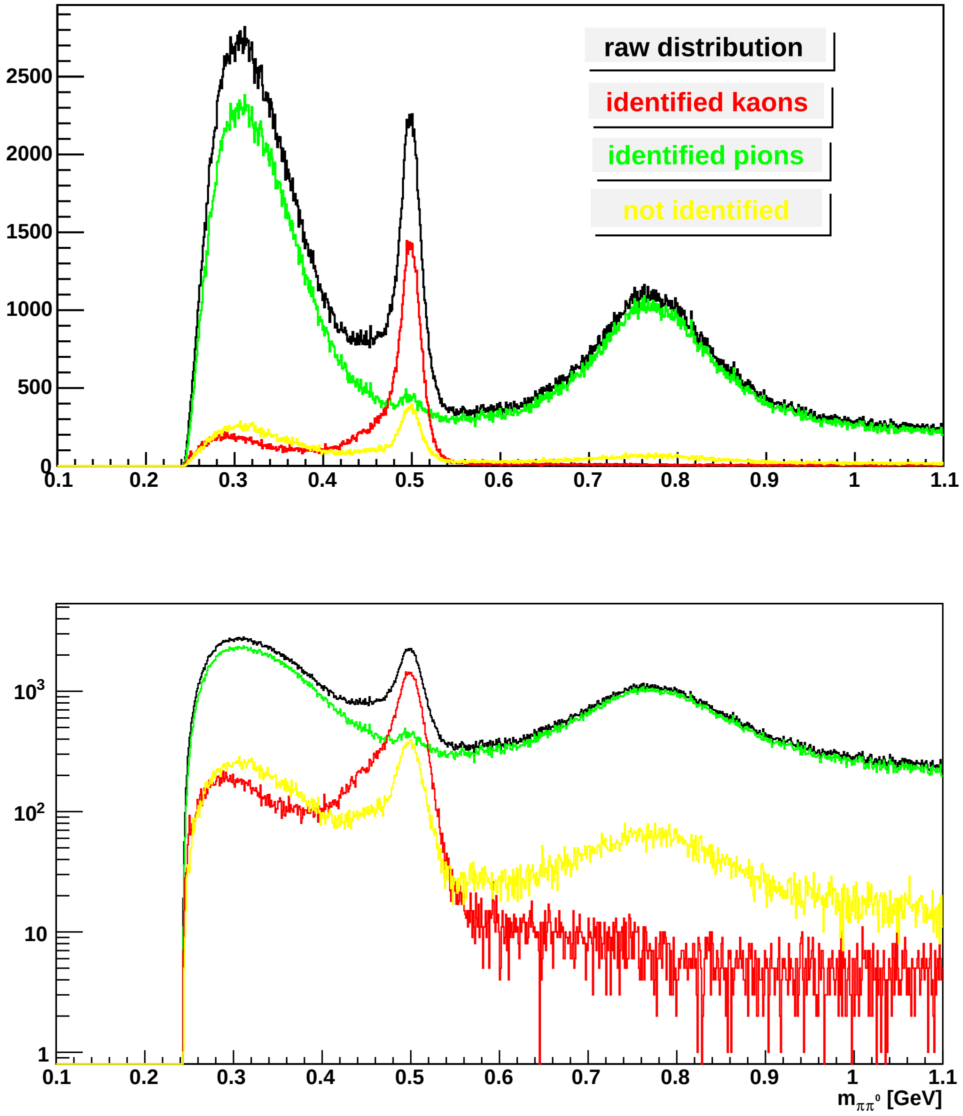

Figure 16: Decomposition of the $m_{\pi\pi^0}$ spectrum into the single contributions by CEDAR beam identification. By subtracting e.g. the kaon histogram, multiplied by an appropriate weighting factor, from the pion histogram, such that the remainder kaon signature disappears, the impurities in Tab. 3 have been obtained.

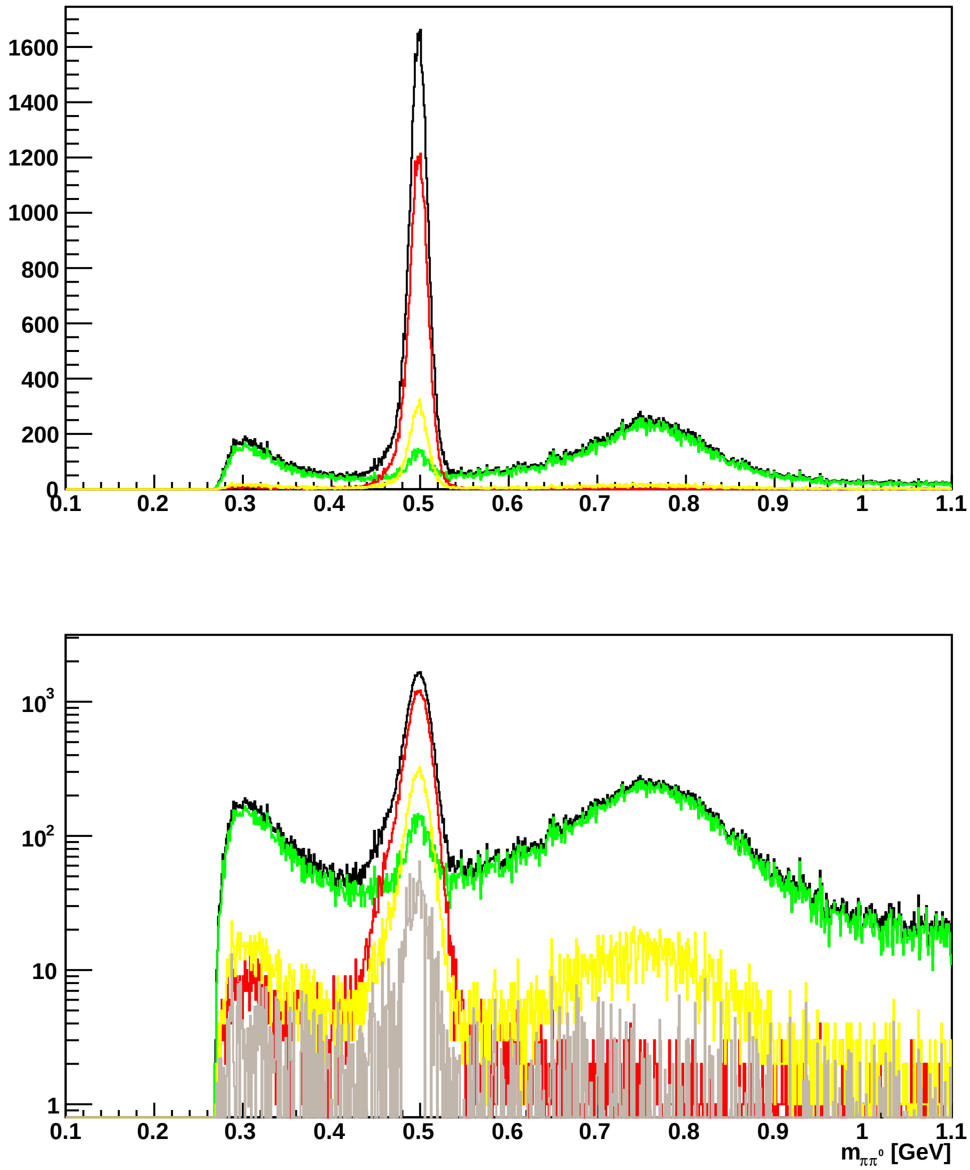

Figure 17: Same like Fig. 16, but with tight Primakoff cuts. Subtracting from the flat wave (yellow distribution) appropriately weighted the kaon and pion distributions, results in the light-grey distribution.

Reconstruction of the Pion Beam Energy from Beam Optics

Jan Friedrich[*], Markus Krämer

Physik-Department, TU München

April 2012

Abstract

The trajectories of the incoming beam particles are determined with high precision in the COMPASS silicon microstrip beam telescope. Since for hadron beams there is no beam momentum station installed, the momentum is known only to lie within the momentum distribution given by the beam line (*i.e.* by the scrapers). Yet, the beam line optics incorporates correlations between the momentum of the beam particle and its position and angle, even downstream of the COMPASS target. This information can in turn be used to constrain the momentum of the beam particles.

While it is obviously good advice to apply this correction in analyses where the beam energy plays a role, it also opens a whole new field of investigating energy dependencies over the quite considerable spread of about 3% (188.5 – 194.5 GeV). The gaussian energy resolution is about 1.2 GeV.

1 Data set, definitions

In order to determine the beam parameter correlations, exclusive diffractive 3-charged-pion final states are selected, at small momentum transfer ($t' < 0.2\,\mathrm{GeV}^2/c^2$) from the Primakoff 2009 data. Those events are triggered by the calorimetric trigger due to the electromagnetic component of hadronic showers started by at least one of the charged pions, which leads to a complicated, certainly energy-dependent efficiency. For the present considerations, this efficiency plays only a secondary role. About 1.37 million events are extracted from the 2009 Primakoff data set (pre-production T51; as the analysis is performed on the subset of events with maximum energy of the outgoing pions $E_{\pi^\pm} < 155\,\mathrm{GeV}$, so the full statistics of the final state is expected to be higher).

The chosen final state relies on the momentum resolution of the charged-particle tracking only. Since the data are dominated by low momentum transfers, correction for energy loss to the recoiling particle is neglected. At higher momentum transfers, indications of the target recoils could be identified after the presented energy correction was applied. This, however, is not further discussed here.

The direction and position of the incoming beam particles is described by the transverse coordinates (x, y) at the Ni target position $z = 72.5\,\mathrm{cm}$, and the respective slopes $(dx/dz, dy/dz)$, abbreviated in the following by (dx, dy). Units are cm and rad.

2 Representation and determination of $E(x, y, dx, dy)$

The beam line optics leads to a correlation of E with the spatial coordinates (x, y, dx, dy), which can be determined from the described data set. Without prior knowlegde on the details of the beam

---

[*] jan@tum.de

optics, this was achieved in a first step using a neural network in a `x,y,dxs,dys:50:25:6:6:E` 4-layer configuration (notation of the employed `root` implementation `TMultiLayerPerceptron`, cf. `http://root.cern.ch`). The quantities `dxs` and `dys` refer to the slopes scaled by a factor 10.000, such that the pion beam divergence of about $\pm 200\mu$rad spreads over a range of the order of one, as required for the training process of the neural network. The given neuron/layer structure with 4 hidden layers and 92 neurons has been manually optimized in several steps to match the complexity of the present problem.

Because this neural network takes quite a considerable time to evaluate (∼msec per evaluation on a standard desktop computer), in a second step it is reduced to a multidimensional polynomial. Terms up to 5th order in each variable x, y, dx, dy and all possible mixed terms are taken into account, resulting in 441 free parameters. The 4^{th}-power components turn out to be quite large and presumably a consequence of (non-linear) effects in the beam line optics. The parameterization is given in the appendix, including a C-code for implementation.

In Fig. 2 the original spectrum of the exclusivity signal for $E_{3\pi} = E_{\pi^-} + E_{\pi^-} + E_{\pi^+}$ is shown with the most probable value 191 GeV subtracted, in comparison to the corrections applied. The width of the exclusivity peak is reduced from about 2.0 GeV to 1.5 GeV (signal RMS), equivalent to a deconvolution of a beam momentum distribution with an RMS of 1.3 GeV.

The correlation of the beam energy with each of the 4 coordinates is given in Fig. 2, comparing the uncorrected case with the two discussed parameterizations.

The corresponding beam energy profiles are given in Fig. 2.

Other final states, especially those including photons in the final state which do not depend on the tracking but rather on the e.m. calorimetry, confirm that applying the given energy correction deconvolutes a gaussian width of about 1.3 GeV.

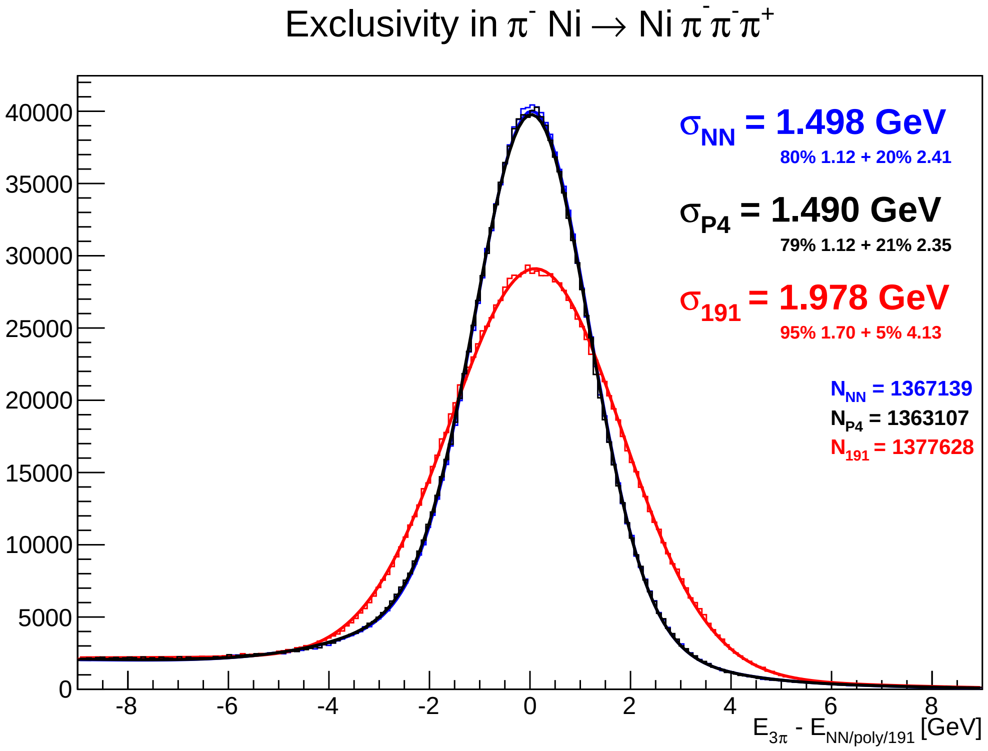

Figure 1: Exclusivity peak for diffractive $\pi^-\pi^-\pi^+$ final states at low momentum transfer. The signal obtained from the momenta of the outgoing pion trajectories only (denoted “191”) is compared to the neural network (“NN”) and polynomial fit (“P4”) using also the spatial parameters of the incoming beam pion. The quoted “σ” are RMS of the signal distributions fitted as the sum of two gaussians. The background is parameterized by an *arctan* function, smoothly connecting a flat background at lower energies with vanishing strength at high energy.

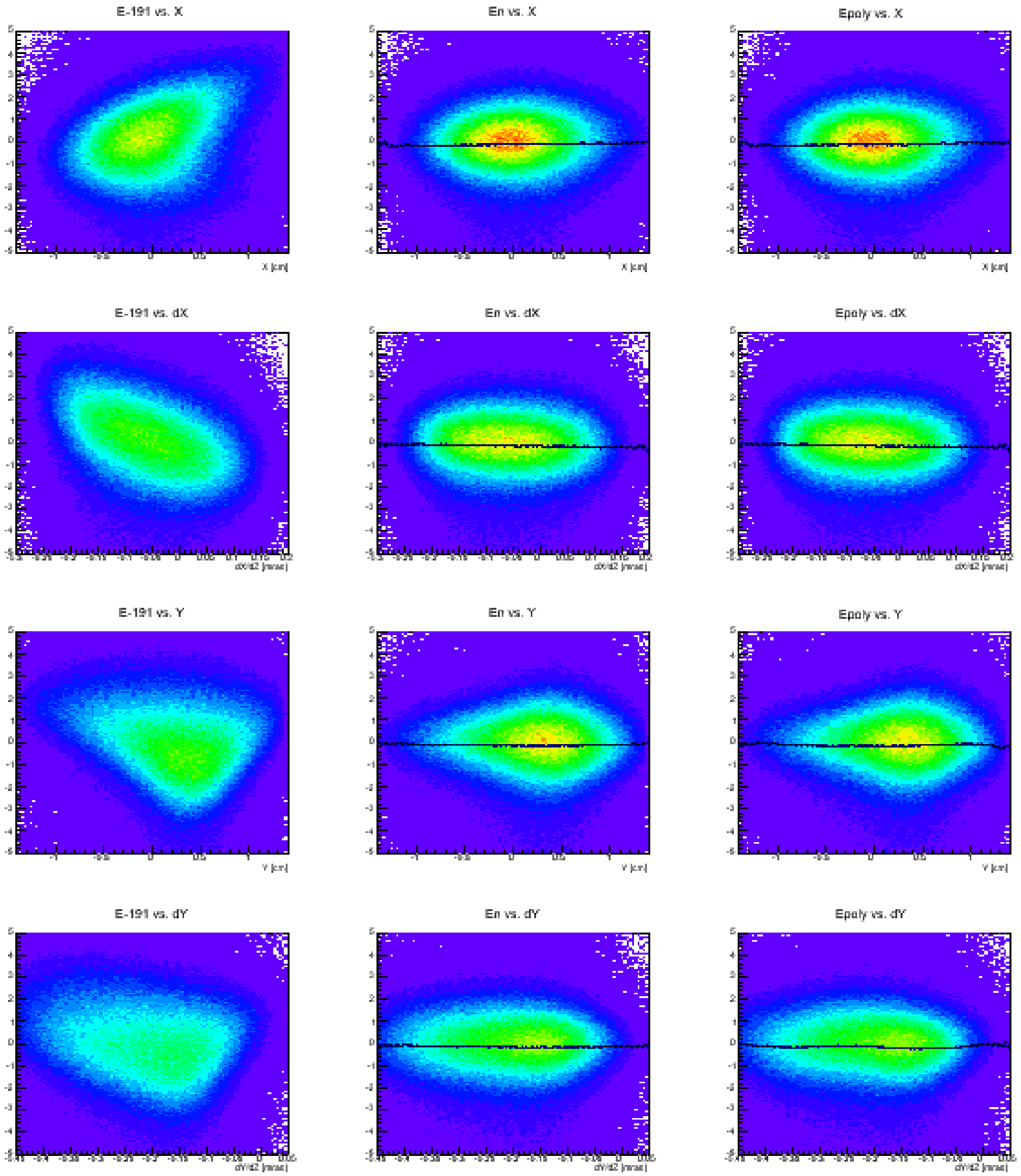

Figure 2: Left column: Uncorrected correlations of $E_{3\pi}$ with x, dx, y and dy. Middle column: The NN correction applied. Right column: The polynomial correction applied. The vertical scale is always GeV.

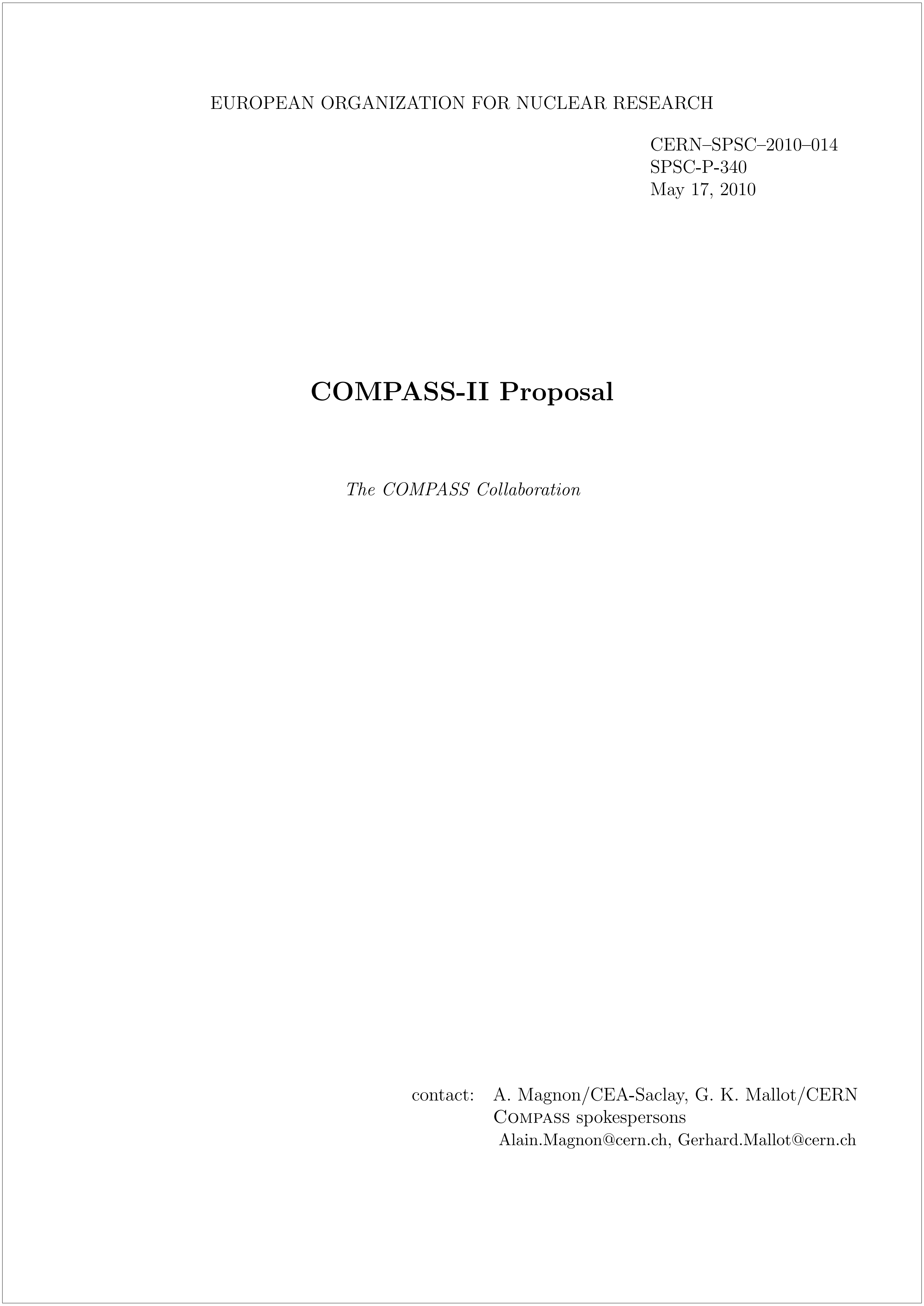

EUROPEAN ORGANIZATION FOR NUCLEAR RESEARCH

CERN–SPSC–2010–014
SPSC-P-340
May 17, 2010

COMPASS-II Proposal

The COMPASS Collaboration

contact: A. Magnon/CEA-Saclay, G. K. Mallot/CERN
COMPASS spokespersons
Alain.Magnon@cern.ch, Gerhard.Mallot@cern.ch

Contents

Executive Summary *3*
PHYSICS CASE *7*
1 **Hard exclusive photon and meson production** *8*
1.1 *Generalised parton distributions and hard exclusive reactions* *8*
1.2 *Kinematics and observables* *12*
1.2.1 Kinematic domains *12*
1.2.2 Deeply virtual Compton scattering *12*
1.2.3 Deeply virtual meson production *18*
1.3 *Simulations and projections* *19*
1.3.1 The t-slope of the DVCS cross section *20*
1.3.2 Beam charge & spin asymmetry and difference *22*
1.3.3 The t-slope of the ρ^0 cross section *25*
1.3.4 Transverse target spin asymmetries *29*
1.4 *A first look at exclusive photon production in 2008* *30*
1.4.1 Overall efficiency and performances to select BH and DVCS events *31*
1.4.2 Improved analysis using ECAL timing information *34*
1.5 *A first hint of "pure" DVCS events from the 2009 test run* *34*
2 **Measurements of unpolarised PDFs and TMD effects in SIDIS** *37*
2.1 *Strange quark distribution function and quark fragmentation functions* *37*
2.1.1 Strange quark distribution function *38*
2.1.2 Quark fragmentation functions *39*
2.1.3 Expected statistical precision *40*
2.2 *Transverse-momentum-dependent effects in SIDIS* *41*
3 **Pion-induced Drell–Yan muon pair production** *44*
3.1 *Transverse spin-dependent structure of the nucleon* *44*
3.2 *SIDIS contributions to transversity and TMDs* *45*
3.3 *Drell–Yan formalism and observables* *46*
3.3.1 Kinematics of the Drell–Yan process *46*
3.3.2 General expression for the Drell–Yan cross section *48*
3.3.3 Asymmetries in the LO QCD parton model *48*
3.3.4 Observables *50*
3.3.5 Study of the J/ψ production mechanism and J/ψ–DY duality *51*
3.4 *Kinematic domain and spectrometer acceptance* *52*
3.5 *Event rate and projected statistical precision* *55*
3.5.1 Expected rate of Drell–Yan events *55*
3.5.2 Expected statistical precision and theory predictions for asymmetries *58*
3.6 *Feasibility of Drell–Yan measurements at* COMPASS *63*
3.6.1 Results of 2007–2008 beam tests *63*
3.6.2 Preliminary results of 2009 beam test *65*
3.6.3 Background studies *68*
3.6.4 Systematic errors in the asymmetries *69*
3.7 *Competition and complementarity* *72*
4 **Experimental studies of chiral perturbation theory** *73*
4.1 *Pion and kaon polarisability measurement* *73*
4.2 *Primakoff reactions with neutral pions in the final state* *79*
HARDWARE UPGRADES *83*

5 **Muon trigger** *84*
5.1 *Trigger hodoscopes 84*
5.2 *Veto system 86*
5.3 *Inclusive trigger 87*
5.4 *Trigger for Drell–Yan measurements 88*
6 **Target and proton recoil detector for the GPD programme** *89*
6.1 *Liquid hydrogen target 90*
6.2 *Recoil Proton Detector 91*
7 **Upgrades of the electromagnetic calorimetry** *97*
7.1 *ECAL1 and ECAL2 upgrades 98*
7.2 *Large-angle electromagnetic calorimeter ECAL0 99*
7.3 *Test of the new ECAL0 prototypes 101*
8 **Radiation Protection issues for Drell–Yan measurements** *104*
9 **Transversely polarised target for Drell–Yan measurements** *105*
10 **Absorber for Drell–Yan measurements** *106*
10.1 *Concept and design 106*
10.2 *Results from the beam test in 2009 108*
11 **Pixelised Micromegas detectors** *111*
12 **Upgrade of the RICH-1 gaseous photon detectors** *112*
13 **Cost estimate** *116*
Acknowledgements *120*

Executive Summary

The research fields of hadron spectroscopy and hadron structure are closely connected since their very beginnings. In 1964, spin-1/2 quarks were conjectured to be the building blocks of baryons and mesons in order to explain their quantum numbers observed in hadron spectroscopy. In 1969, when interpreting data from first direct studies of the structure of the proton, partons were hypothesised as its internal constituents and soon after identified with quarks. In the early 1970's, Quantum Chromodynamics (QCD) became accepted as the theory of strong interactions, explaining the observed weakening of the interquark forces at short distances or large momentum transfers. QCD not only describes hard processes through perturbative expansions, but also the non-perturbative dynamics of the strong interaction, down to soft and extremely soft processes which are involved in meson spectroscopy and linked to chiral perturbation theory.

Parton Distribution Functions (PDFs) describe the structure of the nucleon as a function of the nucleon momentum fraction carried by a parton of a certain species. They are studied primarily in Deeply Inelastic Scattering (DIS) where the longitudinal momentum structure of the nucleon is explored in the collinear approximation, *i.e.* neglecting transverse degrees of freedom. Up to now, PDFs were investigated independently from nucleon electromagnetic form factors that are related to ratios of the observed elastic electron–nucleon scattering cross section to that predicted for a structureless nucleon. The recently developed theoretical framework of Generalised Parton Distributions (GPDs) embodies both form factors and PDFs, such that GPDs can be considered as momentum-dissected form factors which provide information on the transverse localisation of a parton as a function of the fraction it carries of the nucleon's longitudinal momentum. Obtaining such a “3-dimensional picture” of the nucleon is sometimes referred to as “nucleon tomography”. In a complementary approach, the subtle effects of intrinsic transverse parton momenta are described by Transverse-Momentum-Dependent PDFs (TMDs). These effects become visible in hadronic Drell–Yan (DY) and Semi-Inclusive DIS (SIDIS) processes. The structure of hadrons can not yet be calculated in QCD from first principles. However, the deformation of the shape of a hadron in an external electromagnetic field, described by polarisabilities, can be predicted by chiral perturbation theory which is a low-energy expansion of the QCD Lagrangian.

More than 10 years ago, the COMPASS experiment was conceived as “COmmon Muon and Proton apparatus for Structure and Spectroscopy”, capable of addressing a large variety of open problems in both hadron structure and spectroscopy. As such, it can be considered as a “QCD experiment”. By now, an impressive list of results has been published concerning nucleon structure, while the physics harvest of the recent two years of hadron spectroscopy data taking is just in its beginnings. The COMPASS apparatus has been proven to be very versatile, so that it offers the unique chance to address in the future another large variety of newly opened QCD-related challenges in both nucleon structure and hadron spectroscopy, at very moderate upgrade costs. It consists of a high-precision forward spectrometer and either an unpolarised, longitudinally or transversely polarised target. It is located at the unique CERN SPS M2 beam line that delivers hadron or naturally polarised $\mu^{\pm}$ beams in the energy range between 50 GeV and 280 GeV.

This proposal lays the ground for a new decade of fascinating QCD-related studies of nucleon structure and in hadron spectroscopy. It details the physics scope and related hardware upgrades for those topics for which data taking can be envisaged to start in 2012. This implies mainly studies of chiral perturbation theory, “unpolarised” generalised parton distributions, and transverse-momentum-dependent parton distributions.

More distant projects, as the whole complex of future QCD studies using hadron spectroscopy and also studies of "polarised" GPDs, will be described later in an addendum to this proposal. All these studies will significantly expand our knowledge on key aspects of hadron structure and spectroscopy which are inaccessible to any other facility existing or under construction.

The concept of GPDs attracted much attention after it was shown that the total angular momentum of a given parton species, J^f for quarks ($f = u, d$ or s) or J^g for gluons, is related to the second moment of the sum of the two GPDs H and E. As of today, it is by far not fully understood how the nucleon spin $\frac{1}{2}$ is shared between the contributions of intrinsic and orbital angular momenta of quarks of various flavors and gluons. Constraining quark GPDs experimentally by measuring exclusive Deeply Virtual Compton Scattering (DVCS), $\mu\, p \to \mu\, \gamma\, p$, or Deeply Virtual Meson (M) Production (DVMP), $\mu\, p \to \mu\, M\, p$, is the only known way to constrain the quark components of the nucleon's spin budget $\frac{1}{2} = \sum_{f=u,d,s} J^f + J^g$. Such data will also be very important to experimentally validate GPD moments calculated from first principles through QCD calculations on the lattice. In order to ensure exclusivity of DVCS and DVMP events, a new recoil detector will surround a 2.5 m long liquid hydrogen target. The kinematic domain accessible with 160 GeV muon beams cannot be explored by any other facility in the near future. The DVCS cross section will be determined as a function of both the momentum transfer between initial and final nucleons and the fraction of the longitudinal nucleon momentum carried by the struck parton. A new electromagnetic calorimeter (ECAL0) will provide coverage of substantially higher values of this fraction as compared to the existing calorimeters ECAL1 and ECAL2. One key result will be the first, model-independent answer on the question how the transverse nucleon size varies gradually from the gluon/sea-quark region to that dominated by valence quarks. Only COMPASS can explore the kinematic region between the H1/ZEUS collider range and the HERMES/JLAB fixed-target range, so that particularly important results can be expected from 3-dimensional nucleon "tomography" within this kinematic domain. The transverse structure of the nucleon in the COMPASS kinematic range is considered to be important input for background simulations in proton-proton collisions at LHC. The second key result is information on the GPD H, obtained by separating the real and imaginary parts of the DVCS amplitude. This will be accomplished by combining data from positive and negative muon beams. The azimuthal dependence of the cross section will be used to isolate the contribution of the GPD H, which is of particular importance for the evaluation of the spin sum rule. The measurements with the liquid hydrogen target will mainly constrain H. An extension of the programme is envisaged using a transversely polarised target, mainly to constrain E. This will be subject of an addendum to this proposal. After completion of data taking, the combined DVCS and DVMP data set of H1, ZEUS, COMPASS, HERMES and JLAB will constrain the nucleon-helicity-conserving u and d quark GPDs over a wide kinematic range in parton longitudinal momentum versus parton transverse localisation, and virtual-photon resolution scale. It is expected that ongoing activities towards global fits of GPDs will lead to a reliable determination of total and also orbital quark angular momenta.

Simultaneously with the GPD programme, high-statistics data will be recorded on unpolarised semi-inclusive deep inelastic scattering, $\mu\, p \to \mu\, h\, X$. The pion and kaon multiplicities will be used to extract at leading order α_s (LO) the unpolarised strange quark distribution function $s(x)$ as well as fragmentation functions describing how a quark fragments into a hadron. Presently, the poor knowledge of these quantities is the limiting factor in the determination of the polarisation of strange quarks from SIDIS data. These multiplicities will also represent important input to future global analyses beyond LO.

The transverse momentum of partons is a central element in understanding the 3-dimensional structure of the nucleon. From the measured azimuthal asymmetries of hadrons produced in unpolarised SIDIS and DY processes a sizable transverse momentum was derived. When this intrinsic transverse momentum is taken into account, several new functions are required to describe the structure of the nucleon. Transverse spin, in fact, couples naturally to intrinsic transverse momentum, and the resulting correlations are encoded in various transverse-momentum-dependent parton distribution and fragmentation functions. The SIDIS cross section contains convolutions of these two types of functions, while the convolutions in the DY cross section comprise only PDFs and/or TMDs. In spite of the widespread interest in this approach which goes beyond collinear QCD, the field is still in its infancy and only data can sort out which correlations are appreciably different from zero and relevant. Of particular interest are the correlations between quark transverse momentum and nucleon transverse spin, and between quark transverse spin and its transverse momentum in an unpolarised nucleon, which are encoded in the so-called Sivers and Boer–Mulders functions, both (naïvely) T-odd. The Boer–Mulders function contributes to the azimuthal modulations in the cross sections of unpolarised SIDIS and DY processes which have been observed since many years. We intend to accurately measure such modulations both in DY and in SIDIS (this last measurement in parallel to the GPD programme). Much attention in the recent years has been devoted to the Sivers function originally proposed to explain the large single-spin asymmetries observed in hadron–hadron scattering. From T-invariance arguments, for a long time it was believed to be zero. One of the main theoretical achievements of the recent years was the discovery that the Wilson-line structure of parton distributions, which is necessary to enforce gauge invariance of QCD, implies a sign difference between the T-odd distributions measured in SIDIS and the same distributions measured in DY. According to this "restricted universality", the Sivers function can be different from zero but must have opposite sign in SIDIS and DY. There is a keen interest in the community to test this prediction which is rooted in fundamental aspects of QCD, and many laboratories are planning experiments just to test it. The Sivers function was recently measured by HERMES and COMPASS in SIDIS off transversely polarised targets and shown to be different from zero and measurable. In order to test its sign change, DY experiments with transversely polarised hadrons are required, but none were performed so far. The main goal of our DY programme is to measure for the first time on a transversely polarised target the process $\pi^- p^\uparrow \rightarrow \mu^+\mu^- X$. This will be a unique measurement as at COMPASS energies the virtual photon originates mainly from the fusion of a $\bar{u}$ quark from the pion and a u quark from the nucleon, both in valence-like kinematics. In two years of data taking with the 190 GeV π^- beam and the COMPASS spectrometer with the NH_3 transversely polarised target, the fundamental prediction for the sign of the u quark Sivers function can be tested for the first time.

Measurements of exclusive final states produced by incoming high-energy pions at very small momentum transfer to the recoiling nucleus, explore the Primakoff region where the cross section is dominated by the exchange of a quasi-real photon. The initial $\pi^-\gamma^*$ system may scatter into $\pi^-\gamma$ (Compton reaction), $\pi^-\pi^0$, $\pi^-\pi^0\pi^0$, $\pi^-\pi^+\pi^-$, or final states containing more pions. In QCD, chiral Perturbation Theory (ChPT) predicts the low-energy behaviour for all these reactions at small intermediate-state masses $m^2_{\pi\gamma}$, from threshold to a few pion masses. The chiral expansion of the cross section contains several low-energy constants which describe important physical properties of the pion. For the Compton reaction, the ChPT calculations result in deviations from the QED bremsstrahlung cross section that is exactly calculable for a point-like particle. The first term in the expansion in $m_{\pi\gamma}$ originates from the electric and magnetic dipole polarisabilities of the charged pion, α_π and β_π, and is proportional to their difference $\alpha_\pi - \beta_\pi$. In order to resolve these two polarisabilities independently, *i.e.* to also determine $\alpha_\pi + \beta_\pi$, it is necessary to measure the cross section differential in the centre-of-momentum scattering angle θ_{cm}, in which the two contributions have a complementary functional dependence. At that level of precision, it is possible (and necessary) to also account for the most relevant combination of the pion quadrupole polarisabilities, $\alpha_2 - \beta_2$. Its effect has a similar θ_{cm} dependence as that of $\alpha_\pi - \beta_\pi$ but is proportional to $m^4_{\pi\gamma}$ instead of $m^2_{\pi\gamma}$. The planned measurements will also allow for the determination of the two combinations $\alpha_\pi + \beta_\pi$ and $\alpha_2 - \beta_2$, for the first time. The neutral (electromagnetic) trigger permits at the same time the precise measurement of final states containing one or more π^0. The threshold behaviour of $\pi^-\pi^0$ determines the chiral anomaly constant $F_{3\pi}$, for which the new data set will allow a new level of experimental precision beyond that of the theoretical prediction of about 1%.

The physics programme described in this proposal covers a period of five years, one year for the tests of chiral perturbation theory and two years each for the GPD and DY programmes. The tentative schedule for the first three years is as follows:

- 2012: Tests of chiral perturbation theory,
- 2013: GPD programme,
- 2014: Drell–Yan programme.

On the basis of the results from the 2008 and 2009 hadron runs, an addendum to this proposal aiming at further hadron spectroscopy measurements will be submitted in due time. The schedule of these measurements will be considered together with that of the remaining parts of the proposed GPD and DY programmes, possibly taking into account extensions of the latter as sketched in the proposal.

4 Experimental studies of chiral perturbation theory

From the earliest attempts to understand the strong interaction more than 70 years ago, the pion and its properties have played a key role, first as an exchange particle in the nucleon–nucleon interaction, and later as the lightest quark–gluon bound state of Quantum Chromodynamics (QCD). Revealing and explaining the pion's global properties and the details of the internal structure, is still a challenge for experimental and theoretical particle physics, specifically in verifying the validity of QCD for the dynamics of non-perturbative bound states and low-energy reactions.

Exploiting the smallness of the u, d, s quark masses, the approximate chiral symmetry of the QCD Hamiltonian, $\mathrm{SU(3)_L \times SU(3)_R}$, can be used to construct the low-energy effective field theory, which allows to expand the strong interactions systematically in the particle momenta. This approach is called Chiral Perturbation Theory (ChPT). According to the Goldstone theorem, the spontaneous breaking of the chiral symmetry in the QCD vacuum manifests itself in the occurrence of (almost) massless pseudoscalar Nambu-Goldstone bosons. These are identified with the observed pions and kaons (and the eta). Within this theory, their small masses originate from the non-vanishing quark masses, which break the chiral symmetry explicitly. The first complete treatment of ChPT up to one-loop order has been presented by Gasser and Leutwyler in Ref. [154], where also references to earlier work can be found. For a recent overview of the current status of ChPT in the meson sector, see Ref. [155].

The crucial feature of ChPT is to establish various connections between physical observables as a consequence of the (approximate) chiral symmetry of QCD, often referred to as low-energy theorems. Working out the systematic corrections, ChPT can give firm predictions for the strong interaction dynamics of the Goldstone bosons, which is often very difficult to determine experimentally. The most striking example concerns the long-standing problem of the pion electromagnetic polarisabilities. In ChPT, the (dominant) difference of the electric and magnetic polarisabilities is directly related to the strength of the radiative pion decay. Beyond that, higher-order corrections and a theoretical error estimate have been worked out recently in Ref. [156]. The pion polarisabilities (together with chiral loop contributions) give rise to deviations of the pion Compton cross section $\sigma(\pi\gamma \to \pi\gamma)$ from the QED expectation valid for a structureless spin-0 particle, as discussed in detail in Sect. 4.1.

Moreover, within ChPT the coupling constants for reactions including more pions in the final state are equally well controlled, *e.g.* the chiral anomaly driving the low-energy behaviour of the reaction $\pi^{\pm}\gamma \to \pi^{\pm}\pi^{0}$. The potential of measuring also those reactions, closely related to the Compton reaction and consequently measurable in parallel as reviewed in Ref. [157], is addressed in Sect. 4.2.

4.1 Pion and kaon polarisability measurement

The pion electric and magnetic dipole polarisabilities α_π and β_π characterise the response of a (charged) pion, as a composite $q\bar{q}$ system, to external electromagnetic fields in the low-frequency limit. Clearly these are fundamental structure parameters of the pion, and the comparison between theoretically predicted and directly measured values provides a stringent test for various theoretical approaches, like ChPT, dispersion sum rules, QCD sum rules and quark confinement models. The theoretical predictions disagree markedly with each other and lie in the range $(2-8) \times 10^{-4}$ fm^3 for the absolute values of α_π and β_π [157–159]. Several attempts were made in the past to measure these quantities (see, *e.g.* Ref. [160]) using different experimental approaches. The results obtained are affected

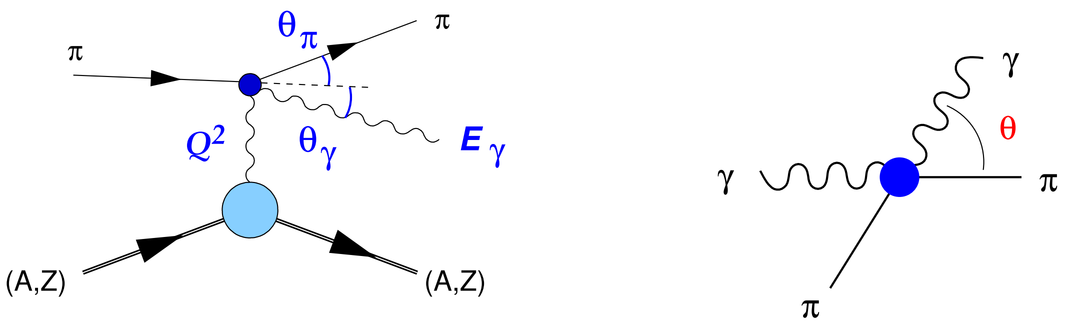

Figure 40: Pion Compton reaction (right graph) embedded in the Primakoff reaction (left graph) on a nucleus of charge Z. Kinematical quantities in the laboratory and the CM scattering angle are indicated.

by large uncertainties and there are even large discrepancies between them. The ongoing dispute about the compatibility of the ChPT results for the pion polarisabilities with the those of the dispersion relation approach, as expressed in Refs. [161, 162], demonstrates once more the urgent need for experimental clarification.

The COMPASS experiment provides unique tools to measure precisely the pion polarisabilities in the Primakoff reaction

$$\pi^- Z \to \pi^- Z \gamma \tag{53}$$

embedding the pion Compton scattering reaction as depicted in Fig. 40. The cross section for the Primakoff reaction (53), treating the nuclear vertex in the equivalent photon approximation [163] is given by

$$\frac{\mathrm{d}\sigma}{\mathrm{d}s\,\mathrm{d}t\,\mathrm{d}Q^2} = \frac{\alpha}{\pi(s-m_\pi^2)} \cdot F_{\mathrm{eff}}^2(Q^2) \cdot \frac{Q^2 - Q^2_{\mathrm{min}}}{Q^4} \cdot \frac{\mathrm{d}\sigma_{\pi\gamma}}{\mathrm{d}t} \tag{54}$$

where $Q_{\mathrm{min}} = (s - m_\pi^2)/2E_{\mathrm{beam}}$, s and t are the Mandelstam variables in the $\pi\gamma$ system. Using the threshold expansion for the $\pi\gamma$ subprocess, the polarisabilities are introduced at the level of Compton amplitudes (following Ref. [156])

$$\frac{\alpha}{m_\pi} H_{+\mp}(t, s = m_\pi^2) = (\alpha_\pi \pm \beta_\pi) + \frac{t}{12}(\alpha_2 \pm \beta_2) + \ldots \tag{55}$$

where the leading Born terms are subtracted to obtain the reduced (spin-flip and spin-nonflip) helicity amplitudes $H_{+\mp}$. This leads (to linear order) to the pion polarisability term $\mathcal{P}$ for the differential cross section

$$\frac{\mathrm{d}\sigma_{\pi\gamma}}{\mathrm{d}\Omega_{cm}} = \frac{\alpha^2(s^2 z_+^2 + m_\pi^4 z_-^2)}{s(s z_+ + m_\pi^2 z_-)^2} - \frac{\alpha\, m_\pi^3\,(s - m_\pi^2)^2}{4s^2(s z_+ + m_\pi^2 z_-)} \cdot \mathcal{P} \tag{56}$$

which is given by

$$\mathcal{P} = z_-^2(\alpha_\pi - \beta_\pi) + \frac{s^2}{m_\pi^4} z_+^2(\alpha_\pi + \beta_\pi) - \frac{(s - m_\pi^2)^2}{24s} z_-^3(\alpha_2 - \beta_2) \tag{57}$$

and $z_\pm = 1 \pm \cos\theta_{cm}$, θ_{cm} the scattering angle in the CM system of the outgoing $\pi\gamma$ pair. The last term accounts for the quadrupole polarisability difference $\alpha_2 - \beta_2$, which emerges in a consistent treatment in the same order as the dipole polarisability sum $\alpha_\pi + \beta_\pi$. The full expansion in $s = m_{\pi\gamma}^2$ to the given order requires terms quadratic in the polarisabilities. They are omitted here as they do not change the salient features given by the linear terms.

The effect of the difference of electric and magnetic polarisability ($\alpha_\pi - \beta_\pi$) is strongest under backward angles (for this reason, this quantity is also called backward polarisability), while the forward polarisability ($\alpha_\pi + \beta_\pi$) influences the cross section mostly at large $\cos\theta$. While the latter forward polarisability is expected to assume small values, it is enhanced in the cross section by the prefactor s^2/m_π^4. As a consequence, measuring the energy and angular dependence of the cross section allows to extract the two dipole polarisabilities separately. Furthermore, within ChPT the 1- and 2-loop contributions are to be taken into account for a correct interpretation of the experimental cross section.

The effect of the polarisabilities as given by Eq. (56) is depicted in Fig. 41, also showing the kinematical relation with the laboratory quantities. The physically interesting region includes photons with energies in the range from 20 to 180 GeV at angles from 0 to 8 mrad with respect to the incoming beam pion direction.

The study of Primakoff reactions in COMPASS was first started in the pilot hadron run in 2004 using 190 GeV π^- and μ^- beams impinging on a solid Pb target, segmented in longitudinal direction. Additional samples for Cu and C targets were also collected. The total amount of pion Primakoff events from the lead target was about 60,000 events with photon energies above 40 GeV. Instabilities in the amplification of many cells of the electromagnetic calorimeter connected with saturation effects and some features of the Primakoff trigger, including a missing row in the sensitive central region, turned out to cause significant systematic uncertainties of the measurement and do not allow to extract a reliable value for the pion polarisabilities from the 2004 data. However, the measurement allowed to address the full measurement procedure and established the feasibility of a much improved measurement.

The most important achievements of the present analysis are, on the one hand, the selection of Primakoff reactions as exclusive $\pi\gamma$ events (Fig. 42), the identification of the Primakoff peak and the diffractive background in the Q^2 distribution (Fig. 43) allowing to confirm the Z^2 dependence of the Primakoff peak following the theoretical prediction (Fig. 44). On the other hand, we determined important parameters of our setup such as resolutions and Monte Carlo control of detector efficiencies and identified the main sources of background, both, non separable physics processes (the ratio of Primakoff signal to diffractive background for different targets is shown in Fig. 43) and backgrounds stemming from beam impurities for which a set of procedures for background reduction has been developed. Corrections to the pure tree level Primakoff cross section come from the Compton vertex, multiple photon exchange, vacuum polarisation, nuclear charge screening by atomic electrons and contribution of nuclear form factor and have now also been calculated [164, 165]. The full Q^2 dependence was also investigated within the Glauber model in the work of [166, 167], incorporating the influence of the strong interaction.

In the recent Primakoff data taking in November 2009, several of the learnings from the 2004 run have been taken into account, with the perspective of extracting a reliable value for $\alpha_\pi - \beta_\pi$ from a statistics of about a factor three larger than the one of 2004. Those include

– Usage of an unsegmented target with the thickness of $0.3X_0$. This target provides the opportunity to collect large statistics with high data quality (good resolution for Q^2, low background from beam kaon decays due a shorter fiducial volume cut).

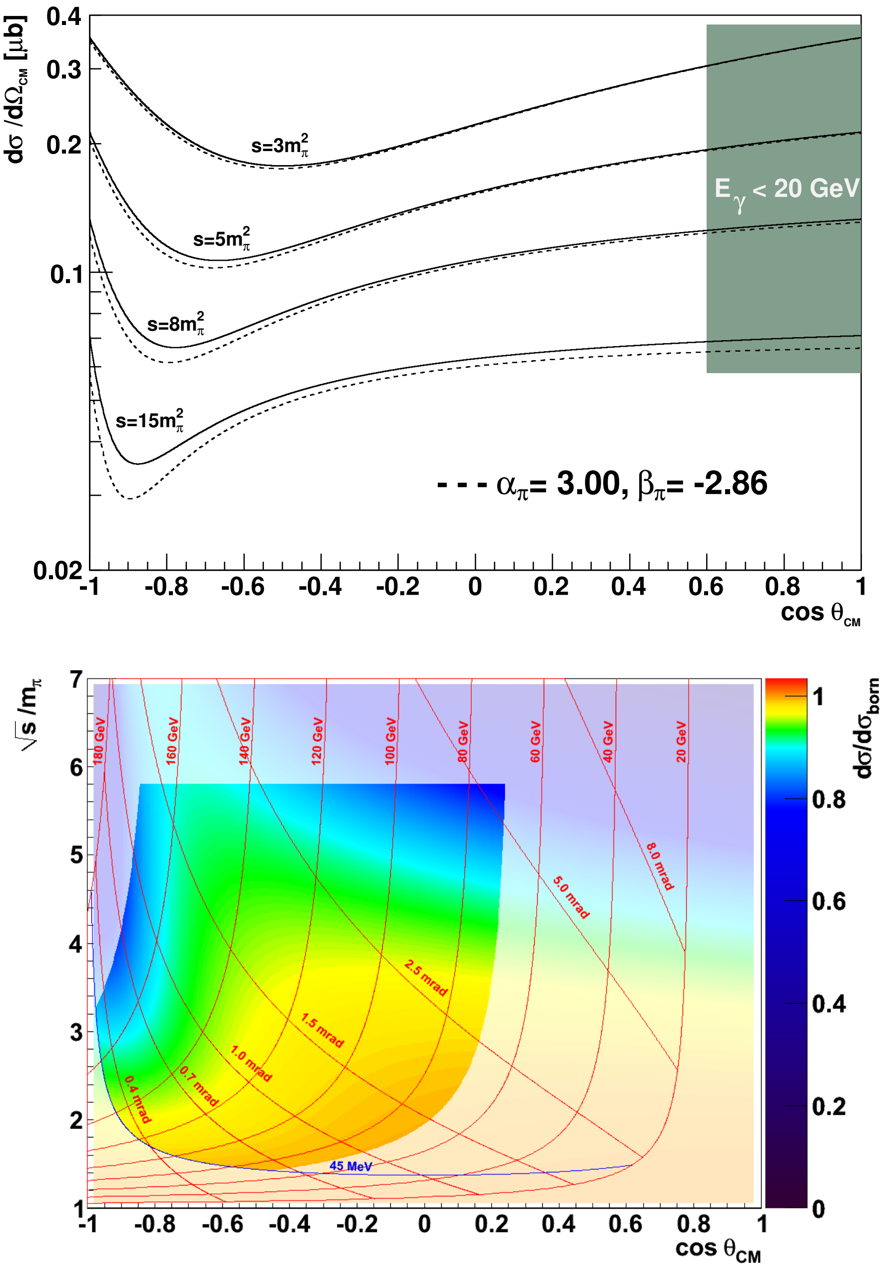

Figure 41: Top: Pion Compton scattering cross section (continuous line: point-like case) and polarisability effect (dashed line: prediction of chiral perturbation theory). Bottom: relation to the photon kinematics (energy and production angle) in the laboratory. In colour, the relative effect of the dipole polarisabilities (ChPT values) on the cross section is shown (in light colour saturation, the region outside of the kinematical cuts is indicated).

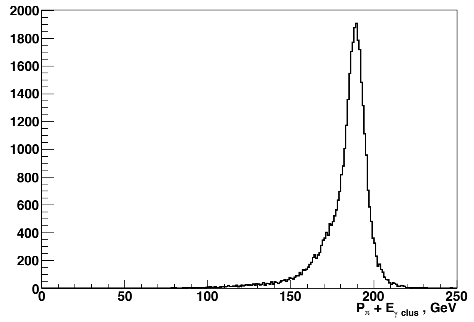

Figure 42: Exclusivity peak of $E_\gamma + E_\pi$ for $\pi\gamma$ events.

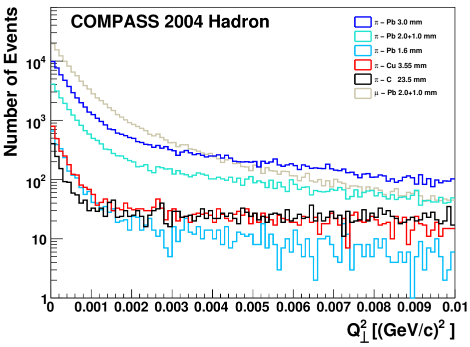

Figure 43: Q^2 distribution for different targets. The Primakoff peak at $Q^2 = 0$ is nicely visible.

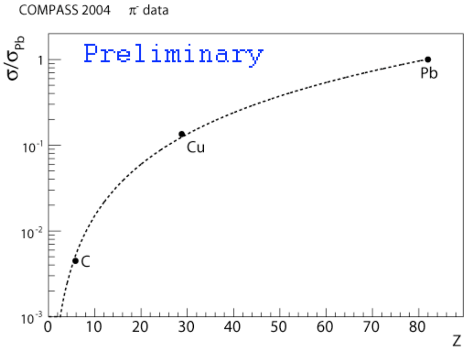

Figure 44: Z^2 dependence of the Primakoff cross section.

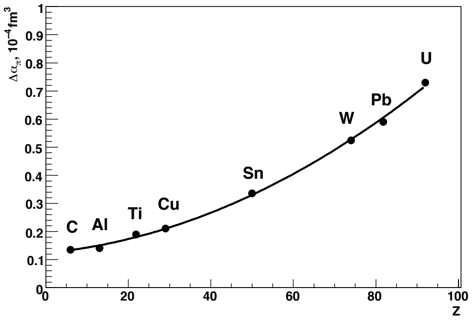

Figure 45: Systematic shift of α_π due to radiative corrections.

Replacing Pb by Ni as target material reduces the effect radiative corrections more significantly for lead, and the correction related to the nuclear form factor. The spin-0 $^{58}_{28}$Ni nucleus simplifies the estimation of radiative corrections.

- The layout of the target region was kept similar to the hadron run 2009, with the hydrogen target being replaced by a solid target. The present geometrical positions of silicon and PixelGEM detectors allow to measure the scattering angle of pions with the required precision of $\Delta p_T < 10$ MeV, and to also collect the statistics for beam kaons decay up- and downstream of the target, which is important for $K^- \to \pi^-\pi^0$ background determination, though kaon background will be much reduced owing to the CEDARs.
- The new digital ECAL2 trigger on the Primakoff photons was installed. As these photons are concentrated in the central part of ECAL2, it was sufficient to include the 12×12 central cells. For the other processes of interest, as outlined in the next section, will require a larger active ECAL area to be included in the trigger.
- The trigger hodoscopes downstream of the concrete wall, used in the muon program in order to provide particle identification in the range 15 GeV/$c < p <$ 20 GeV/c, was activated in order to provide muon–pion separation.

Table 13: Proposed running time, the respective total beam flux for pions and muons, and expected total errors on the pion polarisabilities (units 10^{-4} fm^3, except quadrupole polarisability values in units of 10^{-4} fm^5).

Days	π beam, days	μ beam, days	Flux $\pi, 10^{11}$	Flux $\mu, 10^{11}$	$\alpha_\pi - \beta_\pi$ σ_{tot}	$\alpha_\pi + \beta_\pi$ σ_{tot}	$\alpha_2 - \beta_2$ σ_{tot}
120	90	30	59	12	±0.27	fixed	fixed
					±0.26	±0.016	fixed
					±0.66	±0.025	±1.94
					ChPT prediction		
					5.70	0.16	16

- CEDARs are required for beam kaon identification. Their performance in 2009 is still to be studied.
- An optimised electron converter was installed on the beam line to decrease the admixture of the electrons in the hadron beam. It is positioned close to the last major bending dipoles or downstream of CEDAR 2.
- The VetoBox surrounding the target and used in 2004 was replaced by the new recoil proton detector, serving as veto system. The forward sandwich veto suppresses reactions of particles under large angles.

One of the key features for this measurement within Compass is the study of systematic effects using a well known calibration process, Primakoff scattering by muons. In the following we assume all of the systematic effects to be measured using muons, thereby neglecting for the moment effects on beam shape and intensity, secondary interactions and systematic effects based on concurring physics processes different for the two particle species. In order to keep the systematic uncertainty below the statistical one, we need to collect data shared between pion and muon beams as given in Table 13. Using a $0.3X_0$ Ni target and beam intensities of 4×10^7 per spill for pions and 4×10^8 per spill for muons we have calculated event rates and uncertainties, where we assume the geometrical acceptance for Primakoff events and the efficiency of our selecting cuts to be the same as in 2004 (but which improved performance of ECAL 2 and trigger hodoscopes). Collecting 10 full runs (1000 spills) per day, as was realised in the previous beam times, we give the corresponding values for beam fluxes and the total uncertainties for different periods of data taking in Table 13, subdivided into three different ways to fit the polarisabilities: Fixing the subleading contributions $\alpha_\pi + \beta_\pi$ and $\alpha_2 - \beta_2$ to some value decreases the statistical uncertainty on the free parameter(s) as given in the first two rows. This, however, will lead to an unknown shift of the fitted value(s) due to the correlation between them (especially $\alpha_\pi - \beta_\pi$ and $\alpha_2 - \beta_2$). Since none of the polarisability combinations is constraint in principle, only the full 3-parameter fit (3$^{\text{rd}}$ row) is regarded as the goal for this measurement. For the quadrupole contribution, the full 2-loop result is given [156]. If the 1-loop contribution (12×10^{-4} fm^5) is explicitly taken out, as has been done for the dipole polarisability extraction in the Serpukhov data analysis [168], the ChPT prediction reads 4×10^{-4} fm^5. In Table 13, time needed for detector commissioning is not included. Small data samples with empty target which will help to study the systematic effects are also not included, however their collection should take just a few hours.

So far all experiments performed have only been able to address a combination of electric and magnetic polarisability (namely $\alpha_\pi - \beta_\pi$). Compass can, for the first time,

Table 14: Expected precision of the kaon polarisability measurement obtained in parallel with the proposed running time in Table 13 (units 10^{-4} fm^3).

π/K beam days	Flux $\pi, 10^{11}$	Flux $K, 10^{11}$	$\alpha_K - \beta_K$ σ_{tot}	$\alpha_K + \beta_K$ σ_{tot}	$\alpha_{K,2} - \beta_{K,2}$ σ_{tot}
90	59	1.4	±0.08	fixed	fixed
			ChPT prediction		
			1.0	-	-

also perform an independent measurement of α_π and β_π using the information about both, energy and scattering angle of Primakoff photons. Within the proposed data taking, we can expect a statistical uncertainty on the level of 0.66×10^{-4} fm^3 on the difference of dipole polarisabilities, and 0.025×10^{-4} fm^3 for their sum. Here, it should be stressed that the investigation of the full s dependence includes to account for the 1- and 2-loop contributions predicted by Chiral Perturbation Theory, which are also viewed as dynamic polarisability $\alpha_\pi(s)$, in contrast to the s-averaged measurements discussed so far. The range of s accessible for Compass includes also the region of ρ meson decays, which contains interesting information, as the radiative width of the ρ, by itself.

In addition to the precise measurement of the pion polarisabilities, we can observe Primakoff scattering with charged kaons for the first time and thus obtain the kaon polarisability. For the proposed data taking, we expect about 4000 Primakoff events with kaons in the sensitive range $0.5 < \omega < 0.9$. Thus a first and coarse measurement of the kaon polarisability can also be obtained in parallel to the high precision determination of the pion polarisability outlined above due to the usage of CEDARs for separation of kaons and pions in the beam (Table 14).

The experimental setup has to be optimised in the following ways for the proposed data taking:

- In order to ensure high redundancy in the tracking of incoming and outgoing pions, an additional tracking station will be installed downstream of the target. Precision in the scattering angle requires distances smaller than 1 m between target and closest tracking stations.
- The measurement of the kaon polarisabilities require an improvement in kaon identification by the CEDAR system, which has to be optimised or rebuilt.
- The RICH beam pipe has to be replaced by a solution which minimises the conversion probability for photons and the multiple scattering for charged particles.
- The digital trigger electronics, which came as a very new installation to the 2009 data taking, has to be finalised.

4.2 Primakoff reactions with neutral pions in the final state

In parallel to the Primakoff Compton scattering Eq. (53) Compass also aims to measure Primakoff reactions with neutral mesons in the final state, already been observed in the 2004 pilot run:

$$\pi^- Z \rightarrow \pi^- Z\, \pi^0 \tag{58}$$

$$\pi^- Z \rightarrow \pi^- Z\, \pi^0 \pi^0 \tag{59}$$

$$\pi^- Z \rightarrow \pi^- Z\, \eta \tag{60}$$

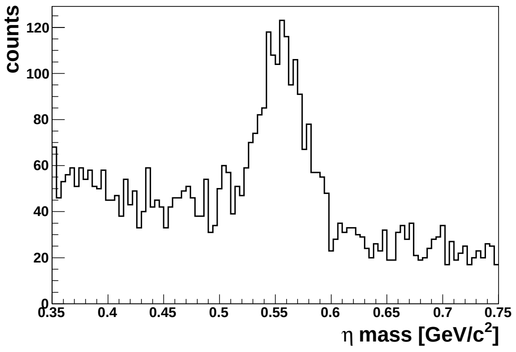

Figure 46: η mass spectrum for the $\pi^-\eta$ final state (no background subtraction, very coarse cut set).

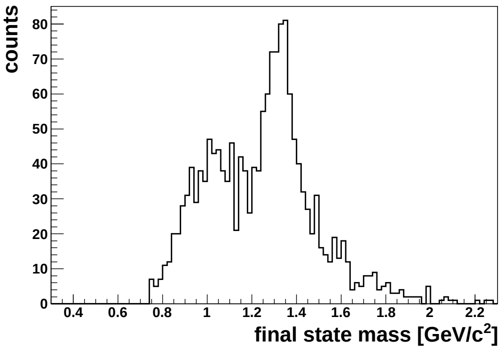

Figure 47: The mass spectrum of the $\pi^-\eta$ final state for $Q^2 < 0.002$ GeV^2 (no background subtraction, very coarse cut set) is dominated by $a_2(1320)$. Improving event selection and subtraction of background is expected to clear up the picture.

The measurement of Eq. (58) allows to determine the chiral anomaly amplitude $F_{3\pi}$, for which Chiral Perturbation Theory (ChPT) makes an accurate prediction by relating the process to the π^0 decay constant f_π and the electric coupling constant α_{em}. This constitutes a test of higher-order ChPT. The reaction Eq. (59) is calculable directly at tree level ChPT [157], using the pion scattering lengths a_0, a_2, combined with the electromagnetic coupling α. Here, the ChPT expansion should be reliable on the percent level, and so, the experiment constitutes a strong test of χPT at tree level and goes much beyond the determination of low energy constants.

Reaction Eq. (58) has already been examined by the Serpukhov experiment [169], however in the relevant region of $s < 10\ m_\pi^2$ only about 200 events were obtained. Reaction Eq. (59) has not been determined up to now.

Reaction Eq. (60) allows the direct observation of $1^-(1^{-+})$ exotics created in photoproduction as the selection of Primakoff events removes a_0 decaying to the same final state (Figs. 46 and 47).

All of these channels have been identified in the 2004 pilot run with effectively three days of COMPASS beam on a segmented 2+1 mm Pb target. About 320 events with exclusive single π^0 production with $s < 10\ m_\pi^2$ (Fig. 48), and 85 events with exclusive double π^0 in the interesting range $s < 22\ m_\pi^2$ have been reconstructed (Fig. 49). The cut on exclusivity was ±10 GeV for the reaction of Eq. (58) and ±15 GeV for that of Eq. (59) around the nominal beam energy, obtained as exclusivity peak in the sum of the outgoing pion energies. The quasi-real photon exchange was selected with cuts of $Q^2 < 0.001$ GeV^2 and $Q^2 < 0.005$ GeV^2 for reactions of Eqs. (58) and (59), respectively. Background has been subtracted using an adjacent Q^2 side band. A new measurement should aim for at least 10,000 events in the $s < 10\ m_\pi^2$ range for the π^0 channel, as it was also originally proposed for COMPASS. We expect about 2,500 events for the $\pi^0\pi^0$ channel at the same time.

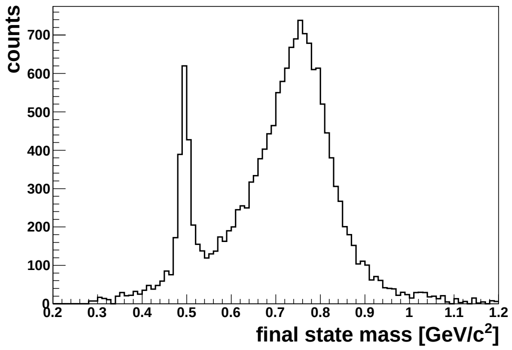

Figure 48: The invariant mass spectrum of $\pi^-\pi^0$ is dominated by ρ^- photo-production. On its left side the decay of beam K^- gives rise to a narrow kaon line. Still further to lower masses, anomal π^0 production can be seen as a rising slope starting at 2 m_π.

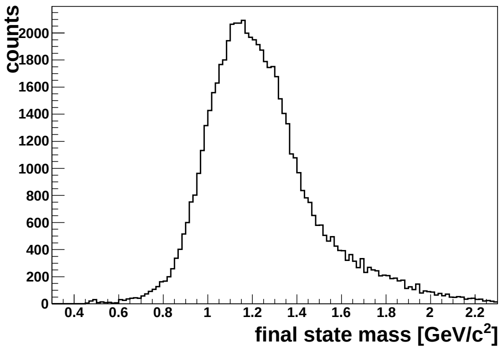

Figure 49: In the invariant mass spectrum of $\pi^-\pi^0\pi^0$, the a_1 photo-production peak is interfering with direct $\pi^0\pi^0$ production, most easily observed close to the 3 m_π threshold.

Appendix D

Articles on $\pi\gamma$ Reactions, Radiative Corrections and Chiral Dynamics

N. Kaiser, J. M. Friedrich: Cross-sections for low-energy $\pi^-\gamma$ reactions [44]

N. Kaiser, J. M. Friedrich: Radiative corrections to pion Compton scattering [45]

N. Kaiser, J. M. Friedrich: Radiative corrections to pion-nucleus bremsstrahlung [46]

C. Adolph et al. [The COMPASS collaboration]:
First Measurement of Chiral Dynamics in $\pi^-\gamma \rightarrow \pi^-\pi^-\pi^+$ [2]
edited and the drafting chaired by J. M. Friedrich

Bibliography

[1] P. Abbon et al. The COMPASS experiment at CERN. *Nucl. Instrum.Meth.*, A577: 455–518, 2007.

cited on pp. 79 and 121

[2] C. Adolph et al. First Measurement of Chiral Dynamics in $\pi^-\gamma \to \pi^-\pi^-\pi^+$. *Phys. Rev. Lett.*, 108: 192001, 2012.

cited on pp. 12, 69, 70, 75, 78, and 169

[3] E.S. Ageev et al. Search for the $\Phi(1860)$ pentaquark at COMPASS. *Eur. Phys. J.*, C41: 469–474, 2005.

cited on p. 13

[4] J. Ahrens et al. Measurement of the π^+ meson polarizabilities via the $\gamma p \to \gamma\pi^+ n$ reaction. *Eur. Phys. J.*, A23: 113–127, 2005.

cited on pp. 8 and 66

[5] A.A. Akhundov et al. Electromagnetic corrections to the compton effect on π meson. *Sov. J. Nucl. Phys.*, 37: 217, 1983.

cited on pp. 10 and 11

[6] A.A. Akhundov et al. About the electromagnetic corrections to the polarisabilities of a charged pion. *Sov. J. Nucl. Phys.*, 42: 426, 1985.

cited on pp. 10 and 54

[7] A.A. Akhundov et al. Radiative corrections for pion polarizability experiments. *Z. Phys.*, C66: 279–284, 1995.

cited on p. 10

[8] M. Alekseev et al. Observation of a $J^{PC} = 1^{-+}$ exotic resonance in diffractive dissociation of 190-GeV/c π^- into $\pi^-\pi^-\pi^+$. *Phys. Rev. Lett.*, 104: 241803, 2010.

cited on pp. 12, 69, 70, and 76

[9] L. Ametller, M. Knecht, and P. Talavera. Electromagnetic corrections to $\gamma\pi^+ \rightarrow \pi^0\pi^+$. *Phys. Rev.*, D64: 094009, 2001.

cited on p. 68

[10] Yu.M. Antipov, V.A. Batarin, V.A. Bezzubov, N.P. Budanov, Yu.P. Gorin, et al. Investigation of $\gamma \rightarrow 3\pi$ chiral anomaly during pion pair production by pions in the nuclear Coulomb field. *Phys.Rev.*, D36:21, 1987.

cited on p. 67

[11] Yu.M. Antipov et al. Measurement of pi- Meson Polarizability in Pion Compton Effect. *Phys. Lett.*, B121: 445, 1983.

cited on pp. 8, 9, 41, 66, and 67

[12] M. Becker. *Diploma thesis: Setup of a Cryogenic System for Silicon Microstrip Detectors of the COMPASS Experiment.* TU München (unpublished), 2004.

cited on pp. 9, 79, and 81

[13] J.C. Bernauer et al. High-precision determination of the electric and magnetic form factors of the proton. *Phys. Rev. Lett.*, 105: 242001, 2010.

cited on p. 11

[14] K. Bicker. *Diploma thesis: Construction and Commissioning of a Cooling and Support Structure for the Silicon Detectors for the COMPASS Experiment.* TU München (unpublished), 2011.

cited on pp. 9 and 79

[15] K. Bicker et al. Cryogenic silicon detectors for the COMPASS experiment at CERN. *Nucl. Phys. Proc. Suppl.*, 215: 310–312, 2011.

cited on p. 9

[16] K. Borer et al. Charge collection efficiency and resolution of an irradiated double-sided silicon microstrip detector operated at cryogenic temperatures. *Nuclear Instruments and Methods in Physics Research Section A: Accelerators, Spectrometers, Detectors and Associated Equipment*, 440(1):17 – 37, 2000.

cited on p. 79

[17] I. Bronstein, K. Semendjajew, G. Musiol, and H. Mühlig. *Taschenbuch der Mathematik.* Verlag Harri Deutsch Thun und Frankfurt am Main, 1977 / 1995.

cited on pp. 47, 88, and 92

[18] L.M. Brown and R.P. Feynman. Radiative corrections to Compton scattering. *Phys. Rev.*, 85: 231–244, 1952.

cited on p. 11

[19] Bürgi, Urs. Charged pion pair production and pion polarizabilities to two loops. *Nucl. Phys.*, B479: 392–426, 1996.

cited on p. 55

[20] Bürgi, Urs. Charged pion polarizabilities to two loops. *Phys. Lett.*, B377: 147–152, 1996.

cited on pp. 11 and 55

[21] Curtis G. Callan Jr., Sidney R. Coleman, J. Wess, and Bruno Zumino. Structure of phenomenological Lagrangians. 2. *Phys. Rev.*, 177: 2247–2250, 1969.

cited on p. 8

[22] Suh-Urk Chung and Jan M. Friedrich. Covariant helicity-coupling amplitudes: A New formulation. *Phys. Rev.*, D78: 074027, 2008.

cited on p. 13

[23] Sidney R. Coleman, J. Wess, and Bruno Zumino. Structure of phenomenological Lagrangians. 1. *Phys. Rev.*, 177: 2239–2247, 1969.

cited on p. 8

[24] [The COMPASS collaboration]. *The COMPASS setup for physics with hadron beams.* (in preparation), 2012.

cited on pp. 59 and 79

[25] R. De Masi. *PhD thesis: Development of a cryogenic silicon detector system and study of strange particle production in deep inelastic scattering.* TU München (unpublished), 2004.

cited on pp. 9, 13, and 79

[26] A. Dinkelbach. *PhD thesis: Characterization of the COMPASS silicon detector – Measurement of the Pion Polarisability* . TU München (unpublished), 2010.

cited on pp. 9, 58, 79, and 81

[27] Göran Fäldt and Ulla Tengblad. Coulomb-nuclear interference in pion-nucleus bremsstrahlung. *Phys. Rev.*, C79: 014607, 2009.

cited on pp. 11, 44, 46, and 97

[28] A. G. Fox, M. A. O'Keefe, and M. A. Tabbernor. Relativistic Hartree–Fock X-ray and electron atomic scattering factors at high angles. *Acta Crystallographica Section A*, 45(11): 786–793, Nov 1989.
cited on p. 44

[29] J.M. Friedrich. *PhD thesis [in German]: Messung der virtuellen Comptonstreuung an MAMI zur Bestimmung generalisierter Polarisierbarkeiten des Protons.* Wiley-Interscience publications. Shaker Verlag, 2000.
cited on pp. 11, 54, and 98

[30] A. Fuchs. *Diploma thesis: Setup for a low Temperature Silicon Detector for the COMPASS Experiment.* TU München (unpublished), 2003.
cited on pp. 9 and 79

[31] J. Gasser, M. A. Ivanov, and M. E. Sainio. Revisiting $\gamma\gamma \to \pi^+\pi^-$ at low energies. *Nucl. Phys.*, B745: 84–108, 2006.
cited on pp. 11, 39, 41, and 55

[32] J. Gasser and H. Leutwyler. Chiral Perturbation Theory to One Loop. *Annals Phys.*, 158: 142, 1984.
cited on p. 8

[33] J. Gasser and H. Leutwyler. Chiral Perturbation Theory: Expansions in the Mass of the Strange Quark. *Nucl. Phys.*, B250: 465, 1985.
cited on p. 8

[34] J. Gasser and H. Leutwyler. $\eta \to 3\pi$ to One Loop. *Nucl. Phys.*, B250: 539, 1985.
cited on p. 8

[35] J. Goldstone. Field Theories with Superconductor Solutions. *Nuovo Cim.*, 19: 154–164, 1961.
cited on p. 8

[36] S. Grabmüller. *Diploma thesis: Studies of Diffractive Particle Production at COMPASS.* TU München (unpublished), 2005.
cited on pp. 9 and 79

[37] S. Grabmüller. *PhD thesis: in preparation.* TU München (unpublished), 2012.
cited on pp. 9, 79, 80, and 81

[38] A. Guskov. *PhD thesis: Analysis of the charged pion polarizability measurement method at COMPASS experiment.* Torino university (unpublished), 2010.
cited on p. 9

[39] Torben Hannah. The Anomalous process $\gamma\pi \to \pi\pi$ to two loops. *Nucl. Phys.*, B593: 577–595, 2001.
cited on p. 68

[40] B. Holzgartner. *Diploma thesis: Installation of a Water Cooling Circuit for the Frontend Electronics of the Silicon Microstrip Detectors for the COMPASS Experiment (in preparation).* TU München (unpublished), 2012.
cited on p. 79

[41] S. Huber. *PhD thesis: in preparation.* TU München (unpublished), .
cited on pp. 10 and 58

[42] N. Kaiser. Chiral corrections to $\pi^-\gamma \to 3\pi$ processes at low energies. *Nucl. Phys.*, A848: 198–217, 2010.
cited on pp. 77 and 78

[43] N. Kaiser. Radiative corrections to real and virtual muon Compton scattering revisited. *Nucl. Phys.*, A837: 87–109, 2010.
cited on pp. 48, 49, 50, and 53

[44] N. Kaiser and J.M. Friedrich. Cross-sections for low-energy $\pi^-\gamma$ reactions. *Eur. Phys. J.*, A36: 181–188, 2008.
cited on pp. 12, 39, 51, 77, 78, and 169

[45] N. Kaiser and J.M. Friedrich. Radiative corrections to pion Compton scattering. *Nucl. Phys.*, A812: 186–200, 2008.
cited on pp. 11, 51, 52, 54, 55, 97, 101, 103, and 169

[46] N. Kaiser and J.M. Friedrich. Radiative corrections to pion-nucleus bremsstrahlung. *Eur. Phys. J.*, A39: 71–80, 2009.
cited on pp. 11, 54, and 169

[47] M. Krämer. *PhD thesis: in preparation.* TU München (unpublished), .
cited on p. 58

[48] R. Kuhn. *Diploma thesis: Simulations for the measurement of the polarizabilities of the pion at COMPASS.* TU München (unpublished), 2001.
cited on p. 9

[49] M. Leeb. *Diploma thesis: Optimization of the Clustering and Tracking Algorithms of the Silicon Microstrip Detectors for the COMPASS Experiment.* TU München (unpublished), 2011.
cited on pp. 9 and 79

[50] Xiao-yuan Li and Yi Liao. Photon-3π and π-2γ form-factors from dynamical constituent quarks. *Phys. Lett.*, B505: 119–124, 2001.
cited on p. 68

[51] L. W. Mo and Y. Tsai. Radiative Corrections to Elastic and Inelastic e p and mu p Scattering. *Rev. Mod. Phys.*, 41: 205–235, 1969.
cited on p. 11

[52] V.V. Molchanov et al. Radiative decay width of the a(2)(1320)- meson. *Phys. Lett.*, B521: 171–180, 2001.
cited on pp. 12 and 74

[53] T. Nagel. *PhD thesis: in preparation.* TU München (unpublished), 2012.
cited on pp. 10, 53, 58, 60, 63, 64, 65, and 66

[54] K. Nakamura et al. Review of particle physics. *J. Phys.*, G37: 075021, 2010.
cited on p. 36

[55] V. Olmos de Leon, F. Wissmann, P. Achenbach, J. Ahrens, H.J. Arends, et al. Low-energy Compton scattering and the polarizabilities of the proton. *Eur. Phys. J.*, A10: 207–215, 2001.
cited on p. 16

[56] M. L. Perl. *High energy hadron physics.* Wiley-Interscience publications. Wiley, 1974.
cited on pp. 45, 70, and 74

[57] I. Ya. Pomeranchuk and I. M. Shmushkevich. On processes in the interactions of gamma-quanta with unstable particles. *Nucl. Phys.*, 23: 452–467, 1961.
cited on p. 17

[58] J. Portoles and M.R. Pennington. Theoretical predictions for pion polarizabilities. 1994.
cited on p. 8

[59] H. Primakoff. Photo-Production of Neutral Mesons in Nuclear Electric Fields and the Mean Life of the Neutral Meson. *Phys. Rev.*, 81: 899, 1951.
cited on p. 17

[60] J. Roche et al. The first determination of generalized polarizabilities of the proton by a virtual Compton scattering experiment. *Phys. Rev. Lett.*, 85: 708, 2000.
cited on p. 11

[61] D. Seeharsch. *Magister thesis: A Microcontroller based Steering Mechanism for the COMPASS Silicon Detector Cooling System.* TU München (unpublished), 2004.
cited on pp. 9 and 79

[62] S. Uhl. *PhD thesis: in preparation.* TU München (unpublished), .
cited on p. 58

[63] M. Vanderhaeghen, J.M. Friedrich, D. Lhuillier, D. Marchand, L. Van Hoorebeke, et al. QED radiative corrections to virtual Compton scattering. *Phys. Rev.*, C62: 025501, 2000.
cited on p. 11

[64] von Weizsäcker, C.F. Radiation emitted in collisions of very fast electrons. *Z. Phys.*, 88: 612–625, 1934.
cited on p. 17

[65] R. Wagner. *Diploma thesis: Commissioning of Silicon detectors for the COMPASS experiment at CERN.* TU München (unpublished), 2001.
cited on pp. 9 and 79

[66] S. Weinberg. Phenomenological Lagrangians. *Physica*, A96: 327, 1979.
cited on p. 8

[67] Weinberg, S. *The quantum theory of fields. Vol. 2: Modern applications.* Cambridge university press, 1996.
cited on p. 7

[68] M. Wiesmann. *PhD thesis: A Silicon Microstrip Detector for COMPASS and a First Measurement of the Transverse Polarization of the Lambda-Hyperons from Quasi-Real Photo-Production.* TU München (unpublished), 2004.
cited on pp. 9, 79, and 80

[69] E.J. Williams. Nature of the high-energy particles of penetrating radiation and status of ionization and radiation formulae. *Phys. Rev.*, 45: 729–730, 1934.
cited on p. 17

[70] D.R. Yennie, Steven C. Frautschi, and H. Suura. The infrared divergence phenomena and high-energy processes. *Annals Phys.*, 13: 379–452, 1961.
cited on p. 54

[71] M. Zielinski, D. Berg, C. Chandlee, S. Cihangir, T. Ferbel, et al. Evidence for the electromagnetic production of the a_1. *Phys. Rev. Lett.*, 52: 1195, 1984.
cited on p. 76

[72] P. Zimmerer. *Diploma thesis: Performance of cryogenic silicon microstrip detectors at the COMPASS experiment.* TU München (unpublished), 2011.
cited on pp. 9 and 79

Acknowledgements

This work could not have been done without the help and the contributios from many people to whom the author has to say thanks.

In the first place, thanks go to Prof. Dr. Stephan Paul who engaged me from my previous work on the generalized polarisabilties of the proton for the much more involved and unexplored, hence much more demanding field of measuring the pion polarisabilities via the Primakoff effect. Many, many problems on this lengthy way had to be solved, such that it took much more time than originally expected to really get a handle on the physics aimed at. Without his continuous support, driven by his interest and enthusiasm, this project would not have been brought so near to the final success as it is now. Many thanks, Stephan.

Thanks are also due to the other two supervisors of my "Habilitationsverfahren", Prof. Dr. M. Faessler and Prof. Dr. W. Weise, who accompanied this work with benevolence and encouragement also when progress seemed to be slow.

On the side of bridging the gap between the experimental challenges and the theoretical aspects, the author deeply appreciates a very constructive cooperation with Prof. Dr. Norbert Kaiser which is documented in a number of common publications, and which, first and foremost, resulted in a trustworthy formulation of the relevant theory and its correct application in the experiment, as it then could be implemented into the analysis code of the COMPASS experiments.

Sincere thanks go to the numerous students, who, in the course of time, joined me in order to complete their scientific education by undertaking specific tasks in the realisation of the Silicon microstrip detectors and in the analysis of data taken at CERN. Their engagement was an indispensable, integral part of the great goal we were aiming at together.

The measurement of the pion polarisability constitutes only part of the scientific program of the COMPASS collaboration, and the specific components for this experiment can only be seen as a part of the enormous effort brought in by many people from different places, to whom I am indebted. I mention the groups from TU München and those from Dubna in the first place, since they were the ones who started the whole Primakoff research.

Last, but really not least, thanks go to my wife Judith, who took care for me and for our children Jeremias, Johanna and Justus, such that I could concentrate on this demanding work in the way that is necessary to accomplish it.